5-1-2013

Assessment of bio-fuel options for solid oxide fuel cell applications

Jiefeng Lin

ASSESSMENT OF BIO-FUEL OPTIONS FOR SOLID OXIDE FUEL CELL APPLICATIONS

by

JIEFENG LIN

A DISSERTATION

Submitted in partial fulfillment of the requirements
for the degree of Doctor of Philosophy
in
Sustainability

Department of Sustainability

Golisano Institute for Sustainability
Rochester Institute of Technology

May 2013

Author: _____
Sustainability Program

Certified by: _____
Dr. Thomas A. Trabold
Associate Professor of Sustainability Program

Approved by: _____
Paul H. Stiebitz
Associate Academic Director of Sustainability Program

Certified by: _____
Dr. Nabil Nasr
Assistant Provost and Director, Golisano Institute for Sustainability and CIMS

NOTICE OF COPYRIGHT

Assessment of Bio-fuel Options for Solid Oxide Fuel Cell Applications

by

Jiefeng Lin

Submitted by Jiefeng Lin in partial fulfillment of the requirements for the degree of Doctor of Philosophy in Sustainability and accepted on behalf of the Rochester Institute of Technology by the dissertation committee.

We, the undersigned members of the Faculty of the Rochester Institute of Technology, certify that we have advised and/or supervised the candidate on the work described in this dissertation. We further certify that we have reviewed the dissertation manuscript and approve it in partial fulfillment of the requirements of the degree of Doctor of Philosophy in Sustainability.

Approved by:

Dr. Thomas Smith _____
(Outside Examiner and Chair) Date

Thomas A. Trabold _____
(Dissertation Advisor)

Dr. Callie W. Babbitt _____

Dr. Gabrielle Gaustad _____

Dr. Denis Cormier _____

Dr. Bernhard Fischer _____
(External Examiner)

SUSTAINABILITY PROGRAM
ROCHESTER INSTITUTE OF TECHNOLOGY
May 2013

ABSTRACT

Golisano Institute for Sustainability
Rochester Institute of Technology

Degree Doctor of Philosophy **Program** Sustainability

Name of Candidate Jiefeng Lin

Title Assessment of Bio-fuel Options for Solid Oxide Fuel Cell Applications

Rising concerns of inadequate petroleum supply, volatile crude oil price, and adverse environmental impacts from using fossil fuels have spurred the United States to promote bio-fuel domestic production and develop advanced energy systems such as fuel cells. The present dissertation analyzed the bio-fuel applications in a solid oxide fuel cell-based auxiliary power unit from environmental, economic, and technological perspectives. Life cycle assessment integrated with thermodynamics was applied to evaluate the environmental impacts (e.g., greenhouse gas emission, fossil energy consumption) of producing bio-fuels from waste biomass. Landfill gas from municipal solid wastes and biodiesel from waste cooking oil are both suggested as the promising bio-fuel options. A nonlinear optimization model was developed with a multi-objective optimization technique to analyze the economic aspect of biodiesel-ethanol-diesel ternary blends used in transportation sectors and capture the dynamic variables affecting bio-fuel productions and applications (e.g., market disturbances, bio-fuel tax credit, policy changes, fuel specification, and technological innovation). A single-tube catalytic reformer with rhodium/ceria-zirconia catalyst was used for autothermal reformation of various heavy hydrocarbon fuels (e.g., diesel, biodiesel, biodiesel-diesel, and biodiesel-

ethanol-diesel) to produce a hydrogen-rich stream reformates suitable for use in solid oxide fuel cell systems. A customized mixing chamber was designed and integrated with the reformer to overcome the technical challenges of heavy hydrocarbon reformation. A thermodynamic analysis, based on total Gibbs free energy minimization, was implemented to optimize the operating environment for the reformations of various fuels. This was complimented by experimental investigations of fuel autothermal reformation. 25% biodiesel blended with 10% ethanol and 65% diesel was determined to be viable fuel for use on a truck travelling with diesel engine and truck idling with fuel cell auxiliary power unit system. The customized nozzle used for fuel vaporization and mixing achieved homogenous atomization of input hydrocarbon fuels (e.g., diesel, biodiesel, diesel-biodiesel blend, and biodiesel-ethanol-diesel), and improved the performance of fuel catalytic reformation. Given the same operating condition (reforming temperature, total oxygen content, water input flow, and gas hourly space velocity), the hydrocarbon reforming performance follows the trend of diesel > biodiesel-ethanol-diesel > diesel-biodiesel blend > biodiesel (i.e., diesel catalytic reformation has the highest hydrogen production, lowest risk of carbon formation, and least possibility of hot spot occurrence). These results provide important new insight into the use of bio-fuels and bio-fuel blends as a primary fuel source for solid oxide fuel cell applications.

ACKNOWLEDGMENTS

I would like to express my deep gratitude to my Ph.D. advisor, Dr. Thomas A. Trabold, who has been patiently guiding me towards the accomplishment of my dissertation research. I sincerely thank him for his encouragement and support.

I am grateful to my dissertation committee members, Dr. Callie W. Babbitt and Dr. Gabrielle Gaustad, for their great support and recommendations during my Ph.D. study. I am also thankful to my dissertation committee members, Dr. Bernhard Fischer and Dr. Denis Cormier, for their dedication and commendable guidance throughout my dissertation work.

I would like to thank my RIT colleagues and friends, Mark R. Walluk, Daniel F. Smith, and Michael Bradley, for their encouragement and inspiration.

I acknowledge the Golisano Institute for Sustainability for a first-year graduate fellowship and for providing me an opportunity to pursue the Doctorate degree of Sustainability, and all the faculty and staff for all their assistances during my study at RIT. I also acknowledge the financial support from the Office of Naval Research, which provided a partial Graduate Assistantship for my Ph.D. research and study.

Finally, I would like to sincerely thank my parents Jinzhou Lin and Huiqi Lin and my wife Yushuai Dai, for their infinite support in my life.

TABLE OF CONTENTS

LIST OF FIGURES

LIST OF TABLES

GENERAL NOMENCLATURE

a_{ik}	number of atoms of element k in molecule i
AAD	absolute average deviation
AFC	alkaline fuel cell
ANL	Argonne National Laboratory
APU	auxiliary power unit
ASTM	American Society for Testing and Materials
ATR	autothermal reforming
b_k	total amount of element k in effluent
BED	biodiesel–ethanol–diesel blend
B-diesel	biodiesel-diesel blend
B25E10D65	25% biodiesel+10% ethanol+65% diesel (volumetric basis)
CAFE	corporate average fuel economy
CHP	combined heating and power
CNG	compressed natural gas
CS	corn stover
DR	dry reforming
EPA	Environmental Protection Agency
EIA	Energy Information Administration
FMEA	failure modes and effects analysis
G	Gibbs free energy
GHG	greenhouse gas
GHSV	gas hourly space velocity
GREET	Greenhouse Gases, Regulated Emissions, and Energy Use in Transportation (modeling software developed by ANL)
H_2O/C	ratio of water to carbon from fuel
ICE	internal combustion engine
LCA	life cycle assessment
LCI	life cycle inventory
LFG	landfill gas
LHV	lower heating value
MCFC	molten carbonate fuel cell
MFC	mass flow controller
MILP	mixed-integer linear program
MINLP	mixed integer non-linear programming
MSW	municipal solid waste
N	number of gas species
N_2/C	ratio of nitrogen to carbon from fuel
NLP	non-linear programming
NREL	National Renewable Energy Laboratory
O_2/C	ratio of oxygen from air to carbon from fuel
P	pressure
PAFC	phosphoric acid fuel cell
PADD	petroleum administration for defense district

PEMFC	proton exchange membrane fuel cell
POx	partial oxidation
PTE	pump-to-electricity
R	gas constant
R/P	reserve to production ratio
RFS	Renewable Fuel Standard
SLP	successive linear programming
SOFC	solid oxide fuel cell
SQP	sequential quadratic programming
SR	steam reforming
STP	standard temperature and pressure
T	temperature
TC	thermocouple
Total O/C	summation of oxygen from fuel, air, and water to carbon from the fuel
ULSD	ultra-low sulfur diesel
V_{cat}	catalyst bed volume
WCO	waste cooking oil
WTE	waste-to-electricity
WTP	waste-to-pump
y_j	molar fraction
λ	Lagrange multiplier
Φ_j	gas fugacity coefficient
η	reforming efficiency

I BACKGROUND

1.1. Need for Bio-fuel and Fuel Cell Technology Development

Peak oil theory was originally recognized and described by Dr. M. King Hubbert (a geologist from the Shell Oil Company) in 1956 and it implies that the production rates of regional oil wells and global total oil reserves both follow roughly symmetrical logistic distribution curve (bell-shaped) [1]. The Hubbert model accurately predicted that the domestic oil production in the U.S. lower 48 states would ultimately reached its peak in 1970. Since then, the Hubbert model has been widely used to forecast oil production worldwide and refined with many dynamic factors (e.g., oil production rate, oil consumption rate, and new oil reservoirs) [2]. A research group from the U.S. Energy Information Administration (EIA) modified the Hubbert model by including several variables (e.g., oil production growth, reserve to production (R/P) ratio, and technically recoverable resources) to predict the global peak oil production. They hypothesized that the Hubbert curve extends its production with a constant percentage growth path until the production peak is reached, followed by a declined production post-peak at a constant R/P ratio. Their modified Hubbert model was presented as an asymmetrical logistic distribution curve [2]. Assuming a constant annual production growth of 2% and R/P = 10, the result from the EIA report indicates world conventional crude oil production would be expected to peak in year 2037 at a volume of 53.2 billion barrels per year. The report also includes a sensitivity analysis of several key variables and suggests that global crude oil production will have its peak between year 2021 and 2112. The bottom line conclusion to be drawn from peak oil theory is that inadequate global oil production capacity, not oil depletion is the issue of greatest urgency [3]. Worldwide demand for

crude oil, due simply to population growth, will fast outpace its supply [2,3]. Inadequate supply of crude oil promotes volatility of its price. This not only directly impacts the market supply chains of crude oil and other products, but also affects political strategies and makes it more difficult to plan long-term investments [1,3].

The U.S. has relied heavily on fossil fuel resources for its energy consumption and most of the petroleum is used in the transportation sector. For example, 82% of total energy consumption used in the U.S. in 2011 was derived from fossil fuels (summation of petroleum, natural gas, and coal). Renewable energy only accounted for 9%; and, the remaining portion was derived from nuclear power [4]. Figure 1(a) illustrates the U.S. historical energy consumption in terms of end-use sectors and it shows that transportation, residential, and commercial sectors have increased due to population growth. The industrial sector has not continuously grown since the significant reduction in year 1980. This may be due to the strategy of outsourcing production and energy saving technology developments [4]. Figure 1(b) suggests the imported energy (difference between total energy consumption in U.S. and its domestic energy production) went up to 30% in year 2005. However, it was reduced to 19% in year 2011 and is projected to be further reduced in the next few decades due to the production increments of domestic resources (e.g. natural gas, renewable energy). Figure 1(c) shows the historical trends in consumption of resources (coal, liquid petroleum, natural gas, nuclear, and renewable) in the U.S. Crude oil consumption is projected to decline due to the increasing supply of renewable liquid fuels (e.g., ethanol, biodiesel). Since the early of 1990s, concerns related to uncertain energy supplies, environmental impacts, and

homeland security have propelled policymakers to intensify their efforts to secure long-term energy sources. The development of bio-fuels as way to reduce foreign oil dependence has been intensively promoted since that time [5]. Figure 2 illustrates the historical changes of renewable energy consumption and it shows that the used of bio-fuel and wind based energy have dramatically increased in the last decade. The use of wood as a fuel has gradually declined since the 1980s. The U.S. Energy Policy Act (Epact) of 2005 created the renewable fuel standard (RFS), which required production of 9 billion gallons of bio-fuels in 2008 and 36 billion gallons in 2022 and the blending of this bio-fuel with conventional fossil fuels used in transportation applications [6].

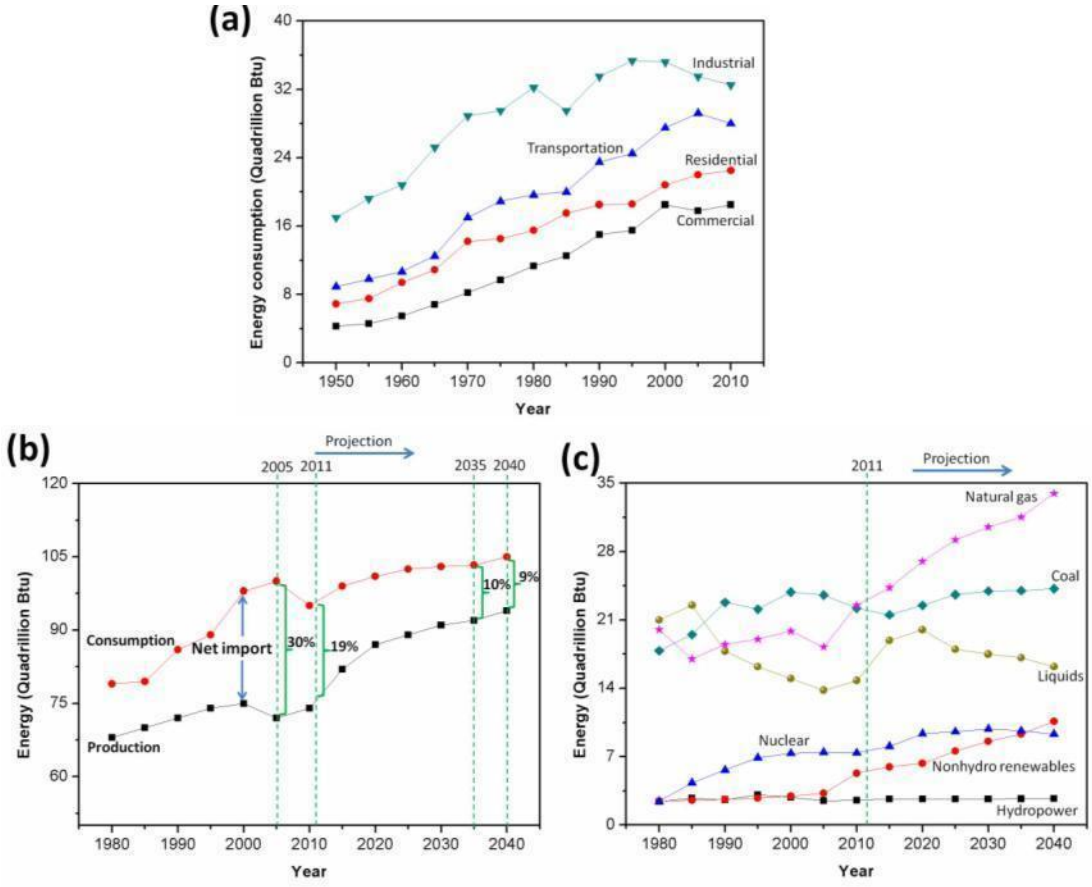

Figure 1: (a) U.S. total energy consumption by end-use sector (1949~2011); (b) U.S. total energy consumption and domestic energy production (1980~2040); (c) U.S. energy consumption resource categories (1980~2040) [4]

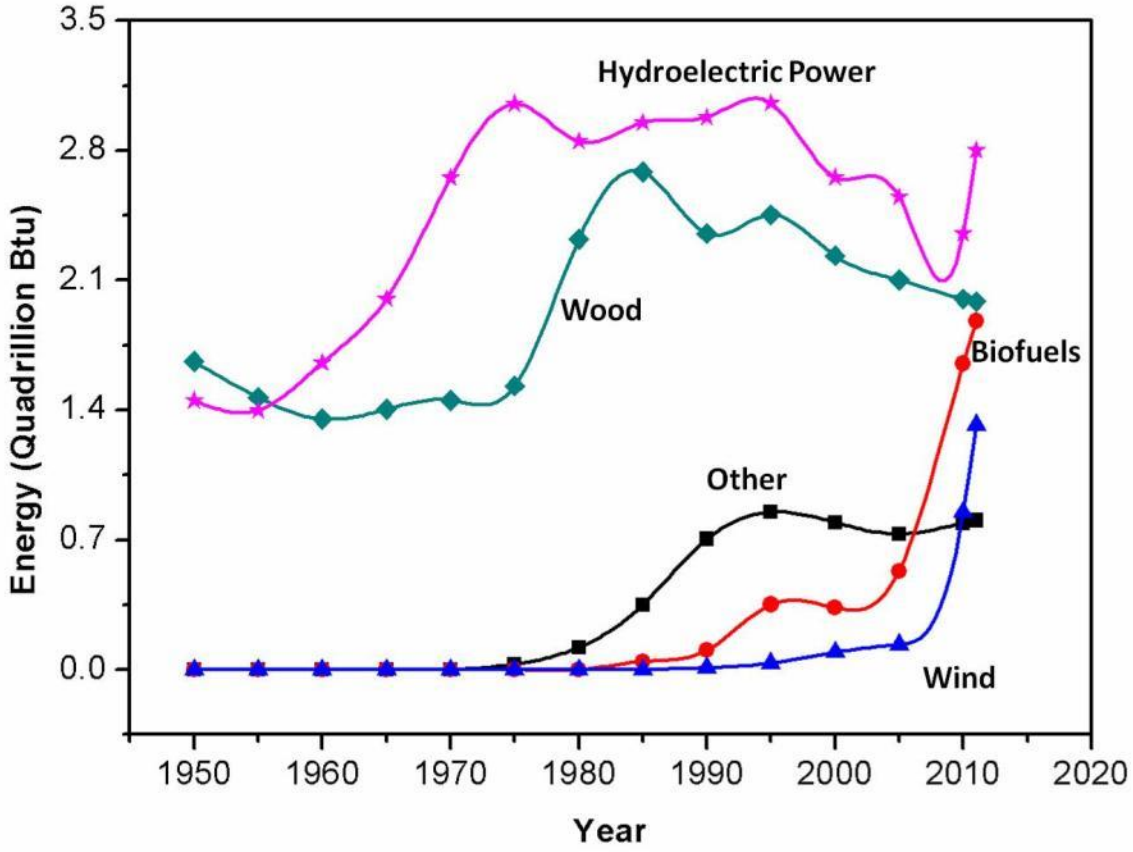

Figure 2: Renewable energy consumption by source (1949~2011) [4]

Besides renewable energy developments, system improvement of fuel conversion efficiency is another strategy implemented to promote energy utilization. Fuel economy enhancements along with stringent exhaust regulations in the transportation sector have been promoted by the U.S. legislating bodies. For example, the corporate average fuel economy (CAFE) standard was first established by the U.S. Congress in 1975 with the intention of improving the average fuel economy of passage cars and light trucks right after the oil crisis in 1973 (Arab Oil Embargo) [7]. The CAFE legislation was recently refined by the Obama Administration and proposed to increase the fuel economy of passage cars from 25 mile per US gallon in 2012 model year of to 35 mile per US gallon

by 2016 model year. Alternative technologies to improve fuel conversion efficiency and emission reduction have also been promoted, such as fuel cells and batteries.

Fuel cells are electrochemical devices that directly convert chemical energy of fuels into electrical energy. They possess high fuel conversion efficiency, because, unlike conventional power generation systems, fuel cells avoid the intermediate steps of producing heat and mechanical work. Fuel cells are thus they are not limited by thermodynamic limitations imposed by Carnot efficiency [8,9]. Fuel cells have higher energy density than batteries and can produce electricity continually, as long as the input fuels are supplied. Fuel cells are classified according to the electrolytes used in the cells, and they include proton exchange membrane fuel cell (PEMFC), alkaline fuel cell (AFC), phosphoric acid fuel cell (PAFC), molten carbonate fuel cell (MCFC), and solid oxide fuel cell (SOFC). The choice of electrolyte determines the cell operating temperature range and the physicochemical properties of other cell components (e.g., catalyst electrodes, interconnects, and current collectors). The power output range and operating conditions of different fuel cell types are applied to various application sectors. For example, the PEMFC using hydrated polymeric ion exchange membranes as electrolyte is typically operated below 100 ^{o}C and it has been used in vehicles propulsion systems, while the SOFC has perovskite ceramics as electrolyte and serves in combined heating and power system (CHP) applications with its operating temperature range of 500~1000 ^{o}C [9].

In fuel cells, hydrogen and oxygen from air serve as the reductant and oxidant, respectively. Besides the high capital cost of fuel cell systems, insufficient hydrogen supply infrastructure is another main factor contributing to the limited market penetration to date. The global hydrogen production capacity is around 5×10^{10} kg/year and the major portion of hydrogen is used as a chemical raw material. Catalytic reformation with steam of methane from natural gas at high temperatures (so-called steam reforming) dominates domestic hydrogen production, even though hydrogen generation paths from renewable resources (e.g., wind, solar) through water electrolysis have been reported as alternative "green" approaches [10]. The methods to store hydrogen and supply on-board fuel for fuel cell vehicles have been widely studied, and include conventional high pressure condensation [11], cryo-techniques for superinsulated hydrogen at low temperature [10], hydrogen adsorption on solid materials of large surface area (e.g., carbon nanotubes) [12], hydrogen storage by metal hydrides [13], and catalytic reformation of on-board hydrocarbon fuels, such as diesel [14]. Figure 3 illustrates both volumetric and gravimetric density of hydrogen storage for these methods and it shows hydrogen derived from heavy hydrocarbon liquid fuels (e.g., gasoline, diesel) has both high volumetric and gravimetric density, which suggests heavy hydrocarbon catalytic reformation could be an effective process for onboard hydrogen supply [10,14].

Fuel catalytic reformation is a process to convert a commonly available hydrocarbon (e.g., natural gas, propane, gasoline, diesel, and biodiesel) into a hydrogen-rich gas stream, which is then supplied to a fuel cell system [15]. Four predominate modes of catalytic reforming have been investigated previously, including steam

reforming (SR, Equation 1) [16], partial oxidation (POx, Equation 2) [17], autothermal reforming (ATR, Equation 3) [14], and dry reforming (DR, Equation 4) [18]. Fuel flexibility is one of the outstanding benefits of implementing hydrocarbon catalytic reforming techniques, which can provide sufficient hydrogen production from a wide range of hydrocarbon fuels in different geographical regions in order to meet the large-scale demand of fuel cells (after fuel cell technologies become more economically viable) [15]. By adjusting the operating conditions of the fuel reformer (e.g., temperature, pressure, input fuel flow, input water/air flow, catalyst type, and space velocity), practical yields of hydrogen-rich reformate can be achieved for specific types of hydrocarbons [14-18].

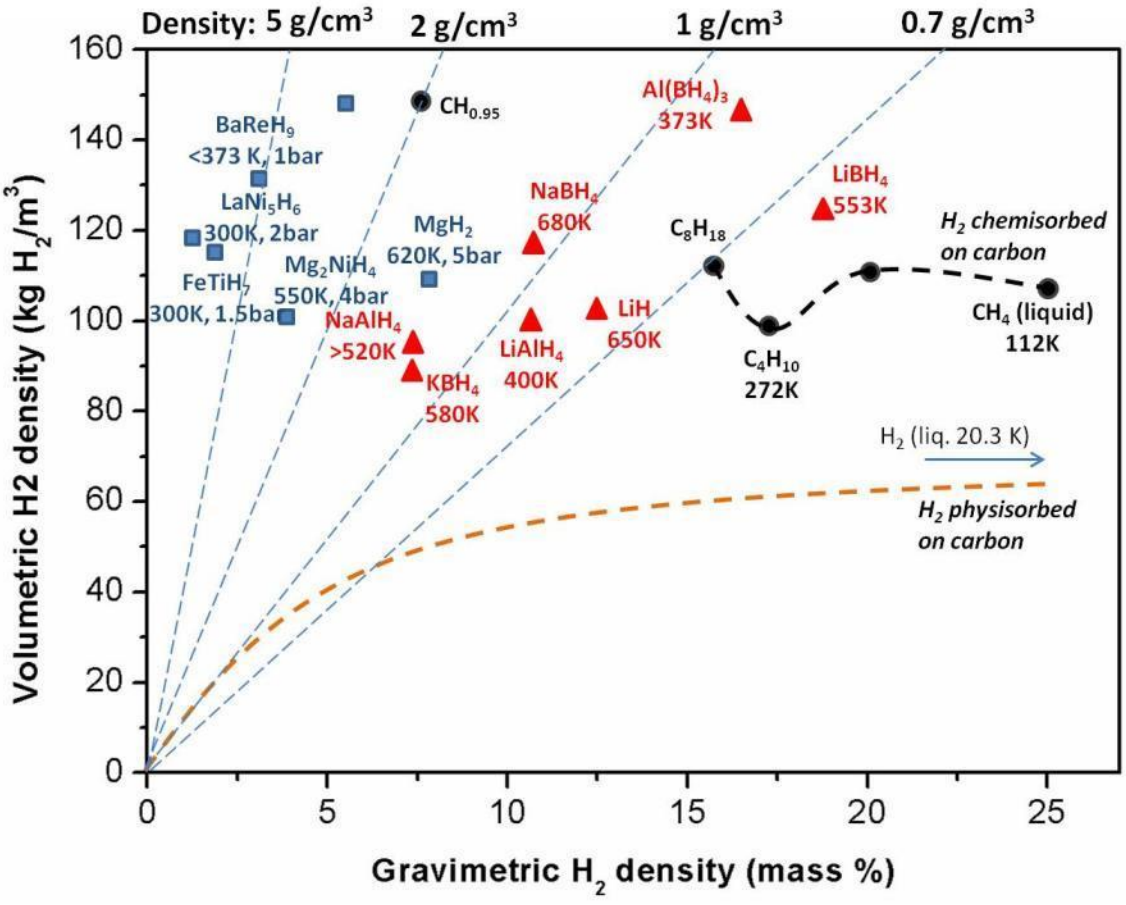

Figure 3: Stored hydrogen per mass and per volume [10]

SR: $C_nH_m + 2nH_2O \rightarrow nCO_2 + (m/2 + 2n)H_2$ (1)

POX: $C_nH_m + n(O_2 + 3.76N_2) \rightarrow (m/2)H_2 + nCO_2 + 3.76nN_2$ (2)

ATR: $C_nH_m + A(O_2 + 3.76N_2) + 2(n-A)H_2O \rightarrow (m/2 + 2(n-A))H_2 + nCO_2 + 3.76AN_2$ (3)

DR: $C_nH_m + nCO_2 \rightarrow 2nCO + (m/2)H_2$ (4)

1.2. Fuel Catalytic Reformation for Solid Oxide Fuel Cells

Although SOFC-based systems need to be operated at a relative high temperature (500~1000 ^oC), they not only enable utilizing non-noble metal as the catalyst electrode (i.e., Ni-ZrO_2 for anode, Sr-doped $LaMnO_3$ for cathode) and CO with H_2 as the directly useable fuels, but also combine heat and power to promote the system efficiency (up to 88% based on lower heating values of input fuels) [19]. Since the electrolyte of SOFC is solid, the cell can be cast into various shapes (e.g., tubular, planar, or monolithic) [9]. SOFCs have been used in stationary power generation, mobile power, and auxiliary power for vehicles applications [9,14,15]. For example, SOFC-based APU systems are used in long-haul diesel heavy duty trucks to supply auxiliary electricity for the driver during truck idling periods. Anti-idling legislation has been implemented in many states to prohibit diesel trucks and buses from long-term idling [20]. SOFC-based auxiliary power unit (APU) systems with power range of 2-10 kW serve as a promising alternative technology to supply the electrical and thermal needs for trucks during shutdown of the diesel engine. Delphi Corporation has developed, for heavy duty commercial trucks, a 5 kW SOFC-APU with fuel efficiency 40~50% higher than conventional diesel engine APUs for heavy duty commercial trucks (shown in Figure 4) [21]. The main components of this SOFC-APU include SOFC stacks that convert chemical energy of the reactants

(H_2 and CO with air) into electrical energy, a fuel reformer that catalytically reforms hydrocarbon compounds with an oxidant (water/air) to produce a hydrogen-rich gas stream, a desulfurizer bed to remove the sulfide compounds from the input fuels, fuel and air supply/control modules, and heat exchange manifolds.

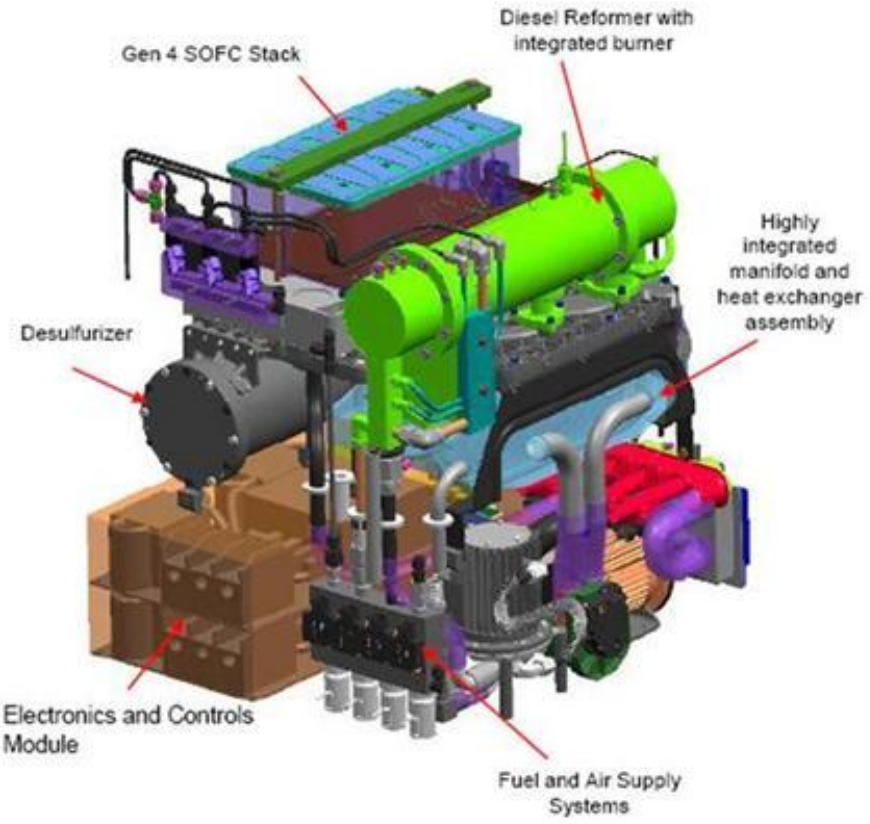

Figure 4: 5 kW SOFC-based APU system (Gen 4, *Delphi Corporation*) [21]

ATR is the thermally-balanced combination of SR (endothermic reaction) and POx (exothermic reaction) and has a number of advantages in terms of system mechanization [14]. With a well-designed system-integrated configuration, the SOFC-APU enables self-sustained conversion without any external heating supply [15]. Diesel trucks tend to utilize one type of fuel for both diesel engine combustions during traveling

and idling service with the SOFC-APU system, because of the complexity of introducing an additional tank to carry another type of fuel on the truck. Thus, from a practical standpoint, it is necessary for the SOFC-APU to be integrated with a fuel reformer and convert petro-diesel into onboard reformate (gas mixture containing H_2, CO, CO_2, and small fractions of light hydrocarbon gases), which is then fed into the anode side of the SOFC stacks to generate the auxiliary electricity. Because of the lack of onboard water sources in transportation applications, SOFC-APUs partially recycle the exhaust gases containing an appreciable amount of steam from the anode side of the SOFC stacks to the reformer inlet [14,15]. Therefore, the main effluent byproducts from the SOFC-APU are water, carbon dioxide, and nitrogen.

1.3. Dissertation Motivation and Outline

Rising concern over inadequate supply of crude oil has promoted bio-fuel development and technological improvements in energy supply systems with high fuel conversion efficiency. The combination of these two initiatives has created numerous new opportunities in energy consumption. These opportunities come with many technical barriers and social concerns. For example, economic incentives for bio-fuels have spurred ethanol production and consumption in transportation applications (approximately 13.9 billion gallons in year 2011) [22], however, large portions of ethanol production are derived from edible food crops, which lead to various social concerns (e.g., food price, land use, soil fertility, and water conservation) [23-25]. Therefore, it is necessary to develop the methodologies to analyze bio-fuel applications in the advanced energy supply systems from environmental, economic, social, and technical perspectives. With

this goal in mind, the present dissertation study focuses on investigating bio-fuel options and performance in SOFC-based APU systems for truck auxiliary power supply applications.

In the last two decades, the United States has witnessed dramatic growth in bio-fuel production and consumption in the transportation sector. This has been driven by political mandates, economic incentives, private and public investments, as well as active research and development. However, there are still many challenges to be addressed before promoting widespread bio-fuel production, such as the unclear net benefits of bio-fuels derived from various feedstocks (especially agricultural products), lack of robust frameworks to quantify economic feasibility and environmental impacts of bio-fuels, geographical variations in bio-fuel selection, and the complexities of compatible energy conversion technologies for utilizing bio-fuels, such as fuel cells. To develop a system-level analysis of bio-fuel production and the potential applications in SOFC-based system, this dissertation evaluates the environmental impact, economic feasibility, and technological viability of various bio-fuel-to-SOFC pathways by applying a variety of sustainability and engineering analytical techniques, including LCA, multi-criteria optimization, and equilibrium thermodynamics modeling. These tools are applied in conjunction with extensive fuel reforming experiments that analyze the performance of converting the bio-fuels or bio-fuels blended with conventional fuels into a hydrogen- and carbon monoxide-rich reformate that possible to be used in the SOFC stack. The dissertation outline is provided below.

Chapter I provides the background on bio-fuel developments and fuel cell technologies to alleviate the inadequate crude oil supply in the United States. The production and consumption trends of bio-fuels were analyzed within the context of bio-fuel applications in transportation sector. The current technological challenges of fuel cells were reviewed (e.g., hydrogen availability, high capital cost). The combination of bio-fuel developments and SOFC-APU systems was specifically focused on and it motivated the analysis of bio-fuel options for SOFC applications from environmental, economic, and technological perspectives in the present study. .

Chapter II describes the environmental aspects of bio-fuels derived from waste feedstock and their applications in SOFC-APU systems. A methodology that integrates LCA with thermodynamic analysis was developed to evaluate the environmental impacts of producing bio-fuels from waste biomass, including biodiesel from waste cooking oil (WCO), ethanol from corn stover, and compressed natural gas from municipal solid wastes. SOFC-based APUs using these bio-fuels as the hydrogen precursor enables generation of auxiliary electricity for idling heavy-duty trucks. Thermodynamic analysis was applied to evaluate the bio-fuel conversion efficiency and determine the amount of primary feedstock needed to generate a unit of electrical power. These data were inputted to an LCA that compares energy consumption and greenhouse gas emissions of different fuel pathways. Compressed natural gas from municipal solid wastes and biodiesel from WCO are both suggested as promising bio-fuel options for SOFC-based applications in New York State. When using biodiesel or its blend in transportation applications, no further modifications of fueling infrastructures are required due to the similar fuel

properties of biodiesel and diesel. Therefore, biodiesel would be a viable fuel for SOFC-APUs from a practical standpoint, which will be further analyzed in Chapters III and IV from economic and technological perspectives, respectively.

Chapter III presents the economic aspect of bio-fuels blended with conventional diesel. A nonlinear optimization model was developed to analyze biodiesel–ethanol–diesel (BED) ternary blending processes. The model establishes optimal blends to maximize the system profitability given production costs, market demand, and fuel prices while meeting multiple property criteria including kinematic viscosity, density, lower heating value, cloud point, cetane number, fuel stability and sulfur content. Pertinent fuel mixing rules for predicting the fuel properties of BED blends were extrapolated from previous works and applied as constraints to the present model. Several dynamic and/or uncertainty factors were explored in depth to quantify their impacts on the fuel composition of BED blends, including petro-diesel supply reduction, diesel production cost, diesel blend market retail price, and policy changes affecting on bio-fuel subsidies. By examining key optimization sensitivity analyses such as shadow prices and opportunity costs, the crucial limits or constraints on fuel specifications can be identified and used to proactively identify and promote the development of potential additives. The model also suggests the government policy of simultaneously implementing bio-fuel tax credits and mandates may not have a higher contribution to promoting bio-fuel production than the case with only tax credits for the firms with the goal of profit maximization. The firms enable 5–8% increase of the optimal profit from BED blends by utilizing ethanol derived from food waste feedstocks instead of edible biomass. An

optimal blended composition of BED has been identified as 25 vol.% biodiesel blended with 10 vol.% ethanol and 65 vol.% diesel (B25E10D65) to achieve system profit maximization while satisfying all proposed constraints. This fuel blend optimization motivated the investigation of B25E10D65 fuel reformation, which was analyzed in Chapter IV.

Chapter IV provides the technological aspects associated with ATR of diesel, biodiesel, B-diesel, and BED for SOFC-APU systems. This chapter firstly illustrates a new configuration of a mixing chamber integrated with a customized porous nozzle to completely vaporize heavy hydrocarbon fuels (e.g., diesel, biodiesel) and achieve homogenous mixing of fuel/air/steam. This proposed configuration directly suppresses hydrocarbon thermal pyrolysis and solid carbon formation in the fuel vaporization step. The porous nozzle promotes the micro-explosion of emulsified fuel and accelerates secondary atomization to reduce the droplet size. The mixing chamber with customized nozzle was integrated in a single-tube reformer system in order to analyze the effect on diesel and biodiesel ATR. The customized nozzle not only improves the hydrogen yield and the reforming efficiency, but it also stabilizes the chemical reactions within the reformer and prevents the reactor inlet from high temperature sintering. After addressing the technical barrier of heavy hydrocarbon fuel vaporization, this chapter analyzes the ATR performance of diesel, biodiesel, B-diesel, and BED in a single-tube catalytic reformer under various operating conditions (reformer temperature, input fuel flow, air flow, water flow, and gas hourly space velocity). A mass spectrometer was used to measure the effluent gas composition, while a photo-acoustic micro-soot meter was

simultaneously applied to quantify the condensed carbon from the single-tube reactor and identify the carbon formation boundaries for ATR of the considered fuels. Thermodynamic analysis based on the method of total Gibbs free energy minimization was applied to determine the optimum operating regimes with high hydrogen yield and minimum solid carbon (soot) formation for fuel ATR. Correlations between solid carbon and ethylene (a key precursor of carbon) were also explored in this chapter for these studied fuels.

Chapter V summarizes the key findings in this dissertation regarding the viable bio-fuel options for SOFC-based APU system applications from economic, environmental, and technological perspectives. Future research directions are also provided to improve the robustness of SOFC-APU systems prior to their commercialization.

II LIFE CYCLE ASSESSMENT OF BIO-FUEL OPTIONS FOR SOLID OXIDE FUEL CELLS

2.1. Introduction

Heavy duty trucks (gross vehicle weight rating above 14,969 kg) serve as a common mode of long-distance product delivery within the United States. Conventionally, drivers tend to rest inside the truck cabin and keep the full diesel engine running to provide the auxiliary electricity. A recent report from the U.S. Environmental Protection Agency (EPA) [26], however, indicates that trucks and locomotive engines idling for long durations consume over 4.55 billion liters of diesel fuel annually and release over 11 million metric tons of carbon dioxide as well as 150,000 metric tons of nitrogen oxides, which is equivalent to the greenhouse gas emissions (GHG) from 2.3 million passenger vehicles each year [27]. Anti-idling legislation was implemented in 31 states and prohibits running the diesel engine for long periods while the vehicle is at rest [20]. A promising alternative technology is the solid oxide fuel cell auxiliary power unit (SOFC-APU) to provide power in the range of 2 to 20 kW for heavy duty trucks during rest intervals. The SOFC system not only possesses high fuel efficiency, low GHG emissions and quiet operation, but the system can also utilize a wide range of fuels and reform them into hydrogen-rich gas delivered to the anode side of the fuel cell stack. Domestically-derived bio-fuels are considered promising candidates for fuel cell technologies in future transportation applications, due to their primary advantages of energy security and low direct GHG emissions. Even though the net benefit of some bio-fuels like corn-based ethanol is still unclear, fuels derived from waste biomass appear attractive from both environmental and economic standpoints. For example, Mintz *et al.* recently reported a detailed analysis of landfill gas as a vehicle fuel using the *GREET*

(Greenhouse Gases, Regulated Emissions, and Energy Use in Transportation) model provided by Argonne National Laboratory (ANL). They concluded that landfill gas can be one of the lowest GHG-emitting fuel options for light and heavy-duty vehicles [28].

LCA is a technique to capture the environmental impacts of a product or service during its life cycle stages (from cradle to grave). In terms of bio-fuel LCA studies, these considered stages may include feedstock production/acquisition, transportation, biomass treatment, bio-fuel delivery, bio-fuel use, and bio-fuel end-of-life [29]. Many LCA studies have been conducted to evaluate the environmental perspectives of bio-fuels. Soratana and Landis apply a comparative LCA on 20 scenarios of microalgae cultivation and indicate the material choice for constructing the algae photobioreactor has a relatively high environmental impact [29]. Spatari *et al.* analyzed the life cycle environmental impacts in terms of GHG emissions and fossil energy consumption for emerging lignocellulosic-based ethanol technologies and integrated Monte Carlo analysis to evaluate the sensitivities of ethanol conversion efficiency and plant scale effects [30]. However, because LCA methodology strongly depends on data availability and quality, and the quantitative methodologies that enable simulation of the real systematic conditions are lacking, the outcomes of many bio-fuel LCA studies are highly dependent on data inputs from previous studies or assessments performed in different regions [31]. Thus, LCA results often don't comprehend geographical feedstock variations and technological differences in the processes under comparison factors which are crucial for bio-fuel analysis [32].

Given the geographically indistinct nature of heavy duty freight transportation, the specific bio-fuel available as an SOFC feedstock may vary significantly over the course of a cross-country trip. Thus, an LCA intended to evaluate candidate bio-fuels must be responsive to expected variations in the technological parameters and fuel properties that have been shown to cause most variability in performance of each potential feedstocks (e.g. chemical fuel formula, boiling point, viscosity, lower heating value, hydrophobicity etc.) [32]. Further, life cycle inventory (LCI) parameters must also account for differences in performance and emissions associated with the bio-fuel-specific conversion efficiency and avoided impacts when bio-fuels are created through waste diversion, which also vary according to specific conversion technologies and geographic feedstock availability. Therefore, this study investigates the addition of thermodynamic analysis as a front-end estimation tool to determine more technologically- and geographically-specific LCA inputs and inventory data.

The addition of thermodynamic analysis in LCA is a rapidly emerging research area. Integrating thermodynamics with LCA has recently led to advances in accounting for natural resource consumption and ecosystem services [33-35]. Some studies have combined LCA with more traditional process design parameters, such as thermodynamics and cost, to evaluate process design alternatives [36]. In this study, thermodynamic modeling is explored in the context of "design-based" LCI, in which bio-fuel- and technology-specific parameters are first estimated using a thermodynamic model and then used to parameterize the life cycle study [37,38].

The main goal of this work is to demonstrate the utility of a combined thermodynamic and LCA model for comparing waste biomass based bio-fuel options for SOFC-APU applications within a specific geographic context (New York State). Given this scope, four different fuel pathways to reformed hydrogen for SOFC systems are analyzed: compressed natural gas (CNG) derived from municipal solid waste in a local landfill, biodiesel from waste cooking oil (WCO) available at local restaurants, ethanol from locally grown corn stover (CS), and commercially available ultra-low sulfur diesel (ULSD) from crude oil. The baseline of these pathways is the incumbent method of ULSD combustion in the primary propulsion internal combustion engine (ICE) during truck idling to provide auxiliary electrical power. Thermodynamic analysis using the method of total Gibbs free energy minimization is applied to evaluate the fuel conversion efficiency and determine the amount of fuel feedstock needed to generate a unit of electrical power, before quantifying the attendant environmental impacts. Although this study considers only waste biomass available in upstate New York, the methodology outlined here can be applied to geographically explicit fuel feedstocks readily available in other regions within the U.S. or internationally.

2.2. Methodology

2.2.1. Life cycle assessment

Goal and scope definition:

The goal of this work is to assess bio-fuel options derived from waste feedstock for SOFC-based APU applications, including WCO to biodiesel, CS to ethanol, and MSW to CNG, in terms of GHG emissions and life cycle energy consumption. The system boundary is set from waste-to-electricity (WTE) and the geographical boundary

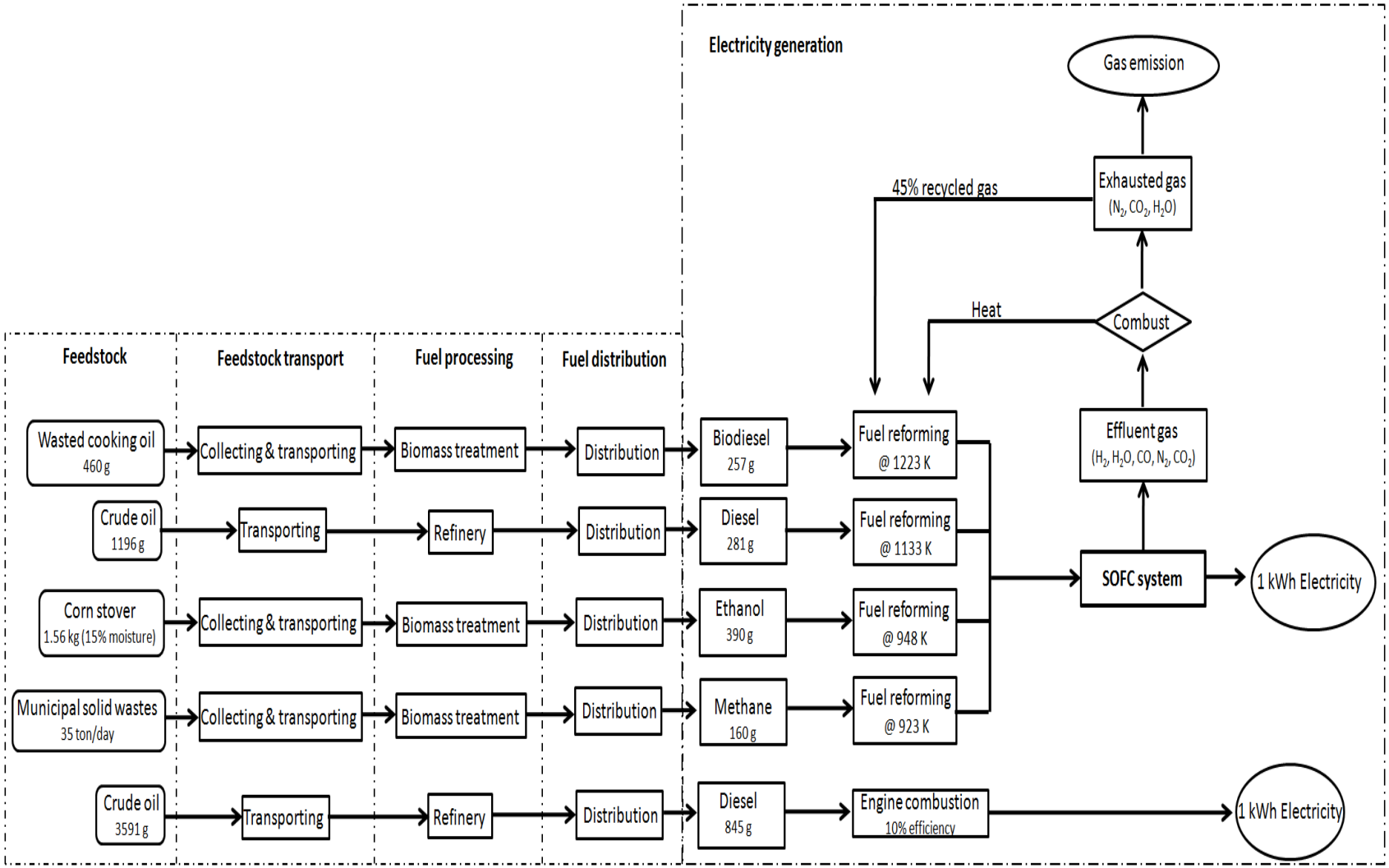

Figure 5: Overview of different fuel production paths to generate auxiliary electricity

within New York State, as shown on Figure 5. Generally, LCA is conducted on a complete cycle from cradle-to-grave; however, the upstream boundary in this assessment is established as the existing waste feedstock, which would otherwise be disposed. The waste-to-pump (WTP) stage includes collection and transport of the waste feedstock to processing sites, processing waste materials into bio-fuels, and distribution to fueling stations. Fuels are then further converted into auxiliary electricity with the SOFC-based system and supplied for truck applications in the pump-to-electricity (PTE) stage. SOFC system start-up is excluded from the system boundary, because the primary on-board fuel supply (diesel) is used for reactor warm up in all cases, and resultant impacts will not vary among feedstocks. All inputs and outputs are normalized to a functional unit of 1 kWh electricity generation by the SOFC.

Life cycle inventory and impact assessment:

To maintain an internally consistent data inventory, the main references for fuel pathways are based on the studies reported by the National Renewable Energy Laboratory (NREL) and Argonne National Laboratory (ANL), as listed in Table 1. Strazza *et al.* [39] have reported the results of a life cycle assessment (LCA) of a 20 kW SOFC-based APU fuelled with methanol for marine shipping applications and they suggest that fuel use and fuel production influence the environmental impacts more than the manufacturing of the SOFC system itself. Thus, this study evaluates the environmental impacts of a proposed 5 kW SOFC-based APU from fuel production and SOFC operation stages, excluding maintenance or SOFC manufacturing. The net fuel efficiency of the converting system is defined as the ratio of the electricity generated

from the system to the energy from the input fuel with respect to its lower heating value (LHV). The net efficiency of the SOFC-based APU is then assumed as 30% whereas that of the idling diesel ICE is considered to be 10% [40]. Electricity inputs are based on the New York State average grid mix with primary energy and GHG emission rates of 10.8 MJ/kWh and 0.31 kg CO_2-eq/kWh, respectively [41]. Table 2 provides additional details on LCA descriptions for this study.

Table 1. Reference sources for different fuel pathways

Feedstock	**Processing**	**Fuel**	**Fuel LHV (MJ/kg)**	**H_2S content (ppm)**	**Main reference source**
Crude oil	Refinery	Diesel ($C_{12}H_{23}$)	42.6	7-17	NREL/SR-580-24089 (NREL, 1998) [42]
WCO	Transesterification	Biodiesel ($C_{14.4}H_{26.76}$)	37.1	3.3	NREL/SR-570-26141 (Wiltsee, 1998) [43] NREL/SR-580-24089 (NREL, 1998) [42]
CS	Fermentation	Ethanol (C_2H_5OH)	27.1	<15	NREL/TP-510-32438 (Aden et al., 2002) [44]
MSW	Anaerobic digestion	Natural gas (CH_4)	47.1	Undetectable	NREL/SR-570-26037 (Steinfeld and Sanderson, 1998) [45] ANL/ESD/10-3 (Mintz et al., 2010) [28]

To develop accurate inventory flows of energy and GHG emissions for the LCA, fuel conversion efficiency and the amount of fuel required to generate the required auxiliary electricity are determined by thermodynamic analysis on the SOFC system. LCI of upstream chemical materials used in bio-fuel treatment processes are obtained from the ecoinvent database V2.2 (ecoinvent Centre, EMPA) and listed in Table 3. In the cases of co-products created during bio-fuel production, allocation is avoided by applying system expansion, where these co-products are assumed to substitute for other products that

Table 2. Life cycle assessment of this work

Goal definition and scoping	Goal	The main goal for LCA in this work is to quantify the ecological benefits from replacing the conventional diesel fuel for truck auxiliary power supply applications with bio-fuel that derived from local available waste feedstock. It also provides the information for policy makers and engineer to choose the optimum wastes to energy path with least effect on the environment.
	Functional unit	To generate 1 kWh electricity auxiliary power supply in truck applications
	Scope	• Geographical boundary: New York State; • Systemic scope: waste feedstock collecting, biomass treatment, fuel distribution, fuel reforming, and electricity production (including biodiesel from waste cooking oil, ethanol from corn stover, compressed natural gas from municipal solid waste, and diesel from crude oil) • Focusing on SOFC APU normal operating stage, exclude the stages of system start-up and shut-down.
	Key assumptions	• The upstream boundary in this study is established as the existing waste feedstock; • The net fuel conversion efficiency of SOFC-APU is considered as 30% and that of the idling diesel engine is assumed as 10%; • The environmental impacts of adding extra weight of SOFC APU and a small volumetric tank to the truck are negligible because they only account for less 0.5% of the total weight. • New York state average grid mixes with primary energy and GHG emission rates of 10.8 MJ/kWh and 0.31 kg CO_2-eq/kWh, respectively, are applied; • Diesel production mode follows GREET model provided by Argonne National Laboratory (ANL); • It is assumed that 88 restaurants near the RIT campus are representative samples in New York State; • 50% of corn stover feedstock can be used as available feedstock to produce ethanol without jeopardizing soil quality; • Energy consumption and greenhouse gas emission are two main contributors on environmental impacts for all the fuel options, so they are considered in this study.
Inventory analysis	Major data types	Electricity use, fossil fuel consumption, bio-fuel use, CO_2 emission, methane emission, and byproduct generation.
	Data sources	Consistent data on biomass treatment processes were obtained from several reports by ANL and National Renewable Energy Laboratory. Cumulative energy and GHG emissions of upstream chemical materials are obtained from the Ecoinvent data V2.2 inventory. Applying thermodynamics in the practical operating conditions helps to overcome the challenge of getting the unavailable process flow data.

	Co-product credit	System expansion was used to determine the co-product credits.
Impact assessment	Impact category	Global warming, energy consumption
	Characterization	Greenhouse gas emission from CO_2 and methane emissions (kg CO_2-eq/kWh), energy consumption from fossil energy and renewable energy (MJ/kWh).
	Grouping	Total greenhouse gas emission, net fossil greenhouse gas emission (kg/kWh), total energy consumption, and net fossil energy use (MJ/kWh).
Interpretation	LCA results	• To generate 1 kWh auxiliary electricity for idling truck applications, the SOFC-based APU of methane derived from municipal solid wastes has the relatively low total energy consumption (9.7 MJ) and GHG emissions (0.09 kg CO_2eq), as compared to the conventional idling diesel engine (43.8 MJ and 4.39 kg CO_2eq); • Fuel converting process (either for diesel engine or for SOFC-APU) is the main contribution on environmental impacts in term of energy consumption and GHG emission, thus it is crucial to improve the efficiency of fuel conversion; • Waste to energy path provides significant ecological benefits of replacing conventional fossil fuel consumption.
	Sensitivity analysis	Co-product credit allocations: energy-based allocation, market value-based allocation, and system expansion.
	Limitations	• Carbon footprint of waste feedstocks in the upstream has not been captured in this study; • Different techniques for biomass treatments have not been considered in this work;

that require energy in their production [46]. Sensitivity analysis is performed to test the impact of allocation decisions using energy- and economic-based allocation methods as well. Impact assessment focused on quantifying cumulative energy demand and total GHG emissions, using methods of cumulative energy demand (V1.08) and TRACI 2 (V3.03), respectively (SimaPro 7.0, PRé Consultants, the Netherlands). Energy and GHG emissions are the focus of impact assessment for two primary reasons: 1) energy data are the most readily available and complete type of inventory data, enabling a much higher degree of certainty in impact estimation; and 2) energy and climate issues are at the

Table 3. Cumulative energy and GHG emission of chemical materials used in the inventory analysis

Chemical	Cumulative energy (MJ/kg)	GHG emission (kg CO_2eq/kg)	Description
Methanol[a]	37.6	0.737	Transport from overseas and European methanol plants to Switzerland. Assumed that 40% of the methanol originate from overseas. Additional 13% from Norway. Other production within continental Europe.
Sulfuric acid[a]	2.36	0.138	Part of the sources considers the average technology used in European sulfuric acid production plants. The others consider the state-of-the-art technology in Europe; it includes the conversion of SO_2 to SO_3 and the absorption of SO_3 into solution (sulfuric acid in water) to yield sulfuric acid.
Potassium hydroxide[a]	37.1	1.94	Potassium hydroxide is manufactured by the electrolysis of potassium chloride brine in electrolytic cells. Technology based on industry data in the US.
Potassium sulfate[a]	11.1	1.53	The unit process inventory takes into account the production of potassium sulfate from potassium chloride and sulfuric acid.
Glycerine[a]	104	5	Glycerine is produced by reacting epichlorohydrin with a 10% sodium hydroxide aqueous solution; technology based on industry data in the US and Europe
Lime[a]	4.42	0.757	Lime from carbonation is a by-product of sugar fabrication. Only transport from the manufacturer to the regional storehouse were taken into consideration for this inventory.
Ammonia[a]	39.9	1.9	Steam reforming process starting with natural gas, air and electricity is considered; Mostly present state of the art technology used in European ammonia production plants.
Gypsum[a]	0.0373	0.00205	Included processes: mining and crushing of gypsum and anhydrite; composition of products: 65% gypsum, 34% anhydrite, 1% others.
Enzyme[b]	80	7.5	Product name: Spirizyme plus FG; Industrial application: production of starch derived sugars; Function: Saccharification of starch.
Zinc oxide[a]	53.8	2.88	Production out of secondary zinc materials by means of the indirect way; average European processes for raw materials, transport requirements and electricity mix used.

[a] Ecoinvent V2.2; [b] Nielsen *et al.*, 2006 [47]

forefront of policy debate regarding bio-fuel technology development. These impacts are quantified not only for total energy consumption and GHG emissions, but also for net fossil-based energy use and fossil-based GHG emissions (e.g., excluding biogenic carbon contributions) in the studied system. For each bio-fuel production pathway, the total system energy efficiency is also calculated, which accounts for cumulative energy inputs required to achieve 1 kWh electricity production by the APU.

2.2.2. Fuel pathways

Ultra-low sulfur diesel from Crude oil

New York State (NYS) is geographically located in Petroleum Administration for Defense District (PADD) I and its petroleum resources are associated to be consisted of 2.68% crude oil domestic extraction and 97.32% foreign import in this study (U.S. Energy Information Administration, 2011) [48]. Petro-diesel production stages (WTP) typically include crude oil extraction, crude oil transport to refinery, crude oil refining, and diesel fuel delivery. Three types of conventional crude oil extraction processes (onshore production, offshore production, and advanced onshore steam-injection) are considered both for domestic crude oil production and foreign production [42]. The Argonne GREET Model 1.8d was applied to evaluate crude oil transport mode, diesel refinery from cruel oil, and the delivery modes for the PADD I region [49]. The energy consumption and GHG emissions for each stage of diesel production was quantified as the flow diagram provided in Figure A1 in Appendix A.1. Besides diesel fuel, other products like gasoline, heavy fuel oil, jet fuel, kerosene, etc. are also produced from the cruel oil refinery process and thus the mass allocation method based on these output

products is applied to determine the contributions of energy use and GHG emissions of diesel fuel in the upstream operations (crude oil extraction, feedstock delivery, and refinery). Energy use and fugitive emissions from crude oil storage and handling in the transportation processes (e.g., crude oil loading and unloading) are not included in this study, because the report from NREL (1998) indicates only 0.02% of total energy use and 0.015% of GHG emissions occur from crude oil handling/storage in transportation stage [42], which both are negligible. In order to supply a unit of auxiliary electricity to the truck, diesel fuel can be either direct engine combusted (Figure A1) or integrated with an SOFC-based APU system (Figure A2). The SOFC stacks need to maintain relatively high hydrogen fuel utilization (68%) in order to be consistent with the previous assumption of 30% net system efficiency for the SOFC-APU. The leftover effluent gases from stacks are combusted to supply heat for the reformer. Partial steam from the exhaust stream is also recycled as an input for fuel autothermal reforming [14].

Biodiesel from waste cooking oil (WCO)

NREL has reported that the average urban waste oil (yellow grease) produced by restaurants in New York State is 3,060 kg/year/restaurant, with a total of approximately 85,400,000 kg WCO produced per year state-wide [43]. Eighty-eight restaurants following the collection path near the Rochester Institute of Technology campus were selected to potentially provide a total of 269,000 kg/year waste oil. The WCO feedstock is collected by a light duty truck following a 19.3 km path (as shown on Figure A3) and filtered to remove organic solid wastes before being dispensed to a BioPro^{TM} 380 Automated Biodiesel Processor, manufactured by Springboard Biodiesel, LLC (Chico,

CA), which has the capacity of producing 59,000 liters of biodiesel annually. Even though it is beyond the system boundary of biodiesel production, it is noteworthy to mention that organic solid wastes filtered from WCO can serve as a potential feedstock for biogas production with anaerobic digestion.

The biodiesel processor is integrated with a two-step catalysis method [50]: WCO with high free fatty acids requires pretreatment in which the acid catalyst (e.g., sulfuric acid) mixes with methanol to reduce free fatty acids, followed by the transesterification reaction (see Eq.(5)) that requires an alkali catalyst like potassium hydroxide mixed with methanol to produce the biodiesel. For each run, it takes 13 hours for WCO to convert into biodiesel and glycerol. Water consumption and waste water off-site treatment are also quantified in this system, even though LCA does not consider water balance as environmental impact because it does not contribute impact to any traditional impact categories [29]. The remaining methanol from the distillation step is reused as the input to the next test run. For more information about the biodiesel production process flow with an SOFC-APU system, please refer to Figure A4.

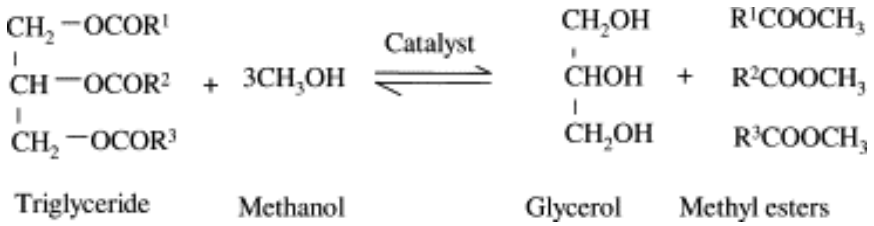

(5)

Glycerol is co-produced in the process and can be used in pharmaceutical and food industries [42]. Experimental data indicate 190 L WCO mixed with 37.8 L

methanol, 380 mL sulfuric acid and 2.35 kg potassium hydroxide yield 181 L biodiesel and 14 L glycerol (Springboard Biodiesel BioPro 380). This mixture has been confirmed in laboratory experiments by the author and in other studies [51]. The electricity for system facilities is assumed to be supplied from the New York State grid and Table 4 provides the sources for the average electricity generation along with respective electricity production efficiency [41].

Table 4. New York State average electricity grid mix (2006-2007)

Average grid mix	Percentage	Electricity production efficiency (MJ/MJ)
Petroleum	5%	4.53
Natural gas	30%	2.83
Coal	15%	3.56
Hydroelectric	18%	1.06
Nuclear	29%	3.24
Other renewable	3%	1.13

*Distribution and transmission loss of electricity is assumed as 8%

Ethanol from corn stover (CS)

The potential production of CS feedstock in New York State is 0.25 million dry tons annually [52]. However, it has been suggested that maintaining a certain amount of CS on the soil after harvest helps maintain soil organic carbon, minimize soil erosion, and retain and recycle nutrients. Spatari *et al.* [30] applied Monte Carlo analysis in a CS LCA and found the available residue (i.e., removable from land) for ethanol production varies from 35% to 70% of total CS production, depending on the agricultural practice and location. For the present analysis, an average of 50% of the available CS was assumed to be used as ethanol production feedstock, without jeopardizing soil quality or introducing other unintended environmental impacts.

A research group at NREL revealed the relationships between the collection distance of CS feedstock and the economically viable plant size [44]. As they suggested, 80 km radius around the plant corresponds to a plant treatment capacity of 2,000 metric ton of CS per day. Wojnar *et al.* [53] also indicate that the average truck travel distance for CS feedstock delivery in New York State is 38.6 km, however, the roundtrip travel pattern should be considered even if the truck returns empty [30]. Thus it is pertinent to consider CS feedstock transport distance as 80 km and the plant size as 2,000 metric ton per day in this study. Aden *et al.* [44] have developed a lignocellulosic biomass treatment process to produce ethanol using co-current dilute acid prehydrolysis followed with enzymatic saccharification and co-fermentation. This treatment process is adapted in this study and further integrated with an SOFC-APU system, as Figure A5 illustrates. CS with assumed 15% moisture content is pretreated with dilute acid (sulfuric acid) and ammonia to improve the accessibility of enzyme for hydrolysis. Overliming treatment is required to remove the liberated compounds that are toxic to the fermenting organism (*Zymomonas mobilis*). The cellulose enzymes are purchased from industrial suppliers and they stimulate saccharification and co-fermentation, which help convert cellulose and xylose into ethanol [47]. Anaerobic digestion is integrated in the system with the organic condensates and waste water from pretreatment. The biogas is combusted with the insoluble lignin to gain the energy recovery and generate electricity, which would cover the electricity and heat needs of the system. The main co-product of this considered system is the remaining electricity after subtracting the electricity use in the system, which will be sent back to the grid. On-site waste water treatment is also included within this system boundary.

Compressed natural gas from municipal solid waste (MSW)

In 2010, there were 27 active MSW landfills operating in New York State that accepted 7.6 million tons of solid waste (Department of Environmental Conservation, NY) [54]. Because comprehensive data on urban wastes in New York State have not been yet reported, the present work refers to a previous study conducted by NorthEast-South Towns [55], a group of municipalities in western New York State. It is estimated that in 2000 the total biomass solid wastes were approximately 252,000 metric tons (59% of the total waste stream) with 89,000 metric tons recovered by recycling or composting, and 163,000 metric tons available as bio-fuel feedstock. Figure A6 in Appendix A.1 shows the flow diagram of CNG derived from MSW with the SOFC-APU system. When the MSW arrives at the landfill, it is sorted into one of four categories: recyclable materials, organic biomass, refuse-derived fuels, and heavy wastes. Because MSW management sites have already involved waste collection, transport and sorting even without the anaerobic digestion process, the energy use and GHG emissions for these steps are not considered in this study. Anaerobic digestion processes decompose the organic fraction of MSW to form landfill gas by controlling the operating conditions (e.g., waste composition, moisture, oxygen content, and temperature) and the effluent gases typically contains 45-50% methane (CH_4), 35-40% carbon dioxide (CO_2), 10-15% nitrogen (N_2), and small amounts of hydrogen (H_2), oxygen (O_2), hydrogen sulfide (H_2S) and ammonia (NH_3) [30]. Instead of flaring to the atmosphere, the landfill gas can be captured by a collection system and further purified to mitigate the hydrogen sulfide (down to 5 ppm) with a zinc oxide desulfurizer and remove carbon dioxide with pressure swing adsorption [28,45]. Even though the LFG is monitored and shown with undetectable hydrogen

sulfide content from the landfill site studied in this work (see in Table 1), a pre-purification process is needed to mitigate hydrogen sulfide in that the compositions of LFG are also geographically varied and the SOFC-APU system is vulnerable to sulfur-containing gases. Because LFG is lighter than air, it spontaneously diffuses and moves upward to the landfill surface. After LFG purification and carbon dioxide removal, it is compressed up to 27,571 kPa in the truck delivery tank and no additional energy is needed during the gas (named as CNG) transfer process from the truck tank to gas stations because the tank pressure is high enough as compared to the local distribution system (1,480 kPa). The electricity needs for the facilities are provided by an on-site power generation based on landfill gas combustion.

2.2.3. Thermodynamic analysis of fuel reforming process

The SOFC system typically operates at high temperatures above 800 K, enabling utilization of both hydrogen and carbon monoxide as the input gases. Hydrocarbon catalytic decomposition process to produce hydrogen-rich reformates is a promising technology that practically integrates with the SOFC-APU system. Autothermal reforming is applied in this work because of its thermally balanced endothermic steam reforming and exothermic partial oxidation reactions. In this sense, the APU can be considered as a thermally self-sustaining system and the SOFC stack exhaust gases (including H_2, H_2O, N_2, CO_2, CO) are combusted to supply the heat for high temperature fuel reforming [14]. In order to identify the optimal operating conditions for fuel reforming with high hydrogen yield and no solid carbon formation, thermodynamic analysis based on total Gibbs free energy minimization (as per Eq. 6, below) is conducted to analyze the effects of several key system parameters (ratio of input steam to carbon,

ratio of input air to carbon, and reformer operating temperature). It is necessary to minimize carbon formation in the reforming process because solid carbon contaminates the fuel cell system and increases particulate matter emissions.

$$G_{\min} = \sum_{j=1}^{N} n_j (G_j^o + RT \ln \Phi_j y_j P) \quad (6)$$

where component j consists of n_j moles, with temperature T, pressure P, gas constant R, fugacity coefficient Φ_j, molar fraction y_j, and chemical potential in the reference state G^0_j.

This thermodynamic analysis simulates the fuel reforming conditions to determine the composition of gaseous effluent from the reformer, which generally includes hydrogen, carbon monoxide, carbon dioxide, and methane. These effluent gases are fed into the SOFC-APU system to generate the auxiliary electricity. Modeling outputs from the analysis include the amount of each type of fuel required to produce 1 kWh of electricity using the SOFC-APU and the potential environmental emissions (e.g. particular matter, GHG emission). These results are input directly to the LCI model described above, to parameterize the LCA results based on the technological performance of the specified SOFC system. For more information about developments of this thermodynamic model of the fuel reforming process, please refer to our previous work [14].

2.3. Results and Discussion

2.3.1. Process optimization using thermodynamic analysis

Thermodynamic analysis with total Gibbs free energy minimization enables identification of the optimal conditions for fuel reforming (i.e., maximum hydrogen yield

with no carbon formation). Figure 6 illustrates ethanol autothermal reforming results with (a) H_2 product yield, (b) solid carbon formation, (c) carbon monoxide, and (d) carbon dioxide production, as functions of molar steam-to-carbon (H_2O/C) ratio and operating temperature. The optimal region with peak hydrogen yield and absence of solid carbon generation is within the temperature range of 940 to 1030 K and steam-to-carbon ratio of 0.6 to 1 (the overlapped area of the labeled regions in Figure 6 (a) and (b)). The total carbon dioxide emissions produced by using ethanol with the SOFC-APU system can be quantified, and consists of carbon dioxide from carbon monoxide oxidation in SOFC

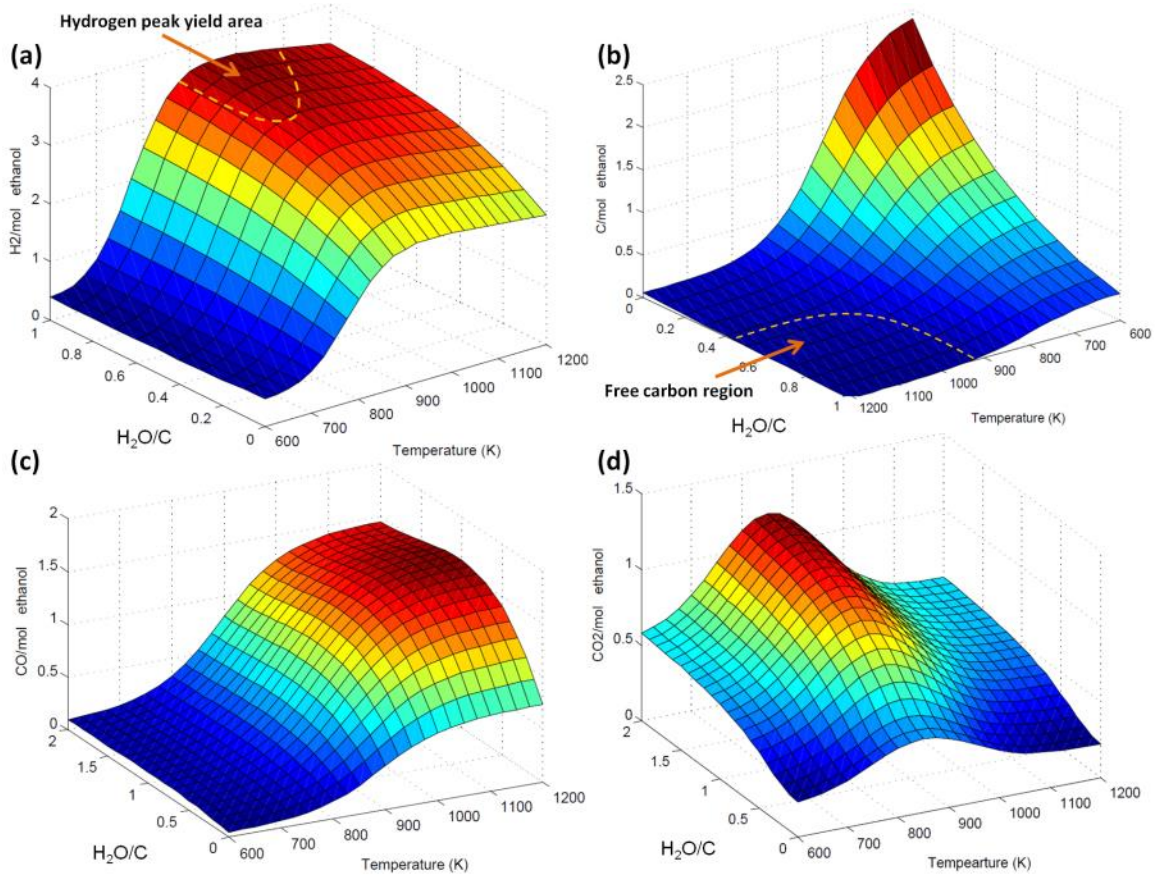

Figure 6: Equilibrium analysis of ethanol autothermal reforming: (a) hydrogen yield; (b) carbon formation; (c) carbon monoxide; and (d) carbon dioxide production (note that the scales are altered to provide adequate visualization of the surface plots)

Table 5. Efficiency of SOFC-based APUs supplied with various fuels, and that of diesel engine for truck auxiliary power applications

	Fuel reformation efficiency [$\eta_{reformer}$] $\frac{H_2 * LHV_{H2} + CO * LHV_{CO}}{Fuel * LHV_{Fuel}}$	**SOFC stacks efficiency [η_{stack}]** $\frac{Electricity_{out}}{H_2 * LHV_{H2} + CO * LHV_{CO}}$	**H_2 and CO utilization in SOFC stacks**	**System net efficiency [η_{system}]**
Data Source	Equilibrium analysis	Assumed based on literature	Computed via $\eta_{system}/[\eta_{reformer} + \eta_{stack}]$	Assumed based on literature
Biodiesel SOFC	85%	50%	70%	30%
Ethanol SOFC	93%	50%	64%	30%
CNG SOFC	95%	50%	63%	30%
Diesel SOFC	88%	50%	68%	30%
Diesel engine	-			10%

Table 6. Optimal operating conditions for fuels and the respective energy consumption and GHG emissions

Feedstock	**Fuel**	**Total energy use (MJ)**	**Fossil energy use (MJ)**	**Total GHG emission (kg CO_2eq)**	**Fossil-based GHG emission (kg CO_2eq)**
460g WCO	257g Biodiesel (SOFC-APU)	9.6	0.65	0.84	0.43
1196g Crude oil	281g Diesel (SOFC-APU)	14.6	14.6	1.47	1.47
1560g CS	390g Ethanol (SOFC-APU)	10.6	0.44	1.23	-0.02
35ton MSW/day	160g Methane (SOFC-APU)	9.7	0.37	0.09	0.03
3591g Crude oil	845g Diesel (ICE)	43.8	43.8	4.39	4.39

stacks (Figure 6(c)) coupled with carbon dioxide resulted from the autothermal reforming process (Figure 6(d)). The same method is applied to analyze autothermal reforming of ULSD, biodiesel, and CNG to identify respective optimal operating conditions for each fuel. The production of hydrogen and carbon monoxide from the reformation of these

hydrocarbon fuels were quantified in order to determine the fuel reformation efficiency. The overall net efficiency of the system for all SOFC-based pathways is defined as the ratio of the electricity generated from the system to the energy from the input fuel with respect to its lower heating value (LHV), and it integrates the fuel reformation efficiency, SOFC stack efficiency (assumed as 50%) [56], and fuel utilization in the stacks, as shown in Table 5. Fuel utilization for each individual path can be computed after normalizing the overall system net efficiency as 30% whereas that of the idling diesel ICE is considered to be 10% [40]. Fuel requirements and GHG emissions to generate 1 kWh auxiliary electricity are also obtained by conducting this modeling. Table 6 summarizes the optimal operating conditions for all fuels and the associated feedstock requirements and direct GHG impacts.

2.3.2. Total energy consumption

Figure 7(a) provides the total energy consumption for each pathway to generate 1 kWh electricity from waste-to-electricity (WTE), including feedstock processing energy from waste-to-pump (WTP) and fuel releasing energy (either by direct combustion or within the SOFC system) from pump-to-electricity (PTE). System expansion determines co-product energy credits for bio-fuel production. For example, glycerol energy credit from biodiesel production reflects the cumulative energy demand avoided by replacing the same amount of petroleum-based glycerol, whereas the electricity gain from lignin combustion in ethanol production results in an offset of the equivalent electricity generated in New York State. These co-product energy credits result in relatively low feedstock processing energy of biodiesel and ethanol (0.05 and 0.04 MJ, respectively), as

compared to diesel production (2.7 MJ). Overall, biodiesel APU operation requires the lowest total energy consumption (9.6 MJ) with a system energy efficiency of 37.5%, followed by methane APU of 9.7 MJ. Figure 7(b) shows the contributions to cumulative energy demand by different processes on the SOFC-APU path and it illustrates the energy use for the APU step represents the major contribution for all fuels, which suggests that improving energy conversion efficiency of SOFC-based APU will lead to most significant reduction of overall energy consumption and should be prioritized, regardless of fuel choice. Electricity consumption and feedstock processing chemical inputs (methanol, sulfuric acid, and potassium hydroxide) are two main contributions for the biodiesel pathway, which is in agreement with an earlier NREL report [42]. Co-products of biodiesel production (glycerol and potassium sulfate) offset around 28% of its total energy consumption, whereas the electricity credit in ethanol production may reduce 10% of its total energy use.

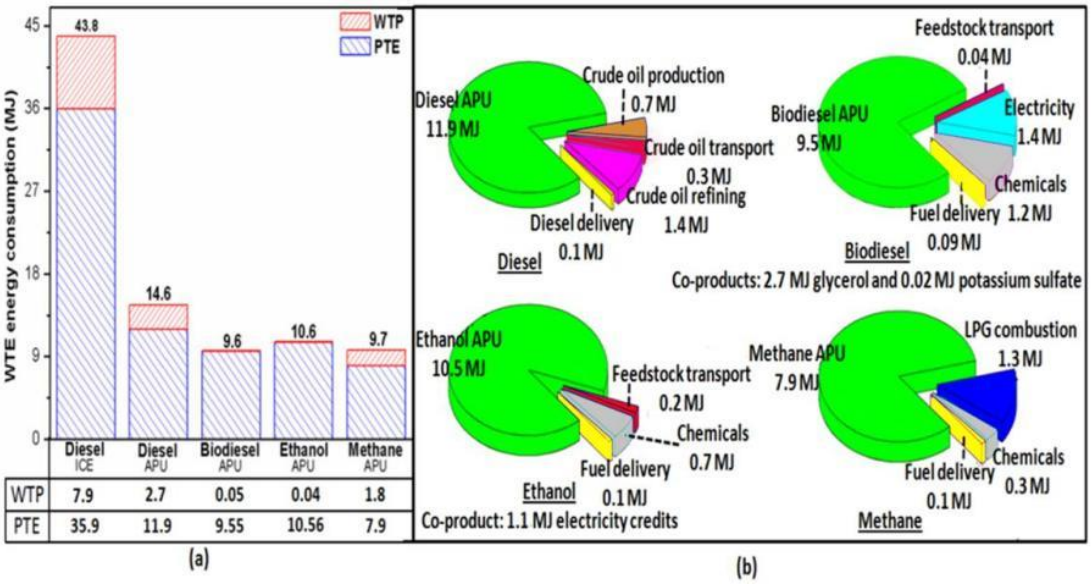

Figure 7: (a) Total energy consumption of different paths to generate 1 kWh electricity; (b) Contribution of all processing energy demands for each fuel path used in the SOFC-based APU

2.3.3. Total GHG emissions

Total GHG emissions (including fossil and biogenic contributions) in CO_2-equivalents (including CO_2, CH_4, and N_2O) for different fuel pathways are illustrated in Figure 8(a). The bio-fuel APU options all emit less GHG than diesel direct combustion and diesel APU. Biodiesel has a low GHG emission in WTP due to the avoided production of petroleum based glycerol. GHG emission contributions of all fuels are shown in Figure 8(b). Although operation of the APU is still the primary contributor to the total for each pathway, more predominant contributions are observed due to direct CO_2 emissions on many of the pathways. Even though ethanol has an emission credit associated with returning partial electricity to the grid, it still shows relatively high GHG emission because of lignin combustion, which accounts for 42% of total GHG emission. The removal of carbon dioxide from anaerobic digestion products results in a major contribution of GHGs for the methane pathway (37%). However, the methane system is dominated by the avoided impact of CO_2 emissions due to use of landfill gases for CNG production rather than conventionally flaring these gases to the environment, this avoided impact credit reflected as the negative value on Figure 8(a). The avoided GHGs associated with diverting the landfill gas offsets about 87% of the total GHG emission on the methane APU pathway, with a corresponding reduction in total GHG emission to 0.09 kg CO_{2eq}/kWh.

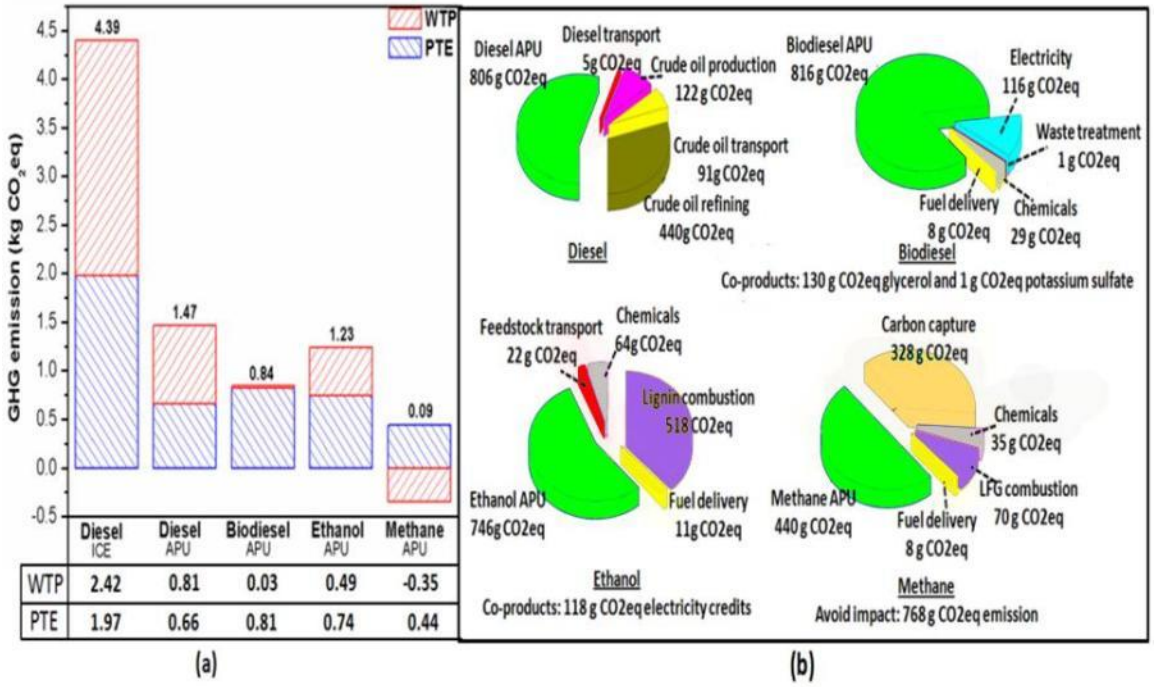

Figure 8: (a) Total GHG emissions of different paths to generate 1 kWh electricity; (b) Contribution to GHG emissions in all processing steps for each fuel path used in the SOFC-based APU

2.3.4. Fossil energy use and fossil-based GHG emissions

In the results described above, cumulative energy and GHG emissions are based on total system inputs and emissions from both fossil and biogenic or renewable resources. However, accounting for biogenic GHGs is a widespread challenge to the robustness of bio-fuel LCA studies. Many studies have reported results in terms of fossil energy and fossil-based GHG emissions, with CO_2 and CH_4 originating from biogenic sources treated as part of the natural carbon cycle, and thus, zero contribution to process impacts [57]. To provide results that are broadly comparable with future studies reporting either total or fossil impacts only, Figure 9 summarizes the cumulative energy and GHG emissions associated with fossil inputs only. Based on the system boundary previously

defined in this study, GHG emissions from direct use of waste biomass (WCO, CS, and MSW) are biogenic in origin. For the cases of ethanol and CNG, GHG effluents from the SOFC system (PTE) are negligible because the carbon footprints embedded in the fuels are mostly derived from waste biomass. Similarly, the net fossil GHG from lignin combustion in CS treatment and landfill gas combustion in MSW process are also zero. However, the biodiesel production process consumes fossil-based methanol inputs to the transesterification reaction, shown in Eq. (1) [50], and therefore, fossil CO_2 contributions are determined by the stoichiometric ratio of inputs. In all of the waste biomass pathways, elimination of biogenic carbon from the inventory renders the options relatively indistinguishable and all impacts are very small, compared to fossil-derived diesel baseline. When considering the energy difference (net fossil energy) between fossil energy input and co-product fossil energy credits (excluding energy of biogenic origin), bio-fuel options all show low fossil energy use and are more attractive than petroleum-based diesel (see on Figure 9). On-site power generations from biogenic sources (e.g. lignin combustion in ethanol production, landfill gas combustion in CNG production) help mitigate the external electricity requirements. For instance, the net fossil energy use of CNG production would increase from 0.37 MJ to 1.7 MJ if the system electricity is instead supplied from the New York State public grid.

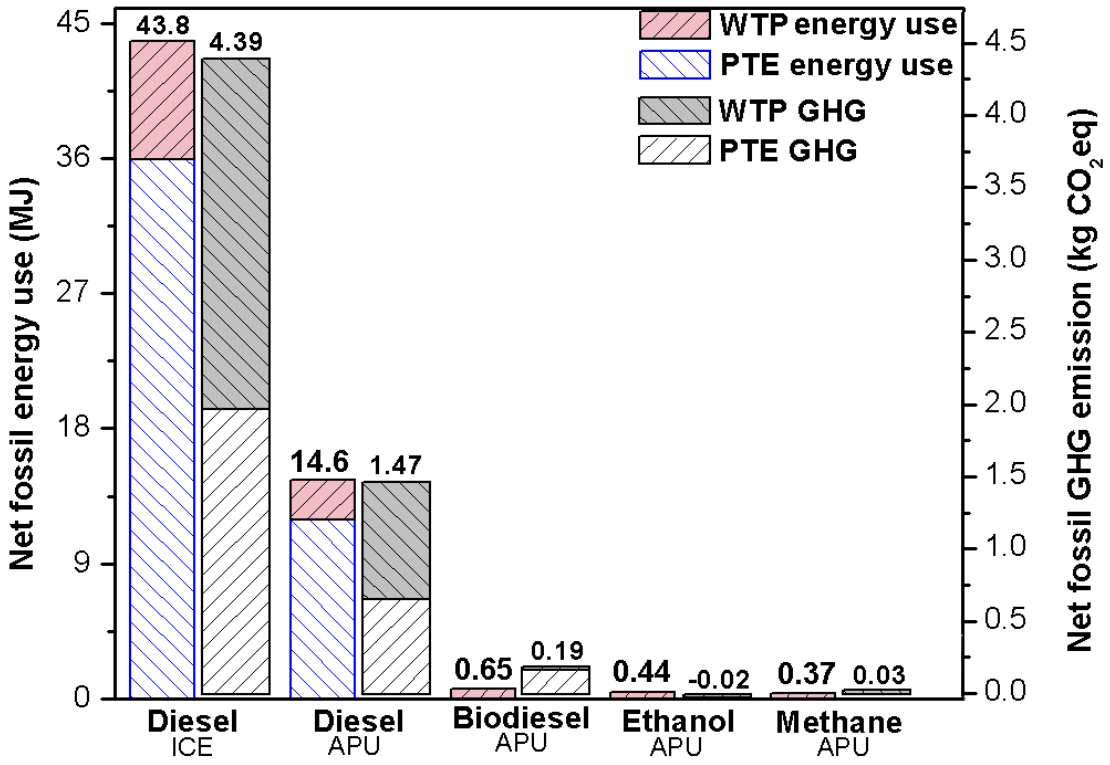

Figure 9: Net fossil energy use and fossil GHG emission of different fuel paths

2.3.5. Interpretation and sensitivity analysis

Table 6 consolidates the energy consumption and GHG emission results for all pathways. From total energy use and total GHG emission standpoints, methane derived from MSW achieves a relatively high fuel efficiency (37%) with lowest total GHG emission (0.09 kgCO_2eq) to generate a unit of auxiliary electricity, and thus it may be the optimum bio-fuel option for truck SOFC-APU applications in New York State region. If stakeholders or governmental agencies (e.g., EPA) promote bio-fuel production with less fossil energy consumption, then ethanol from CS would also be an attractive option due to its least fossil-based GHG emission and low fossil energy use.

Many bio-fuel LCA studies state that several key parameters including feedstock variation, different biomass treatment techniques, transportation options, and co-product credit, directly affected the outcomes [31]. However, out of these key parameters, it might be expected that the most uncertain parameter is the choice of co-product allocation procedure [30,58]. System expansion method was applied in this work to analyze the co-product credits of bio-fuel production, where these co-products are assumed to substitute for the equivalent products that require energy in their productions. This approach enables avoiding product allocation issues and is consistent with the recommendations from LCA principles and practice [59]. However, in order to reduce the uncertainty of co-product credit and improve the robustness of the results illustrated in this work, different allocation methods besides system expansion were applied to glycerol and electricity co-produced in biodiesel and ethanol pathways, respectively. Typically, the co-products have MJ/Btu values equivalent to those of their primary products (energy-based) and are subject to the product with economic price (market value-based). Wang *et al.* have identified the allocation methods of energy-based and market value-based as the major factors for allocating cumulative energy and emissions for bio-fuel productions [60]. A group from the Argonne National Laboratory reported the biodiesel production from soybean with a two-step catalysis method that is similar to the biodiesel production processes described in this study [58]. They conducted a sensitivity analysis on glycerol co-product with different allocation methods. Therefore, the data for glycerol co-product derived from WCO in this work are extrapolated from their presented results. Luo *et al.* [61] analyzed the corn stover-based ethanol based on mass, energy, and economic value-based allocation as well as system expansion. Figure 10 shows the

sensitivity analysis of co-product credits of glycerol and electricity in biodiesel and ethanol pathways, respectively, in term of total energy use and total GHG emission. The result of applying different allocation methods only shows a difference of 10% or less as compared to values presented here using system expansion. Thus, the methodology provides a robust means for evaluating bio-fuel production and use pathways from both life cycle environmental and technological standpoints.

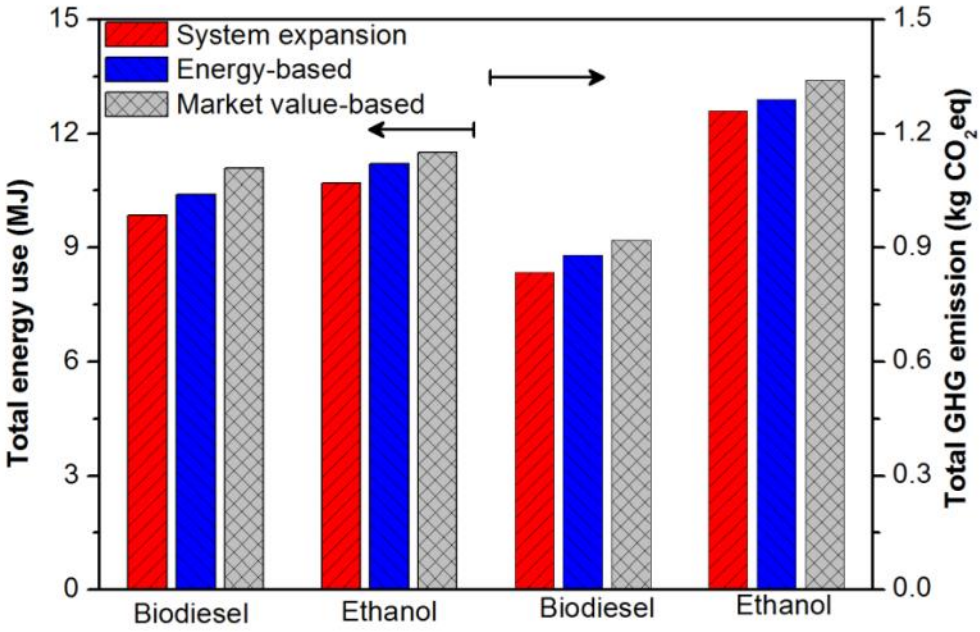

Figure 10: Sensitivity analysis of co-product credits for glycerol and electricity in biodiesel and ethanol production, respectively, with different allocation methods

2.4. Summary

The methodology demonstrated in this work is an interdisciplinary combination of environmental assessments and thermodynamics. It not only allows for environmental impacts to be assessed during systematic process design, but also provides a possible path for LCA to overcome the challenge of data acquisition for realistic operating conditions.

The methodology and associated outcomes of this work can also be replicated for the waste feedstocks and geographic parameters specific to any region, to provide the quantitative information required for decision makers to develop feasible local bio-fuel options for fuel cell-based energy systems. Total potential auxiliary electricity derived from available waste feedstock in the New York State (85,400 tons of WCO, 0.25 million tons of CS, and 7.6 million tons of MSW) can be determined as ~345 GWh (see in Table 6) [43,52,54], which accounts for approximately 0.77% of total auxiliary electricity needs used for truck idling service in the United States (1.2 billion gallon of diesel with diesel engine [26]). Therefore, a large portion of electricity demand still needs to rely on other energy sources (e.g., battery, bio-fuels from other paths). Liquid bio-fuels such as biodiesel derived from WCO and ethanol from corn stover, have been demonstrated to have less environmental impacts (both GHG emission and energy consumption), so the applications of these fuels in transportations and SOFC-APUs were further explored from economic and technological aspects in the following chapters.

III MULTI-OBJECTIVE OPTIMIZATION OF BIODIESEL-ETHANOL-DIESEL BLNEDS

3.1. Introduction

During 2010, over 19.1 million barrels of petroleum products were consumed daily within the United States and half were imported from foreign nations [62]. Rising concerns of volatile crude oil price, threats to national security, and adverse environmental impacts from using fossil fuels are propelling many political mandates, economic incentives, and societal investments in alternative fuels [63]. The United States have witnessed a dramatic growth in bio-fuel production in the last two decades and the Energy Independence and Security Act of 2007 mandated the use of 36 billion gallons of bio-fuel by 2022 [64]. Biodiesel (B-diesel) possesses physical and chemical properties that are similar to diesel, which makes it a promising fuel when blended with conventional diesel [65]. It has also been reported that biodiesel not only improves the lubricity of the blended fuel and results in longer engine component life, but also alleviates environmental impacts by reducing CO and particulate emissions [66]. However, two major drawbacks in biodiesel-diesel fuel blends are their poor performances in regards to cold flow and fuel kinematic viscosity limit, which make the blended fuel difficult to atomize into small droplet and deliver to the engine at low temperature [67]. Alcohol based co-solvents (e.g. methanol, ethanol) have been reported as additives to improve B-diesel performance and also considered as oxygenates to accelerate complete fuel combustion [68-70].

To achieve the goal of profit maximization, crude oil refineries generally need to provide a consistent and optimal raw fuel component supply while meeting all quality specifications of blended fuels. Production planning problems in refinery industries have been widely studied by integrating many optimization techniques (e.g., non-linear programming (NLP) [71], mixed integer non-linear programming (MINLP) [72], successive linear programming (SLP) [73], and sequential quadratic programming (SQP) [74]). Off-line fuel blending and production logistics are two major areas that are intensively reported [75]. For example, Glismann and Gruhn [76] analyzed long-range planning by solving a large-scale nonlinear multi-blend problem to generate the optimal blend recipe, which is then incorporated as the fixed decisions to a mixed-integer linear program (MILP) short-term scheduling model that involved resource and temporal aspects. Mendez *et al.* [75] further studied the crude oil optimum production logistics with discrete time and continuous time optimization models. Even though various mathematical programming methods are currently available for refinery optimization, many of the proposed models are based on assumptions which help reduce computational complexity and other inherent modeling challenges but may make the solution unrealistic for the actual operating conditions. Mendez *et al.* have reviewed previous works and summarized three common assumptions, which include predefining the recipe of different fuel blends as an external fixed factor in the system, considering the input raw components and their flow rates constant, and assuming the specifications of final blends are linear with the properties of input raw fuels [75]. Li *et al.* [77] also highlighted that the blending recipe would directly affect scheduling decisions and the outcome of the process control in gasoline refinery system. Thus it is crucial to analyze the acceptable

mixing rules for different fuels and finalize the optimum blend recipes before embarking on the dynamic scheduling optimization.

Most of the prior work on fossil fuel blended with bio-fuels, such as gasoline with ethanol and diesel with biodiesel, have focused on experimentally characterizing the fuel properties and evaluating the blended fuel performance or consequential environmental impacts from using these fuels [66,69,78]. Mathematical optimization models combining technical and economic objectives have not yet been well developed to analyze fuels blended with bio-fuels, which vary geographically and are feedstock source dependent. The goal of this work, therefore, is to develop a non-linear optimization model for biodiesel-ethanol-diesel (BED) ternary blending processes which will be applied to establish the optimal recipe and improve system profitability while meeting multi-criteria such as practical fuel quality specifications (kinematic viscosity, density, lower heating value, cloud point, cetane number, and sulfur contents) and economic viability (fuel production cost, market demand, and fuel market price). Pertinent fuel mixing rules for BED blends were extrapolated from previous work and adapted to be constraints in this model. Several dynamic and/or uncertainty factors (e.g., petro-diesel supply reduction, fossil fuel market price, policy changes on subsidizing bio-fuel production, potential additives, and feedstock selections for bio-fuel production) are further analyzed with this optimization model.

3.2. Blended Fuel Model

3.2.1. Problem statement

The correlations for predicting blended fuel specifications, especially for non-polar fuels such as diesel or biodiesel mixed with polar solvents like alcohol, are complex and typically depend on the properties of the raw components used in the blends with either linear or nonlinear functions of concentration [75]. These correlations need to be analyzed to simulate the key specifications of fuel blends within an acceptable range based on experimental data before evaluating the optimum recipe with certain criteria. Three key dynamics for considering fossil fuel blended with bio-fuel for transportation applications are market disturbances (e.g. fuel price, fuel supply and demand, and biomass feedstock cost), technology evolution (e.g. fuel recipe, potential opportunities for additives, engine compatibility, and various feedstock-based bio-fuels), and policy changes (government tax credits on bio-fuel production, bio-fuel minimum content mandates, and regulations on fuel quality) [68, 79-82]. An optimization model that enables simultaneously capturing these factors and generating the optimum production formula with profit maximization has not yet been well developed for bio-fuels blended with fossil fuels, and economically feasible energy production methods still need to be explored to provide guidance for decision makers and stakeholders.

3.2.2. Proposed optimization model

The American Society for Testing and Materials (ASTM) published standard D7467-10 to provide specifications for diesel-biodiesel blends, which include flash point, kinematic viscosity, copper corrosiveness, sulfur content, cloud point, and cetane

number. A report from the National Renewable Energy Laboratory (NREL) conducts a failure modes and effects analysis (FMEA) to evaluate the safety and performance of ethanol/diesel blends for heavy truck applications, and it suggests the flash point and copper corrosiveness issues from using anhydrous ethanol may not significantly affect the properties of diesel-ethanol blends if ethanol content is less than 15% [83]. Since the ethanol fraction in this work does not exceed 15% of the final blends, flash point and copper corrosiveness are not included in the fuel properties criteria, which only consider kinematic viscosity, lower heating value (LHV), sulfur content, cloud point, density, cetane number and single phase liquid [66, 81].

Some fuel property requirements (e.g. cloud point, kinematic viscosity, density, and liquid phase behavior) are temperature-dependent factors and are also geographically and seasonally heterogeneous, thus it should be tailored for a given geographical region when conducting the studies. Also bio-fuel production would preferentially consider the locally available feedstock [32]. Therefore, this work is conducted within the geographical boundary of New York State, but the methodology can be applied to other regions as well.

Gallagher *et al.* [84] highlighted the relations between capital costs and plant size to determine the economies of scale of bio-fuel production, thus it is important to predefine the plant size before embarking on the study. The representative bio-fuel production volumes for large, modern plants were assumed to be 245 million L/yr for ethanol and 110 million L/yr for biodiesel [85]. By adapting various recipes of BED

blends, the firms enable refining different grades of final products based on the blended fuel quality. This work considers two different grades of BED blends (regular and premium) in order to simplify the analysis and because there are no grade categories yet for commercial petro-diesel blends, the premium BED blend is considered to possess the same economic value as diesel for all studied years while the price of regular BED blend is $ 0.05/L less than that of diesel, which is based on the difference between the retail prices of regular gasoline and premium gasoline [86].

BED blend fuel mixing rules

By comparing the data derived from different mixing rules that are commonly applied in oil refinery fields with the experimental results reported by other researchers, the pertinent mixing rules for each specific property of the BED blends were determined. Absolute average deviation (AAD, Eq.(7)) was used as a measurement to determine the degree of difference between the predicted data and the experimental results [81], and the mixing rule with the lowest AAD value was chosen and further used in the optimization model.

$$AAD = \frac{\sum_{i=1}^{N} \left| \frac{R_P - R_E}{R_E} \right|}{N} \tag{7}$$

where N is the number of data points, and R_p and R_E are the predicted and experimental value, respectively.

Kinematic viscosity measures the resistance of a fluid and higher viscosity indicates more difficult liquid flow [87]. A mixing equation originally proposed by Lederer *et al.* was further modified for ternary blends; see Eq. (8) [88,89].

$$\ln \nu_{mix} = \left(\frac{\alpha f_D}{\alpha f_D + \beta f_B + f_E}\right) \ln \nu_D + \left(\frac{\beta f_B}{\alpha f_D + \beta f_B + f_E}\right) \ln \nu_B + \left(\frac{f_E}{\alpha f_D + \beta f_B + f_E}\right) \ln \nu_E \quad (8)$$

where ν_{mix}, ν_D, ν_B, and ν_E are the kinematic viscosities of the blends, diesel, biodiesel, and ethanol; f_D, f_B, and f_E are the volumetric fractions of diesel, biodiesel, and ethanol in the blends; α and β are both empirical constants, which can be extrapolated from several reports as 6.82 and -0.75, respectively [69,90,91]. Different mixing rules (Kay's, Semilogarithmic, Grunberg-Nissan, and modified Lederer) were applied to determine the deviations of predicted results and the empirical data of viscosity of various blends (diesel-ethanol, biodiesel-ethanol, diesel-biodiesel, and BED); see Figure A7 in Appendix A.2. The modified Lederer equation shows the lowest AAD (4.73%) as compared to other mixing rules, and appears suitable for viscosity prediction for BED blends. Eq.(8) is also applied to predict the kinematic viscosity of BED blends at temperatures ranging from 0 to 70^{o}C based on the viscosities of individual components at corresponding temperatures; see Figure A8.

Cloud point indicates the temperature at which the fuel starts to form wax crystals and cannot be pumped or injected into the engine. In cold temperature, fuels with both relatively high cloud point and high viscosity (e.g., biodiesel) would cause poor fuel atomization into small droplet and need more energy to pump [92]. Upon comparison to other mixing rules (including Kay's, and Semilogarithmic), the Hu-Burns Equation (Eq.

(9)) illustrates the lowest AAD (5.11%) and is thus used to predict the cloud point in this work [93]; see Figure A9.

$$T_{mix}^{1/a} = \sum_{i}^{3} f_i^{1/b} * T_i^{1/a} \tag{9}$$

where T_{mix} and T_i are the cloud points of the blends and ith component; f_i is the volumetric fraction of ith component in the blends, a and b are empirical constants, 0.074 and 0.97, respectively [94].

Cetane number is a measure of the ignition delay properties of the fuel and is defined by the relative proportions of n-hexadecane and α-methylnapthalene [95]. A high cetane number indicates a short ignition delay and provides more time for fuel to burn completely. Even though Kay's mixing rule by mass and the Grunberg-Nissan Equation (Eq.(10)) both show relatively low AAD in predicting cetane number (4.64% and 3.07%, respectively), the latter is applied in this work because it shows a close match for BED blends [81]; see Figure A10.

$$\ln \gamma_{mix} = \sum_{i}^{3} f_i * \ln \gamma_i + \sum_{i}^{3} \sum_{k}^{3} f_i * f_k * G_{ik} \tag{10}$$

where γ_{mix} and γ_i are the cetane number of blends and ith component; G_{ik} is the interaction term of i and k fuel components, $G_{ik} = 0$ if $i = k$ [69]. Fuel interaction terms $G_{B-D} = 15.12$, $G_{D-E} = 26.37$, and $G_{B-E} = 9.37$ [66,91,96].

Fuel lower heating value (LHV) is defined as the amount of heat released by completely combusting the fuel and returning the temperature of the combustion products

to 150^{o}C, which is assumed as an indicator of fuel combustion performance in the engine [97,98]. Similar to the fuel specifications of density (see Figure A11) and sulfur content, LHV can be extrapolated from Kay's mixing rule, Eq. (11):

$$\kappa_{mix} = \sum_{i}^{3} f_i * \kappa_i \tag{11}$$

where κ_{mix} and κ_i are the properties (LHV, density, or sulfur content) of blends and the ith component. Phase behavior of fuel blends has been analyzed by many studies to determine the relative compatibilities of biodiesel, ethanol, and diesel fuel [68,99,100]. Fuel stability of BED blends in this work is derived from the results reported by Fernando and Hannan [68]. Table 7 summarizes the data sources along with the chosen mixing rules for each fuel property.

Table 7. Mixing rules for key specifications of BED blends

Fuel specification	Data sources	Chosen mixing rule
Kinematic viscosity	66,67,69,87,91,96, 98-100	Modified Lederer equation
Cloud point	85,90,93,98,100	Hu-Burns Equation
Cetane number	66,83,91,94-97	Grunberg-Nissan equation
Density	67,69,82,90,95,98-100	Kay's volumetric
Lower heating value	66,67,70,90,93-97,99	Kay's volumetric
Sulfur content	66,68,85,93,95,99	Kay's mass
Liquid single phase behavior	68	-

Model formulation and definition of base case

Figure 11 illustrates the proposed system framework of BED blends that consists of diesel derived from crude oil, ethanol and biodiesel from various representative biomass feedstocks in New York State [101]. Regular blended diesel and premium blended diesel are two grades of final fuel products that are used in diesel truck engines for transportation purposes. The main objective of the model is to maximize the net profit

of the fuel production firms, which is simplified as the total blended product revenue minus the total component cost:

$$\max \sum_{j}^{2} (P_j * B_j - \sum_{i}^{3} C_i * Q_{ij}) \quad (12)$$

where P_j is the price of j[th] grade of BED blends; B_j is the batch size of j[th] grade blend; C_i is the cost of i[th] component; and Q_{ij} is the i[th] component volumetric quantity used in j[th] grade blends.

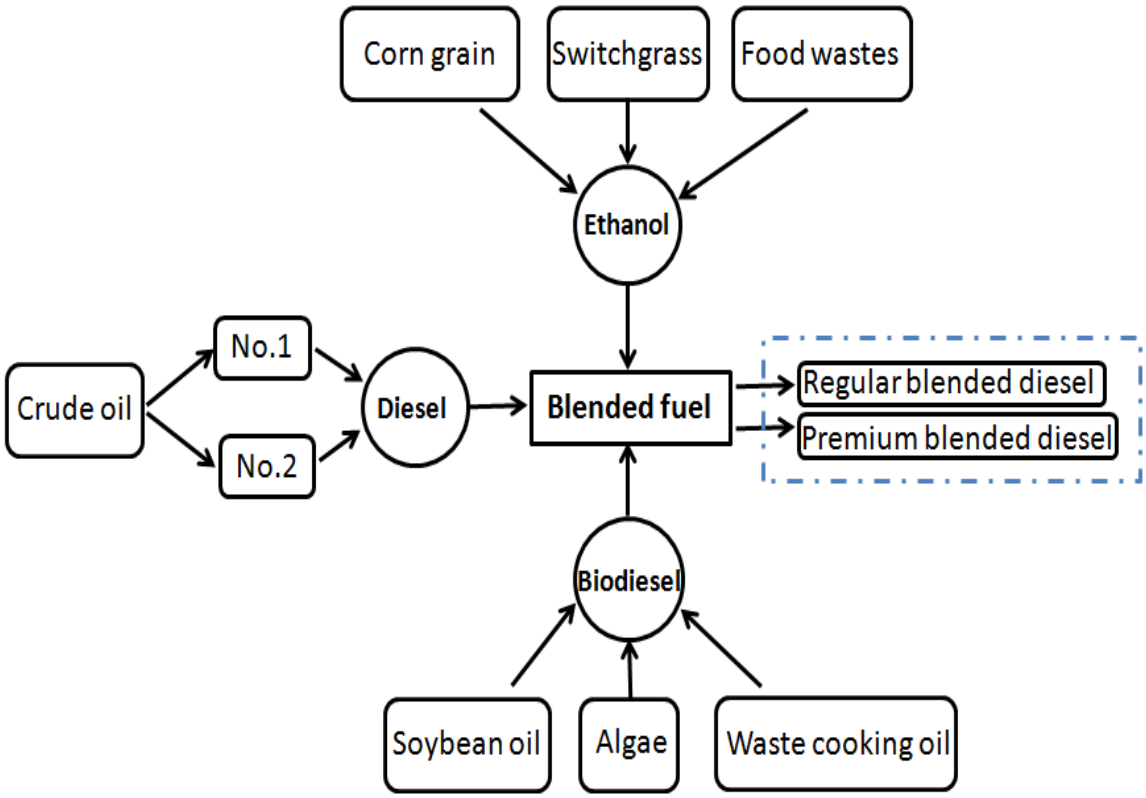

Figure 11: Various combinations of feedstocks for biodiesel–ethanol–diesel (BED) blends

Fixed costs and other overhead are not considered in this objective and therefore actual profit gained by any specific firm from these blends would be less than these reported values. The objective function is subjected to multiple constraints, including fuel

quality requirements (Eq.(13)), market energy demand in the diesel sector for transportation applications (Eq.(14)), and regional fuel production (Eq.(15)):

$$\forall_j, \psi_j^{\min} \le \psi_j \le \psi_j^{\max} \tag{13}$$

$$\forall j, \tau * LHV_j * B_j \ge D_{Dem,j} \tag{14}$$

$$\forall i, \sum_j^2 Q_{ij} \le A_i \tag{15}$$

where ψ_j are the jth grade blend properties (kinematic viscosity, cloud point, sulfur content, LHV, cetane number, and density); $\psi_j^{\min}$ and $\psi_j^{\max}$ are the minimum and maximum fuel requirements of corresponding properties; τ is the energy conversion efficiency of a diesel engine with respect to fuel LHV, and is assumed to be 45% [102]; LHV_j and $D_{Dem,j}$ are the lower heating value and market total energy demand of jth grade blend, respectively; A_i is the availability of ith fuel produced in New York State.

Table 8. Properties of raw components and BED blends for the base case

Specifications	**Raw component**			**blended product**	
	No.2 diesel	Corn-ethanol	Soybean-biodiesel	Regular blends	Premium blends
Density (kg/L) @15 ^{o}C [66-70]	0.833	0.792	0.885	<0.86	<0.855
Lower heating value (MJ/L) [66,68,70,90,98]	35.7	19.9	33.5	>33	>34
Kinematic viscosity (cSt) @40 ^{o}C [69,96]	3.14	1.13	5.15	<3.8	<3.5
Cloud point (^{o}C) [93,95]	-10	-35	1	< -7	< -10
Cetane number [69,70,90]	46.2	6	56.4	>43	>45
Sulfur content (ppm)[83,103]	15	0	5	<15	<15
Availability (Million liter)[a], [103]	13.35	5	8	-	-
Market demand (terajoule, TJ) [102,104]	-	-	-	>400	>250
Production cost ($/L)[b], [87,93,102]	0.33	0.29	0.42	-	-
Market price ($/L) [104,105]	-	-	-	1.01	1.06

[a] Only considering the regional fuel production in New York State (excluded import portions).
[b] Include both federal and state tax credit of $0.41/L for biodiesel and $0.26/L for ethanol production.

The case of No.2 ultra-low sulfur diesel blended with ethanol derived from corn grain and biodiesel from soybean oil is considered as a baseline for this study. Table 8 provides the key features of these raw fuel components and BED blended products. Regular BED blends and premium BED blends possess specific fuel qualities and market demands [69,103]. Optimization modeling software (LINGO 13.0, Lindo Systems Inc., IL, US) was applied to solve the problem based on the analytical expressions of objective function and constraints described above.

3.2.3. Model applications

Time-varied factors (diesel production, market retail price, and policy change on bio-fuels)

Figure 12 shows the historical data trends of No.2 diesel production cost, diesel market retail price, and amount of diesel produced in New York State with polynomial regression fittings and it projects future changes of diesel supply and possible fluctuations of blended diesel retail price [104,105]. The overall trend of diesel production cost behaves similarly to its retail price. These two factors along with diesel production were simultaneously integrated in the studied model to generate the time-dependent optimum BED blended compositions while maintaining other variables as constants.

The renewable fuel standard (RFS) established by the Energy Independence and Security Act (2007) mandates a minimum percentage of bio-fuels in the transportation fuels [64]. Ethanol and biodiesel production also received significant government support with financial subsidies (both from federal and state) to reduce their production costs

($0.41/L tax credit for biodiesel and $0.26/L for ethanol) [84,106]. But recently, these programs were terminated at the national level [106]. The optimum recipes of BED blends are thus explored under scenarios with bio-fuel tax credit changes and the minimum mandated percentage of bio-fuels in the blends, measured by Eq.(16). The base case model considers the tax credits of bio-fuel but excludes the mandate constraint.

$$\forall j, \sum_{k}^{2} f_{kj} \geq f_{reg}^{\min} \tag{16}$$

where $f_{reg}^{\min}$ is the mandated minimum bio-fuel volumetric ratio content in blends, and f_{kj} is k^{th} bio-fuel in j^{th} grade blends.

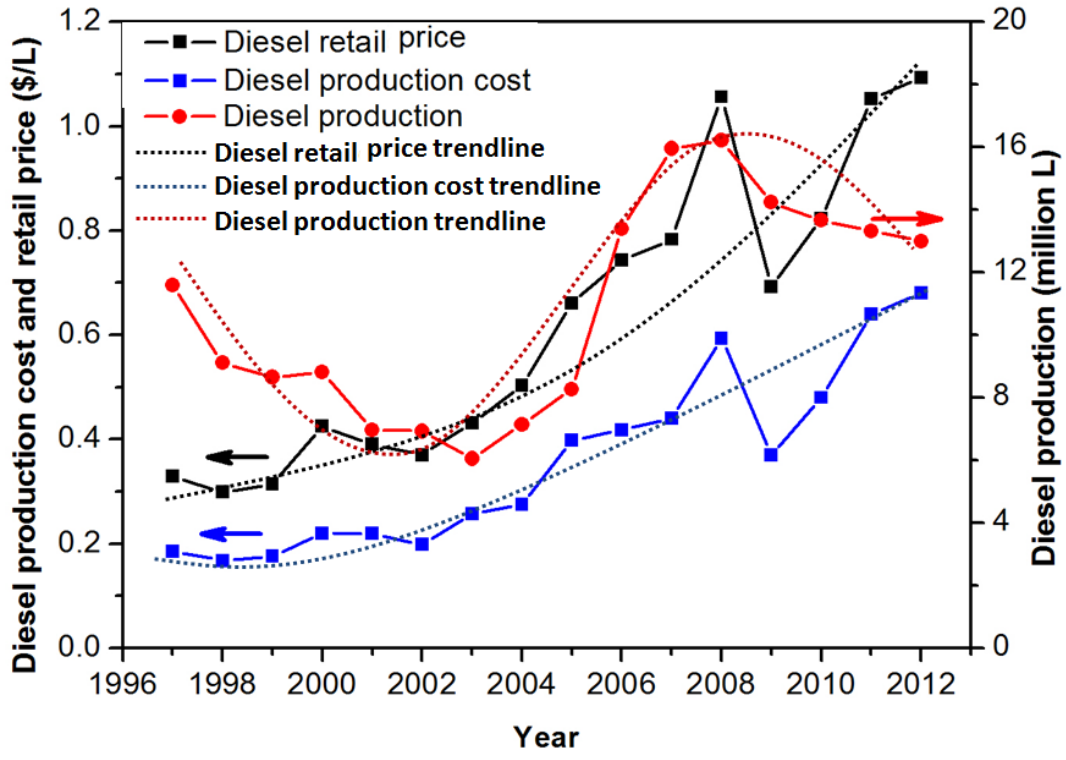

Figure 12: Historical data of No. 2 diesel production and its market retail price in New York State

Explore potential opportunities for fuel additives

Many additives such as ignition promoters, oxygenate additives, lubricity additives, cetane number additives, and wax dispersants, have been proposed to mix with blended diesel fuel to improve the fuel performance [107,108]. By implementing the strategy of constraint relaxations to fuel specification requirements of BED blends in the optimization model, it would reveal the magnitude of the maximum profit change with one unit relaxation of a specific constraint and identify the crucial specification constraint, which may promote the potential opportunity to develop an additive to improve that specification.

Feedstock sources

The specifications of bio-fuels are heavily dependent on their feedstock sources and there are various biomasses available in New York State for ethanol and biodiesel production. This work selected ethanol derived from corn grain, switchgrass, and food wastes, which represent 1^{st}, 2^{nd}, and 3^{rd} generations of bio-fuel feedstocks [109]. Similarly, biodiesel from soybean oil, algae, and waste cooking oil (WCO) were chosen. Fuel specifications of these bio-fuels are extrapolated from the open literature and listed in Table A1. The fuel requirements of BED blends with combinations of different feedstocks were kept consistent with that in the baseline scenario.

3.3. Results and Discussion

Figure 13 illustrates a ternary diagram of the regular BED blends based on regular blend fuel requirements listed in Table 8. For the base case study, the sulfur content

requirement is less than 15 ppm for regular BED blends and the raw components (ultra-low sulfur diesel, ethanol, and biodiesel) are all less than 15 ppm, therefore the sulfur content constraint is non-binding and is not shown in this diagram. Consistent with the work done by Fernando and Hannan [68], the boundaries of the single phase liquid blends under two different low temperature conditions (-5 and -13 ^{o}C) are highlighted in the ternary region on Figure 13. The feasible region for regular BED blends used in New York State only occupies a small area of the whole ternary diagram, which suggests that practical BED blending without additives is challenging. Premium BED blends that have even stricter constraints will be even more difficult. The maximum net profit is $12.98 million from producing 11.94 million liter of regular BED blends and 7.18 million liter of premium BED blends. Point P highlighted in Figure 13 identifies the optimal composition of raw components in regular BED blends for the base case model. In the solution report, Lingo generates the slack or surplus value for each constraint, which indicates how many more units of the variable could be added to the optimal solution before the constraint is bound when the slack is positive. Table A2 provides the positive slack of several constraints generated in the base case. For example, when the model reaches its optimal condition, there is still bio-fuel production capacity remaining (3.7 and 3.5 million L per year for ethanol and biodiesel, respectively). It implies the strategy of either blending more bio-fuels in BED fuels or importing more diesel to blend may enable higher optimal profit, which provides the opportunities for the stakeholders to utilize these available slacks of the constraints. The Lingo solution report also provides the dual or shadow price, which describes the magnitude change of the maximum net profit in the objective function if the constraining value is increased or decreased by one

unit. After ranking out the dual price of all the constraints (see in Table A3), it shows the upper limits of kinematic viscosity for both grades of blends have relatively high dual prices followed by the diesel availability constraint. If these viscosity constraints are relaxed to increase one unit on regular and premium blends, the maximum profit would increase $1.7 and $1.1 million dollar, respectively. Therefore, it may be rational to further conduct the constraint relaxation on kinematic viscosity and diesel production, which will be described in the following section.

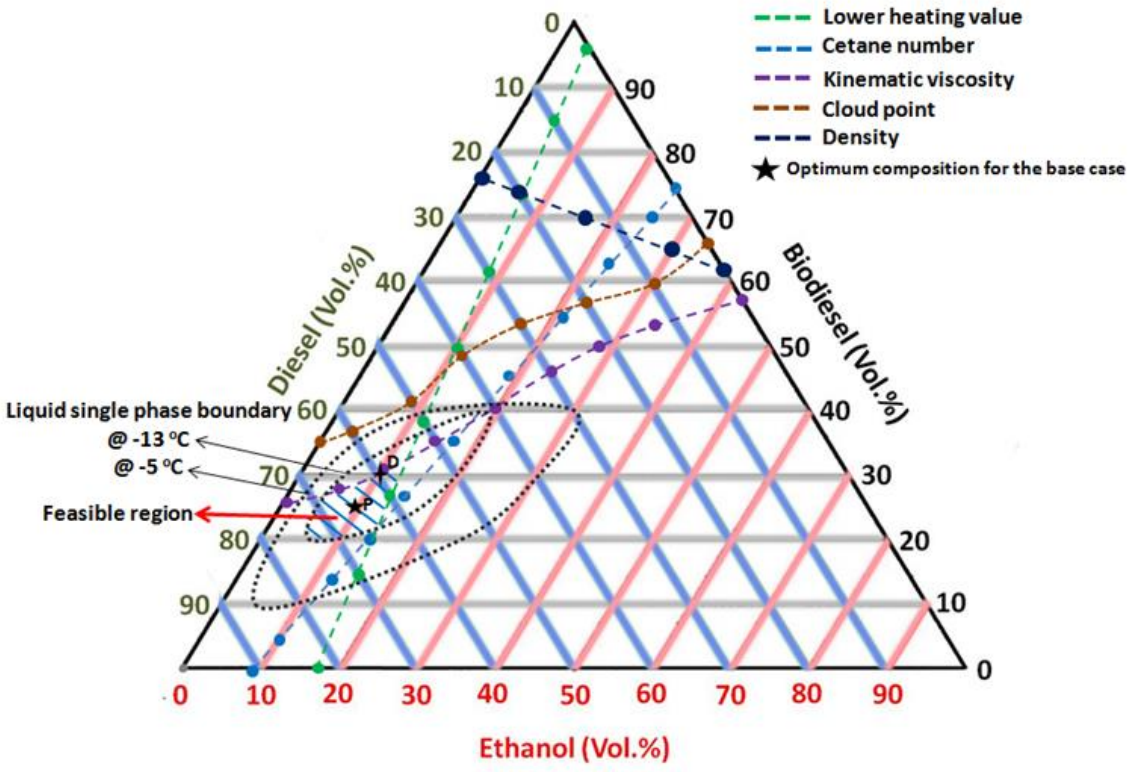

Figure 13: Ternary diagram of regular BED blends

3.3.1. Petro-diesel production and retail price changes

By keeping other variables constant and simultaneously changing diesel production cost, diesel blends market retail price, and diesel regional production as functions of time (based on the trendlines shown in Figure 12), the optimum recipes for BED blends and the maximum net profits for each projected year can be generated from the optimization model. The optimum compositions of all raw components (biodiesel, ethanol, and diesel) for regular BED blends start to change after year 2030 with diesel gradual reduction and biodiesel-ethanol augment (see in Figure 14). Graphically speaking

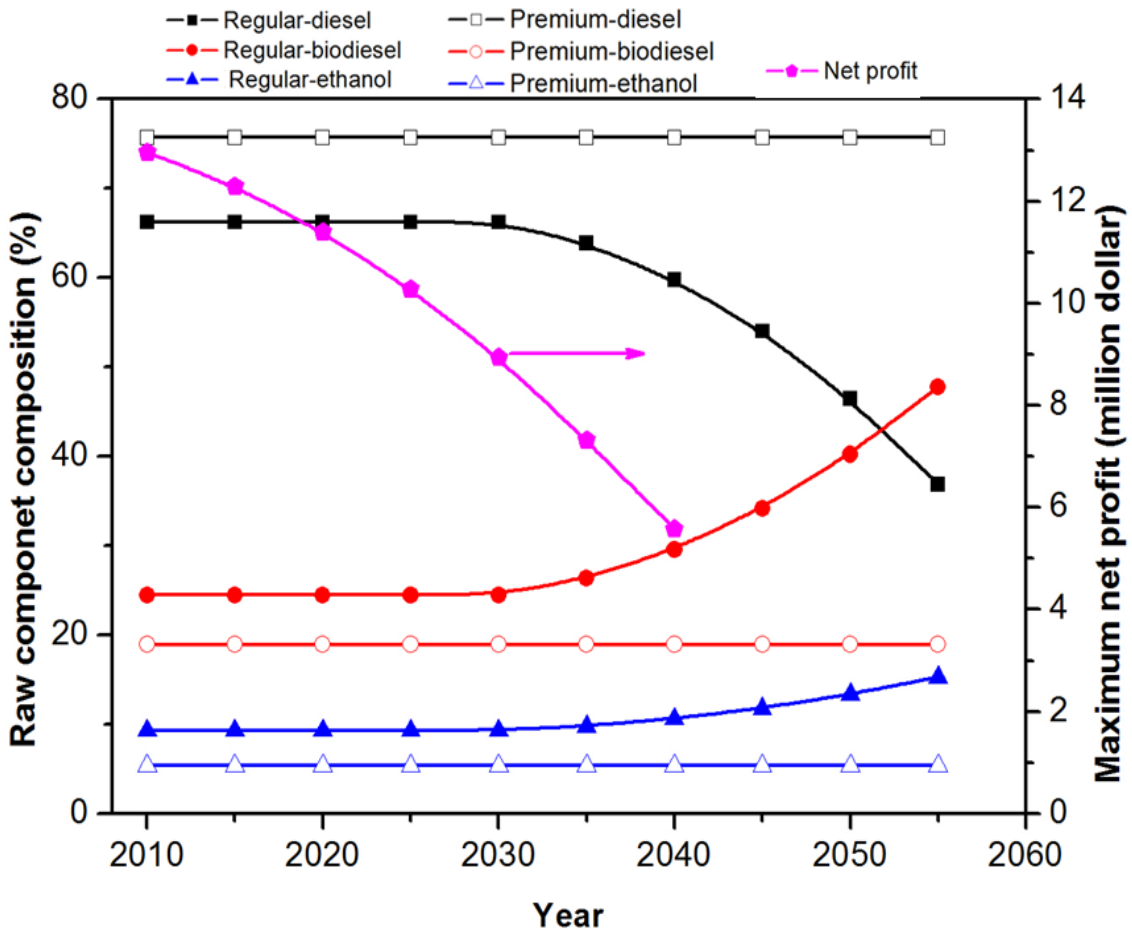

Figure 14: Effects of time-varying diesel supply and retail price on optimum component compositions of BED blends and the maximum profits

the optimum recipe of regular blends is gradually moving from point P (the base case) in Figure 13 towards Point D, which is the optimum composition in year 2040. Figure 13 also illustrates that kinematic viscosity is the main constraint hindering the continued reduction of diesel for the practical regular BED blends. Meanwhile, Figure 14 shows the optimum recipe of premium BED blends maintains the same mix as the base case because premium blends sell at a higher market price than regular blends and are thus resistant to certain levels of market disturbances. Even though the market retail price of both grades of BED blends are expected to increase, diesel production cost is also proportionally increased due to limited reserves of crude oil in New York State and this causes the profit to gradually diminish over time. After year 2040, the model starts to violate the kinematic viscosity constraint and no feasible solution is generated.

3.3.2. Tax credit changes for bio-fuels

Figures 15a and b show the optimum recipes of regular BED blends with the effects of bio-fuel tax credits on ethanol and biodiesel production, respectively. It is assumed that tax credits for ethanol and biodiesel are independent. Figure 15a considers the biodiesel tax credit as constant ($0.41/L) whereas Figure 15b keeps the ethanol tax credit constant ($0.26/L). They compare the scenarios of bio-fuel policy with only bio-fuel tax credit and one with both tax credit and bio-fuel minimum content mandates. For the case with only bio-fuel tax credit, bio-fuel composition (ethanol and biodiesel) increases proportionally with the amount of tax credit while diesel fraction is declining. Meanwhile, the optimal profits gradually increase. For example, with ethanol tax credit from government incentives increases from $0/L to $0.26/L, the maximum profit gained

for the firm increases from $11.65 million to $12.98 million, indicating the overall impact of $0.01/L ethanol tax credit increment helps promote $0.05 million for the profit of the firm. Similarly, the effect of $0.01/L biodiesel tax credit on promoting firm's optimal profit is around $0.03 million.

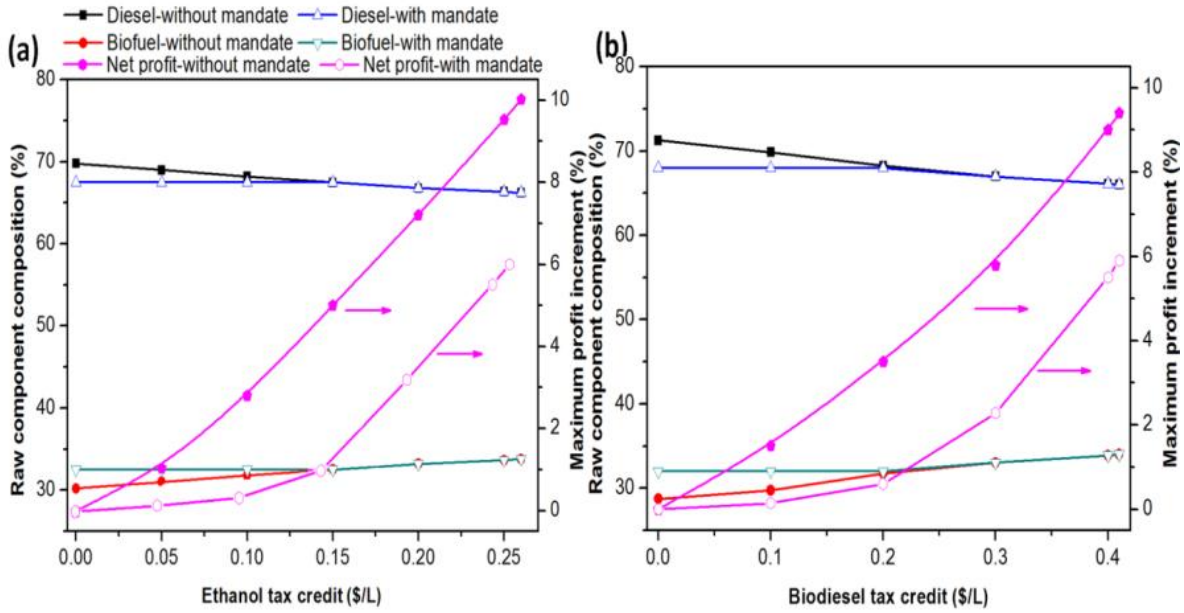

Figure 15: Impacts of (a) ethanol tax credit and (b) biodiesel tax credit on the optimum recipes for regular BED blends and the maximum profits

The optimal fuel compositions of regular BED blend for the scenario without ethanol tax credit shown in Figure 15a are 69.3% diesel, 22.1% biodiesel, and 8.6% ethanol. If the minimum bio-fuel mandate is set below 30%, its implementation may not affect the strategies of BED production firms because the stakeholders would maximize their profit by adapting the optimal recipes, which have higher bio-fuel content than the mandate requires. If the mandate is implemented above 30% as shown in Figure 15, its effect on promoting bio-fuel production would be changed with different bio-fuel tax

credits. When the government simultaneously implements this mandate and the bio-fuel tax credits, the firms may adapt a different strategy to produce BED blends as compared to the case with only bio-fuel tax credit. Figure 15a shows if the ethanol tax credit is less than $0.15/L, the mandated effect dominates the BED blends and this constraint renders the firm unable to adapt the optimal recipes generated from the model, which leads to less maximum profit increment gained by the firm and counteracts the goal of bio-fuel tax credit implementation to promote bio-fuel production. This impact also occurs when the biodiesel tax credit is less than $0.2/L (Figure 15b). Even though this analysis assumes the diesel price is exogenous (unaffected by other considered variables) and does not capture consumer behaviors, it suggests that policies implementing both mandates and bio-fuel tax credits may not entice stakeholders to make heavy investment on bio-fuel in blends unless the tax credits are provided above the critical points ($ 0.15/L for ethanol or $ 0.2/L for biodiesel). Gorter and Just [110] investigated the effects of ethanol tax credits and mandates on gasoline-ethanol blended fuel consumption and they highlighted that tax credits always reduce fuel price and if tax credits are implemented alongside bio-fuel mandates, tax credits would subsidize all fuel consumption instead of bio-fuels uses. Although Gorter and Just modeled the market performances from economic perspectives and this work simulates the supply behavior in term of profit optimizations, the results from these two studies arrive at a similar conclusion: simultaneously implementing bio-fuel tax credits and mandates may not result in greater bio-fuel application than just adapting either one of them.

3.3.3. Constraint relaxations

From the ternary diagram of BED blends depicted in Figure 13, the major constraints binding the feasible regions are kinematic viscosity, LHV, cetane number, and liquid single phase boundary. In order to further analyze the possible profit gain from investing in developing additives to improve these properties, they are assumed to be relaxed. Many viscosity improver additives such as a high shear stable polymer reported by Carvalho *et al.* [111], have been proposed to improve fuel kinematic viscosity and fuel combustion in diesel engine applications. If the upper limits of the kinematic viscosity of BED blends are relaxed with some improver additives, bio-fuel portions of optimal blends (both for regular and premium) are proportionally increased to substitute diesel reduction (see in Figure 16). The maximum profit increases linearly with the relaxation of viscosity upper limit and the effect of one unit increment of viscosity contributes to $3.14 million profit augment. For instance, if 15% relaxation of viscosity occurs for both regular and premium blends (e.g. from 3.8 to 4.37 centistokes (cSt), and 3.5 to 4.02 cSt, respectively, at 40^{o}C), the maximum profit gained by the firm would increase correspondingly from $12.98 million to $14.69 million (13.2% increment). Similarly, the constraint relaxations of LHV and cetane number are analyzed with the optimization model. For example, Figure A12 provides the relaxation of the minimum cetane number constraint by mixing with the additives like 2-ethylhexylnitrate or ditertiary butyl peroxide [112], and its contribution on rising profit gain is diminishing as the relaxation increases. Figure A13 shows biodiesel is gradually replaced with ethanol portion in the blends as the relaxation of LHV constraint increases because of the relatively high production cost of biodiesel, whereas diesel fraction maintains stable. The optimal profit

increases linearly from $12.98 million to $16.61 million when minimum LHV constraints of regular BED blends and premium blends relax from 33 MJ/L to 31 MJ/L and from 34 MJ/L to 32 MJ/L (6%), respectively. By leveraging the cost of adding the additives to relax fuel requirement constraints and the profit gained from them, the stakeholders can determine the practical strategy for developing potential fuel additives.

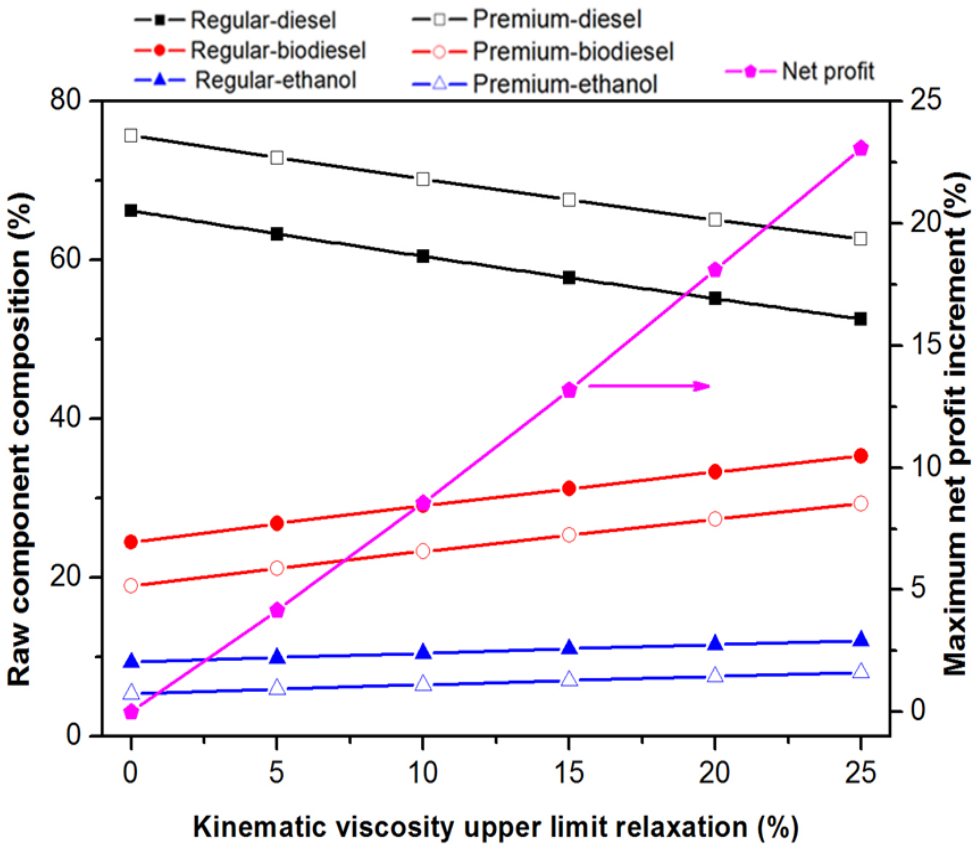

Figure 16: Changes of optimum raw component compositions of BED blends and the maximum profits with the relaxation of kinematic viscosity upper limits

3.3.4. Impacts of feedstock selection

The performance of bio-fuels from both technical and economic aspects is directly influenced by the feedstock sources. For example, the cost of edible feedstocks

for biodiesel production (e.g., soybean and rapeseed oil) accounts for 70-80% of total production cost [113]. Table 9 lists the optimal raw component compositions of BED blends and maximum profit for the combinations of bio-fuels (ethanol and biodiesel) derived from various feedstocks. By taking advantage of lower or even zero cost of waste feedstocks, the case with a combination of ethanol from food wastes and biodiesel derived from either soybean oil or algae enables high optimal profits ($13.42 million and $12.59 million, respectively). However, bio-diesel derived from waste feedstock may jeopardize the properties of BED blends and result in unpractical blends for transportation applications, which are reflected as the infeasible solutions shown in the model (Table 9). BED blends with biodiesel from waste cooking oil (WCO) cannot be directly used as the viable final fuel due to the poor fuel specifications of WCO-based biodiesel, including high kinematic viscosity (5.5 cSt) and low LHV (31.8 MJ/L). To explore the potential benefits by using WCO-based biodiesel in BED blends, some additives (e.g. ignition promoters, oxygenate additives, and viscosity improver additives) were hypothetically mixed with WCO-biodiesel to improve its fuel properties before iteratively running the model to identify the viable BED blends. The feasible solution indicating the pertinent blends of diesel, biodiesel from WCO, and ethanol from corn grain, starts to occur when kinematic viscosity of WCO-biodiesel is reduced to 5.3 cSt and LHV reaches 32.6 MJ/L with $13.85 million maximum profit. These results indicate the research opportunities available in developing potential additives to promote WCO-based biodiesel applications.

Table 9. Optimum compositions of BED blends and maximum profits with bio-fuels derived from different feedstocks

	Corn grain-ethanol		**Switchgrass-ethanol**		**Food wastes-ethanol**	
Soybean oil-biodiesel	Profit: $12.96 million		Profit: $12.78 million		Profit: $13.42 million	
	Regular	Premium	Regular	Premium	Regular	Premium
	C-ethanol:9.3% S-biodiesel:24.5% Diesel:66.2%	C-ethanol:5.3% S-biodiesel:18.9% Diesel:75.8%	S-ethanol:9.5% S-biodiesel:25.4% Diesel:65.1%	S-ethanol:5.5% S-biodiesel:19.6% Diesel:74.9%	F-ethanol:9.1% S-biodiesel:26.2% Diesel:64.7%	F-ethanol:4.3% S-biodiesel:20.2% Diesel:75.5%
Algae-biodiesel	Profit: $12.14 million		Profit: $11.62 million		Profit: $12.59 million	
	Regular	Premium	Regular	Premium	Regular	Premium
	C-ethanol:9.5% A-biodiesel:25.4% Diesel:65.1%	C-ethanol:5.5% A-biodiesel:19.6% Diesel:74.9%	S-ethanol:9.3% A-biodiesel:24.5% Diesel:66.2%	S-ethanol:5.4% A-biodiesel:18.9% Diesel: 70.7%	F-ethanol:9% A-biodiesel:27.2% Diesel:63.8%	F-ethanol:5.2% A-biodiesel:20.6% Diesel: 74.2%
WCO-biodiesel	Infeasible solution		Infeasible solution		Infeasible solution	

3.4. Summary

It is challenging to determine strategies for BED blend production, not only due to the small region of practical blend recipes out of the entire ternary diagram (Figure 13), but also it is difficult to capture the dynamic disturbances from market behaviors, bio-fuel feedstock sources, and policy changes. The proposed optimization model in this study integrated with pertinent mixing rules of fuel properties enables establishing the optimum recipes to improve the system profitability while meeting multi-objectives, and promoting opportunities to develop potential additives to improve blend fuel quality. The model also suggests the government policy of simultaneously implementing bio-fuel tax credits and mandates may not have a higher contribution to promoting bio-fuel production than the case with only tax credits with the goal of profit maximization. By utilizing waste-feedstock based bio-fuels in BED blends, the fuel producer can realize the benefits of reducing product cost and gaining high optimal profit. The maximum profit obtained from BED blends using ethanol from food waste is 5% to 8 % higher than that from edible feedstocks (Table 9). Even though the model considers only three raw components for the blends in this preliminary study, similar methodology can be used for multiple blends optimizations. Future work will focus on evaluating the environmental impacts of BED blends (e.g.. greenhouse gas emissions, particulate matter), exploring the actual effects of additives, and sensitivity analysis of several key variables, including various bio-fuel production technologies, BED blends retail price, and impact of plant size. The methodology developed to determine the optimum BED blend composition based on profit maximization has been covered in a provisional U.S. patent application.[1]

[1] J.F. Lin, G. Gaustad, T.A. Trabold, "Optimized biodiesel-ethanol-diesel fuel blends", U.S. Provisional Patent Application Serial No. 61/720,256, filed October 2012.

An optimal composition of biodiesel blended with diesel and ethanol to maximize system profitability while satisfying considered constraints was identified as 25 vol.% biodiesel with 10 vol.% ethanol and 65 vol.% diesel (B25E10D65) using the proposed model. It motivates an investigation of B25E10D65 from technological aspect with fuel reformation for SOFC-APU system under various operating conditions, which was analyzed in the following chapter.

IV BIO-FUEL REFORMATION FOR SOLID OXIDE FUEL CELLS

4.1. Fuel Vaporization and Reactant Mixing

4.1.1. Introduction

Fuel cell technologies have been intensively studied in recent decades due to their potential benefits (e.g., high efficiency in energy conversion, environmentally friendly), and this research has promoted significant growth in patents related to fuel cell technologies [114]. Solid oxide fuel cells (SOFCs) operated at relatively high temperature can serve as combined heat and power (CHP) systems for stationary or transportation applications. For example, SOFC-based auxiliary power units (APUs) are used in long-haul diesel heavy duty trucks to supply auxiliary electricity for the driver during truck idling periods. Rather than keeping the full diesel engine running at rest, diesel trucks enable utilizing SOFC-APU systems within the range of 2-10 kW to provide a secondary electrical power supply [115]. Hydrogen serves as the main fuel for fuel cell systems, but it is also considered as one of the technical challenges to achieve fuel cell commercialization [116]. Even though hydrogen can be stored physically or chemically in various gaseous, liquid or solid phases, these techniques are still not efficient nor sufficiently cost-effective [117]. Catalytic reformation of hydrocarbon fuels is widely recognized as a practical method to produce hydrogen-rich reformates used in fuel cell systems, and it has the advantage of utilizing various fuel sources (e.g., natural gas, ethanol, propane, gasoline, diesel, and biodiesel) [14,32,118,119]. For transportation applications, the catalytic reformer can be integrated with the onboard fuel cell system and utilize the same hydrocarbon fuel (gasoline or diesel) used in the internal combustion engine system, which requires no modifications of conventional fuel tanks and associated

fueling infrastructure [32,119]. Common reformation techniques include steam reforming (SR), partial oxidation (POx), dry reforming (DR), and auto-thermal reforming (ATR). ATR is the thermally-balanced combination of SR (endothermic reaction) and POx (exothermic reaction), and has a number of advantages in terms of system mechanizations [14]. A typical reforming system is comprised of a pretreatment process, a reformate reactor, and a gas purification step [32,118]. The function of the mixing chamber is to supply to the catalytic reaction zone a continuous flow of a homogenous mixture consisting of air, steam, and vaporized fuel, where high hydrocarbons are catalytically decomposed at high temperatures into hydrogen-rich reformates along with other species (e.g., CO, CO_2, CH_4, C_2H_4, and C_2H_6) [120]. Appreciable amounts of steam produced in the fuel cell stack can be recycled back to the fuel reformer as an input. For example, our earlier work analyzed the performance of diesel ATR under various operating conditions for a 5 kW SOFC-based APU applications and demonstrated that recycling a fraction of effluent gas from the anode side of the SOFC stack enables increasing the overall system efficiency [14].

Many studies have demonstrated the major failure mode of the fuel reformer as catalyst degradation resulting from sulfur poisoning and solid carbon (coke) formation. The organic sulfur compounds in the petroleum-based fuels like diesel are usually present in the derivatives of dibenzothiophene (DBT), and they would react with the catalytic metal to form stable metal sulfide and lead to deactivation of the active sites during fuel reformation [121]. The sulfur poisoning issue can be prevented if sulfur compounds in the fuel are removed through hydro-desulfurization processes before entering the

reformer. Coke formation, however, is challenging to prevent because the dynamic evolution of solid carbon formation in the reactor is difficult to detect and control, especially under rigorous operating conditions (e.g., heavy hydrocarbon fuels, low reformer temperature, no adequate input air or water as the oxidants)[32,120,122]. Therefore, intensive research has been focused on mitigating solid carbon formation and improving the performance of fuel reformation, either by optimizing the operating conditions within the reactor (such as the reformer temperature, H_2O/C, O_2/C, and gas hourly space velocity) or by developing highly active and durable catalyst test beds [14,121,123]. However, most of this earlier research specifically emphasized performance within the reactor during fuel reformation and few investigated the potential for carbon formation in the mixing chamber, where the input hydrocarbon fuels like diesel or biodiesel are vaporized and have propensity for self-pyrolysis to form carbonaceous solid residues if the fuels are poorly mixed with steam/air [119,124]. Kang *et al.* [119] applied an ultrasonic injector in the mixing chamber for diesel atomization and suggested the injector not only improved diesel reformation efficiency, but also dramatically reduced the ethylene content (known as a key precursor to form solid carbon) in the gas products. Solid carbon buildup around the inner wall of the fuel delivery tubes was observed in our previous work on biodiesel ATR, and significant amounts of carbon were directly deposited in the front end of the catalyst bed [32]. Thus, it is crucial to design a mixing chamber that enables vaporizing the hydrocarbon fuels completely and mixing the oxidants (air/steam) homogenously to avoid carbon formation in the mixing zone.

Air-assisted fuel injectors are commercially available and commonly used in diesel engines to atomize the fuel and improve the fluid dynamics to provide complete fuel combustion [125]. Similar techniques have also been introduced in diesel reforming systems to completely vaporize the input fuel and enhance mixing with steam/air [119,120,126-129]. For example, Salge *et al.* [129] applied an automotive fuel injector to spray soy oil with ~400 μm droplet diameter onto the catalyst foam with rhodium-cerium based particles, and the oil along with air were introduced at room temperature (20^{o}C). Porš *et al.* [124] used a twin fluid nozzle to deliver diesel and air to the catalytic reformer and suggested that the spraying nozzle could improve the long-term reforming performance of diesel ATR. However, when considering adapting the conventional high-pressure fuel nozzle to the reformer system, there are several drawbacks which need to be overcome: requirements of large external power supplies; challenges in integrating the reformer/stack system; difficultly in atomizing heavy hydrocarbons with high surface tension like biodiesel; and the need to cover a large range of fuel test scales [119,130]. Kang *et al.* [119] suggested that the reforming efficiency of diesel ATR would increase up to 20% when the diesel fuel was sprayed through an ultrasonic injector to improve mixing with the reactants. An *et al.* [126] determined that air-assisted fuel injection may accelerate the strong air flow recirculation around the nozzle and large portions of the fine fuel drops would follow the recirculating air and flow upward instead of penetrating into the catalyst bed, which not only leads to hot spots near the nozzle, due to the convection of heat transfer from the catalyst bed, but it also promotes thermal cracking of hydrocarbons and forms solid carbon near the sprayer. Also, if the input fuel is injected at a high rate, fuel without sufficient mixing with the oxidants would directly contact the

catalyst surface or reactor wall [119]. Therefore, it is important to explore other potential methodologies to atomize heavy hydrocarbons for fuel reformation applications and develop a mixing chamber with flexible integration in the reforming system.

Micro-explosion of emulsified fuels has been widely studied as a path to improve the combustion characteristics of diesel engines because this technique enables the reduction of solid and gaseous pollutants such as carbonaceous residues and NO_x [131-133]. When heavy hydrocarbon fuels like diesel emulsify with a small fraction of water, the water droplets are encapsulated inside the emulsified fuel phase (i.e., water-in-diesel). Because water and diesel have different boiling points and vaporization rates, the water phase would reach its superheated stage faster than diesel when the temperature around the emulsified droplets increases. The vigorous volumetric expansion of steam creates the momentum to disintegrate the whole emulsified droplets and finely breakdown the diesel droplets, and this physical phenomenon is called "micro-explosion" [131]. Micro-explosion would promote the secondary atomization of hydrocarbon fuels and enhance the mixing of fuel and air to increase the combustion efficiency [132,133]. Previous studies also demonstrate it is practical to conduct the micro-explosion of emulsified fuels under ambient pressure [132-134].

The objective of the present work is to develop a mixing chamber integrated with a customized nozzle that enables vaporizing diesel ($C_{15.5}H_{28}$) and biodiesel ($C_{19}H_{35.4}O_2$) completely without fuel pyrolysis and mixing homogenously with steam/air for fuel ATR applications. A new configuration design of the nozzle embedded with a 2 μm porous

filter accelerates the emulsification of hydrocarbon with water and promotes the occurrences of micro-explosions to finely atomize the fuel droplets. This study also analyzed the ATR performances of diesel and biodiesel using a single-tube reactor integrated with the proposed mixing chamber in order to elucidate the effects of the customized nozzle on fuel reformation. A direct photo-acoustic based micro-soot meter was used to analyze carbon dynamic evolution with different reformer operating temperatures while a mass spectrometer was applied to measure the composition of gaseous effluent from the reformer.

4.1.2. Experimental

Fuel Vaporization Device

Figure 17(a) illustrates the schematic diagram of the proposed mixing chamber along with the actual device used in the experimental setups. This device consists of the regions of fuel and steam delivery, fuel/steam emulsification, and fuel/steam micro-explosion. Superheated steam at 350^{o}C was continuously generated from a heated stainless steel coil and flowed through the inner tube of the nozzle, and it sprayed out of a porous filter with 2 μm pore size. Input hydrocarbon fuel with nitrogen carrier gas was preheated to 70^{o}C to improve fuel flow performance by lowering the kinematic viscosity, and then flowed around the outside of the porous filter. Steam was partially condensed due to the heat transfer to the fuel/nitrogen and the fuel was spontaneously emulsified with water because of the inherent hydrophobicity of hydrocarbon fuels [131,132]. With continuous supply of steam, bubble nucleation of the emulsified fuel occurred around the porous filter, which is also shown in Figure 17(a). As the temperature near the porous

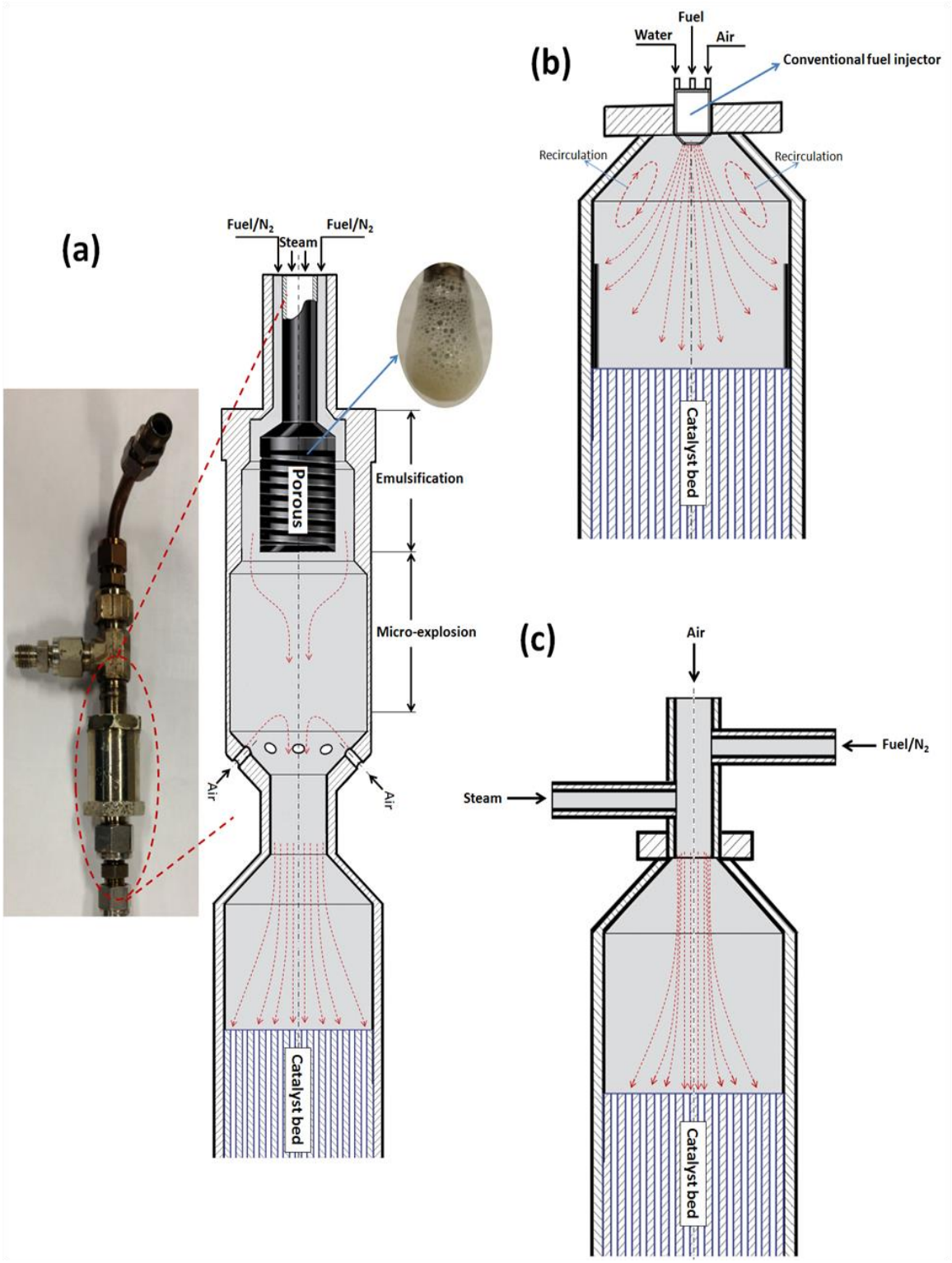

Figure 17: Schematic diagrams of the mixing chambers with (a) a customized porous nozzle, (b) a swirl nozzle, and (c) direct mixing of fuel/air/steam

filter increased, vigorous volumetric expansion from water-to-steam conversion and heated steam produced a rapid explosion of the surrounding oil droplets and accelerated the occurrences of micro-explosion to fragment the fuel into a large number of fine secondary droplets, which consequently enhanced the fuel-steam mixture [131]. Nam and Alvarado [133] have analyzed the micro-explosions of emulsified hexadecane and emulsified canola oil with the initial droplet diameters measured as 0.13 mm and 0.3 mm, respectively, and they demonstrated that micro-explosion reduced droplet size by roughly an order of magnitude: hexadecane droplets down to 13 μm and canola oil to 32 μm. In the current work, the initial droplet sizes of the emulsified fuel after bubble nucleation are overall below 0.3 mm, indicating the droplet size of the fuel/steam mixes would be potentially below 35 μm after their micro-explosions based on the results of Nam and Alvarado. Air was introduced upwardly to create additional turbulence to improve the mixing with the fuel/steam droplets and avoid the occurrence of recirculation in the downstream section. For comparison purposes, a swirl nozzle and a direct mixing configuration of fuel/air/steam (without a nozzle) are shown in Figure 17(b) and Figure 17(c), respectively. Similar to the conventional air-assisted fuel injectors, the swirl nozzle tends to promote the air/fuel recirculation and result in coke deposition near the sprayer, even though it enables effective atomization of fuel droplets [119,126]. It is also challenging to adjust the spraying angle of pressurized fuel injectors to prevent the fuel from colliding against the side-wall of the reactor and forming a liquid film to flow down along the wall without vaporization [126]. Based on our previous experiments and the results reported from other studies, the overall gaseous flows for different configuration of fuel mixing chambers are broadly represented by the three configurations shown in

Figure 17 [14,119,124-126]. The proposed fuel vaporization and mixing device (Figure 17a) homogenously distributed the gaseous mixture to the catalyst bed without pressure buildup in the upstream, whereas the mixtures in the configuration without nozzles only utilized the central region of the catalyst bed (Figure 17c).

Single-tube Reformer Apparatus and Experimental Tests

To analyze the effects of the customized nozzle on fuel ATR, the mixing chamber was integrated in a single-tube reformer system, as shown in Figure 18. The reformer was comprised of an Inconel 625® tube (1.91 cm outside diameter with 0.09 cm wall thickness) packed with 4 separate sections of catalyst wash-coated ceramic monolith (1.27 cm diameter × 5.08 cm lengths of 400 cpsi alumina substrate). Each catalyst section has 0.5g of washcoat consisting of 2 wt.% rhodium in ceria-zirconia; thus, each section of monolith contained 0.01g rhodium. Five thermocouples (labeled as TC1~TC5) located at five different locations along the catalyst test bed centerline were used to acquire the temperature profile of the catalyst and a thermocouple (TC 0) was applied to monitor the trumpet tube temperature of the front end of the reactor (see Figure 18). An AVL micro-soot meter (Model No. 483, AVL List GmbH, Graz, Austria) was applied to directly measure the carbon concentration in the reformate stream. This instrument utilizes the photo-acoustic effect to obtain accurate carbon concentration measurement as low as 5 $\mu g/m^3$ [135]. By the photo-acoustic effect, periodic heating and cooling of the dispersed carbon particles caused by a modulated laser beam produces pressure fluctuations that can be detected by sensitive microphones. The microphone signal is linearly proportional

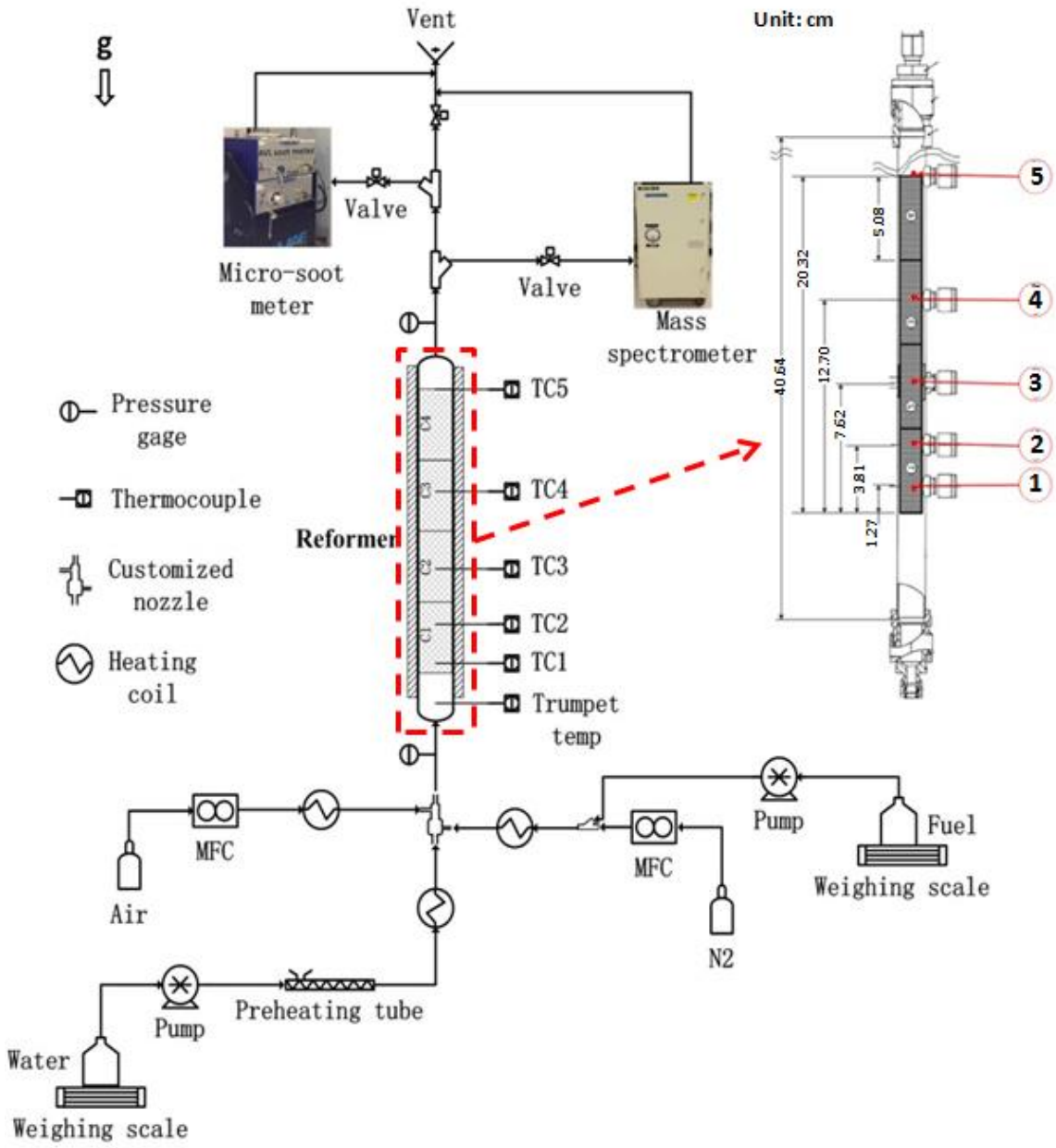

Figure 18: Schematic diagram of the single-tube reformer system integrated with the proposed mixing chamber

to the carbon concentration in the sampling volume. This approach has the capability to detect dynamic carbon evolution during fuel ATR at different operating conditions and provides time-resolved results. The micro-soot meter was calibrated and a stable zero

baseline was established under nitrogen flow through the fresh reformer at 950^{o}C. The mass spectrometer (Applied Instrument Technologies, CA, USA) was used to quantify the effluent gas species, including N_2, H_2, O_2, CO, CO_2, CH_4, C_2H_4, and C_2H_6.

In this work, diesel and biodiesel were considered as the representative heavy hydrocarbon fuels and used in the ATR processes for SOFC-based APU applications. Although the experimental setup does not involve the anode recycled gases from the SOFC stacks, we have simulated the amount of steam recycled from fuel cell stacks based on our previous work [14]. Table 10 provides the initial operating conditions for diesel and biodiesel ATR with H_2O/C = 0.6, total O/C (summation of oxygen from fuel, air, and water to carbon from the fuel) = 1.47, and with the reformer temperature of 950^{o}C. The input flow rates of diesel or biodiesel were varied to achieve the same theoretical reformate (CO+H_2) yield. To alleviate the pressure oscillation derived from the vapor lock of water vaporization, water was gradually heated to 120^{o}C through a heated tube before reaching a heated stainless steel coil where superheated steam at 350^{o}C was generated. Before introducing the hydrocarbon fuel, water and air into the reactor, the reformer temperature was ramped up with the furnace temperature set point at 1000^{o}C and low flow rate of nitrogen. After initializing the experimental test points under the conditions listed in Table 10, the furnace temperature controller was gradually reduced with a 0.1^{o}C/s reduction rate in order to identify the carbon formation boundaries of diesel and biodiesel ATR in terms of the reformer temperature. For comparison purposes, this study also evaluated the performance of diesel ATR with the inlet

configuration of fuel/air/steam direct mix (without nozzle; Figure 17c). The outcome of this experimental comparison has been documented by Lin *et al.* [136].

Table 10. Initial experimental test points for diesel and biodiesel ATR

Fuel	Input fuel flow rate (10^{-3}×mol/s)	O_2/C	H_2O /C	Total O/C	Reformate (CO+H_2) theoretical yield (10^{-3}×mol/s) @ 950 $^oC^*$
Diesel	0.088	0.43	0.6	1.47	2.75
Biodiesel	0.075	0.38	0.6	1.47	2.75

* Reformer temperature: average temperature of the catalysts (TC1~TC5, shown in Figure 18)

Condensation of Vaporized Biodiesel

As compared to conventional diesel, biodiesel is challenging in regards to its atomization and vaporization using conventional fuel injectors because of its fuel properties (e.g., relatively high surface tension, boiling point, molecular weight, and kinematic viscosity) [130]. Biodiesel has the tendency to pyrolyze and thermally crack to form solid carbon under high vaporization temperatures [136,137-139]. In order to analyze the conditions of biodiesel breakdown and the compounds of the gaseous effluents from the mixing chamber with the customized nozzle, the products from the mixing chamber were condensed to room temperature and collected prior to entering the reactor. Many studies have demonstrated that the normal boiling points of paraffin hydrocarbon fuels are strongly correlated with their carbon content within the fuels [140-142]. For example, reports from the American Society for Testing and Material (ASTM) provide these correlations between the paraffin carbon number and their corresponding boiling temperatures, along with the common non-paraffin hydrocarbons present in petroleum fuels [140]. Figure 19 suggests that the correlations reported by ASTM are in agreement with the results reported by other studies, thus this work utilized these

correlations to investigate the carbon number of the condensates derived from the vaporized gaseous products. Figure 20 illustrates the schematic diagram of the experimental setup for investigating the boiling points of the condensed liquid mixture. After removing the water, the liquid mixture was gradually heated up using a temperature-controlled heating plate. The heating plate was kept at each sampling temperature for 5 minutes to ensure complete vaporization of hydrocarbons at that temperature, before the next 15 ^{o}C increment. Nitrogen gas at low flow rate was heated at the same temperature as the heating plate and used as the carrier gas, and thermocouples were used for temperature measurement. The weight of the liquid mixture was monitored as the temperature of the heating plate was increased from room temperature to 450^{o}C.

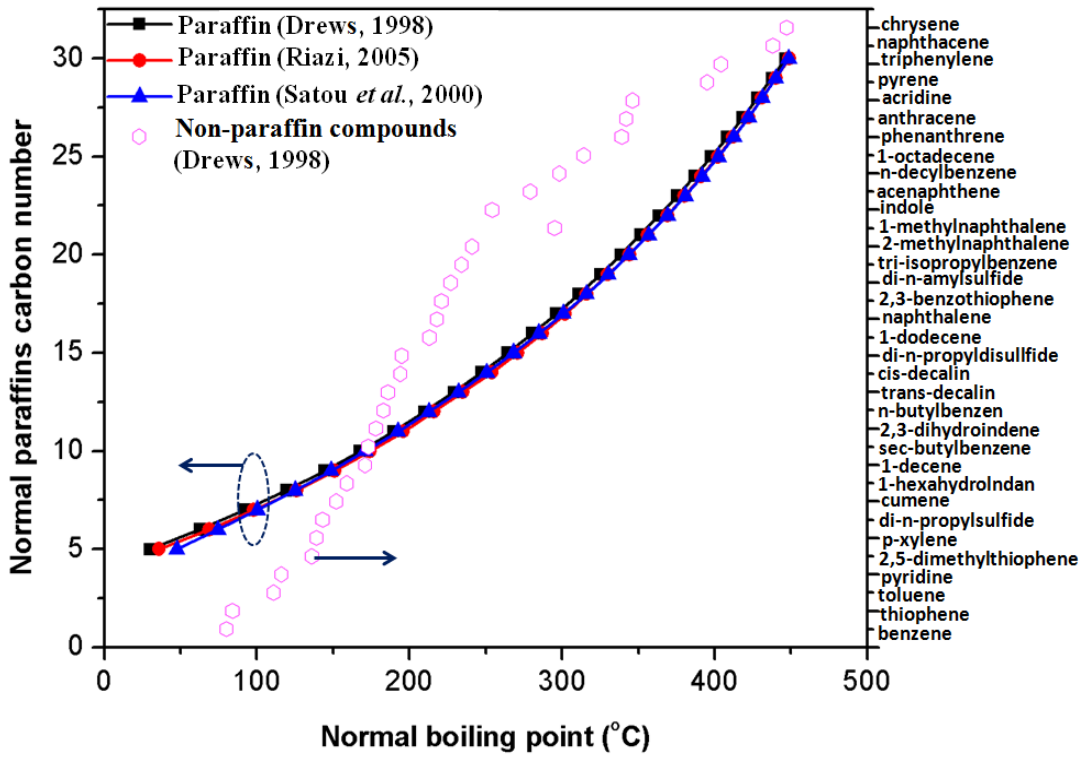

Figure 19: Correlations between boiling point and carbon number for paraffin hydrocarbons and the common non-paraffin compounds in petroleum

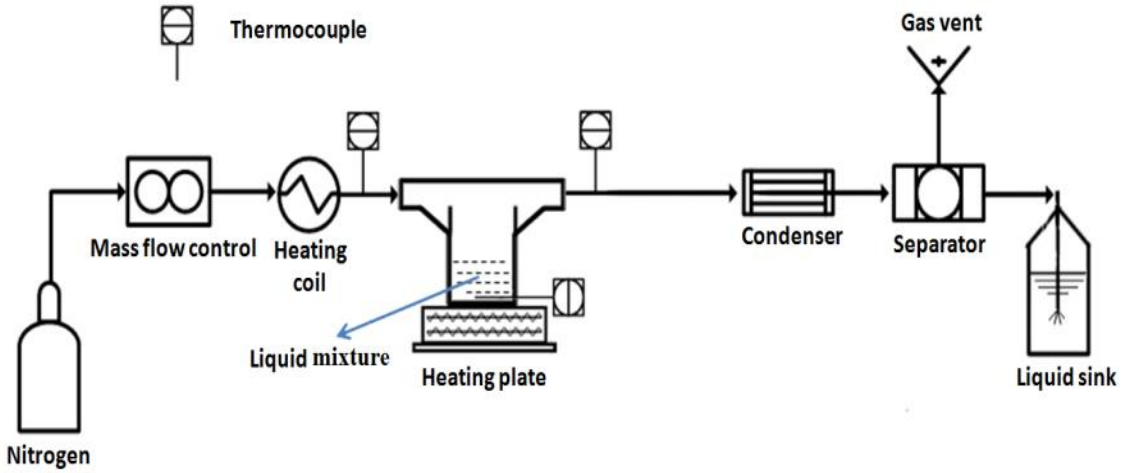

Figure 20: Schematic diagram of experimental apparatus to identify the boiling point distributions of the condensed hydrocarbons

4.1.3. Results and discussion

Performance of Auto-thermal Reformation

Figure 21 shows the time-resolved hydrogen yields and the temperature of the front end of the catalyst bed (TC 1) for three experimental sets: diesel ATR with the customized nozzle, diesel ATR with fuel/air/steam direct mixing (without nozzles), and biodiesel ATR with the customized nozzle. For the reformer system with the customized nozzle, both diesel and biodiesel have relatively stable hydrogen production rate and temperature profile, indicating the thermodynamic conditions of the chemical reactions in the reactor are consistent. However, the performance of diesel ATR without the nozzle shows significant fluctuation, both for the hydrogen yield and catalyst temperature variation. Kang *et al.* [119] applied an ultrasonic injector to atomize the diesel down to 40 μm diameter droplet size before delivery to the reformer, and they reported that the upper temperature of the catalyst bed when using the ultrasonic injector is around 20^{o}C

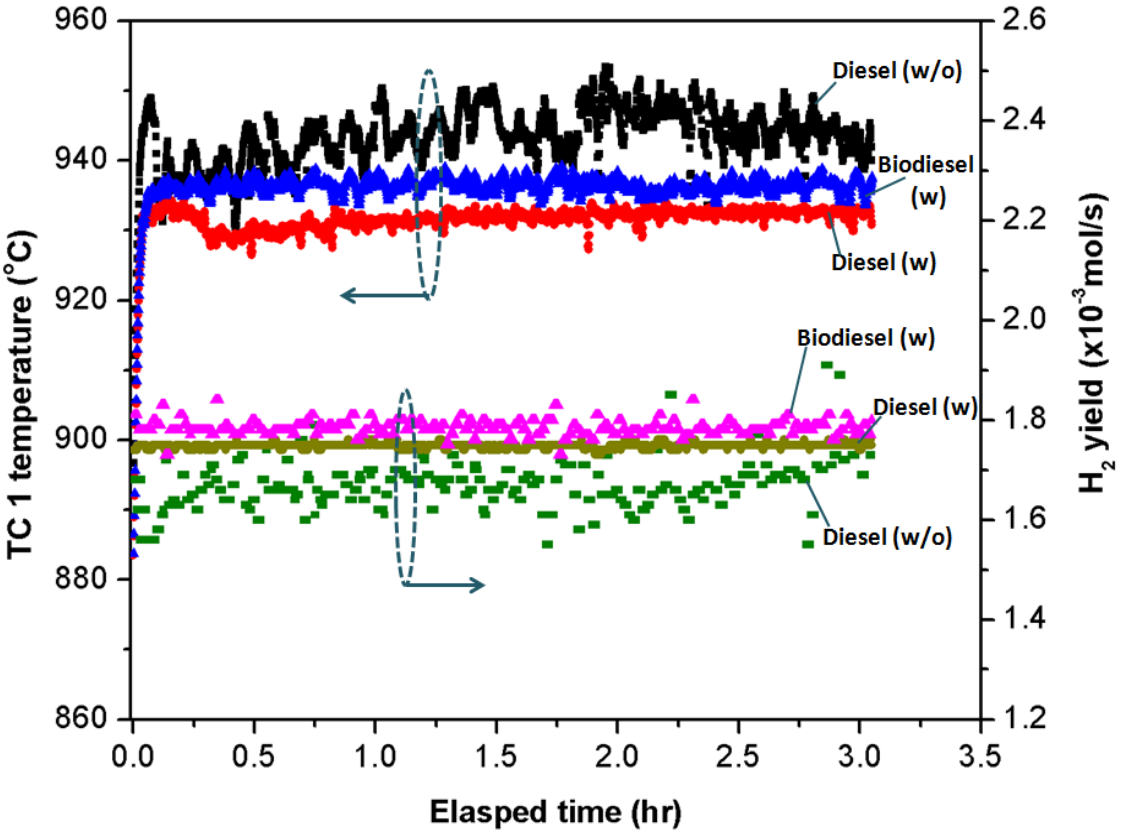

Figure 21: Time-resolved hydrogen yields and temperature profiles of the front end catalyst bed for three experimental sets: diesel ATR with the customized nozzle (w), diesel ATR with fuel/air/steam direct mixing (w/o), and biodiesel ATR with the customized nozzle (w).

lower than without the ultrasonic injector. Similar experimental phenomena were observed in the present work for diesel ATR with and without the customized nozzle, as shown in Figure 21 For the case of diesel ATR without the nozzle, poor mixing of diesel with the oxidants (air/steam) in the vaporization step would lead to formation of fuel-rich and fuel-lean regions, which result in hydrocarbon thermal pyrolysis and unwanted fuel combustion, respectively [119]. These reactions not only release large amounts of heat and promote an unstable environment near the reactor inlet, but they also reduce the

hydrogen production rate and the reformation efficiency. Our previous study has identified high temperature sintering as a potential degradation mode for the catalyst bed in diesel ATR, especially for the front end of the catalyst bed where the exothermic reaction dominates [14]. The nozzle design described herein enhances the homogenous mixing of fuel and oxidants and prevents formation of hot spots at the reactor inlet.

Although this work particularly investigated the effects of reformer temperature reduction on the effluent species from the reactor with diesel ATR, other system variables also needed to be evaluated in order to fully elucidate the comparison of the reformer with and without the nozzle. Figure 22 shows the gas composition changes of diesel ATR both with and without the customized nozzle and the one without nozzles, as the reformer temperature reduces from its initial condition. In Figure 22(a), the reformer with the nozzle enabled achieving higher and more stable H_2 and CO yields than the reformer without using the nozzle. High yield of CO_2 in the reformer without the nozzle suggests that some diesel was completely oxidized instead of being partially oxidized to CO due to the inhomogeneous mixing [124]. Figure 22(b) provides the effect of the reformer temperature on the light hydrocarbon gases and the system reformation efficiency. Diesel ATR without fuel atomization promotes the formation of methane and ethylene (known as a coke formation precursor), and reduces the reformation efficiency [14]. It is worthwhile to mention that the benefits of using the nozzle as shown in Figure 22 include the enhancement of reformate production rate and promotion of reformation efficiency, and these benefits are become more significant as the reformer temperature is reduced.

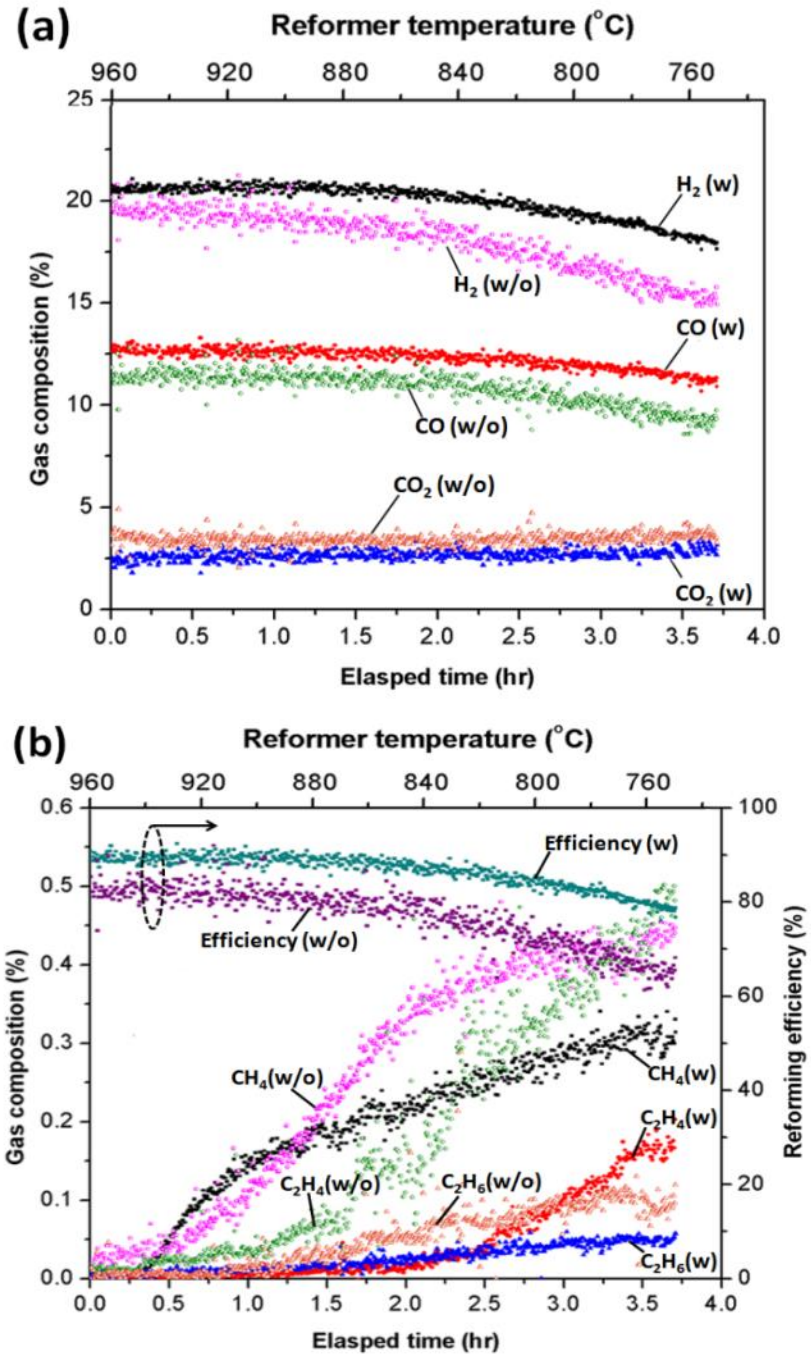

Figure 22: Effects of the reformer temperature on (a) H_2, CO_2, and CO, (b) light hydrocarbon gases and system efficiency of diesel ATR for the reformer with the nozzle (w) and without the nozzle (w/o)

Significant coke formation was observed during biodiesel vaporization with directly mixing of fuel/air/steam (without nozzles), and the carbonaceous solid residues buildup around the inner wall of the delivering tubes plugged the reactor inlet. To avoid the irreversible catalyst degradation from carbon deposition over a long period of time and prevent unstable chemical reactions in the reactor, this work only considered the case of biodiesel ATR with fuel atomization by using the customized nozzle. Figure 23 illustrates the effects of reformer temperature on the gas composition and the reformation efficiency of biodiesel ATR. As the reformer temperature reduces, CO and H_2 are both gradually reduced and lead to the reduction of the reformation efficiency, while CO_2 is kept fairly stable. The nozzle accelerates the micro-explosions of emulsified biodiesel to reduce the droplet size and enhance mixing with oxidants, which largely suppressed the formation of light hydrocarbon gases.

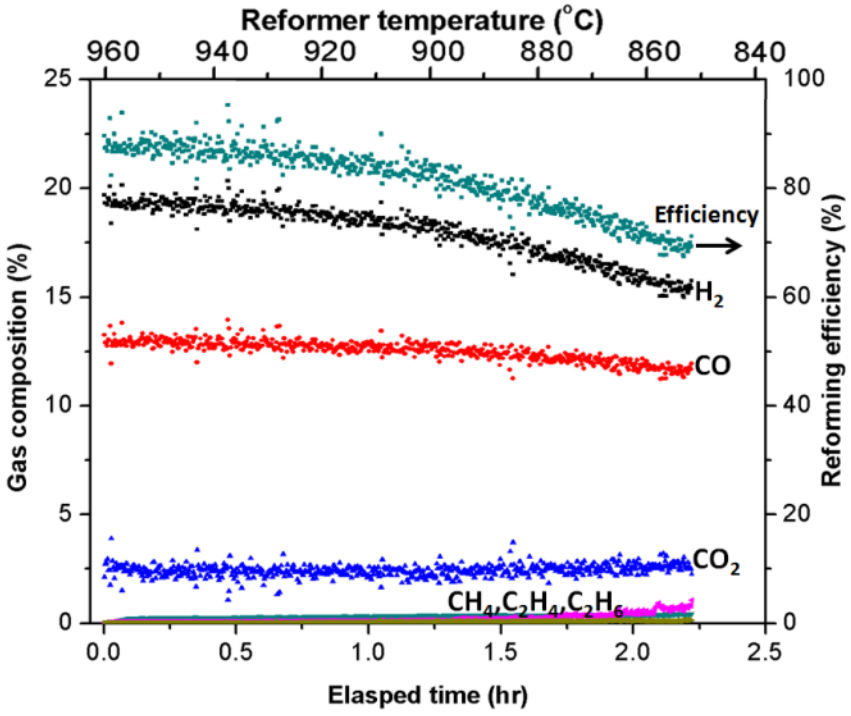

Figure 23: Effects of reformer temperature on gas composition of biodiesel ATR with the customized nozzle

A direct photo-acoustic based micro-soot meter was applied during the experimental tests to quantify the solid carbon concentration in the effluents from the reformer. Figure 24 shows the carbon concentration associated with the reformer temperature for the experimental sets: diesel and biodiesel ATR with the nozzle, and diesel ATR without the nozzle. The system resolution of the micro-soot meter (5 $\mu g/m^3$) is also included in Figure 24 and the carbon concentration values below this value are considered as zero. The critical reformer temperature at the onset of solid carbon formation for diesel ATR with the nozzle, diesel ATR with direct mixing of fuel/air/steam, and biodiesel ATR with the nozzle are located near 825, 850, and 900^oC, respectively. It suggests that the customized nozzle enables suppressing the carbon formation in the fuel vaporization step and the reformation processes for diesel fuel. Furthermore, the carbon evolution processes in these three experimental sets behave differently. For example, diesel ATR with the nozzle shows a more gradual growth of solid carbon concentration prior to the significant carbon spike at 725^oC reformer temperature, while diesel ATR without the nozzle and biodiesel ATR with the nozzle tend to frequently have sudden jumps of carbon concentration. When combining the carbon evolution data (Figure 24) with the gas composition results shown in Figure 22 and Figure 23 for diesel and biodiesel ATR, it is observed that the yields of H_2 and CO are declining significantly while the concentration of light hydrocarbons increases dramatically after the reforming system enters the carbon formation boundaries, especially for reformation without using the nozzle. The sprayer of the conventional fuel injectors has been reported as the vulnerable component to deposit solid carbon due to the thermal cracking of heavy hydrocarbons and recirculation issues [119,124]. Figure 25(a)

shows the image of the porous sprayer in the customized nozzle with its initial condition, while Figure 25(b) shows the sprayer after 13 hours continuous fuel vaporization in the reformer system (7 hours diesel ATR and 6 hours biodiesel ATR). No tar deposition was observed on the surface of the porous device, indicating the occurrence of fuel thermal pyrolysis was significantly suppressed.

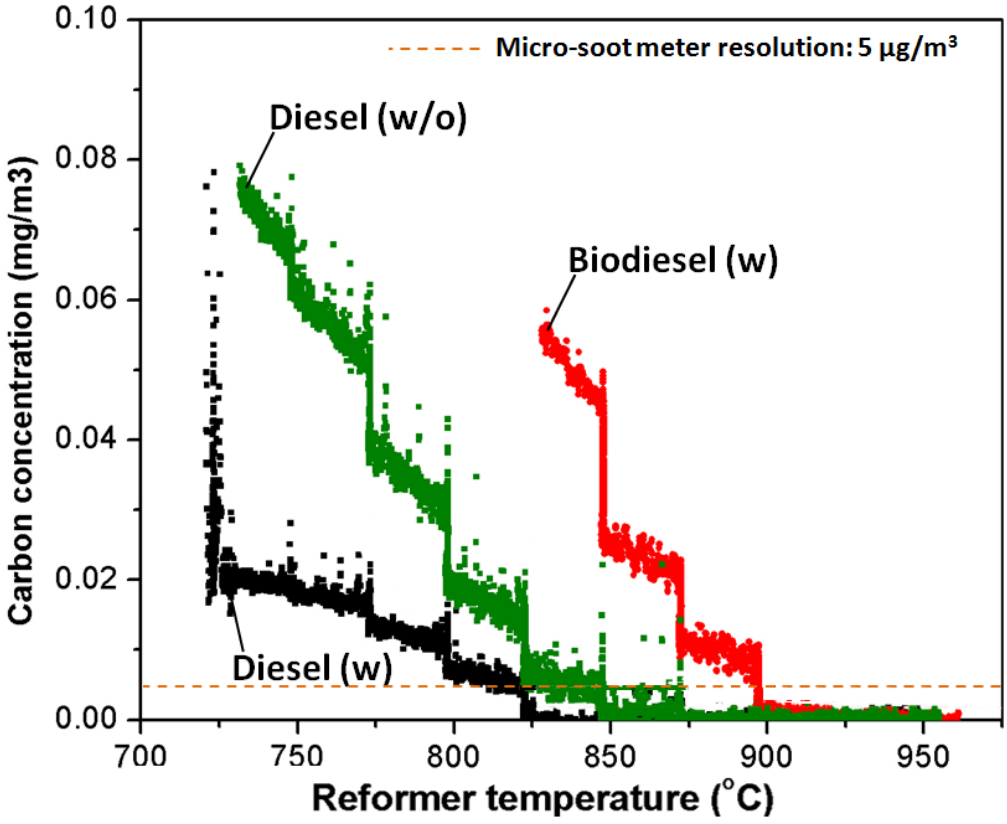

Figure 24: Effects of reformer temperature on carbon concentration for diesel ATR with the customized nozzle (w), diesel ATR with fuel/air/steam direct mixing (w/o), and biodiesel ATR with the customized nozzle (w).

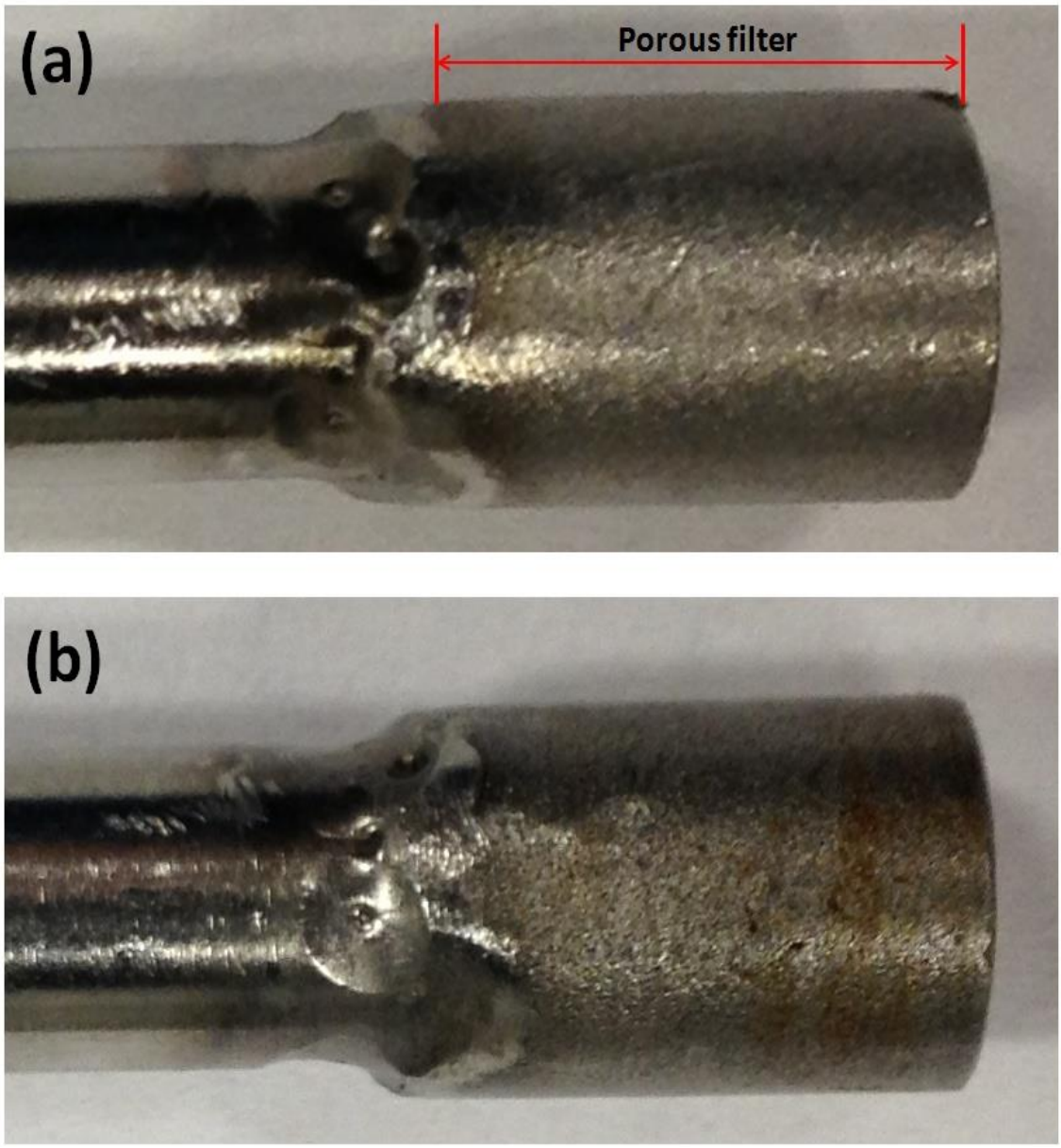

Figure 25: Images of the porous sprayer (a) before, and (b) after 13 hours continuous fuel ATR.

Analysis of Condensate

Because biodiesel possesses a relatively high boiling point and molecular weight, it is difficult to vaporize completely without fuel self-pyrolysis using the conventional techniques. To demonstrate the breakdown conditions of the biodiesel using the proposed

nozzle, the vaporized gaseous products from the mixing chamber were cooled to room temperature and condensed instead of entering the reformer. Figure 26 compares the liquid condensates of biodiesel vaporized with conventional direct mixing method (without the nozzle, Figure 26b) and the one with the customized nozzle (Figure 26c), along with the original biodiesel fuel (Figure 26a). The top layer of the condensed liquid is the decomposed hydrocarbons (e.g. dodecane, isooctane, isopentane) while the bottom

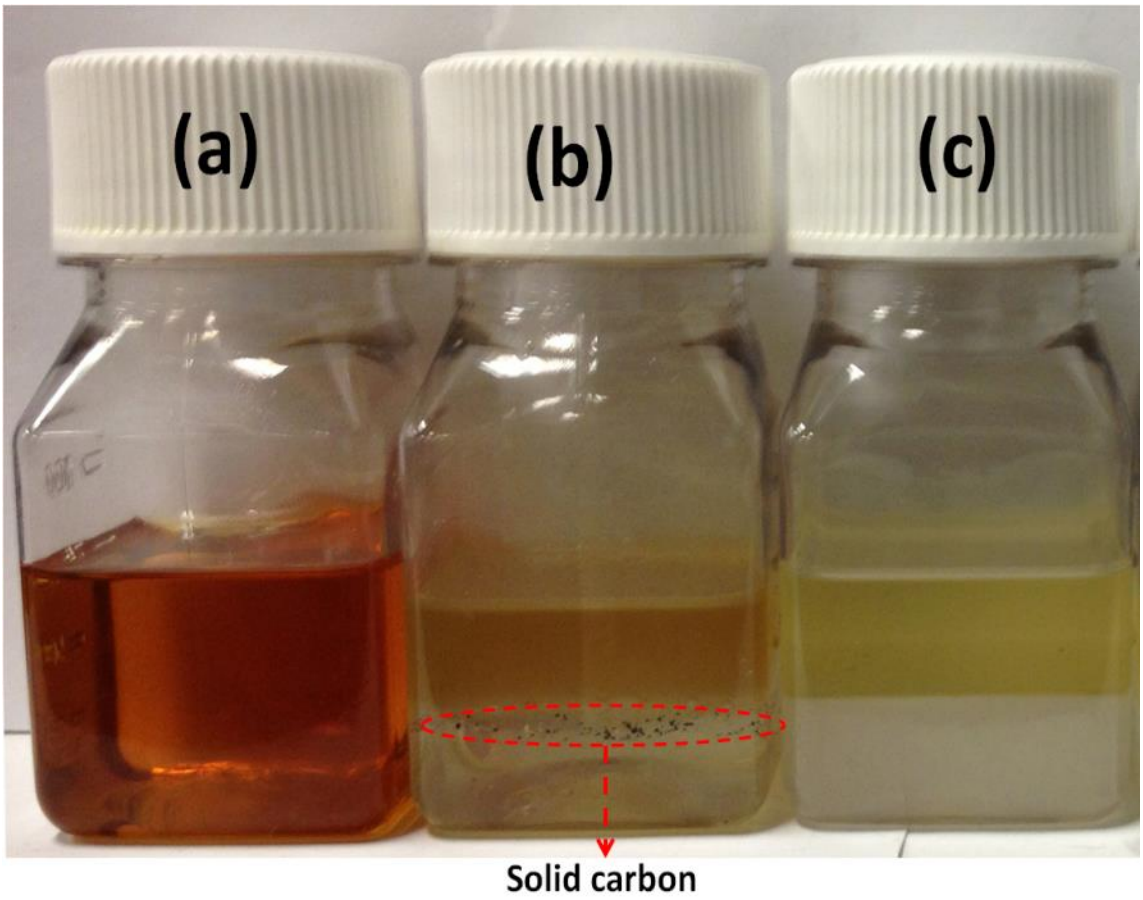

Figure 26: Images of (a) biodiesel fuel, (b) condensate after biodiesel vaporizing and direct mixing with air/steam, and (c) condensate after biodiesel vaporizing through the proposed mixing chamber

layer is the condensed water. The color of the condensed mixture vaporized with the proposed nozzle is lighter than that with the direct mixing approach, indicating the customized nozzle accelerates the biodiesel decomposition into lower hydrocarbon compounds. Furthermore, because the duration of the micro-explosion occurring inside the nozzle during fuel vaporization is so short (less than 0.2 ms), the period of time available for the pyrolytic reaction of fuel to form carbonaceous residues is limited [132], and thus no solid carbon was formed in the biodiesel vaporization step. However, significant amounts of carbon particles are found in the condensate with the direct mixing method (highlighted on Figure 26b) and these solid particles would consequently flow along with the vaporized gases into the reformer and contaminate the catalyst bed.

To further analyze the hydrocarbon compounds in the condensate, a temperature-controlled vaporization method was applied to identify the boiling point distributions of the condensed hydrocarbons after the water portion was removed from the mixture. Even though this work explored the carbon number ranges based only on the correlations between the boiling point and carbon number for the paraffins (shown in Figure 19), it is pertinent to assign a higher carbon number to a non-paraffin compound (olefins, naphthenes, and aromatics) than the inherent carbon number within the hydrocarbon. For example, benzene (C_6H_6) is a common aromatic byproduct of thermal pyrolysis of heavy hydrocarbons, and it is difficult to chemically decompose as compared to C_6H_{14}. Since benzene has a boiling point similar to that of C_7H_{16} (shown in Figure 19), the fraction of benzene present in the condensate was assigned to the paraffin hydrocarbons with carbon number ranging from C7 to C9. Figure 27 shows the mass fraction of carbon number

distributions for the condensates shown in Figure 26, including the initial biodiesel fuel, the condensed hydrocarbons with direct mixing of fuel/air/steam, and the condensed hydrocarbon with the nozzle. Figure 27 (a) identifies the average carbon number content in biodiesel as being between C19 and C21, which is in agreement with the fuel certification for biodiesel ($C_{19}H_{35.5}O_2$) used in this work. When comparing the carbon number distribution of the condensates without using the nozzle (Figure 27b) to the one with the nozzle (Figure 27c), the latter condensate has a lower average carbon number (C7 to C12) than the former (C13 to C18), which confirms that the customized nozzle enhances the biodiesel breakdown in the mixing chamber while suppressing fuel self-pyrolysis.

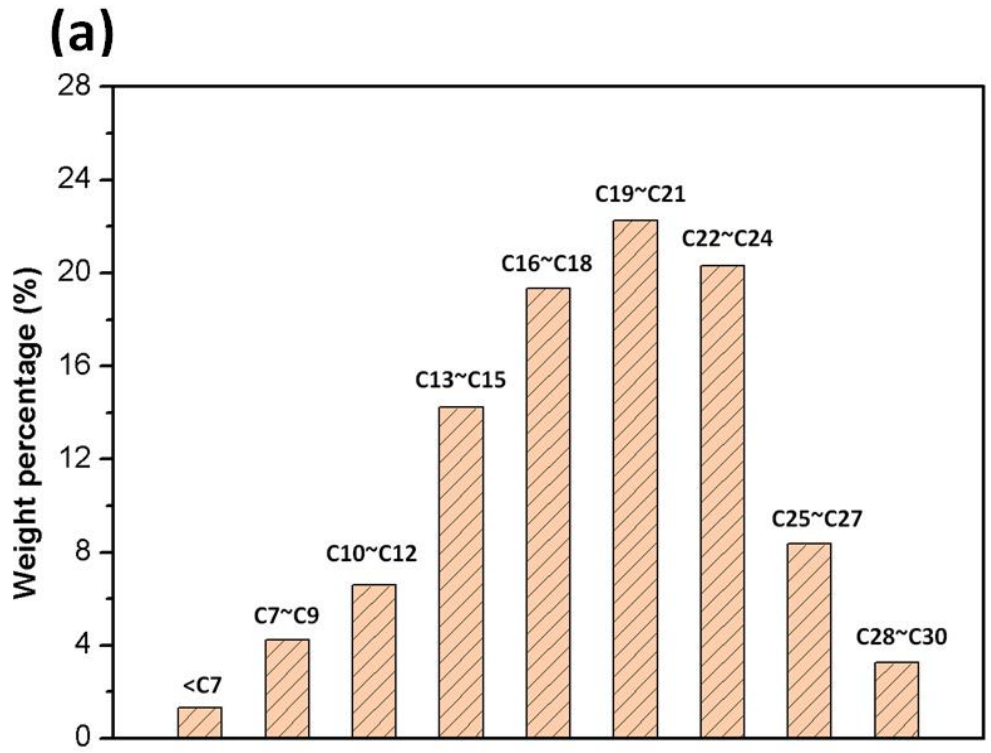

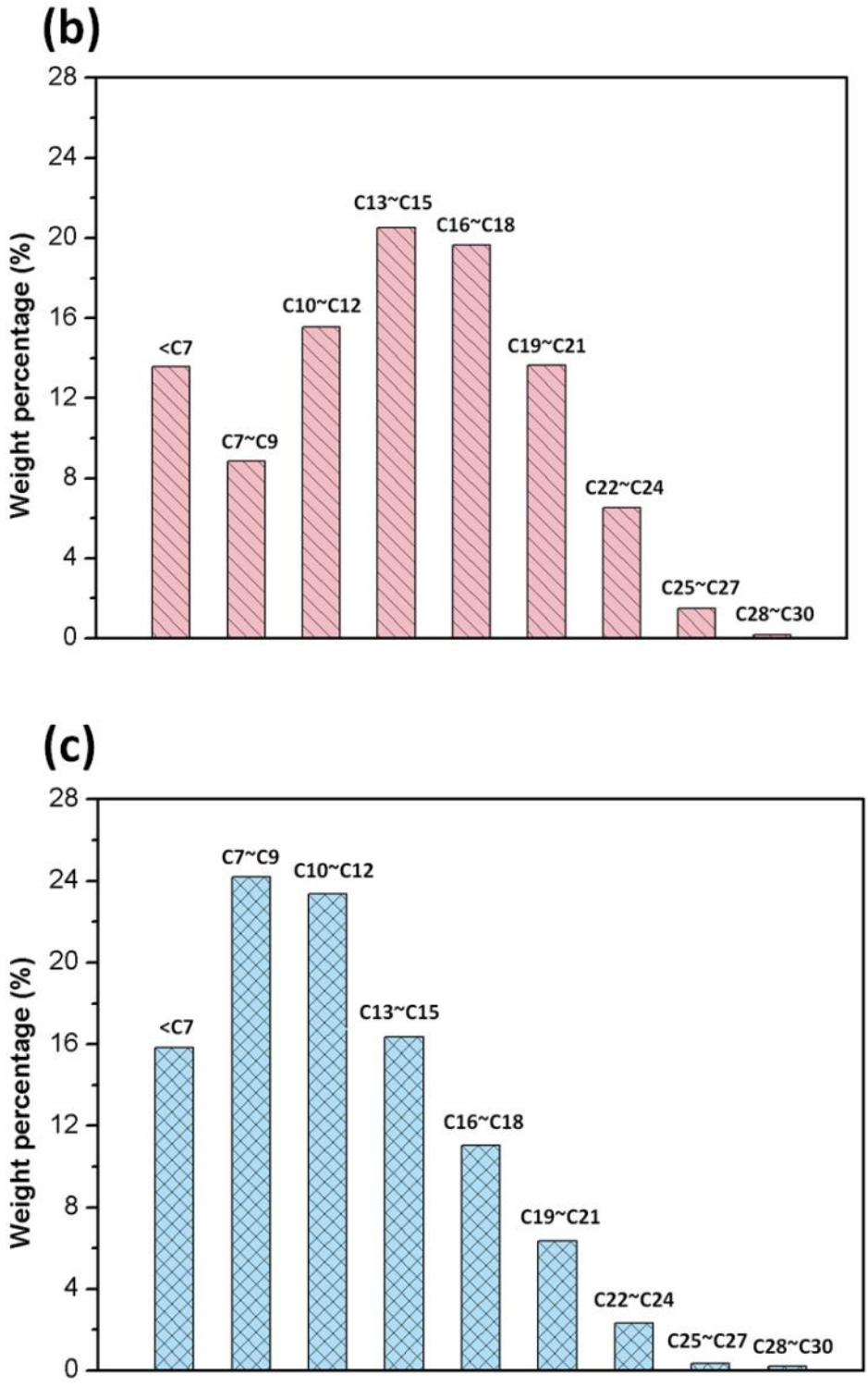

Figure 27: Carbon number distributions of (a) biodiesel fuel, (b) condensate after biodiesel vaporizing and direct mixing with air/steam, and (c) condensate after biodiesel vaporizing through the proposed mixing chamber

4.1.4. Summary

Fuel vaporization and mixing with oxidants (air/steam) is a crucial step for catalytic reformation because the heavy hydrocarbons in this step have the tendency for thermal self-pyrolysis and coke formation, which would directly affect the reformate production and reforming efficiency. To overcome these technical challenges, a novel configuration of the mixing chamber integrated with the porous nozzle was developed to achieve complete vaporization of fuels (e.g., diesel, biodiesel) and homogenous mixing with air/steam based on micro-explosion techniques. To evaluate the effects of the customized nozzle, biodiesel was first vaporized and mixed with air/steam through the mixing chamber, and then its gaseous products from the chamber were condensed to room temperature. No solid carbon was observed in the condensate, which suggests the thermal cracking of biodiesel was suppressed. Furthermore, the carbon number distribution of the condensed hydrocarbons was explored based on the correlations between the carbon number and normal boiling points of the hydrocarbons. Results show that biodiesel vaporized with the customized nozzle has a better breakdown than without the nozzle. The proposed mixing chamber was integrated in a single-tube reformer system to evaluate the performances of diesel and biodiesel ATR, and it was demonstrated that the customized nozzle not only improves the reformate composition and reforming efficiency, but it also stabilizes the chemical reactions within the reformer and prevents the reactor inlet from causing hot spots. Diesel ATR with fuel atomization using the customized nozzle enabled operation at a relatively low reformer temperature without forming solid carbon, as compared to the conventional approach with

diesel/air/steam direct mixing. The customized nozzle device developed as an outcome of this work has been covered in a provisional U.S. patent application.[2]

4.2. Diesel and Biodiesel Autothermal Reformation

4.2.1. Introduction

Many hydrocarbon fuels have been reported as viable hydrogen precursors, such as methane [143], ethanol [144], dimethyl ether [145], butanol [146], gasoline [147], diesel [148], and even vegetable-oil [149]. But from the perspective of developing a sustainable and feasible pathway for fuel cell applications in the transportation sector, hydrocarbon fuels need to be derived from clean energy sources that are compatible with the existing fuel delivery infrastructure. Biodiesel is an oxygenated fuel and possesses physical and chemical properties that are similar to petroleum diesel, which suggests biodiesel could potentially replace conventional diesel with no significant modifications of the truck fuel system. However, reports of biodiesel ATR have not yet appeared in the open literature, and its optimum operating conditions still need to be explored.

In this study, biodiesel ($C_{19}H_{35.4}O_2$) with sulfur content of 7 ppmw and lower heating value of 37.2 MJ/kg, was used as the primary fuel feedstock to a single-tube reactor with ATR under various operating conditions (reformer operating temperature, H_2O/C, GHSV, and O_2/C). Ultra-lower sulfur diesel (ULSD, $C_{15.5}H_{28}$) with sulfur content of 8 ppmw, aromatic content of 32%, and lower heating value of 42.6 MJ/kg, was used to establish a baseline. A single-tube reformer with rhodium/ceria-zirconia catalyst wash-

[2] J.F. Lin, M.R. Walluk, "Device for vaporization of hydrocarbons and multi-fuel blends", U.S. Provisional Patent Application Serial No. 61/720,177, filed August 2012

coated ceramic monoliths was integrated with the vapor pretreatment process described in Section 4.1 to help the fuel completely vaporize with less hydrocarbon self-pyrolysis before entering the reactor. A direct photo-acoustic based micro-soot meter was used to analyze carbon dynamic evolution under different conditions while a mass spectrometer was applied to measure the gas composition in the effluent from the reformer. This study explored the correlations between carbon concentration and ethylene under each set of parameter changes (O_2/C, H_2O/C, reformer temperature, and GHSV), and developed correlation formulae with polynomial regressions, which revealed the contributions of ethylene to carbon formation associated with diesel and biodiesel. Thermodynamic analysis based on total Gibbs free energy minimization was applied to evaluate the equilibrium compositions of effluents from biodiesel as well as diesel ATR. The main objective of this work was to identify the optimum operating conditions with high hydrogen yield and no carbon formation for biodiesel ATR, using both thermodynamic modeling and experimental measurements. Combinations of H_2O/C and O_2/C to reach a carbon-free boundary at certain temperatures were also investigated.

4.2.2. Thermodynamic analysis

Generally, two approaches have been used to predict the equilibrium compositions of hydrocarbon reformation: equilibrium constant (stoichiometric) and Gibbs free total energy minimization (non-stoichiometric) [145,148]. The latter method was applied in this work to simulate the equilibrium specie effluent from the reformer with diesel ATR and biodiesel ATR under various operating conditions, because this method has the advantage of quantifying the presence of condensed species in the

reaction products without necessarily knowing the exact chemical reactions involved [148].

The total Gibbs energy with two phases can be expressed as:

$$G = G_{gas} + G_{condensed} = \sum_{i=1}^{N} n_i (G_i^o + RT \ln \Phi_i y_i P) + \sum_{i=N+1}^{Ns} n_i G_{c(s),i} \tag{17}$$

where n_i is the number of moles of species i; G_i^o is standard state free energy of species i; y_i mole fraction of species i; N is the number of gas species and Ns is the number of condensed species; T, P, R are temperature, pressure, and gas constant, respectively. When solid carbon is considered in the system, its Gibbs free energy $G_{c(s),i}$ equalizes to zero [145,149]. The gas phase species were assumed to behave ideally because of the high operating temperature and low pressure (slightly above atmospheric) in the reactor, so the fugacity coefficient Φ_i =1. Also, Eq. (17) is subjected to the constraint of elemental mass balance:

$$\sum_{i=1}^{N} n_i a_{ik} = b_k \qquad k = 1, ..., M \tag{18}$$

where a_{ik} is the number of atoms of element k in molecule i and b_k is the total amount of element k in the effluent gases.

By introducing the Lagrange multipliers, Eq. (18) can be rewritten as:

$$\lambda_k (b_k - \sum_{i=1}^{N} n_i a_{ik}) = 0 \qquad k = 1, ..., M \tag{19}$$

In biodiesel ATR, there are total four elements present (C, H, O, N) in the reactor, and thus M = 4 in Eqs. (18) and (19). For these four elemental restrictions, Eq. (19) may be represented by:

$$\sum_{k=1}^{4} \lambda_k (b_k - \sum_{i=1}^{N} n_i a_{ik}) = 0 \qquad k = 1, ..., 4 \tag{20}$$

The combination of Eq. (1) and the constrained function Eq. (20) is shown as:

$$C = \sum_{i=1}^{N} n_i (G_i^o + RT \ln y_i) + \sum_{i=N+1}^{Ns} n_i G_{c(s),i} + \sum_{k=1}^{4} \lambda_k (b_k - \sum_{i=1}^{N} n_i a_{ik}) \tag{21}$$

In order to minimize the value of Eq. (21), the partial derivatives with respect to n_i are set equal to zero:

$$\frac{\partial C}{\partial n_{i,gas}} = (G_i^o + RT \ln y_i) + RT(1 - y_i) + \sum_{k=1}^{4} \lambda_k a_{ik} = 0 \qquad i = 1, 2, .., N \tag{22}$$

$$\frac{\partial C}{\partial n_{i,condensed}} = \sum_{k=1}^{4} \lambda_k a_{ik} = 0 \quad i = N+1, .., Ns \tag{23}$$

,

Many studies show that when the operating temperature in the reactor is above 600^{o}C, the constituents of the effluent gas that are considered pertinent are: CH_4, H_2, H_2O, CO, CO_2, C_2H_4, C_2H_6 and solid C [15,145,147,148]. Thus there are a total of twelve variables (including eight for molar fractions, y_i, of species i and four for Lagrange multipliers λ_k) in twelve non-linear Eqs. (22) and (23), which can be solved by applying the Newton-Raphson method and employing the fsolve function in Matlab [148]. The amount of input fuel was normalized as 1 mol/s and the compositions of the mixed gases were predicted in the temperature range of 400-1000^{o}C with H_2O/C range of 0~2.0 and

O_2/C range of 0~0.6. Carbon free boundaries at different set temperatures (500 to 1100^{o}C) are also extrapolated from thermodynamic models with functions of H_2O/C and O_2/C.

4.2.3. Experimental

The description of the single-tube catalytic reformer apparatus for diesel and biodiesel ATR is provided in Figure 18. Because of the lack of onboard water sources in transportation applications, SOFC-based APUs partially recycle the exhaust gases from the anode side of the stacks to the reformer inlet. Although the experimental setup in this study does not involve anode recycled gases, we have simulated the amount of steam recycled from SOFC stacks based on our previous work [14]. The operating conditions for diesel and biodiesel were both initially set at H_2O/C = 0.6, total O/C (summation of oxygen from fuel, air, and water to carbon from the fuel) = 1.47, and with the reformer temperature (average temperature of TC1~TC5) of 950^{o}C. Nitrogen, which serves as a carrier of the liquid fuel, was used to adjust the system GHSV during the tests. Borup *et al.* [120] highlighted that high hydrocarbon fuels like diesel and biodiesel have the propensity to incompletely vaporize in the pretreatment process and partially self-pyrolyze, which may lead to formation of solid carbon before entering the reformer, and thus results in fuel conversion efficiency reduction. Therefore, the customized nozzle integrated with a 2 μm porous filter proposed was developed and used to improve fuel atomization and promote homogenous fuel/steam mixing. The AVL micro soot meter was applied to directly measure the carbon concentration in the reformate stream while the mass spectrometer was used to analyze gas compositions of the effluents from the

reformer. The soot meter was calibrated and established a stable zero baseline under nitrogen flow through the reformer at 950^{o}C reformer temperature.

Carbon monoxide and hydrogen both serve as the main input fuels for the SOFC system to electrochemically generate electricity, and their equilibrium gas yields from reforming diesel or biodiesel can be derived from the thermodynamic analysis described in Section 4.2.2. Thus, the required flow rates of diesel and biodiesel under the same operating conditions can be determined in order to provide the same reformate production rate. Table 10 provides the operating conditions of initial test points for diesel and biodiesel ATR with the goal of delivering a 0.00275 mol/s reformate production rate. To identify the carbon formation boundaries in diesel or biodiesel reformation and capture the effects of each parameter (O_2/C, H_2O/C, GHSV, and average reformer temperature) on the effluent species, four series of experimental tests were conducted (listed in Table 12): total O/C reduction from 1.47 to 1.07 by reducing air flow, H_2O/C reduction from 1.0 to 0.6, reformer temperature reduction by adjusting the temperature controller of the furnace from 1000 to 750^{o}C, and GHSV at standard temperature and pressure (STP) condition (defined as Eq. 24 [15]) changes from 30,500 to 53,000 hr^{-1}:

$$GHSV(\frac{m^3(STP)/h}{m^3}) = \frac{V_{feed}@STP(m^3/h)}{V_{cat}(m^3)} = \frac{V_{feed}@STP(m^3/h)}{V_{net} \times V_{monolith}(m^3)} \quad (24)$$

where $V_{feed}@STP$ is total volumetric flow rate of the feed at STP condition, V_{cat} is the catalyst bed volume, and V_{net} is the effective volumetric fraction of catalyst in the whole monoliths $V_{monolith}$ ($V_{net} = 0.66$ in this work).

Table 11. Experimental test plan to evaluate four key parameters for diesel ATR and biodiesel ATR

Test series	Variable	Total O/C	H_2O /C	Furnace set point (^oC)	GHSV@STP hr^{-1})
1	O_2/C	1.47~1.07	0.6	1000	34,120
2	Reformer temperature	1.47	0.6	1000~750	34,120
3	GHSV	1.47	0.6	1000	30,000~52,000
4	H_2O/C	1.47~1.07	1~0.6	1000	34,120

After each set of experimental tests, methane partial oxidation (POx) with O/C=1.3 at 950^{o}C reformer temperature was conducted in the single-tube reactor for catalyst regeneration; more description of the methane POx process is available in our previous work [14]. The experimental data were also used to validate the results obtained from the equilibrium analysis. Many studies have confirmed that ethylene has a higher rate of carbon formation than other hydrocarbons, and serves as a major carbon precursor in catalytic reformation [15,147,150], thus the fundamental understanding of the correlations between condensed carbon content and ethylene in each set of experimental conditions need to be explored. Polynomial regression was applied to fit the experimental data for carbon concentration and ethylene composition in order to obtain their correlation expressions.

4.2.4. Results and discussion

Equilibrium analysis

Chemical equilibrium computations were applied to analyze both diesel and biodiesel ATR. Figure 28 illustrates the reformate equilibrium compositions as a function of reformer temperature under the conditions of H_2O/C = 0.6 and total O/C = 1.47. Diesel ATR and biodiesel ATR have similar variations of effluent products with reformer

temperature changes. For example, as the reformer temperature ramps up, the light hydrocarbon gases (e.g., CH_4, C_2H_4, and C_2H_6) are reduced dramatically (Figure 28b) while CO is continuously increased (Figure 28a). The peak of H_2 yield for either diesel or biodiesel ATR is located near 750^{o}C and the hydrogen yield slightly decreases above 750^{o}C because of the reverse water gas shift reaction [151-153]. Figure 28(b) also depicts the condensed carbon evolution with reformer temperature changes for diesel and biodiesel ATR. Even though solid carbon formation increases from 400 to 500^{o}C due to thermal cracking of C_6H_6, C_3H_8, C_2H_4, and C_2H_6, the solid carbon content is substantially diminished at temperatures above 550^{o}C [14]. The threshold temperatures to mitigate carbon formation for diesel and biodiesel ATR are 825 and 900^{o}C, respectively. It is worthwhile to mention that the temperature range from 500 to 800^{o}C is the main regime to accelerate CO evolution and solid carbon reduction, because the molar concentrations of CH_4 and H_2O are relatively low and the reverse Boudouard reaction dominates the coke activity [154]. Figure 29 shows the equilibrium analysis of diesel ATR and biodiesel ATR with a functional unit of mol/mol carbon from input fuel for comparison purpose with Figure 28.

Despite a limited amount of water available from anode recycled gas for SOFC-based APU applications [120], it is relatively simple to adjust O_2/C by changing compressed air flow to improve reformate performance. Figure 30 shows the biodiesel ATR equilibrium gas products as functions of O_2/C and temperature. Maximum hydrogen yield is achieved with O_2/C of 0.32 at 750 ^{o}C (Figure 30a) and CO reaches its peak production rate with O_2/C of 0.35 at high temperature (1000 ^{o}C, Figure 30d). Figure 31(a)

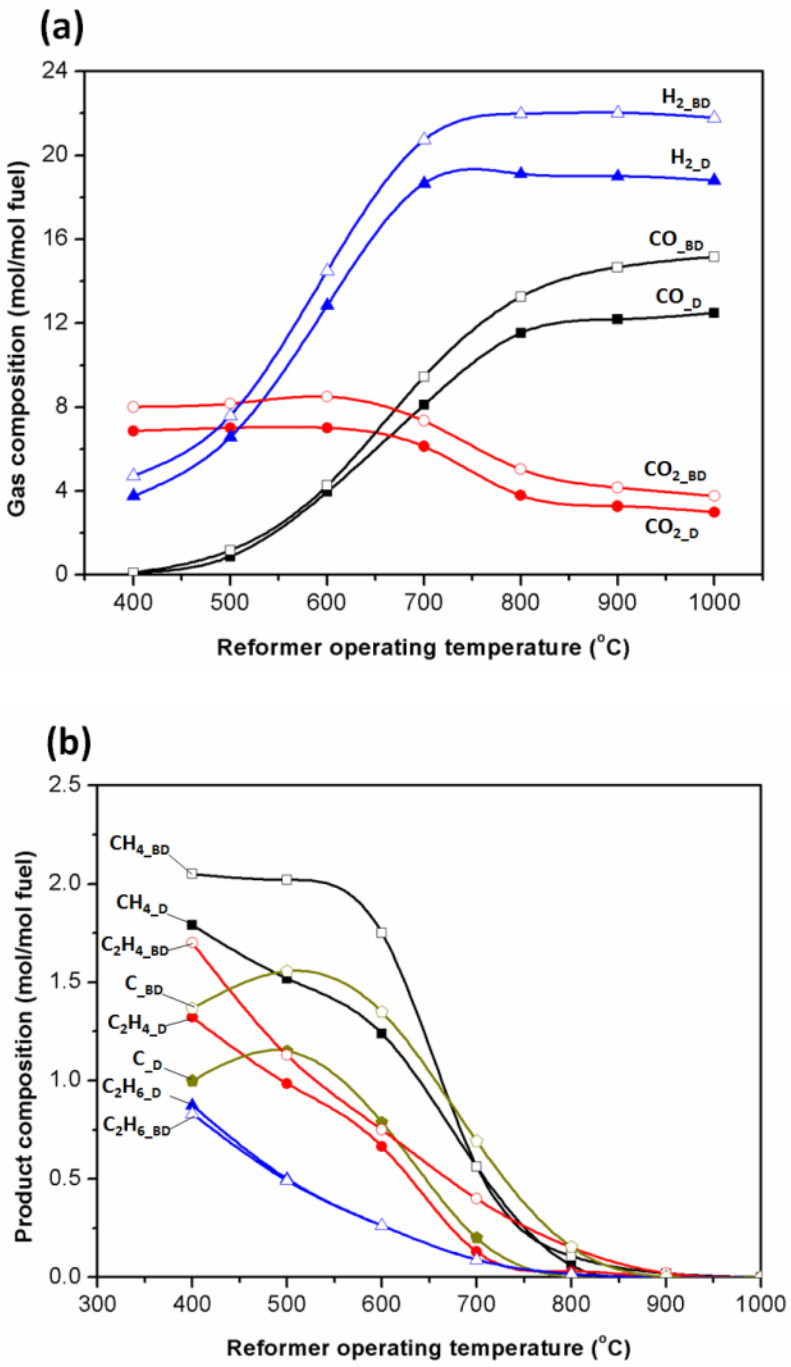

Figure 28: Equilibrium analysis of (a) H_2, CO, CO_2, and (b) CH_4, C_2H_4, C_2H_6, for diesel and biodiesel ATR as a function of reformer operating temperature (mol/mol fuel)

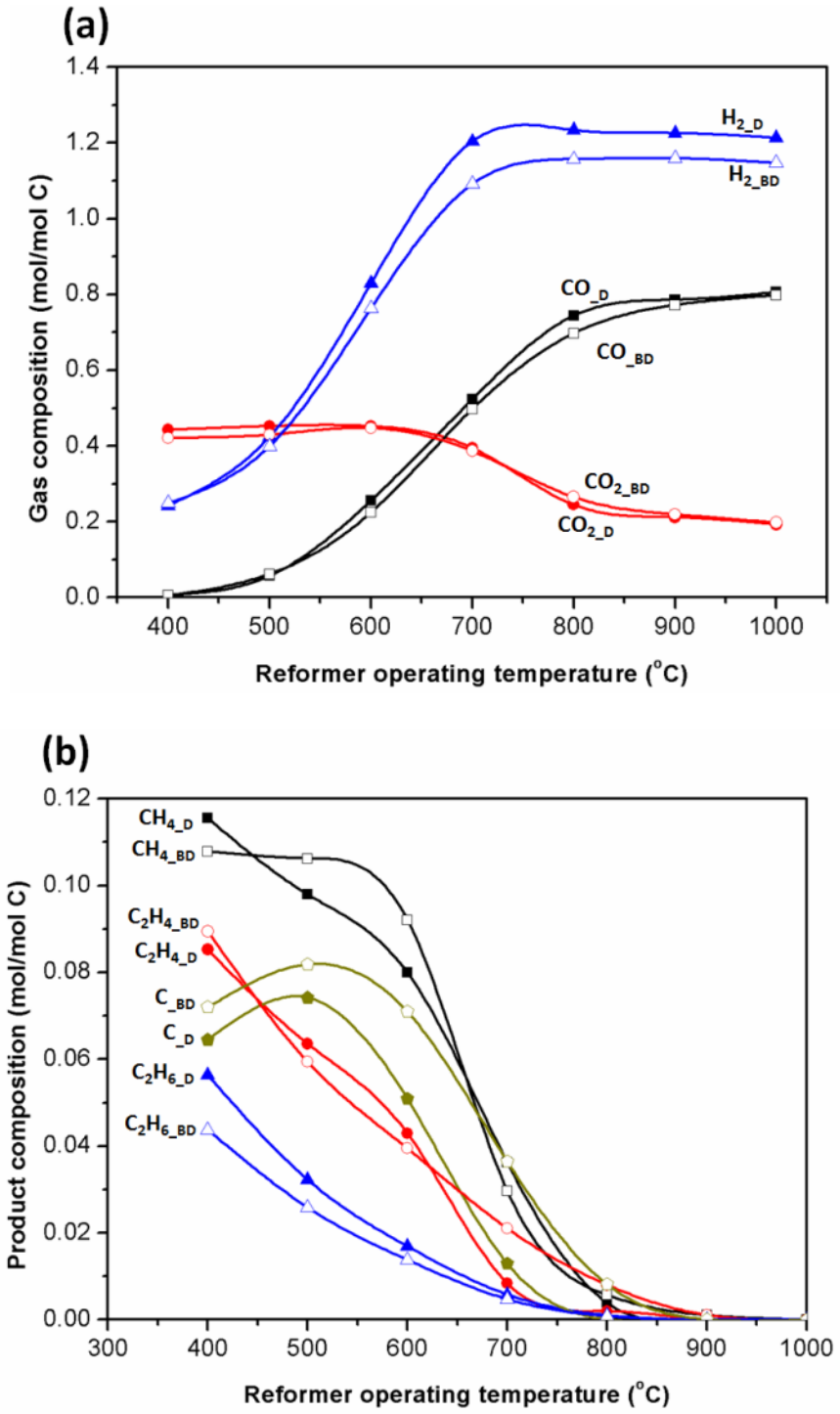

Figure 29: Equilibrium analysis of (a) H_2, CO, CO_2, and (b) CH_4, C_2H_4, C_2H_6, for diesel and biodiesel ATR as a function of reformer operating temperature (mol/mol C)

depicts the equilibrium composition of solid carbon formation as functions of O_2/C and reformer temperature for biodiesel ATR. With the increase of O_2/C, solid carbon content dramatically declines, indicating that increasing the input air may be an effective approach to mitigate carbon formation. The carbon free boundary was identified and highlighted on Figure 31(a), indicating it is crucial to control both air flow and reformer temperature to mitigate carbon formation. Carbon formation boundaries for biodiesel ATR with different combinations of H_2O/C and O_2/C at certain temperatures are also extrapolated from thermodynamic models, as shown on Figure 31(b). The carbon free region is located on the upward regime of the boundary of the corresponding temperature while the carbon formation area is below the boundary. It suggests that the temperature contribution to carbon mitigation is diminished as temperature increases from 600 to 1100^{o}C. Many works have experimentally identified the carbon formation boundaries of biodiesel ATR with various combinations of H_2O/C and O_2/C at 800 and 900^{o}C reformer temperatures [155,156], and these test points are provided on Figure 31(b) for the purpose of validating the equilibrium results. The equilibrium carbon-formation boundaries with intermediate O_2/C (0.3 to 0.5) enable modeling well the trend of the experimental test points, whereas those with a relatively high H_2O/C (> 0.75) do not show a close fit with the theoretical prediction, because the equilibrium model proposed in this work does not consider the thermal transfer loss in the reactor and it may show differences between equilibrium results and experimental data when exothermal steam reforming dominates the reforming process [157]. When considering SOFC-APUs for transportation applications in particular, there are several restrictions that need to be comprehended in designing a viable system architecture, which include the limited water

supply, maximum reactor temperature, thermal balance of the system, and fuel conversion efficiency [157,14]. The area highlighted by the dotted line on Figure 31(b) is the pertinent range for practical applications based on the present experimental data and the results reported in several studies [120,147,150, 158].

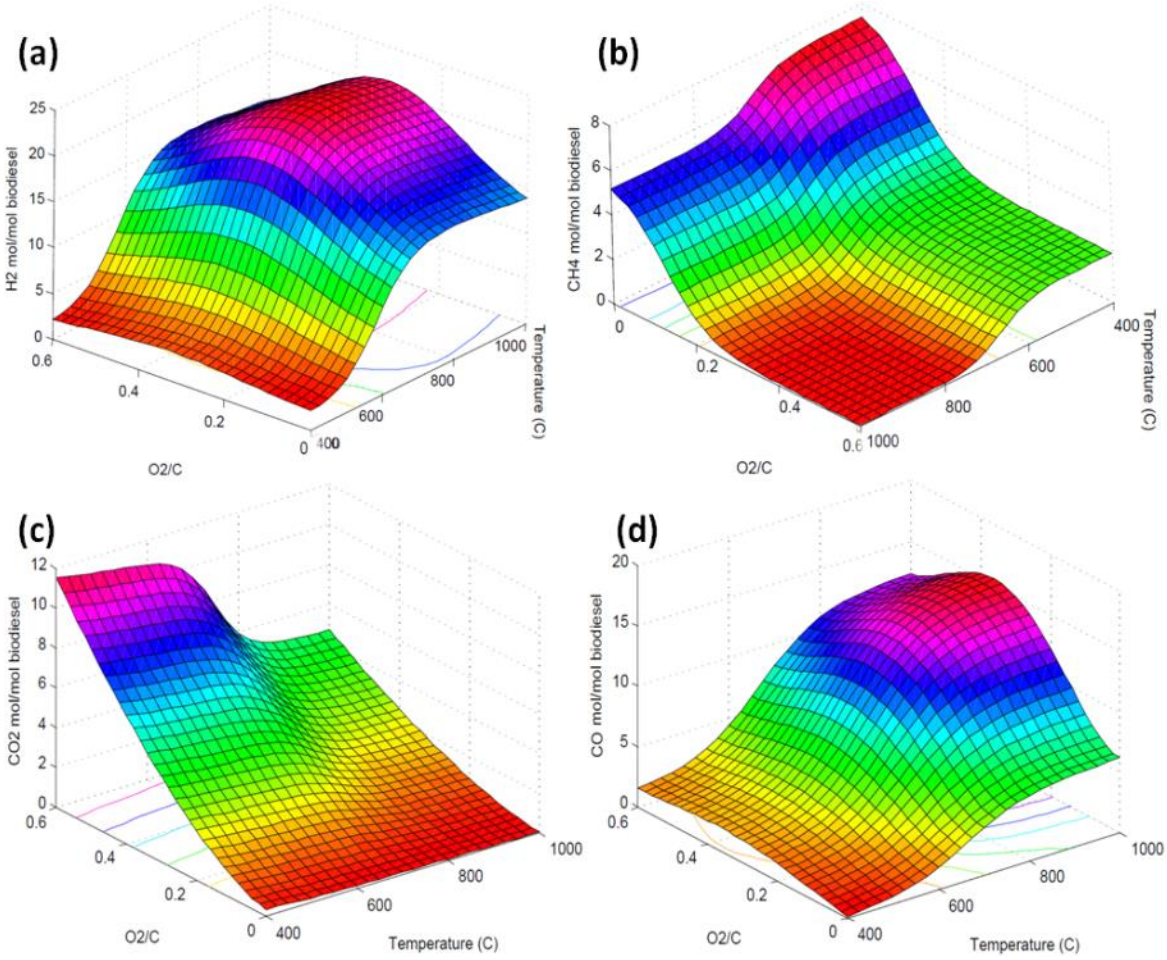

Figure 30: Thermodynamic equilibrium gas products of biodiesel ATR (a) H_2, (b) CH_4, (c) CO_2, and (d) CO with $H_2O/C = 0.6$, as functions of O_2/C and reforming temperature (the scale are altered to provide adequate visualization of the surface plot)

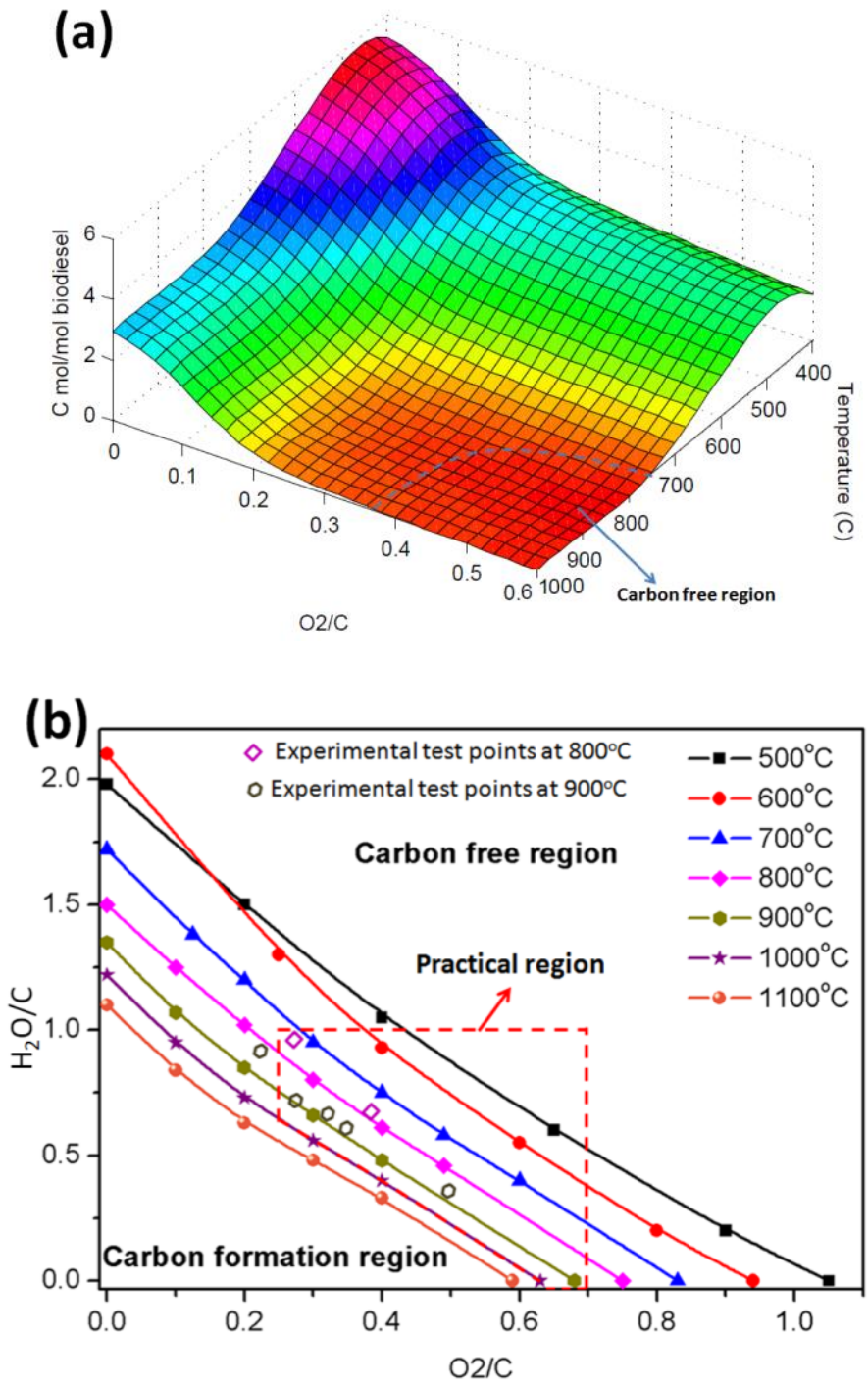

Figure 31: (a) Thermodynamic equilibrium of solid carbon product in biodiesel ATR with $H_2O/C = 0.6$, (b) carbon formation boundaries of biodiesel ATR for different iso-temperatures with the combinations of H_2O/C and O_2/C

Experimental Test Points

Table 13 compares the gas yields of the initial test points measured from the mass spectrometer for diesel and biodiesel ATR under the same operating conditions (H_2O/C = 0.6 and total O/C = 1.47 with the reformer temperature at 950^oC). With the goal of achieving the same equilibrium reformate yield, the amount of required input fuels (diesel and biodiesel) were determined (as shown in Table 11) and the differences between the measured and predicted yields are within 3%. Relatively low or undetectable amounts of light hydrocarbon gases (CH_4, C_2H_4, and C_2H_6) were observed for both diesel and biodiesel ATR, indicating the initial test points are within the carbon-free boundary, which was also confirmed by the AVL micro-soot meter.

Table 12. Gas yields from diesel and biodiesel ATR (H_2O/C = 0.6 and total O/C = 1.47 at 950^oC reformer temperature)

Input fuel	Experimental output (10^{-3}×mol/s)						
	H_2	CO	CO_2	CH_4	C_2H_4	C_2H_6	Total reformate
Diesel	1.705	1.102	0.207	0.012	Undetectable	Undetectable	2.807
Biodiesel	1.665	1.164	0.217	0.026	0.004	Undetectable	2.825

Parametric Variation: Air Flow

Keeping other key parameters (H_2O/C, furnace control temperature, and GHSV) constant, the total O/C was gradually reduced for diesel and biodiesel ATR by reducing the input air flow. To avoid irreversible catalyst degradation from carbon deposition over a long period of time, air reduction was stopped when significant effluent carbon concentration was detected by the micro-soot meter. Figure 32 provides the effects of air changes on the resulting gas compositions and reforming efficiency for both diesel ATR and biodiesel ATR. As the input air flow is decreased, H_2, CO, and CO_2 (Figure 32a)

were reduced while CH_4, C_2H_4, and C_2H_6 (Figure 32b) rapidly increased, especially for biodiesel ATR. The reforming efficiency of either biodiesel ATR or diesel ATR declined with the air reduction (Figure 32a). These impacts on the gas composition and reforming efficiency become more significant after the reformer reaches the carbon formation boundary (total O/C < 1.12 for diesel ATR, total O/C < 1.26 for biodiesel ATR; Figure 33). The system resolution of the micro-soot meter (5 $\mu g/m^3$) is also included on Figure 33 and the carbon concentration values below this value are considered as zero. After air flow reaches the threshold points (total O/C = 1.12 for diesel, total O/C = 1.26 for biodiesel) and continuously reduces, diesel ATR gradually accelerates the carbon formation whereas there is a sudden large increment of carbon concentration for biodiesel ATR (total O/C = 1.13), and it may be challenging to anticipate and control these rapid changes during biodiesel ATR. Auto-thermal reformation is a combination of exothermic partial oxidation reaction and endothermic steam reforming to achieve the goal of thermal balance and the partial oxidation of hydrocarbon fuels occurs primarily in the front end of the reformer while steam reforming takes place sequentially through the reactor [159]. To demonstrate this effect, Figure 34 provides the temperature changes at five different locations along the reactor centerline (TC1~TC5 on Figure 18) with air flow reduction. It shows the temperature of the front end of the first catalyst monolith (TC 1) is affected the most while the middle part of the reactor (TC2~TC4) has the least impact for both cases of diesel ATR and biodiesel ATR, indicating fuel oxidation is completed near the location of TC 1. Even though diesel and biodiesel ATR both have the same initial total O/C (1.47), biodiesel ATR has a relatively low amount of air (O_2/C) because biodiesel itself possesses a certain molar fraction of oxygen content within the fuel (O/C = 0.105).

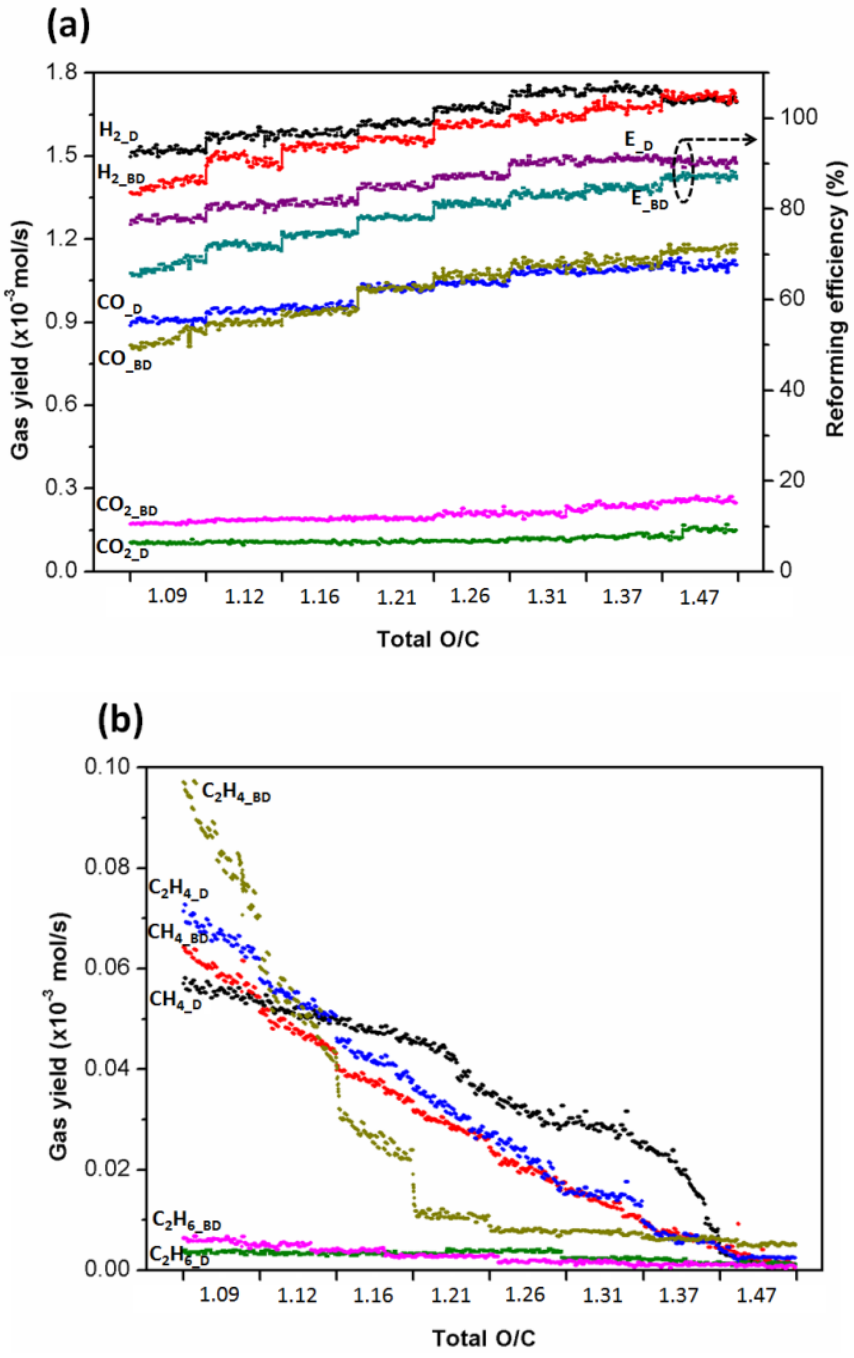

Figure 32: Effects of air in diesel and biodiesel ATR on (a) reforming efficiency and gas yields of H_2, CO, CO_2, and (b) gas yields of CH_4, C_2H_4, C_2H_6

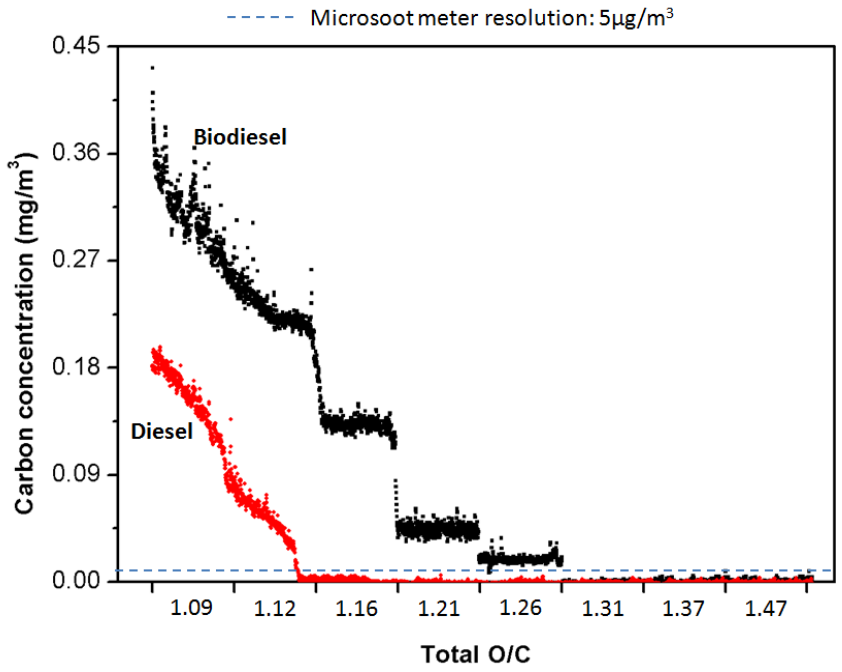

Figure 33: Effects of air in diesel and biodiesel ATR on solid carbon formation

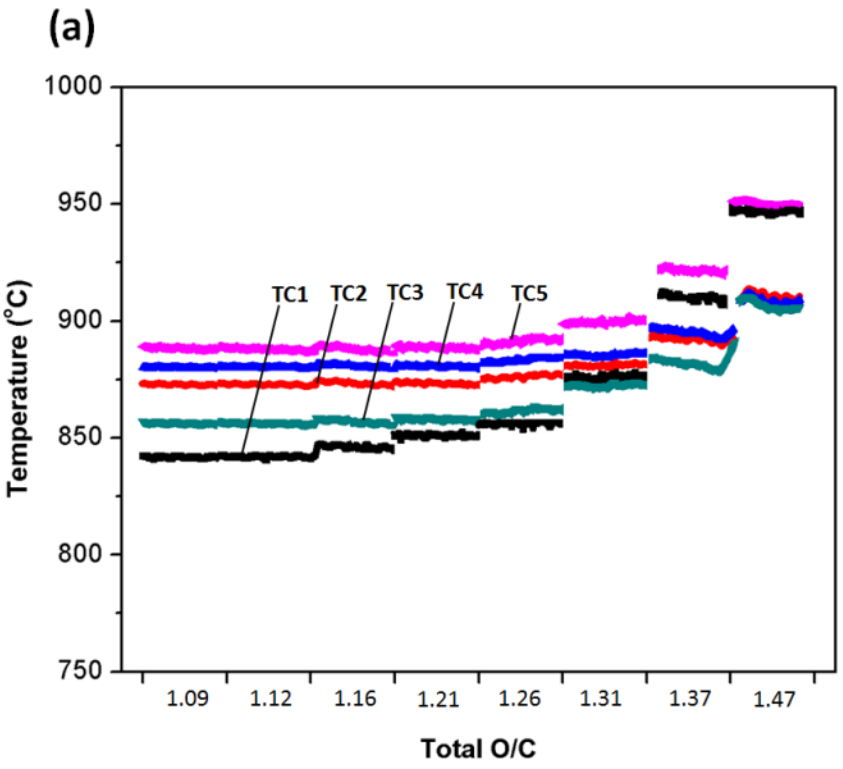

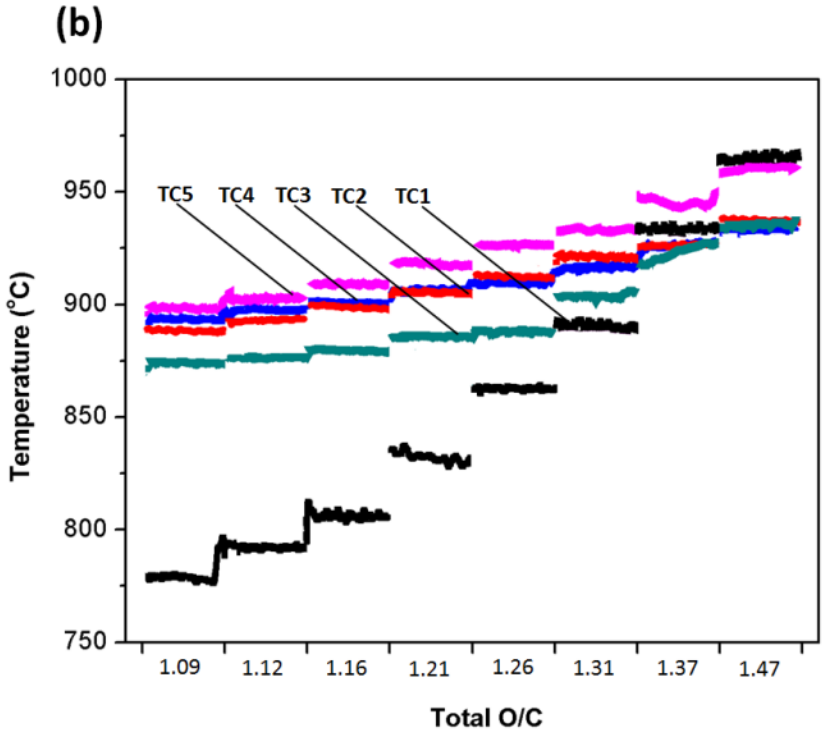

Figure 34: Effects of air on temperature profiles of the catalyst bed (TC1~TC5) for (a) diesel ATR and (b) biodiesel ATR

Thus, biodiesel ATR reacts more sensitive with the air changes than diesel ATR, which leads to the dramatic decline of biodiesel partial oxidation as the input air reduces (reflected in the reductions of TC 1).

Parametric Variation: Reformer Temperature

Before introducing the hydrocarbon fuel, water and air into the reactor, the reformer temperature was ramped up with the furnace temperature set point at 1000^{o}C and low flow rate of nitrogen. After initializing the experimental test points under the conditions of H_2O/C = 0.6 and total O/C = 1.47 at 950^{o}C reformer temperature, the furnace temperature controller was gradually reduced at a 0.1^{o}C/s rate. Figure 35 shows

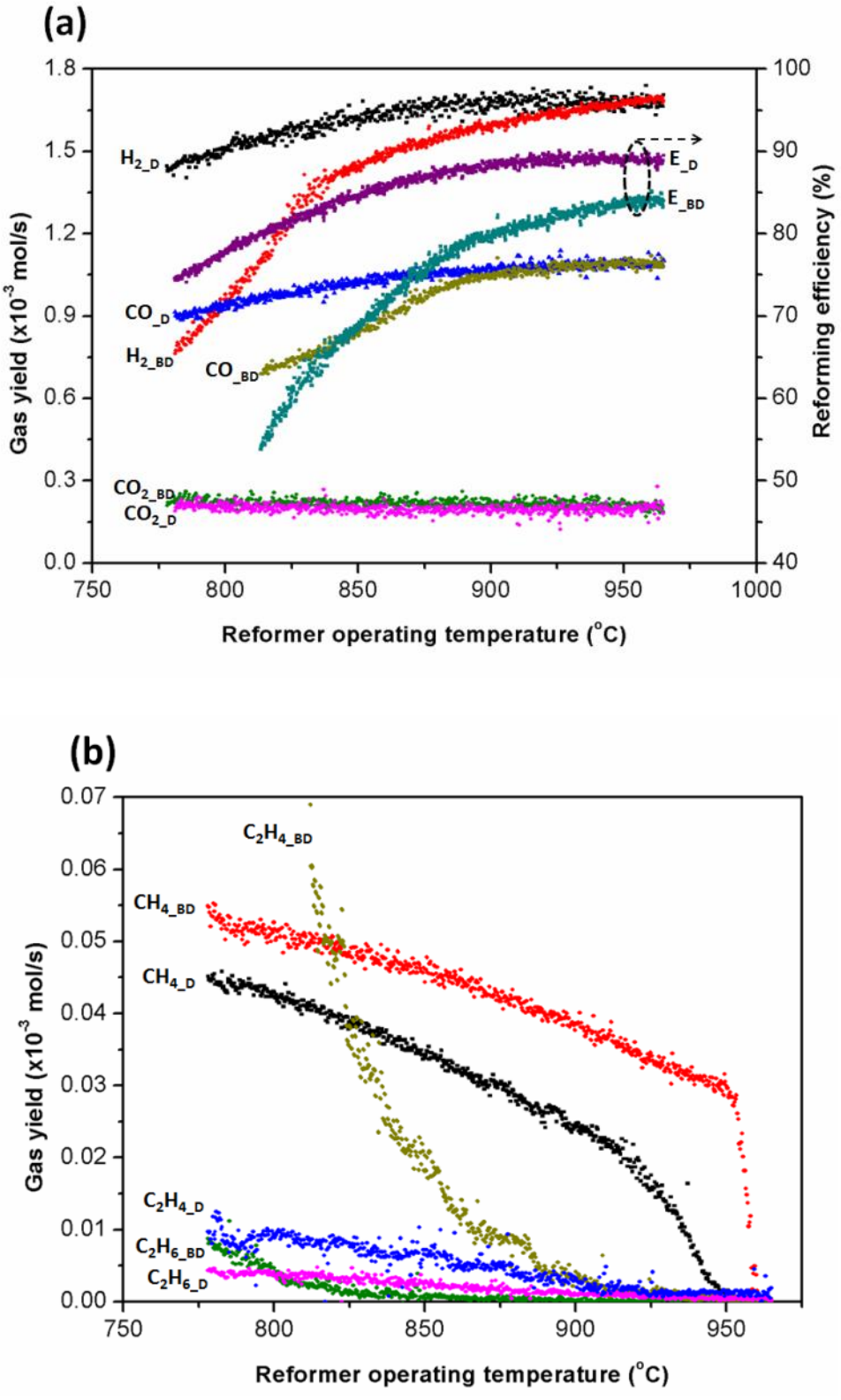

Figure 35: Effect of reformer temperature in diesel and biodiesel ATR on (a) reforming efficiency and gas yields of H_2, CO, CO_2, and (b) gas yields of CH_4, C_2H_4, C_2H_6

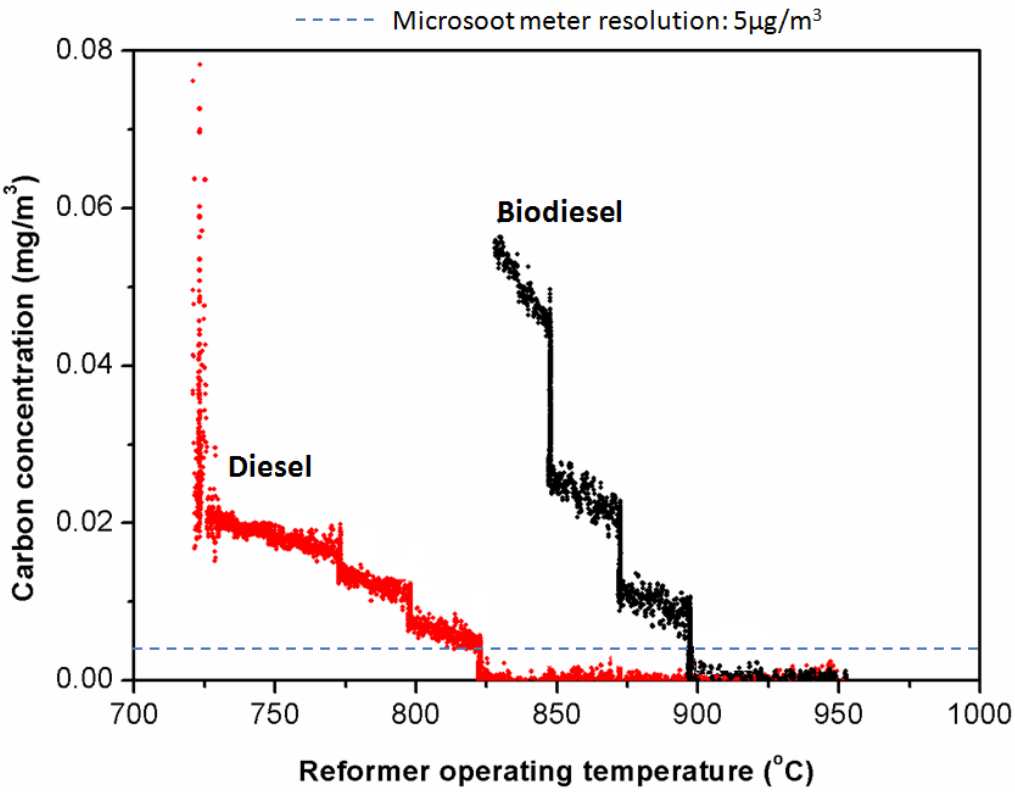

Figure 36: Effects of reformer temperature in diesel and biodiesel ATR on solid carbon formation

the effects of the reformer temperature on the gas composition and reforming efficiency for diesel and biodiesel ATR, and Figure 36 shows the carbon concentration changes with the reduction of reformer temperature. As the reformer temperature is reduced, the magnitudes of H_2 and CO reduction for diesel ATR are less than those for biodiesel ATR, which may be due to the high molecular weights of hydrocarbon compounds in biodiesel fuel, and thus biodiesel ATR being more sensitive to the reforming temperature. After reaching the threshold temperatures to form solid carbon (825°C for diesel, 900°C for biodiesel), reformate production significantly declines whereas ethylene and methane dramatically increase, especially for biodiesel ATR. CO_2 concentration is largely

independent of the reformer temperature. When combining Figure 35 with Figure 36, it is seen that C_2H_4 and solid carbon concentration for the reformation of each fuel not only have a similar pattern as a function of reformer temperature, but they also both have similar instantaneous changes below the same threshold temperatures (i.e., C_2H_4 production rate rapidly increases when solid carbon starts to form). These results confirm the consistency of the experimental data acquisition from mass spectrometer and the micro-soot meter, and emphasize the strong correlation between ethylene and solid carbon formation. The critical temperatures to form solid carbon are generally consistent with the results of the equilibrium model (see in Figure 28).

Parametric Variation: Gas Hourly Space Velocity

By gradually adjusting the nitrogen flow rate and keeping other variables constant at the initial test point, the single-tube reformer enabled evaluating the impacts of GHSV at STP changes from 30,500 to 53,000 hr^{-1}. Figure 37 illustrates the changes of gas composition and reforming efficiency for both diesel and biodiesel ATR with different GHSV test points. With low GHSV (low nitrogen carrier gas flow), unstable chemical reactions occurred and it affected the consistent production of reformates. Figure 38 illustrates the effect of GHSV on carbon formation and it suggests that biodiesel ATR has a relatively narrow range of GHSV (below 44,000 hr^{-1}) to achieve stable carbon-free performances, as compared to diesel ATR (below 48,500 hr^{-1}). High GHSV accelerates the carbon formation with volatile carbon activities and may result in hydrocarbon fuel breakthrough in the reactor [14]. Increasing the residence time of the reactants in contact with the catalyst bed would enhance the complete conversion of the fuels and improve

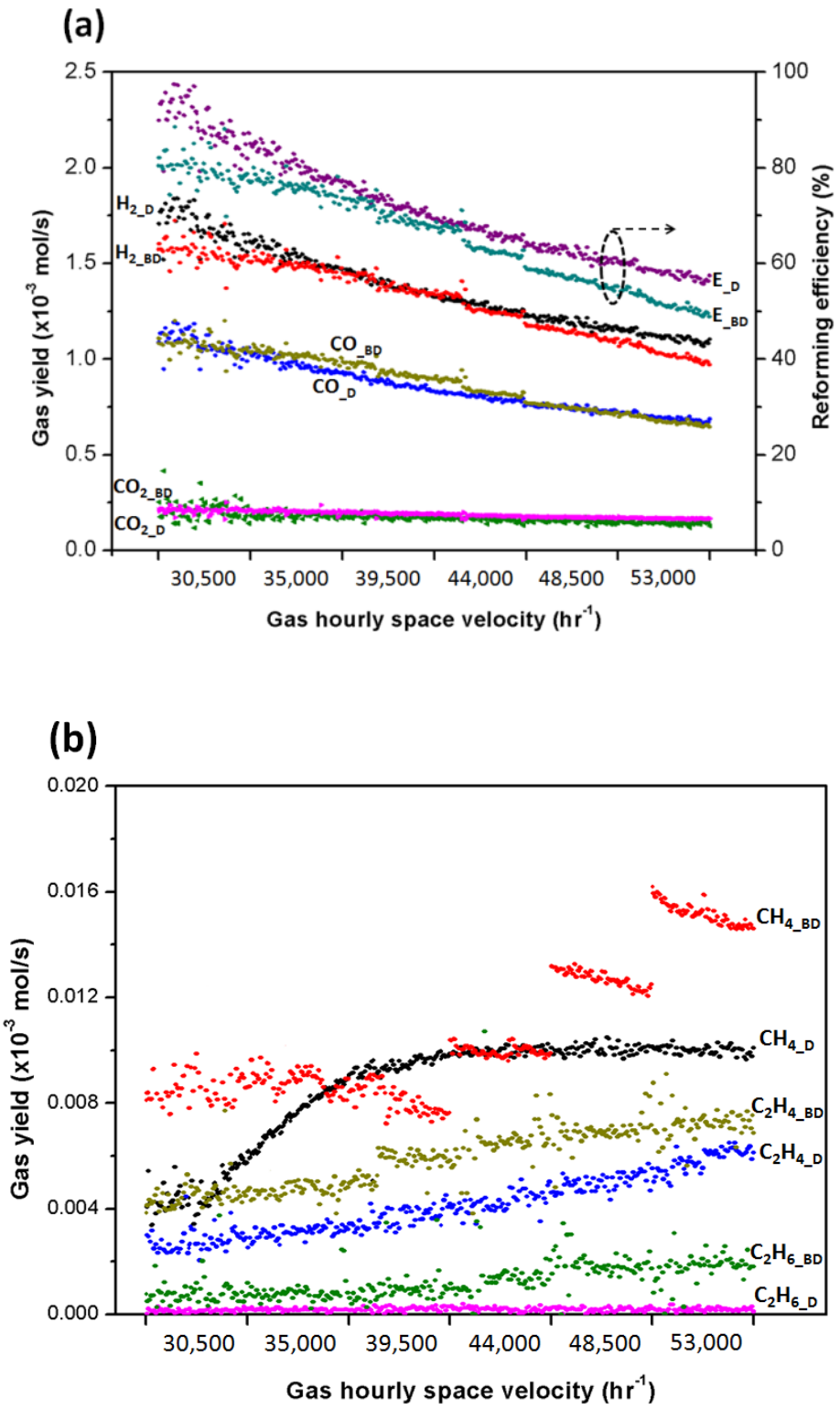

Figure 37: Effect of GHSV in diesel and biodiesel ATR on (a) reforming efficiency and gas yields of H_2, CO, CO_2, and (b) gas yields of CH_4, C_2H_4, C_2H_6

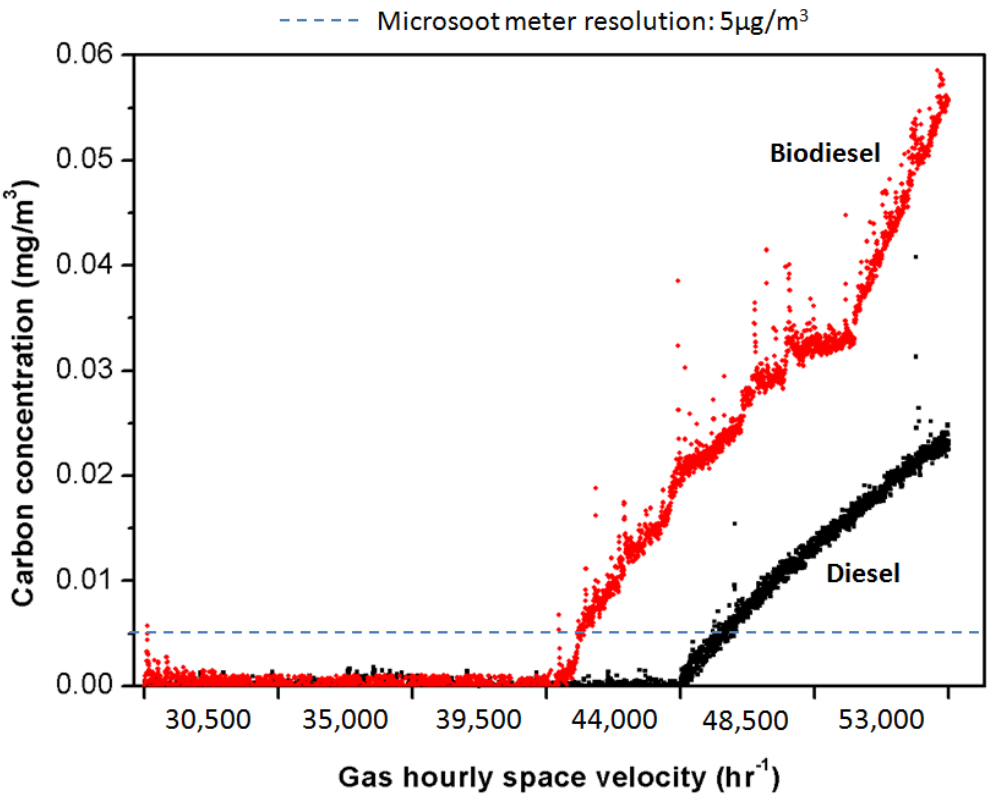

Figure 38: Effects of GHSV in diesel and biodiesel ATR on solid carbon formation

the reforming performance, especially for olefins and aromatics [159,160]. Berry *et al.* [159] developed a reaction kinetics based model to analyze the effects of GHSV and operating temperature on the reformation of three types of hydrocarbon fuels (n-tetradecane, 1-methylnaphthalene, and decalin) and suggested a series of olefins (e.g., alkenes, dienes, trienes, and alkynes) would be promoted under high space velocities. Figure 37 shows that H_2 and CO concentrations both declined with increase of GHSV and the light hydrocarbon gas concentrations increased as well, which are consistent with the results reported by Berry *et al.*

Parametric Variation: Water Flow

In order to cover a representative range of H_2O/C and evaluate its impacts on the fuel reformation, the amount of the input water was increased from its initial condition $H_2O/C = 0.6$ to $H_2O/C = 1.0$ and the total O/C was kept same at the initial test condition (1.47) by simultaneously reducing the input air input flow (see in Table 11). Then water was gradually reduced with other variables (O_2/C, GHSV, and reformer temperature) kept constant to investigate the effects of H_2O/C on diesel and biodiesel ATR. Under these conditions of varying water input, gas compositions and reforming efficiency of diesel ATR behave differently from those of biodiesel ATR (Figure 39). For example, with the increments of H_2O/C, H_2 yield of biodiesel ATR was first increased and then decreased because the temperature of the front end of the catalyst bed (TC1) for biodiesel ATR was reduced to 805^oC with $H_2O/C = 1.0$ and it reduced the fuel conversion. Conversely, the amount of H_2 produced by diesel ATR (TC1 = 865^oC when $H_2O/C = 1$) was continuously increased with the increase of H_2O/C. Water increment enabled suppressing light hydrocarbons either for diesel ATR or biodiesel ATR (Figure 39b). The water gas shift reaction was promoted as the input water increases, which led to the increase of CO_2 and the reduction of CO [161].

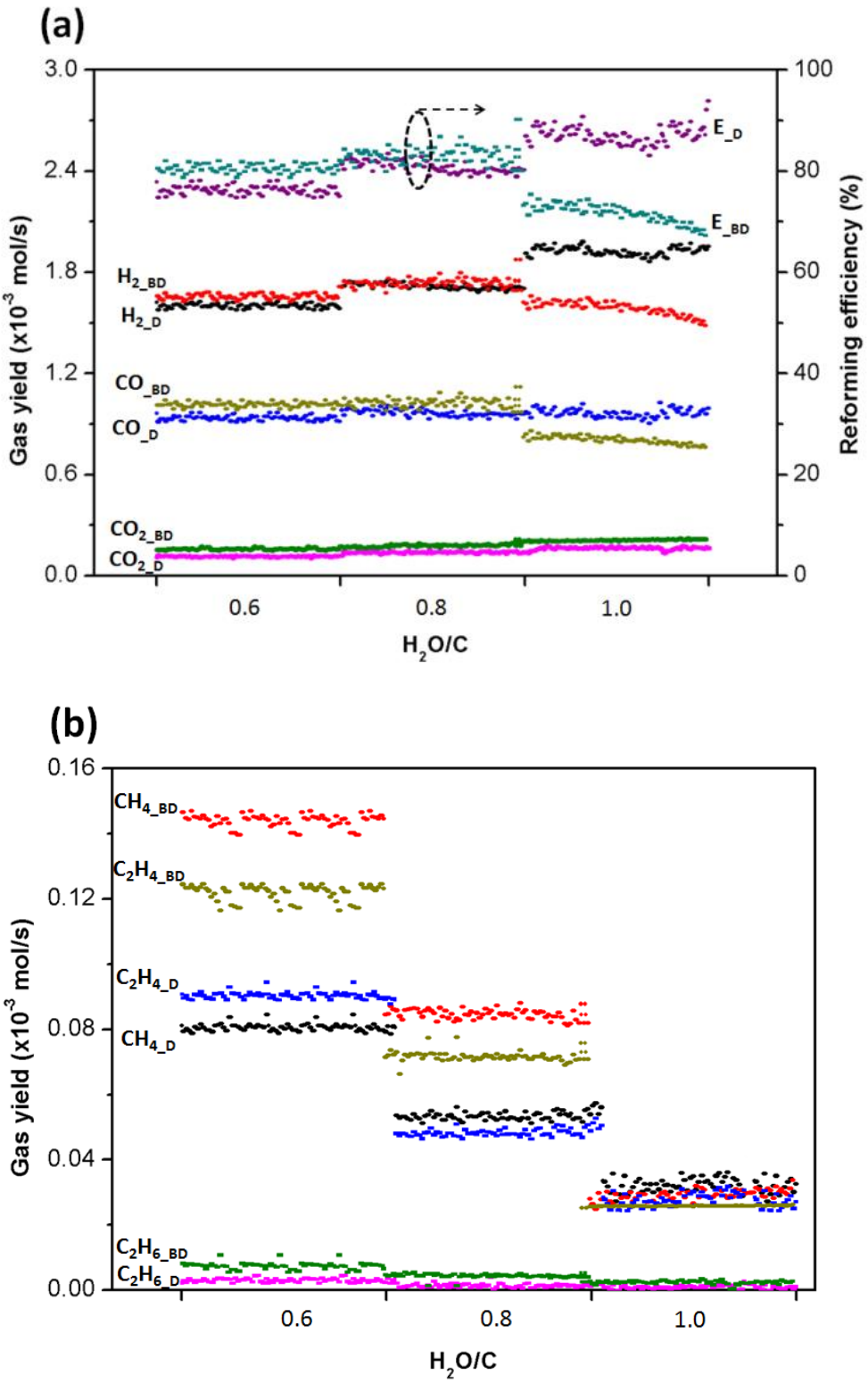

Figure 39: Effect of water in diesel and biodiesel ATR on (a) reforming efficiency and gas yields of H_2, CO, CO_2, and (b) gas yields of CH_4, C_2H_4, C_2H_6

Routes of Carbon Formation

Even though it is challenging to model all the complicated chemical reactions of the heavier hydrocarbon fuels in the reforming system due to their complex constituents (olefins, paraffins, and aromatics), the routes to form solid carbon at high temperature can be determined by analyzing the gas composition as operating conditions change [151]. Several key chemical reactions facilitated at high temperatures to form carbon include Boudouard reaction, light hydrocarbons (C1~C4) thermal decomposition, reverse gasification, and medium hydrocarbon (C5~C8) cracking [14,147,150,159]. Table 13 summaries the tendencies of three criteria (H_2/CO, CO_2/CO, and $H_2/(CO+CO_2)$) proposed by Ahmed *et al.* [151] and identifies the main routes of carbon formation. Methane and ethylene decomposition serve as the major contributors to the formation of carbon with air reduction while Boudouard reaction dominates the carbon activity with reformer temperature reduction. Because biodiesel ATR has unstable chemical reactions occurring at low GHSV and potential for fuel breakthrough with high GHSV, only the pertinent GHSV range from 30,500 to 39,500 hr^{-1} enables achieving high fuel conversion, thus the main route for carbon evolution in term of GHSV changes is due to hydrocarbon fuel cracking. As the input water reduces, the reverse water gas shift reaction is facilitated, which consequently promotes the reverse reaction of gasification to form solid carbon. Also, due to the relatively low temperature at the front end of the catalyst bed, significant amounts of light hydrocarbon gases remain in the effluent and may decompose to form solid carbonate residues.

Table 13. Main routes of carbon formation under each set of key parameter changes

	Fuel	**Air reduction**	**Temperature reduction**	**GHSV increase**	**Water reduction**
H_2/CO	Diesel	Increased	Reduced	Constant	Reduced
	Biodiesel	Increased	Reduced	Reduced, increased, reduced	Reduced
CO_2/CO	Diesel	Constant	Increased	Increased	Reduced
	Biodiesel	Constant	Increased	Increased	Reduced
H_2/(CO+CO_2)	Diesel	Increased	Reduced	Reduced	Reduced
	Biodiesel	Increased	Reduced	Reduced, constant, reduced	Reduced
Main routes of carbon formation		Methane, ethylene decomposition	Boudouard reaction	Light/medium hydrocarbon fuel cracking	Light hydrocarbon gases decomposition , reverse gasification

4.2.5. Summary

Biodiesel derived from waste feedstock is considered a promising alternative fuel for transportation applications and solid oxide fuel cell based auxiliary power units. In this study, biodiesel ATR was investigated under different operating conditions (H_2O/C, O_2/C, GHSV, and reformer temperature), based upon both experimental tests and equilibrium analysis to evaluate the carbon formation boundary and effluent gas composition, with a baseline of diesel ATR. Thermodynamic analysis based on total Gibbs free energy minimization was applied to model the behavior of effluent species under the changing environments in the reactor and extrapolate the practical conditions with the pertinent combinations of H_2O/C and O_2/C to mitigate carbon formation with high hydrogen yield at temperatures ranging from 500 to 1000^{o}C. This work enabled quantification of the carbon concentration by applying an AVL micro-soot meter that

utilizes the photo-acoustic effect, and measuring the gas composition of effluents from the reactor by using a mass spectrometer. The results from the equilibrium model were generally well validated by the experimental data. This study also investigated the fundamental routes of carbon formation during diesel and biodiesel ATR and explored the correlations between carbon concentration and ethylene under each set of parameters change (O_2/C, H_2O/C, reformer temperature, and GHSV), which enabled extrapolating the formulae with polynomial regressions to model their correlations.

4.3. Biodiesel-diesel (B-diesel) Blends Autothermal Reformation

4.3.1. Introduction

Fuel catalytic reformation, a subcategory of hydrocarbon processing techniques, is considered as a promising path for hydrogen production and its potential applications have been further studied in recent years as clean energy technology developments are promoted [162]. Fuel catalytic reformation enables generating a hydrogen-rich stream from a variety of hydrocarbon feedstock ranging from methane (CH_4) to biodiesel ($C_{19}H_{35.4}O_2$) and vegetable-oil [15], and this unique advantage facilitates fuel reforming technologies to integrate with many energy conversion systems in different applications. For example, more than 95% of hydrogen in the United States is produced from methane steam reforming and predominantly used in the industrial synthesis of ammonia [163]. Hydrogen from hydrocarbon reformation serve as the main fuel for fuel cell systems (e.g., solid oxide fuel cell, proton exchange membrane fuel cell) to generate electricity in either stationary or transportation applications [164,165]. Several studies proposed to apply the on-board fuel reformer with internal combustion engine (ICE) compatible fuels

(diesel, gasoline) to recover the exhaust gas and heat from ICE and generate hydrogen, which will be fed into the engine to improve the fuel combustion efficiency and reduce the engine emissions [166-168]. Subramanian and Schmidt also suggested that biodiesel catalytic reformation could serve as an alternative path to produce both short-chain and long-chain olefins, which have considerable values in polymer and copolymer productions [169].

Even though ATR is reported as the thermally-balanced combination of SR (endothermic reaction) and POx (exothermic reaction), many studied demonstrated that POx of hydrocarbon fuel dominates only the front end of the catalyst bed within a few millimeters whereas SR takes place in the downstream section of the catalyst bed, which challenges the thermal management in the catalytic reactor [120,164]. The partial oxidation of hydrocarbon fuels without adequate mixing with the steam is prone to create local hot spots and sinter the front end of catalyst bed, which would lead to catalyst degradation and temperature shift toward downstream of the reactor [120]. Coke formation in the catalyst bed during hydrocarbon reformation has been recognized as a common contributor to catalyst degradation, because the dynamic evolution of carbon formation is difficult to detect and control [14,120]. Solid carbon particles deposited on the surface of the catalyst directly decays the active site of the catalyst, blocks the catalyst support pores, and disintegrates the physical support of catalyst [148,157]. Solid carbon has been identified to form in the fuel vaporization step and the hydrocarbon catalytic reformation process [126,160]. Prior to entering the reformer, the liquid hydrocarbon fuel (especially heavy hydrocarbons such as diesel, JP8, biodiesel) needs to be well mixed

with the oxidants (air/water) in its vaporization step to prevent fuel pyrolysis in fuel-rich region to form solid carbons and avoid unwanted fuel combustion in fuel-lean region [119]. Many fuel atomization techniques were developed to finely break down the droplet size of the hydrocarbon fuel and homogenously mix with oxidants (e.g., ultrasonic injector [119], twin fluid nozzle [157]). Section 4.12 describes the customized nozzle used to atomize hydrocarbon fuel (below 35 μm droplet size) based on micro-explosion behavior of the emulsified fuel, and it not only is compatible with a board spectrum of liquid hydrocarbons, but also avoids local pressure buildup in the upstream of the reformer and prevents strong gas flow recirculation around the nozzle with coke deposition [119]. Another region for solid carbon formation is within the catalyst bed of the reactor, which has been intensively reported in numerous studies [15,169,157]. Both experimental tests and thermodynamic modeling of fuel reformation with different reforming techniques have been investigated to determine the practical reformer operating conditions (e.g., reformer temperature, H_2O/C, O_2/C, and GHSV) to prevent carbon formation in the catalyst bed for specific hydrocarbon fuels (such as methane [170], ethanol [171], propane [172], diesel [14], biodiesel [164]). However, most of these studies specifically focused on analyzing the reactor after the reformation was completed by applying some analytical techniques such as temperature programmed oxidation (TPO) [157], transmission electron microscopy (TEM) [173], X-ray photoelectron spectroscopy [172], or thermal gravimetric analysis (TGA) [174], rather than evaluating the in-situ carbon formation under changing environments in the reformer. From a practical standpoint, the catalytic reformer should be well integrated in the energy system and aimed to continue operating for a long-period of time, so it is necessary to develop

in-situ monitoring techniques to prevent carbon formation and identify the optimum operating environment for hydrocarbon fuel reformation.

Biodiesel has been gradually introduced into the transportation sector and blended with petro-diesel for use in diesel engine combustion. Biodiesel improves the lubricity of the blended fuel and reduces the engine emissions of CO and particulate matter [175]. Furthermore, biodiesel possesses physical and chemical properties similar to diesel and thus it is compatible with conventional fueling infrastructures and fuel delivery paths [5]. With less or no sulfur and aromatic species contained in the fuel, biodiesel is also considered a promising candidate for fuel reformation to produce syngas used in the SOFC-APU system to supply on-board electrical power in vehicles and trucks [157]. The typical composition of biodiesel derived from soy oil consist of methyl palmitate (12%), methyl stearate (5%), metyl oleate (25%), methyl linoleate (52%), and methyl linolenate (5%) [169]. There are a few reports available in the open literature describing the reformation of biodiesel fuel [176-178]. For example, Nahar and Kendall [177] applied thermodynamic analysis based on total Gibbs free energy minimization to model biodiesel ATR under various operating conditions (water input, air input, and reformer temperature) and suggested that methane selectivity from the reformates reduces as the unsaturated esters in biodiesel increase, as coke selectivity increases as the esters increase (either saturation or unsaturation). However, most of these works do not provide a comprehensive study of biodiesel reformation (both from experimental tests and thermodynamic modeling), nor do they and compare the reforming performances of biodiesel and conventional diesel. Therefore, Section 4.2 focused on analyzing biodiesel

and diesel ATR under various operating environments (H_2O/C, O_2/C, GHSV, and reformer temperature) and identified the carbon formation boundaries for these two fuels as well as the optimum operation conditions to achieve high yield of syngas production. This section focuses on further evaluating the reformation of diesel blended with various proportions of biodiesel (B-diesel), which include B5 (5% of biodiesel blended with 95% of diesel, volumetric), B10, B20, B40, and B80.

Table 14. Specifications of B-diesel with various biodiesel contents

Fuel type	**Molecular formula**	**Density (g/cm^3) @25°C**[a]	**Sulfur content (ppmw)**[a]	**Aromatic content (vol.%)**[a]	**Kinematic viscosity (cSt) @40°C**[b]	**Lower heating value (MJ/kg)**	**Boiling point at 1 bar (°C)**
Diesel	$C_{15.5}H_{28}$	0.828	8.8	31.8	2.64	42.6	180~290
B5	4% $C_{19}H_{35.4}O_2$ + 96% $C_{15.5}H_{28}$	0.831	8.7	30.7	2.73	42.3	180~350
B10	8% $C_{19}H_{35.4}O_2$ + 92% $C_{15.5}H_{28}$	0.833	8.6	29.6	2.82	42.1	180~350
B20	16% $C_{19}H_{35.4}O_2$ + 84% $C_{15.5}H_{28}$	0.839	8.4	27.5	3.02	41.5	180~350
B40	34% $C_{19}H_{35.4}O_2$ + 66% $C_{15.5}H_{28}$	0.851	8.1	23.1	3.44	40.4	180~350
B80	75% $C_{19}H_{35.4}O_2$ + 25% $C_{15.5}H_{28}$	0.873	7.4	14.5	4.51	38.3	180~350
B100	$C_{19}H_{35.4}O_2$	0.885	7.1	10.2	5.15	37.2	315~350

[a] B-diesel specifications were based on the Kay's mixing rule (volumetric), [b] B-diesel specifications were based on the Semilogarithmic mixing rule

The objective of this work is to analyze the ATR performances of diesel blended with different proportions of biodiesel (B5, B10, B20, B40, and B80) using a single-tube reactor with rhodium/ceria-zirconia catalyst wash-coated ceramic monoliths for SOFC-based APUs applications. For comparison purpose, ATR reforming of pure biodiesel

(B100) and pure diesel were conducted under the same operating conditions as B-diesel with the goal of achieving a consistent syngas production rate. Table 15 provides the specifications of these studied fuels and the properties of B-diesel blends were predicted with the mixing rules described in Chapter 3. The initial reformation condition of these fuels was set as total O/C = 1.47, H_2O/C = 0.6, and GHSV = 33,950 hr^{-1} at 950^oC reformer temperature. The impacts of air reduction and reformer temperature reduction on effluents species from the reformer were investigated for the ATR of these seven studied fuels, and the carbon formation boundary for each type of fuel was identified. A direct photo-acoustic based micro-soot meter was used for in-situ measurement of carbon concentration in the reactor effluent under different conditions, while a mass spectrometry was applied to measure the composition of gas reformates. This work also explored the correlations between carbon concentration and ethylene (a key precursor to form solid carbon) associated with the changes of air flow and reformer temperature for the ATR of B-diesels with various biodiesel contents.

4.3.2. Experimental apparatus and test plans

A detailed description of the single-tube catalytic reformer was provided in Figure 18. Absolute pressure gauges were used to monitor the differential pressure in the reactor, which provided an indication of excessive carbon buildup in the reactor. Input water and fuel were measured with weighing scales and continuously pumped into the reformer, while air and nitrogen were measured with mass flow controllers (MFC). Nitrogen served as a carrier of the liquid fuel and it was also used to adjust the system GHSV during the tests. Prior to entering the reformer, hydrocarbon fuel needed to be vaporized and well

mixed with the oxidants (air/steam) to mitigate fuel thermal pyrolysis and hot spot occurrences. For heavy hydrocarbons (e.g., diesel, biodiesel), however, it is challenging to vaporize the fuel without pyrolysis due to their wide range of high boiling points and flow pulsation resulting from high viscosity (see in Table 15). There are two types of pretreatment techniques commonly applied in many studies, which include isolated vaporization (i.e., liquid fuel is vaporized with an external heating element prior to blending with air) and direct vaporization (liquid fuel is directly introduced into hot air and the exothermic oxidation of hydrocarbon further increases the temperature) [179]. Although the direct vaporization approach simplifies the system setup, it increases the risk of fuel ignition and hot spots in the upstream of the reactor [120]. Superheated steam has been employed as an atomizing gas in the fuel nozzle to vaporize liquid hydrocarbon followed by air mixing (an isolated vaporization method) and it not only effectively suppressed the formation of carbon deposits in the mixing chamber, but also enhanced the homogeneity of thermal distribution [179]. Therefore, the current work adopted the approach of using superheated steam to facilitate hydrocarbon vaporization in the customized nozzle described in Section 4.1.2. The AVL micro-soot meter was applied to directly measure the carbon concentration in the reformate stream and the mass spectrometer was used to analyze the gas compositions of effluents from the reformer.

The equilibrium yields of syngas from reforming diesel, biodiesel or B-diesel can be derived from thermodynamic analysis using total Gibbs free energy minimization method (as described in Section 4.2.2). Thus, the required flow rates of B-diesel with various biodiesel contents can be determined in order to produce same reformate

production rate under the same operating conditions (total O/C, H_2O/C, GHSV, and reformer temperature). Table 16 provides the initial operating condition of the ATR of diesel, B-diesel, and biodiesel with the target of generating a 0.00275 mol/s syngas production rate at 950^oC reformer temperature (average of TC1~TC5, Figure 18). Approximately 14% more biodiesel is required than diesel on a volumetric basis (mL/s), while 12% less biodiesel than diesel is required on a molar basis (mol/s) to achieve the same syngas production rate. H_2O/C and total O/C were kept as 0.6 and 1.47, respectively for the ATR of all studied fuels. Because there is a certain fraction of oxygen content in biodiesel (O/C = 0.105) and O/C in B-diesel is different depending on biodiesel fraction in each blends, O_2/C was varied in different blends to maintain a constant total O/C. Input nitrogen flow (N_2/C) was also varied to achieve an approximately constant GHSV of 33,950 hr^{-1} at standard temperature and pressure (STP) condition. Temperature profiles of the reformer and compositions of gas effluents were monitored at these initial test points for the ATR of these seven studied fuels.

Table 15. Initial operating condition for B-diesel ATR with various biodiesel contents

Fuel type	Input fuel flow rate			H/C in fuel	O/C in fuel	O_2/C	H_2O/C	Total O/C	N_2/C	GHSV @ STP (hr^{-1})	Theoretical syngas yield (10^{-3}×mol/s) @ 950 ^oC[b]
	g/s	mL/s	mol/s ×10^{-3}								
Diesel	0.0188	0.0227	0.088	1.806	0	0.435	0.6	1.47	3.968	33,940	2.75
B5	0.0196	0.0236	0.091	1.808	0.004	0.433	0.6	1.47	3.795	33,951	2.75
B10	0.0207	0.0248	0.094	1.811	0.008	0.431	0.6	1.47	3.563	33,950	2.75
B20	0.0214	0.0255	0.095	1.815	0.016	0.427	0.6	1.47	3.464	33,943	2.75
B40	0.0217	0.0255	0.089	1.825	0.035	0.417	0.6	1.47	3.539	33,963	2.75
B80	0.0223	0.0256	0.081	1.849	0.079	0.395	0.6	1.47	3.643	33,954	2.75
B100	0.0229	0.0259	0.077	1.863	0.105	0.382	0.6	1.47	3.649	33,963	2.75

In order to identify the carbon formation boundaries of B-diesel ATR and analyze the reforming performances (e.g., effluent gas composition, reforming efficiency) with the effects of air and reformer temperature, two sets of experimental tests were designed and conducted as follows: (a) keeping other key parameters (H_2O/C, furnace controller temperature, and GHSV) constant, total O/C was reduced from the initial test condition of 1.47 to 1.09 by gradually reducing the input air flow. To avoid irreversible catalyst degradation from carbon deposition over a long period of time, further air reduction ceased when significant effluent carbon concentration was detected by the AVL micro-soot meter. Nitrogen flow rate was increased to offset the reduced air in order to keep GHSV same as the initial condition. (b) Because the single-tube reformer was entirely contained within the electrically heated tube furnace, the operating temperature of the reformer (average of TC1~TC5) could be controlled by adjusting the set point of the furnace temperature. With the initial furnace temperature at 1000^{o}C, the reformer temperature reached about 950^{o}C (±2.5^{o}C) for the ATR of each type of fuel (diesel, B5, B10, B20, B40, B80, and B100). The reformer temperature was reduced by adjusting the temperature controller of the furnace from 1000 to 750^{o}C with a 0.1^{o}C/s reduction rate while other system inputs were kept constant.

After each set of experimental tests, the sample chamber windows of the micro-soot meter were cleaned and various filters were replaced to prevent instrument contamination and ensure the accuracy of the measurement. Methane partial oxidation with O_2/C = 0.65 at 950^{o}C reformer temperature was conducted in the single-tube reactor for solid carbon removal and catalyst regeneration. The micro-soot meter was used to

sample the reformate effluent under methane partial oxidations which were confirmed to be well outside of the carbon formation regime. The meter was then calibrated to establish the zero baseline for the next experimental sequence.

4.3.3. Results and discussion

Initial Condition

Table 17 provides the gas yields of the experimental test points for the ATR of diesel, B-diesel, and biodiesel under the initial operating condition of total O/C =1.47, H_2O/C = 0.6, and GHSV = 33,950 hr^{-1} at 950^oC reformer temperature. The experimental syngas yields in the ATR of seven studied fuels were all higher than their equilibrium yield (0.00275 mol/s, Table 16), which may be because the thermodynamic modeling method (non- stoichiometric) applied in this study does not include several system variables (e.g., thermal gradient, space velocity, and heat loss), which affect hydrogen production rate in the reactor [180]. However, since the differences between the actual production rates of syngas and the theoretical syngas yield are within 2.5% and the derivations of experimental syngas yields of all studied fuels are within ±0.8%, it is reasonable to consider the ATR of diesel, B-diesel, and biodiesel overall achieving the same syngas production rate under the initial operating condition. The intensity of the microphone signal from the micro-soot meter shows the carbon concentration below 5 $\mu g/m^3$ during these test points, indicating there is no detectable solid carbon formed under the initial conditions for the ATR of these fuels. Relatively low or undetectable amounts of C_2H_4 and C_2H_6 also confirm the initial test points are within the carbon-free boundary.

Figure 40 illustrates the reforming efficiency (defined as Eq.(25)) and the selectivity of H_2, CO, CO_2, and CH_4 (Eq.(26) and Eq.(27)) in order to compare the ATR performances of B-diesel with various biodiesel contents under the initial condition. As biodiesel content increased, CO selectivity monotonically increased whereas CO_2 selectivity declined. This experimental phenomenon can be explained by the mechanism of autothermal reformation: ATR is the combination of POx and SR, POx occurs in the front end of the catalyst bed and consumes almost all the oxygen from air while SR dominates the remaining length of catalyst bed [15]. By keeping total O/C constant, the required oxygen from air decreases with the increment of biodiesel content because of the inherent oxygen content in the fuel itself (see in Table 16). Therefore, with less biodiesel fraction in the blends, more available oxygen from air is consumed in the POx zone and produces more H_2O and CO_2, which eventually leading to less CO selectivity due to the promotion of water gas shift reaction in the downstream of the reactor. To illustrate this effect, temperature profiles across the reactor for the ATR of all studied fuels were analyzed, as shown in Figure 41. With the same furnace temperature controller set point at 1000^oC and reactor inlet temperature at 440^oC (measured by trumpet temp thermocouple, Figure 18), the temperature at the front end of the catalyst bed (TC1) behaves differently with respect to different fuel types. TC 1 decreases with the increment of biodiesel content in the blends and TC 1 of pure diesel ATR with O_2/C = 0.435 is around 15 ^oC higher than TC 1 of pure biodiesel ATR with O_2/C = 0.382. Figure 40 also show H_2 selectivity and reforming efficiency have the similar pattern with the function of biodiesel content in the blends. For example, hydrogen selectivity and reforming efficiency significantly decreased when changing the input fuel from diesel to

B20, and both of them are slowly increased as the biodiesel content in B-diesel was further increased from B20 to B100. The opposite behavior was observed for CH_4 selectivity with a peak around B20. It is hypothesized that diesel and biodiesel are competing to consume the oxygen from air in the POx zone to break down their individual heavy hydrocarbon compounds, and diesel tends to utilize most of the oxygen from air due to its low molecular weight compounds. Therefore, as biodiesel content increases from 0% to 20%, diesel consumes larger proportions of oxygen from air in POx and only a small fraction of oxygen remained for biodiesel. Although there are significant amounts of oxygen from water and containted in the biodiesel that promote the reformation of B-diesel after POx, oxygen from air is still the preferred approach to initially reform the methyl ester functional groups in biodiesel [177]. With the increase of biodiesel content from 20% to 100%, incrementally more oxygen from air is used in its POx reaction. Figure 40 suggests diesel ATR has the highest reforming efficiency and H_2 selectivity under the initial condition and B20 ATR shows the lowest reforming efficiency and H_2 selectivity. The reformation of pure biodiesel has higher reforming efficiency than the ATR of B10, B20, B40, and B80. The competition effect in B-diesel catalytic reformation has not well understood yet and will be further studied in our future work.

Reforming efficiency, $$\eta = \frac{LHV_{H_2} * H_2 + LHV_{CO} * CO}{LHV_{fuel} * Fuel} \quad (25)$$

$$H_2\_selectivity = \frac{2 * n_{H_2}}{2 * n_{H_2O} + N_H * n_{fuel}} \quad (26)$$

$$CO, CO_2, CH_4\_selectivity = \frac{n_i}{N_C * n_{fuel}} \quad (27)$$

where LHV refers to the lower heating value; n_{H_2} and n_{fuel} are the molar yield of H_2 and molar flow rate of input fuel, respectively; n_i is the molar yield of CO, CO_2, or CH_4; N_H and N_C are molar contents of H and C in the fuel.

Table 16. Effluent gas production from ATR of seven studied fuels under initial condition

Fuel type	Effluent reformate production rate ($\times 10^{-3}$mol/s)							
	N_2	H_2	CO	CO_2	CH_4	C_2H_4	C_2H_6	Syngas
Diesel	5.413	1.706	1.103	0.212	0.014	0.002	Undetectable	2.809
B5	5.364	1.707	1.101	0.201	0.016	0.004	Undetectable	2.808
B10	5.288	1.704	1.096	0.195	0.017	0.003	Undetectable	2.801
B20	5.255	1.704	1.075	0.189	0.018	0.004	Undetectable	2.779
B40	5.302	1.733	1.077	0.188	0.017	0.003	Undetectable	2.811
B80	5.367	1.702	1.095	0.184	0.018	0.004	0.001	2.797
B100	5.379	1.682	1.127	0.185	0.017	0.005	0.001	2.809

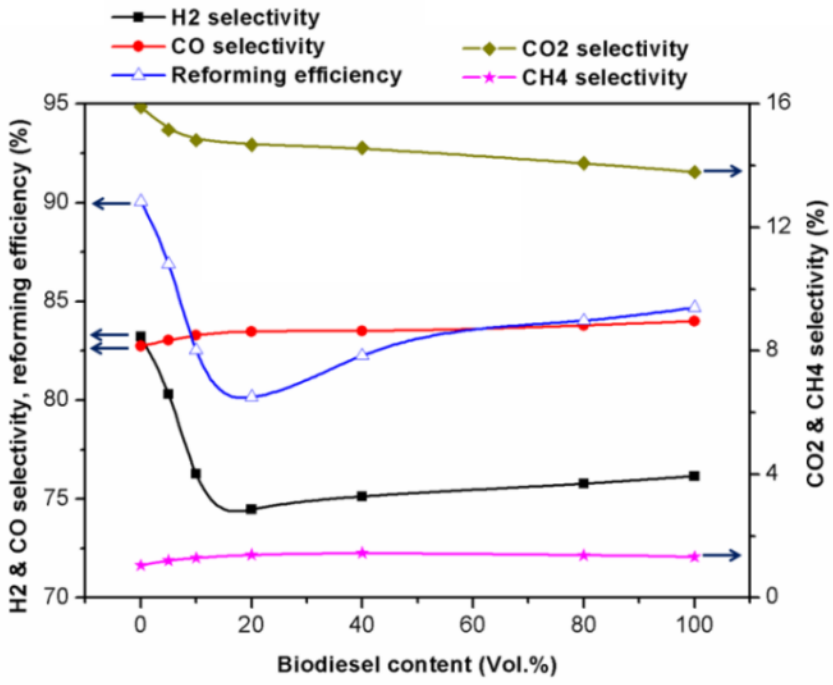

Figure 40: Selectivity of H_2, CO, CO_2, and CH_4, and reforming efficiency of B-diesel ATR under initial operating condition

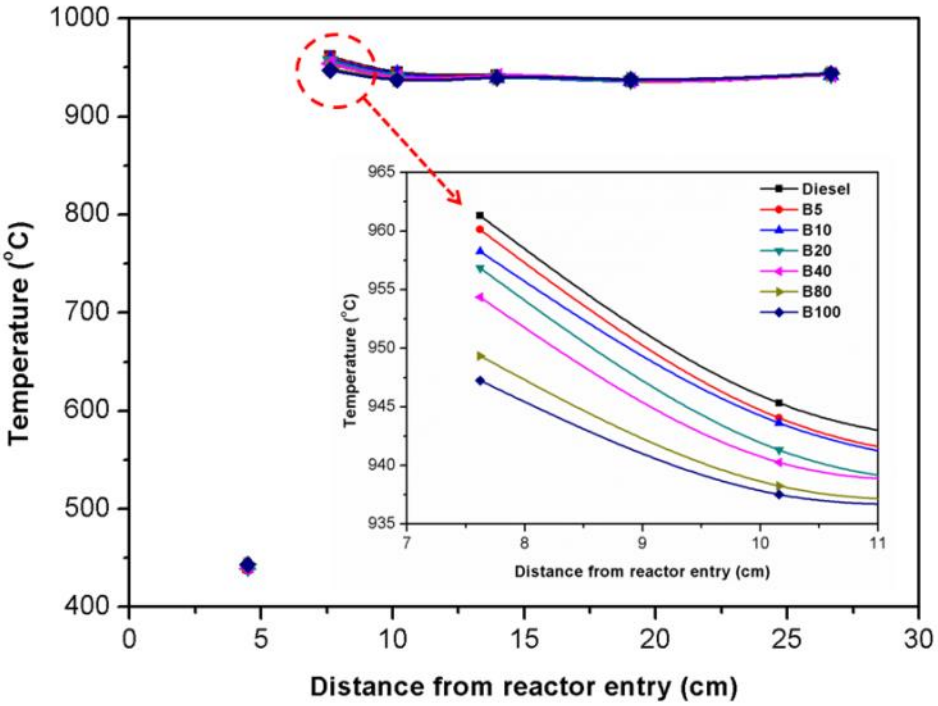

Figure 41: Detector temperature profiles for ATR of seven studied fuels under initial operating condition

Effect of Air Flow

Figure 42 illustrates the effect of air flow reduction from total O/C = 1.47 to 1.09 on the reformate production for the ATR of diesel, B-diesel, and biodiesel. Figure 42(a) suggests the peak H_2 yield of diesel ATR can be achieved around total O/C = 1.37 while H_2 production rate of biodiesel ATR monotonically declines with the reduction of air. As the biodiesel content increases in the blends, the sensitivity of hydrogen production to the air (slope of the curve) is increased, which is due to the limited air availability in B-diesel with more biodiesel content. A similar pattern was also observed for CO production with air reduction (Figure 42b) and CO yield in biodiesel ATR reduced more rapidly than that in diesel ATR. Figure 42 (c) illustrates that CH_4 production from fuel ATR increases with air reduction for all studied fuels because the effect of POx in the front end of catalyst

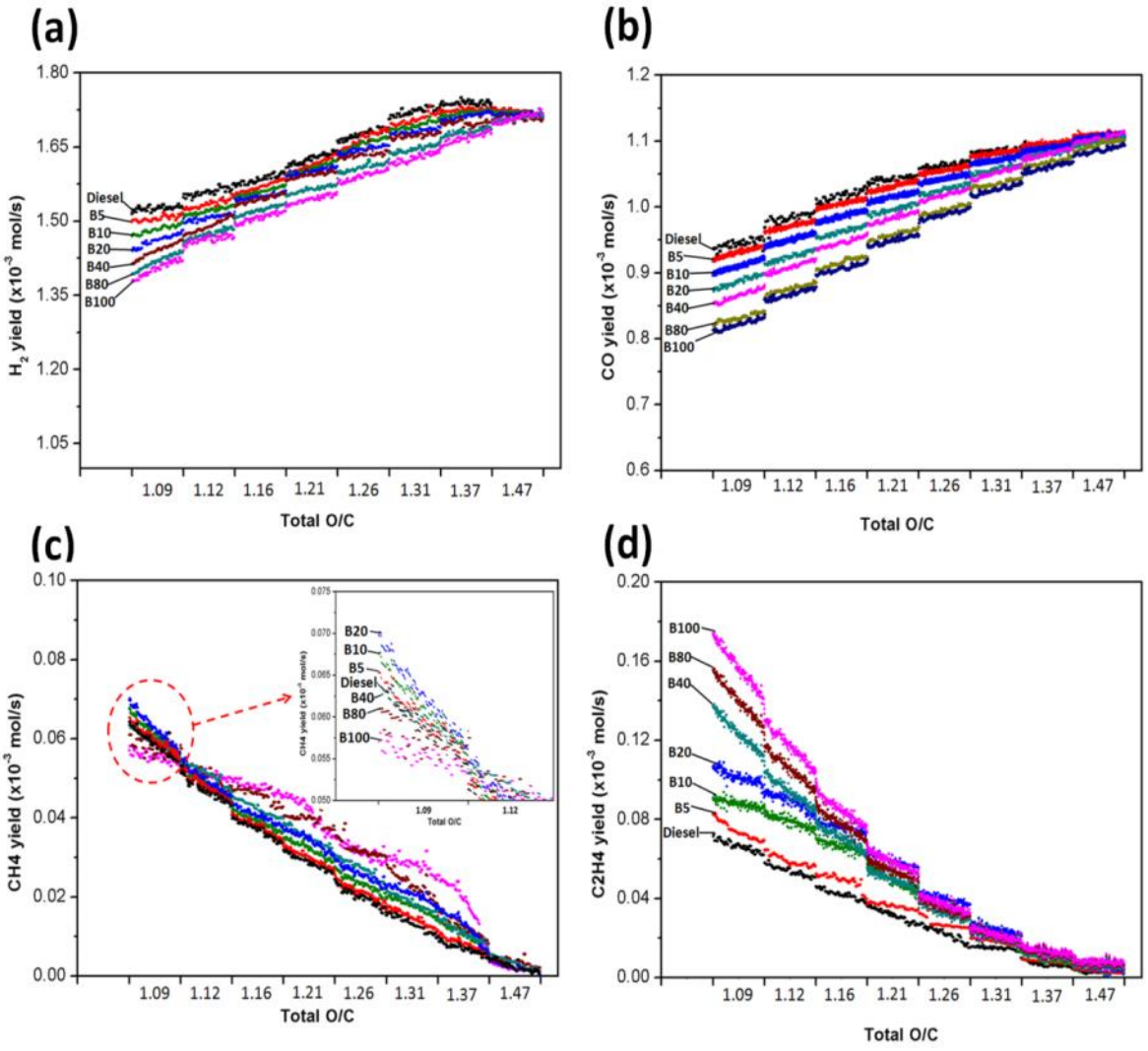

Figure 42: Effect of air flow reduction on production of (a) H_2, (b) CO, (c) CH_4, and (d) C_2H_4 for the ATR of B-diesel with various biodiesel contents

bed is reduced. With total O/C above 1.12 (diesel $O_2/C \geq 0.26$ and biodiesel $O_2/C \geq 0.21$), B-diesel with more biodiesel fraction has a higher CH_4 production because of the heavy molecular weight of hydrocarbon compounds in biodiesel, which is in agreement with several literature reports [176,177,180]. However, the route of CH_4 production changes after the total O/C is below 1.12. With the increment of biodiesel content in the blends, CH_4 production is first increased from diesel to B20 and then reduced from B20

to B100. This experimental result enhances the hypothesis proposed above to explain the behaviors of H_2 selectivity and reforming efficiency of B-diesel ATR under the initial condition (Figure 40). With limited amount of oxygen from air when total O/C is below 1.12, diesel tends to consume most of oxygen in POx (especially for B20) and only a small portion of air remains biodiesel POx, which leads to the promotion of methane production [177]. Figure 42(d) shows that C_2H_4 production is facilitated with air reduction for the ATR of all studied fuel and B-diesel with higher biodiesel blend content has the higher the production rate.

The in-situ micro-soot meter was applied to quantify the carbon concentration with the effect of air reduction from total O/C = 1.47 to 1.09 for the ATR of diesel, B-diesel and biodiesel. In order to capture the carbon formation boundaries associated with different biodiesel blends, Figure 43 displays the data with two different total O/C ranges. When combining with these carbon concentration data with the yields of effluent reformate shown in Figure 42, it is evident that syngas (H_2 + CO) production declines significantly after the reformer enters the carbon formation regime for each type of fuel, and ethylene (a major precursor to form solid carbon) is dramatically increased. For example, after entering the carbon formation regime (total O/C < 1.26), H_2 yield of biodiesel ATR dramatically reduces and C_2H_4 increase rapidly. The system resolution of the micro-soot meter (5 $\mu g/m^3$) is also included on Figure 43 and the carbon concentration value within this range is considered as zero. It is worthwhile to mention that diesel has higher aromatics content (31.8%, Table 15) than biodiesel (10.2%) and a large portion of solid carbon in biodiesel ATR is derived from ethylene whereas the

carbon formation in diesel ATR mainly comes from the combination of ethylene and aromatics [14]. Therefore, the carbon evolution for the ATR of fuel blends with less than 20% biodiesel behaves as a gradual increase with air reduction, whereas the fuels with more than 20% biodiesel display stepwise increment patterns of carbon concentration growth, which are similar to the patterns of ethylene increase shown in Figure 42(d). Figure 44 shows the carbon formation boundaries in term of total O/C for the ATR of B-diesel with various biodiesel blends (both volumetric and molar bases). The upper left region is the carbon formation region, while the lower right region is the carbon free zone. Figure 44 also highlights that B-diesel requires more air to prevent carbon formation than the combination of the individual contributors from diesel and biodiesel. For example, to ensure B50 ATR is operating within the carbon-free region, it needs total O/C above approximately 1.22, which is higher than the average of the total O/C thresholds of diesel (1.12) and biodiesel (1.26). Figure 45 illustrates the changes of reforming efficiency for the ATR of various blends in term of air reduction effect. Although the reforming efficiency for each type of fuel behaves similarly with gradual reduction of input air flow, the reduction rate tends to increase with the increment of biodiesel content. When reducing total O/C from 1.47 to 1.09 by adjusting the air flow rate, reforming efficiencies of diesel, B20, B80, and B100 declined by 12%, 17%, 20%, and 22% from their initial efficiency, respectively. Therefore, air flow change has a greater impact on the reforming efficiency of biodiesel ATR than diesel ATR, and it may be a practical approach to increase the air flow in biodiesel ATR in order to achieve a higher reforming efficiency, as highlighted by González and Pettersson [180].

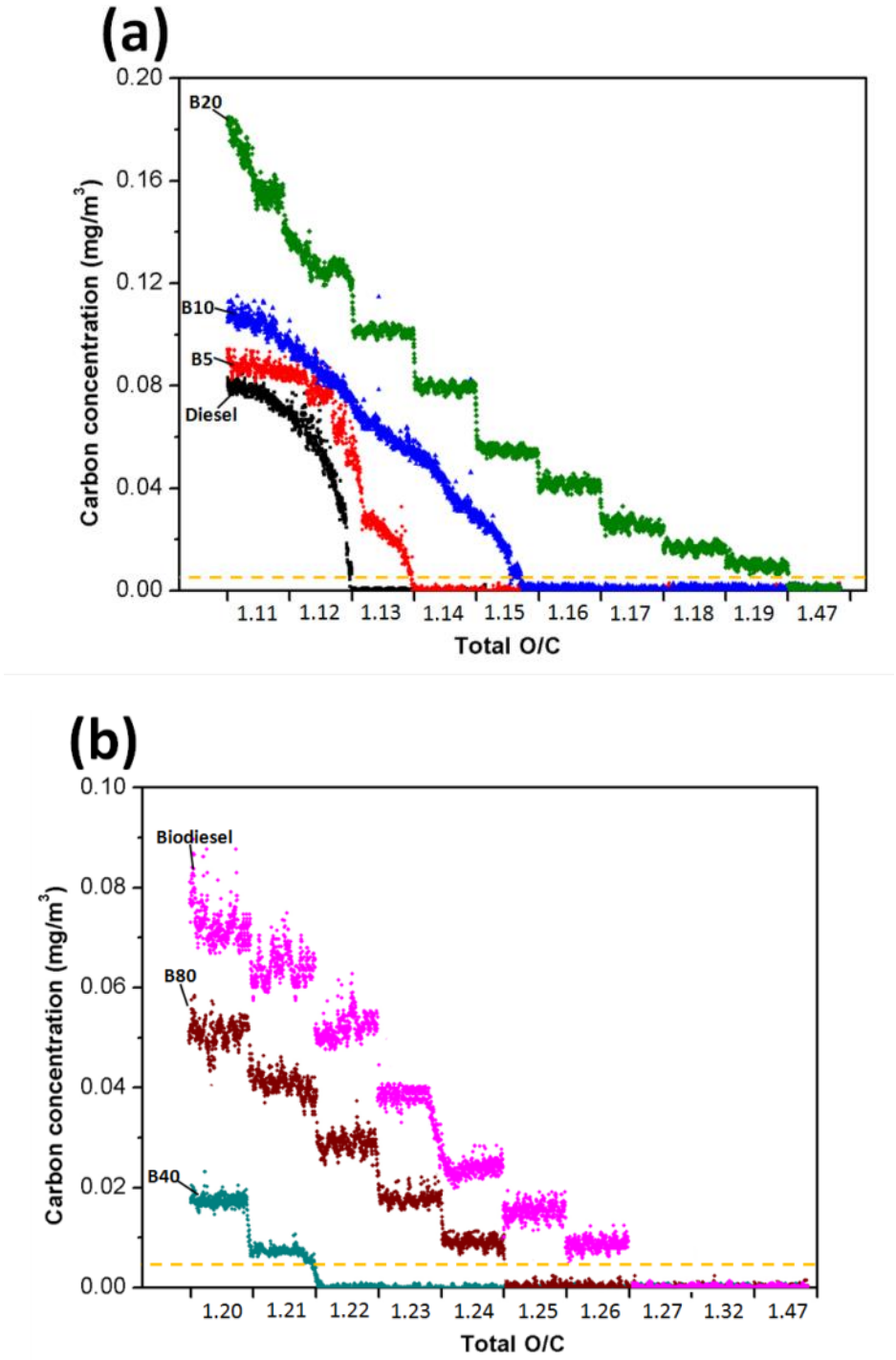

Figure 43: Effect of air reduction on solid carbon formation for the ATR of (a) diesel, B5, B10, B20, and (b) B40, B80, biodiesel

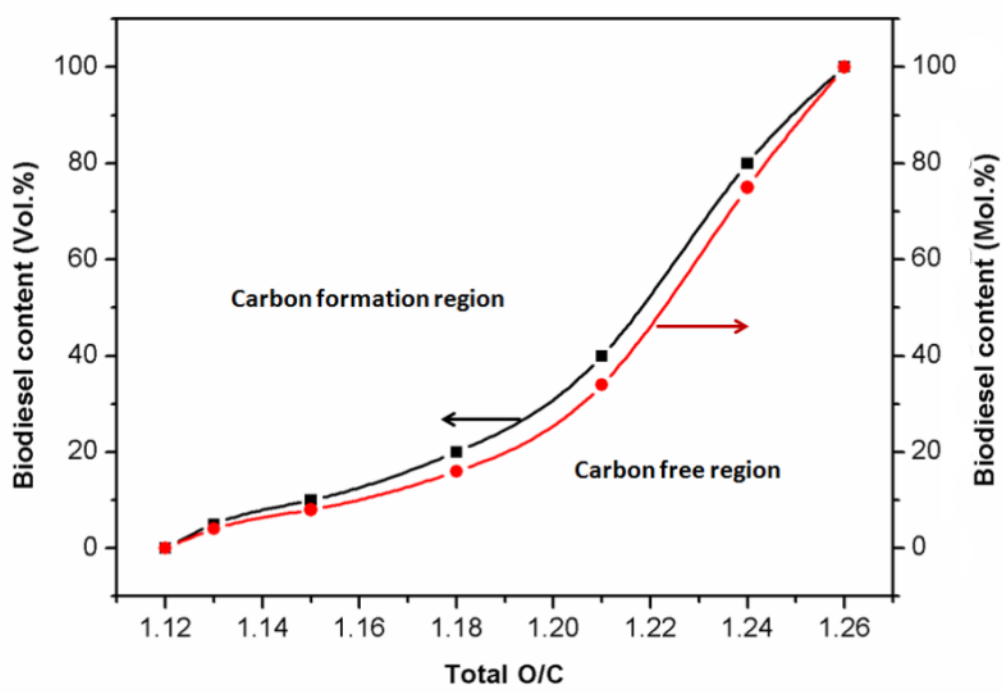

Figure 44: Carbon formation boundaries with respect to air reduction for the ATR of B-diesel with various biodiesel contents (volumetric and molar bases)

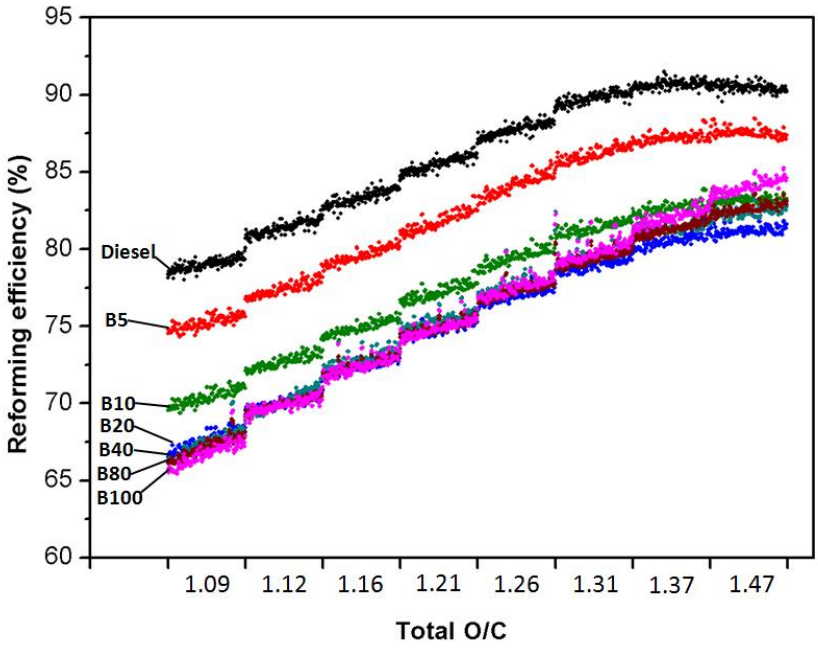

Figure 45: Effect of air reduction on reforming efficiency for the ATR of B-diesel with various biodiesel contents

Effect of Reformer Temperature

Figure 46 shows the effects of reformer temperature on the gas yields for the reformation of different B-diesel blends. As the reformer temperature is reduced from 950 ^{o}C to 770 ^{o}C, syngas production (H_2 + CO) is reduced whereas production of light hydrocarbon gases (e.g., CH_4, C_2H_4, and C_2H_6) is promoted. When combining the carbon formation profile (Figure 47) with the gas reformate composition data in Figure 46, it is apparent that CO yields of B-diesel ATR (Figure 46b) stay fairly stable until the threshold temperature to form solid carbon is reached (e.g., diesel, B10, B40, and B100 at 820, 845, 875, and 905 ^{o}C, respectively), which is because the Boudouard reaction dominates the carbon formation route within these temperature ranges and consumes CO to form CO_2 and solid carbon [148]. H_2 production (Figure 46a), however, is gradually reduced with the reduction of reformer temperature and B-diesel with high biodiesel content (B40 to B100) and displays a sharp drop at a temperature point which is about 60 ^{o}C lower than the temperature at the onset of solid carbon formation. For example, the critical reformer temperature at the onset of carbon formation for biodiesel ATR is 905 ^{o}C, but H_2 yield of biodiesel reformation starts to significantly drop when the reformer temperature is at 845 ^{o}C. Even once the reformer reaches the carbon formation boundary with temperature reduction, hydrogen production is still mainly derived from the combination of fuel catalytic reformation and thermal cracking of hydrocarbons, which explains the experimental result that there is no significant drop of H_2 yield immediately after passing the carbon formation boundary. However, with the cumulative carbon deposition on the catalyst bed and the degradation of catalyst/support structure [148], catalytic reformation of hydrocarbons to produce H_2 is diminished and reflected in the

sudden sharp-drop at the temperature 60 ^{o}C lower than the critical temperature of forming solid carbon. As the biodiesel content in B-diesel blends increases, the initial increment of CH_4 near 950 to 930 ^{o}C in fuel ATR is increased (Figure 46c) while the slope of CH_4 yield versus temperature curves fairly constant at the temperature range below 900 ^{o}C for the ATR of all studied fuels, indicating that CH_4 production from the ATR of B-diesel with various biodiesel contents behaves quite similarly at intermediate reforming temperatures. Figure 46(d) and Figure 47 show that C_2H_4 production and solid carbon concentration for the reformation of each fuel not only have a similar pattern as a function of reformer temperature, but they also both have the instantaneous changes (i.e., C_2H_4 production rate rapidly increases when solid carbon starts to form) under the same threshold temperatures. These results confirm the consistency of the experimental data acquisition from the mass spectrometry and the micro-soot meter, and emphasize the strong correlation between ethylene and solid carbon formation. Similar to the carbon evolution in the ATR of B-diesel with temperature reduction (Figure 47), C_2H_4 production has higher increment rate with more biodiesel content in B-diesel, which is due to the unsaturated hydrocarbon alkenes contained in the methyl groups of biodiesel fuel [169]. Our previous work suggested that CO_2 production is largely independent of the reformer temperature. Figure 48 identifies the carbon formation boundaries associated with temperature reduction for the ATR of B-diesel with various biodiesel blends (both volumetric and molar bases). The left upper area is the carbon formation region while the lower right area is the carbon free region. Figure 48 suggests that B-diesel requires higher reformer temperature to avoid carbon formation than the combination of the individual contributors from diesel and biodiesel, which is similar to the result derived from the

effect of air flow (shown in Figure 44). Figure 49 illustrates that the reforming efficiencies of B-diesel ATR with various biodiesel contents all declined with respect to the reduction of reformer temperature and the reformer efficiency of B-diesel with higher biodiesel content declines faster. When the reformer temperature is reduced from 950 to 810 ^{o}C, the reforming efficiencies of diesel, B10, B20, B80, and B100 are reduced by 7%, 11%, 13%, 32%, and 35%, respectively.

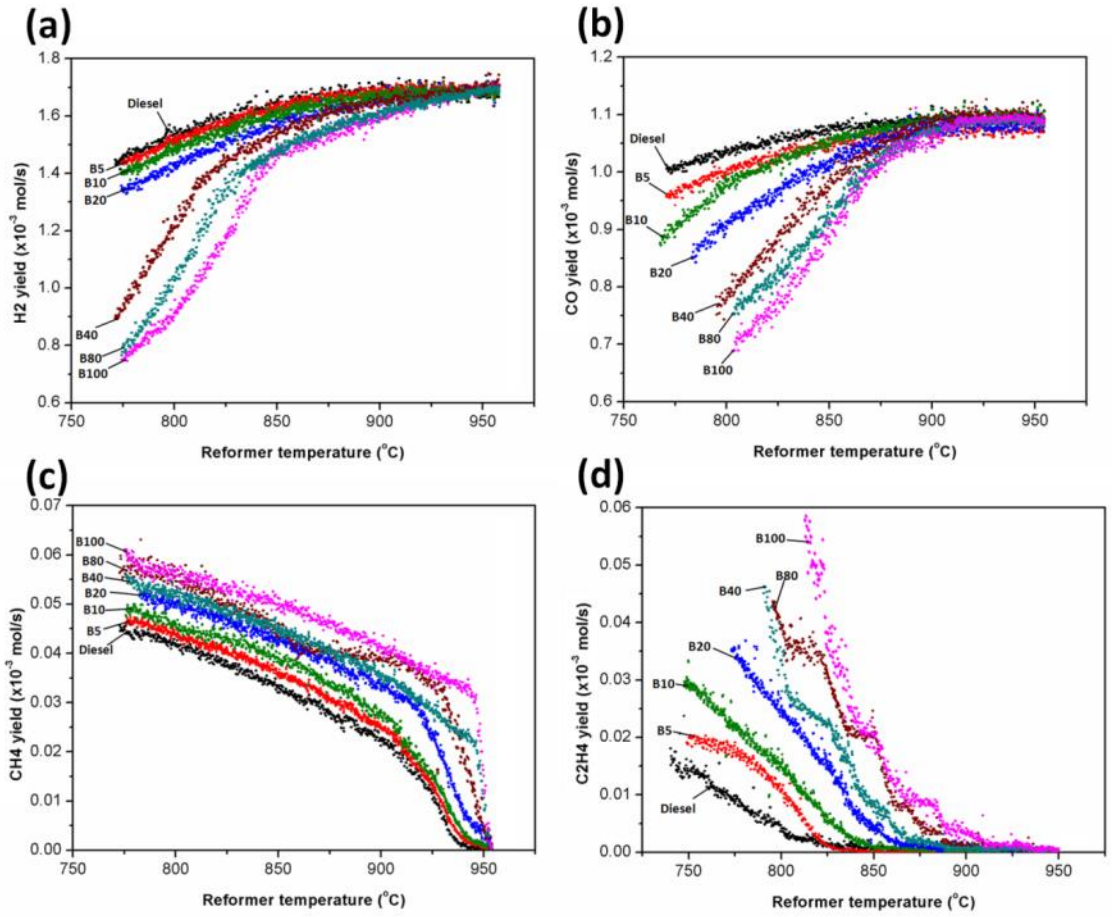

Figure 46: Effect of reformer temperature reduction on the gas productions of (a) H_2, (b) CO, (c) CH_4, and (d) C_2H_4 for the ATR of B-diesel with various biodiesel contents

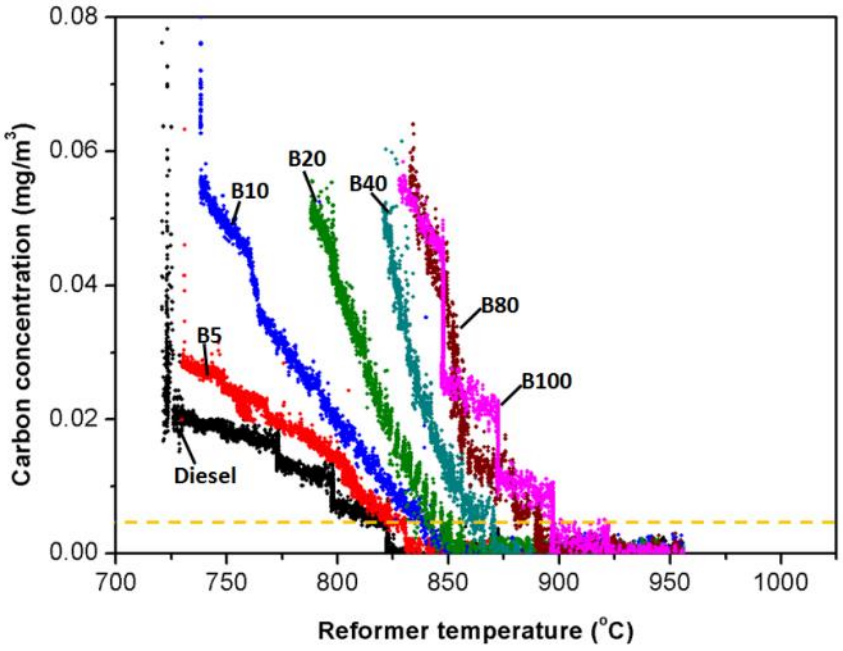

Figure 47: Effect of reformer temperature reduction on solid carbon formation during ATR of B-diesel with various biodiesel contents

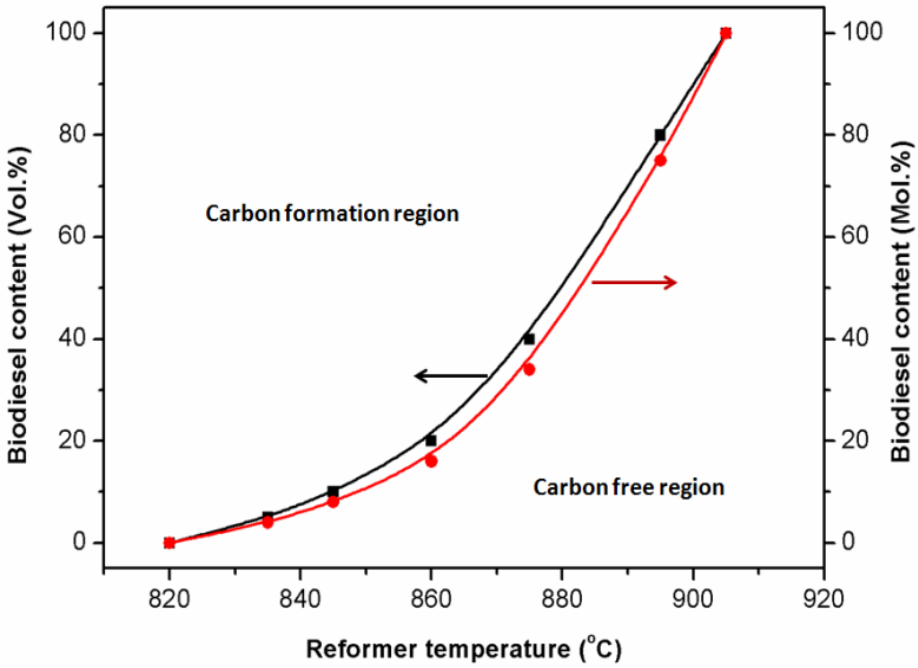

Figure 48: Carbon formation boundaries with respect to reformer temperature reduction for the ATR of B-diesel with various biodiesel contents (volumetric and molar bases)

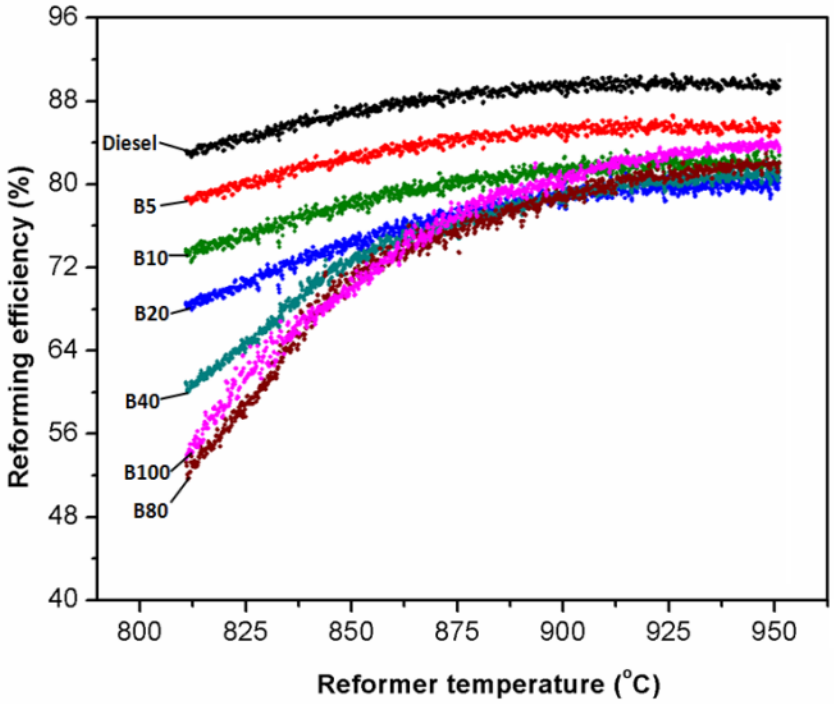

Figure 49: Effect of reformer temperature reduction on reforming efficiency for the ATR of B-diesel with various biodiesel contents

Correlation between Solid Carbon and Ethylene

Unsaturated hydrocarbons like olefins and aromatics are known to be precursors for solid carbon formation during fuel reformation, and naphthenes and aromatics compounds are more difficult to catalytically reform than olefins and paraffins [15,119]. Ethylene is a common byproduct of heavy hydrocarbon pyrolysis, and it has been associated with the highest carbon formation rate among other light hydrocarbons [148,151]. Thus it is necessary to explore the correlation between solid carbon formation and ethylene for the ATR of B-diesel with various biodiesel contents in order to understand their carbon formation routes. Figure 50 shows these correlations for the ATR of diesel, B20, B80, and B100 with respect to air reduction (Figure 50a) and reformer temperature reduction (Figure 50b). Although diesel ATR has low amounts of ethylene

production as compared to the ATR of B-diesel and biodiesel, it has higher carbon concentration either for air reduction or reformer temperature reduction, which suggests that there are significant amounts of other hydrocarbon compounds besides ethylene in diesel ATR to form solid carbon (e.g., aromatics, naphthenes) [148,180]. For the case of biodiesel, it is shown that high carbon concentration is correlated to a large amount of ethylene, indicating that ethylene is a major contributor to solid carbon formation due to the low content of aromatic hydrocarbons in biodiesel. As the biodiesel content in B-diesel increases, the portion of solid carbon derived from ethylene pyrolysis increases. For example, 0.2 mg/m^3 of carbon concentration detected by the micro-soot meter corresponds to 0.05 and 0.175 mol/s ethylene production for diesel and biodiesel, respectively (Figure 50a), indicating significant amounts of ethylene derived from unsaturated methyl groups of biodiesel dominate the carbon formation with high biodiesel contents in the blends. The carbon formation rates from ethylene for the ATR of various fuels under the air reduction scenario (Figure 50a) are higher (2 to 2.5×) than those under the reformer temperature scenario (Figure 50b), which suggests increasing input air flow to eliminate the solid carbon derived from ethylene would be the preferable approach. As the carbon concentration increases, the ATR performance of all studied fuels becomes unstable.

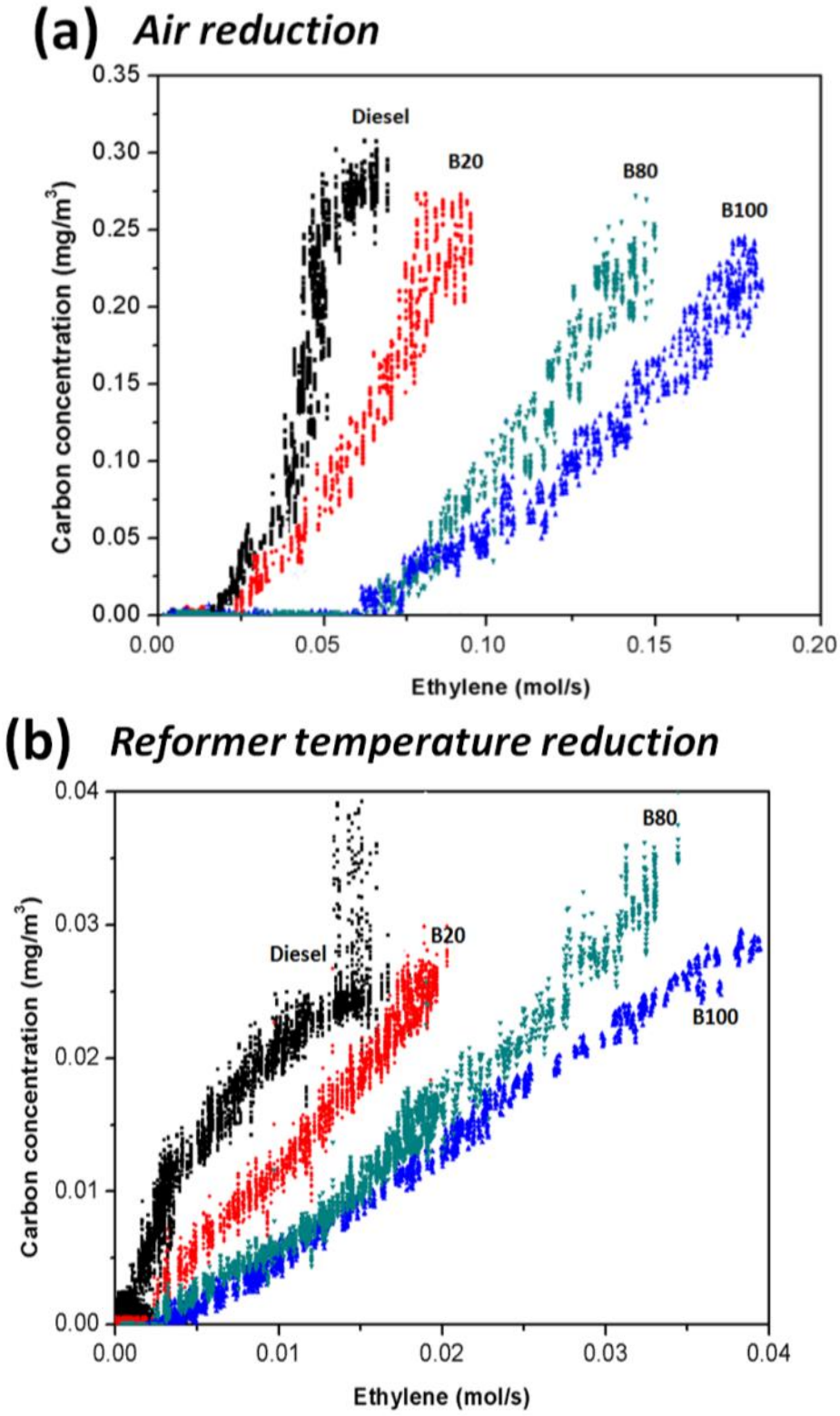

Figure 50: Correlations between carbon concentration and ethylene associated with (a) air reduction and (b) reformer temperature reduction

4.3.4. Summary

Catalytic reformation of diesel blended with biodiesel (B-diesel) was conducted in a single-tube reactor with rhodium/ceria-zirconia catalyst wash-coated ceramic monoliths to analyze the impacts of biodiesel content on the reforming performances. Five B-diesel samples (B5, B10, B20, B40, and B80) along with two baseline samples (pure diesel and pure biodiesel) were catalytically reformed to achieve the same syngas production rate under the same initial operating condition of total O/C (oxygen from air, water, and fuel) = 1.47, H_2O/C = 0.6, GHSV@STP = 33,950 hr^{-1} at 950 ^oC reformer temperature. A customized nozzle integrated with a micro-size porous device was used to finely atomize the fuel (below 35 μm droplet diameter) and homogenously mix with water and air to avoid hydrocarbon thermal pyrolysis prior to entering the reactor. A direct photo-acoustic based micro-soot meter was used to analyze in-situ carbon dynamic evolution, while a mass spectrometry was applied to measure the reformate gas composition. Diesel ATR has the highest H_2 selectivity and reforming efficiency under the initial condition, whereas B20 was identified to have the lowest H_2 selectivity and reforming efficiency. To analyze the effects of air reduction and reformer temperature reduction on reformate composition and identify the carbon formation boundaries with respect to the ATR of various blends, two sets of experiments were conducted with total O/C reduction by adjusting input air flow and reformer temperature reduction by controlling the furnace temperature. B-diesel with more biodiesel content was found to have higher reduction rates of syngas yield and reforming efficiency, and thus requires more air and higher reformer temperature to avoid carbon formation. Strong correlations between ethylene and solid carbon concentration were observed in the reformation of all studied fuels and

they indicate the major contributor of solid carbon formation for biodiesel ATR is mostly derived from ethylene, while there are significant amounts of other compounds (e.g., aromatics, naphthenes) besides ethylene serving as carbon precursors in diesel ATR. This work demonstrated that B-diesel could serve as a promising alternative fuel for SOFC-APU applications in transportation sectors, if their operating conditions are well controlled within the carbon-free regime.

4.4. Biodiesel-Ethanol-Diesel (BED) Blend Autothermal Reformation

4.4.1. Introduction

Many studies have demonstrated the major failure modes of the fuel reformer as catalyst degradation resulting from sulfur poisoning [181], high temperature sintering [182], and coke formation [14,122]. For instance, Shekhawat *et al.* [181] reported that hydrogen yield from n-tetradecane reformation with rhodium catalyst coated on zirconia-doped ceria would decrease from 21% to 15% after introducing 1000 ppmw sulfur in the form of dibenzothiophene for 2 hours, and they suggest that sulfur acts as the kinetic inhibitor for carbon monoxide formation and deactivates sites to resist hydrogen formation. The sulfur poisoning issue can be prevented if the input hydrocarbon fuel has low/no sulfur content or the sulfur compounds are removed from the fuels before entering the reformer. The typical auto-thermal reformer is an adiabatic reactor and the exothermic reaction of fuel oxidation dominates the front end of the catalyst bed within a few millimeters [158], which releases excess heat and increases the risk of damaging the catalyst located in the front end of the test bed. Borup *et al.* [120] indicate the oxidation reactions of hydrocarbon fuels without adequate mixing with steam has the propensity to

create local hot spots and sinter the catalyst at the reactor inlet. Solid carbon formation in the catalyst bed during hydrocarbon ATR has been recognized as the common contributor to catalyst degradation, because the dynamic evolution of carbon formation is difficult to detect and control [14]. Ethylene has been confirmed as the potential precursor to form solid carbon, and naphthenes and aromatics compounds are known to be more difficult to catalytically decompose than olefins and paraffins [120,150]. Numerous studies have investigated the effects of carbon deposition on the catalyst bed by applying characterization tools like TPO (temperature programmed oxidation) or TEM (transmission electron microscopy) [183,184], however, most of this prior work was specifically focused on the analysis of the reactor after the reformation was completed rather than evaluating the in-situ carbon formation under changing environments, and significant amounts of condensed carbon effluent from the reformer along with the gas products were not captured with these techniques [14,120]. Therefore, it is necessary to develop a methodology to monitor the dynamic formation of solid carbon during reactor operation.

Intensive work has been conducted on modifying the structure of reformate catalysts to improve their sulfur tolerance and carbon resistance to achieve stable fuel reformation [158,181]. For example, rhodium-substituted lanthanum strontium zirconate pyrochlore catalyst developed by the National Energy Technology Laboratory (NETL) performs with a stable hydrogen production (±2%) for diesel ATR up to 1000 hours of continuous operation under the conditions of O_2/C = 0.5 and H_2O/C = 0.5 at 900 ^oC reforming temperature [184]. From a systematic perspective, the strategy to control the

key parameters and operate the reactor under optimum conditions (i.e., peak hydrogen yield and carbon-free operation) is also an effective approach to improve the performance of fuel reformation under conditions of varying load, temperature, etc. The key parameters of fuel catalytic reformation include reformer temperature, O_2/C, fuel utilization fraction, anode recycle gas fraction, and GHSV [14, 185].

Biodiesel has been gradually introduced into the transportation sector and blended with petro-diesel for use in diesel engine combustion. However, as described in Section III, two major drawbacks in biodiesel-diesel fuel blends are their poor performance in regards to cold flow and fuel kinematic viscosity limit, which make the blended fuel difficult to atomize into small droplets and deliver to the engine at low temperature [67]. Ribeiro *et al.* [107] reviewed the roles of potential additives for diesel blended with biodiesel to improve ignition and combustion efficiency, stabilize fuel mixtures, protect the motor from abrasion and wax deposition, and reduce pollutant emission. Alcohol based co-solvents (e.g., methanol, ethanol) have been reported as additives to improve biodiesel (B-diesel) cold flow performance and also as oxygenates to accelerate complete fuel combustion [68,70,107]. A nonlinear optimization model was developed in Chapter III to analyze biodiesel-ethanol-diesel (BED) ternary blending processes in a given geographical region with the objective of maximizing the system profitability of a petro-refinery firm while meeting multiple criteria constraints: market disturbances from fuel price changes and fuel demands, blended fuel quality to meet the ASTM D7467 standard, bio-fuel tax credits, availability and diversity of bio-fuel feedstock, and technology innovations on potential additives and desulfurization. The model indicates that the

optimal recipe for BED blends used in diesel engine combustion consists of biodiesel, ethanol, and diesel compositions of 25%, 10%, and 65% (volumetric), respectively. The study focuses on evaluating the reformation of BED blends with this fuel composition, hereafter indicated as B25E10D65.

The object of this work is to analyze the ATR performance of 25% of biodiesel blended with 10% ethanol and 65% ultra-low sulfur diesel using a single-tube reactor with rhodium/zirconia wash-coated ceramic monoliths under various operating conditions: reformer operating temperature, H_2O/C, total O/C, and GHSV. For comparison purposes, autothermal reforming of pure biodiesel, pure diesel, and B25 (25% biodiesel blended with 75% of diesel) was conducted under the same operating conditions as B25E10D65 ATR with the goal of achieving a consistent syngas production rate. The impacts of air reduction and reformer temperature reduction on effluent species from the reformer were investigated for the reformation of these four studied fuels. A vapor pretreatment process was designed with a customized spray nozzle integrated with a 2 μm porous filter that enabled the heavy hydrocarbon fuels to finely vaporize with less fuel self-pyrolysis before entering the reactor. Also, a direct photo-acoustic based micro-soot meter was used to analyze carbon dynamic evolutions under different conditions while a mass spectrometer was applied to measure the gas composition of the reformer effluent. Thermodynamic analysis based on total Gibbs free energy minimization was applied to evaluate the equilibrium composition of effluent species under different operating environments for each type of fuels. The optimum operating conditions with high syngas yield and no carbon formation were determined both from thermodynamic

modeling and experimental tests for the four types of fuel considered. As described in Section 4.3.3, this work also explored the correlations between carbon concentration and ethylene under each set of parameter change (input air, reformer temperature, and GHSV).

4.4.2. Thermodynamic analysis

Thermodynamic analysis based on total Gibbs free energy minimization was applied in this work to simulate the equilibrium effluents from the reformer with the ATR of four studied hydrocarbon fuels (ULSD, biodiesel, B25, and B25E10D65) under various operating conditions. Section 4.2.2 described the mathematical model of thermodynamic analysis methodology. The model and experimental setups in this study simulated the fraction of steam recycled from SOFC stacks with H_2O/C of 0.6. The amount of input hydrocarbon fuels simulated in the thermodynamic model was normalized as 1 mol/s and the composition of the mixed gases was predicted in the temperature range of 400-1000^oC and O_2/C range of 0-0.43.

4.4.3. Experimental apparatus and test plans

The experimental apparatus included fuel and water delivery modules, a single-tube reformer contained within an electrically heated tube furnace, the AVL photo-acoustic based micro-soot meter, and the mass spectrometer (more description of system setup was provided in Section 4.1.2). Rather than using a conventional pressure-based nozzle for fuel delivery, a customized nozzle was developed to improve fuel atomization by the micro-explosion of emulsified fuels and promote homogeneous steam/fuel mixing.

Figure 51 (a) shows the basic configuration of the proposed device (first introduced in Figure 17), which consists of the regions of fuel and steam delivery, fuel/steam emulsification, and fuel/steam micro-explosion. Superheated steam at 350^{o}C was continuously generated from a heated stainless steel coil and flowed through the inner tube of the nozzle, and then it sprayed out of a porous filter with 2 μm pore size. Nitrogen served as a carrier of the liquid fuel and it was also used to adjust the system space velocity during the tests. Input hydrocarbon fuel with nitrogen gas was preheated to 70^{o}C

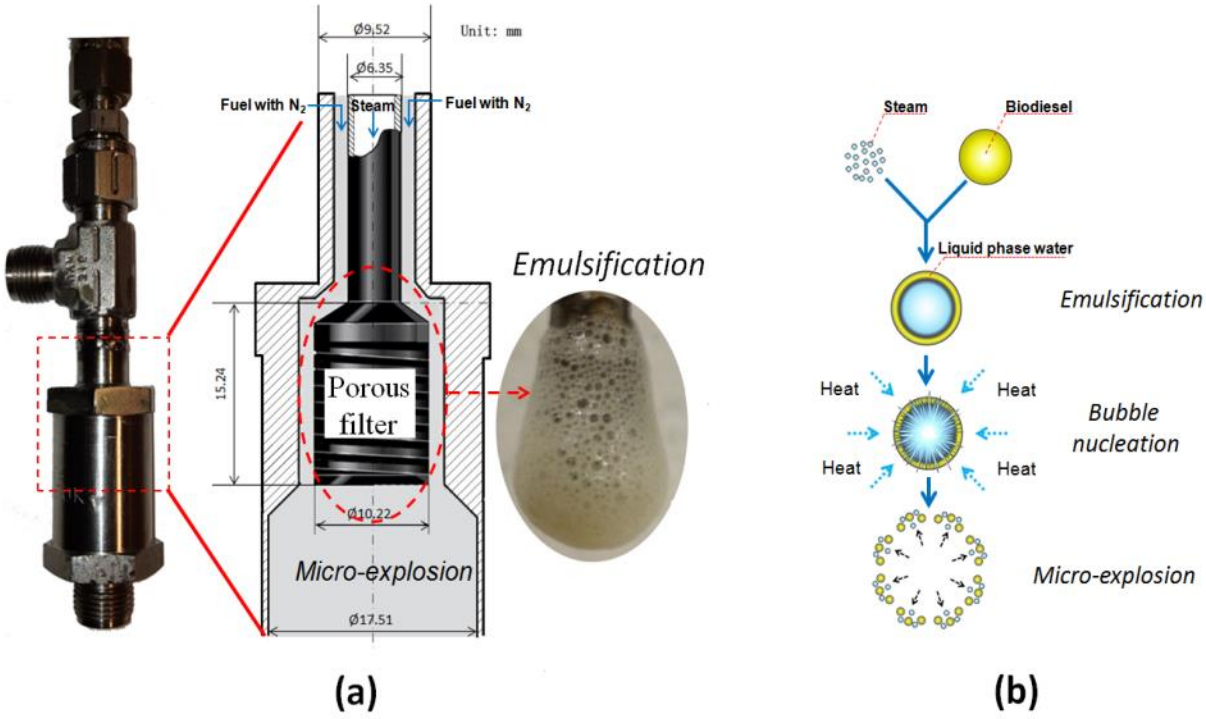

Figure 51: (a) The customized nozzle device, (b) micro-explosion of emulsified hydrocarbon fuels.

with a heated stainless steel coil to improve fuel flow performance by lowering the kinematic viscosity, and then flowed around the outside of the porous filter. Steam was partially condensed due to the heat transfer to the fuel/nitrogen and the fuel was

spontaneously emulsified with water because of the inherent hydrophobicity of hydrocarbon fuels, as illustrated on Figure 51 (b) [187,188]. With the continuous supply of steam, bubble nucleation of the emulsified fuel occurred around the porous filter (see Figure 51a). As the temperature increased downstream near the porous filter, the vigorous volumetric expansion of vaporizing water and heated steam created the momentum to explode the initial emulsified fuel and disperse the fine secondary droplets, which consequently enhances the fuel-steam mixture [187]. The droplet size of the fuel/steam mixes emitted from the customized nozzle would be potentially below 35 μm. The reactant mixture produced from the nozzle was further heated to 350^{o}C before entering the reformer. For visual comparison purposes, additional experiments were conducted to directly mix the fuel, steam, and air without the customized nozzle and the vaporized mixture was condensed down to room temperature instead of entering the reactor.

After each experimental fuel reforming sequence, methane partial oxidation with O/C = 1.3 at 950^{o}C reformer temperature was conducted in the single-tube reactor for catalyst regeneration. The micro-soot meter was used to sample the reformer effluent under methane partial oxidations which were well outside of the carbon formation regime, and recalibrate the zero baseline for the next experimental measurements. Besides the micro-soot meter, the mass spectrometer was also applied to quantify the compositions of gaseous effluent species from the reformer and it is capable to determine the gases (N_2, O_2, H_2, CO, CO_2, CH_4, C_2H_4, and C_2H_6) within ±1% resolution.

Carbon monoxide and hydrogen both serve as the main input fuels for the SOFC system to electrochemically generate electricity, and their equilibrium gas yields from the reformations of four types of studied fuels (diesel, biodiesel, B25, and B25E10D65) can be derived from the thermodynamic analysis described in Section 4.2.2. Thus, the required flow rates of these hydrocarbon fuels under the same operating conditions could be estimated in order to achieve the same syngas production rate.

The operating conditions for the ATR of different input fuels were all initially set as $H_2O/C = 0.6$, total $O/C = 1.47$, and GHSV = 34,120 hr^{-1} with the furnace controller temperature set at 1000^oC. Table 18 provides the operating conditions of these initial test points to produce a 0.00275 mol/s theoretical syngas production rate. Due to the inherent oxygen content in biodiesel and ethanol, fuel blends with biodiesel or ethanol require a lower O_2/C (i.e., less oxygen from air) than diesel. The single-tube reformer was contained within an electrically heated furnace and before introducing the hydrocarbon fuel mixed with steam and air into the reformer, the reactor temperature was ramped up with the furnace temperature set point of 1000^oC and 8^oC/s increment rate while a low flow rate of nitrogen gas passed through the reformer tube. After the temperatures of the heating coils all reached their set-point temperatures, water was introduced into the system, followed by fuel with nitrogen and then air. To avoid the overshoot temperature near the front end of the catalyst bed, the input air was gradually introduced by monitoring thermocouple TC 1. After the fuel reformation reached stable conditions at the initial test points (reflected by the consistent performances of reformates and reactor temperature profiles), the reformer was kept under the same environment for 2-hours of

continuous operation in order to elucidate the stability of the reformer system and obtain the time-resolved data for the initial test points.

Table 17. Experimental test plan to evaluate the ATR of each type of fuel

Test series	Variable	Total O/C	H2O/C	Furnace setpoint temperature (°C)	GHSV@STP (hr^{-1})[C]
1	O_2/C reduction	1.47~1.07	0.6	1000	34,120
2	Reformer temperature reductions	1.47	0.6	1000~750	34,120
3	GHSV changes	1.47	0.6	1000	30,000~52,000

[C] GHSV at standard temperature and pressure condition:

$$\frac{Total\_volume\_of\_inputs@STP(m^3/h)}{Volume\_of\_catalyst(m^3)}$$

To capture the effects of air reduction, reformer temperature reduction, and GHSV changes on the effluent species and the temperature profiles across the reactor during ATR of each type of fuel, three series of experimental tests were designed and conducted (see Table 18). (1) Total O/C was reduced from 1.47 to 1.07 by gradually reducing air flow (O_2/C) and keeping other variables the same as the initial test conditions. Nitrogen gas was adjusted to maintain the same GHSV. (2) With the initial set point of furnace temperature at 1000°C, the reformer temperature enabled reaching around 950 °C for the ATR of each type of fuel. The reformer temperature was reduced by adjusting the temperature controller of the furnace from 1000 to 750 °C while the inputs were kept constant. (3) The GHSV was changed from 30,000~52,000 hr^{-1} by regulating the nitrogen input flow rate. In these three sets of experimental tests, the micro-soot meter and the mass spectrometer were simultaneously applied to determine the solid carbon concentrations and gas species in the effluent from the reformer. To avoid irreversible catalyst degradation from carbon deposition over a long period of time,

these experiments of parameter changes were stopped when significant effluent carbon concentration was detected by the micro-soot meter. The correlation between condensed carbon content and ethylene under each set of experimental conditions was also explored.

4.4.4. Results and discussion

Equilibrium Analysis

Figure 52 illustrates the reformate equilibrium compositions of effluent species from the reformer as a function of the reformer temperature for the ATR of each type of fuel under the conditions of $H_2O/C = 0.6$ and total $O/C = 1.47$. In order to compare the reforming performances of each type of fuel under the same conditions, the equilibrium products were shown in terms of mol/mol carbon from input fuels. At the high reformer temperature region, the hydrogen yield of B25E10D65 ATR is slightly higher than the ATR of other fuels, which is because the molar H/C ratio of ethanol is higher than diesel and biodiesel. Figure 52 suggests the temperature factor has similar impacts on the gas yields and carbon formation for the ATR of diesel, biodiesel, B25, and B25E10D65 fuel. For instance, H_2 and CO both accelerate significantly as reformer temperature increases to 700 and 800 ^oC, respectively, whereas light hydrocarbon gases (e.g., CH_4, C_2H_4, and C_2H_6) reduce dramatically with increasing temperature. Large amount of solid carbon is formed at the temperature near 500 ^oC due to thermal cracking of C_6H_6, C_3H_8, C_2H_4, and C_2H_6, and the solid carbon content is substantially diminished at higher reformer temperature [150]. The threshold temperatures to mitigate solid carbon formation for the ATR of diesel, biodiesel, B25, and B25E10D65 are 800, 900, 850, and 850^oC, respectively. Figure 52 also provides the experimental data at several temperature points

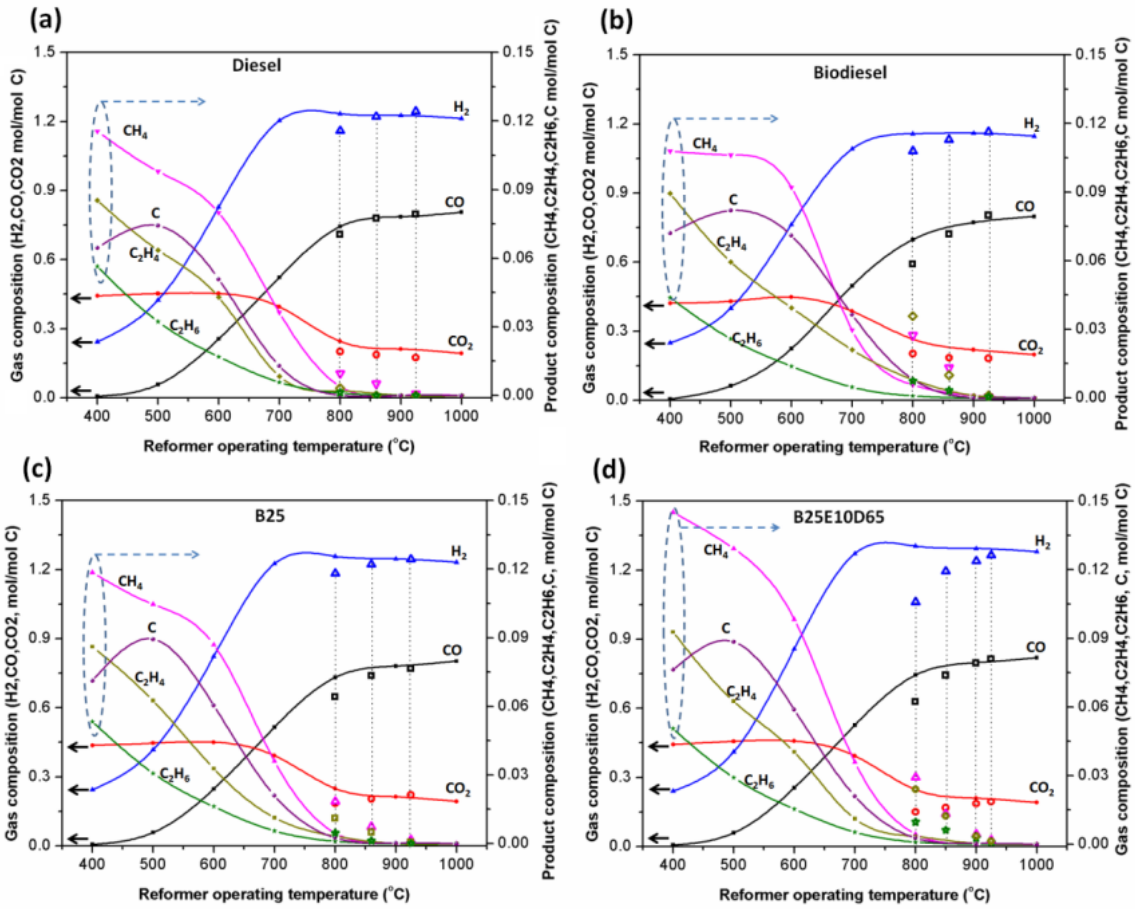

Figure 52: Equilibrium compositions from ATR of (a) diesel, (b) biodiesel, (c) B25, and (d) B25E10D65, as a function of the reformer temperature (H_2O/C=0.6, total O/C=1.47)

(800, 860, and 925 ^{o}C) to validate the equilibrium results, and it shows a closer fit for diesel ATR (Figure 52a), biodiesel ATR (Figure 52b), and B25 ATR (Figure 52c) than B25E10D65 ATR (Figure 52d), which suggests B25E10D65 ATR was unable to achieve the completed reactions of hydrocarbons in the experimental tests and has not reached its chemical equilibrium states at lower temperature ranges. This phenomenon may be due to the oxygen consumption of ethanol oxidation in B25E10D65 fuel vaporization step and the lack of oxygen left for diesel/biodiesel catalytic reformation in the reactor. However,

as the temperature ramps up above 900^{o}C, the experimental results of the blended fuels have a relatively low deviation from the equilibrium predictions.

Despite a limited amount of water available from anode recycled gases of the SOFC stacks [14], it is relatively simple to adjust O_2/C by changing compressed air flow to improve reformate performance. Figure 53 shows results of equilibrium analysis of ATR of B25E10D65 as functions of O_2/C and reformer temperature. Maximum hydrogen yield is achieved with O_2/C of 0.32 at 750 ^{o}C (Figure 53a) and CO reaches its peak production rate with O_2/C of 0.35 at high temperature (1000 ^{o}C, Figure 53d). CH_4 is diminished with the increase of input air and reformer temperature, and increased air flow also accelerates CO_2 production. Figure 54 provides the equilibrium compositions of condensed solid carbon and C_2H_4 as functions of O_2/C and reformer temperature for B25E10D65 reformation. With the increase of O_2/C, solid carbon content drastically declines and ethylene composition is also gradually reduced, indicating that increasing the input air may be an effective approach to mitigate carbon formation. Figure 54 also indicates that there are proportional correlations between solid carbon content and ethylene at the high temperature region (above 500 ^{o}C). These correlations were further explored experimentally in this work. The optimum operating conditions for B25E10D65 ATR are located within the overlap area of the carbon free region and the region with high syngas yield (area P highlighted on Fig 5a).

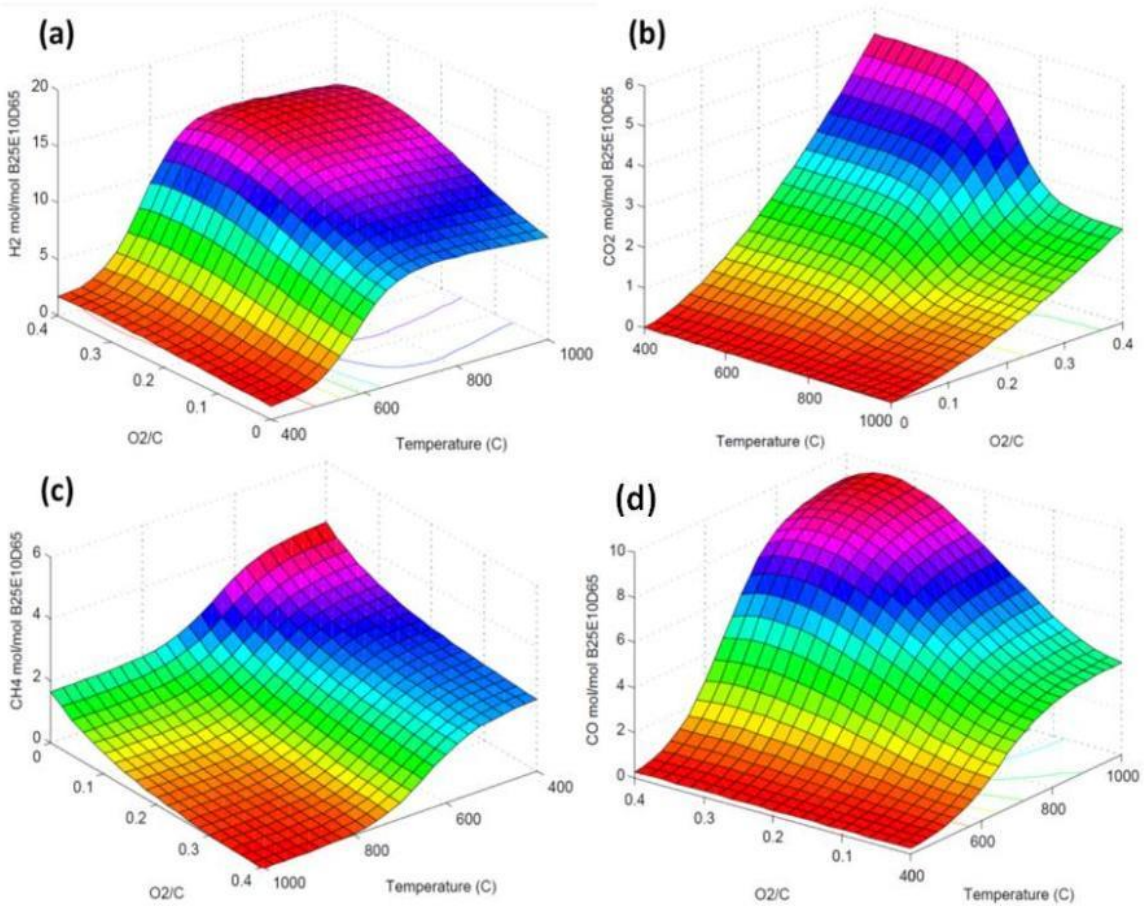

Figure 53: Thermodynamic equilibrium gas products of B25E10D65 ATR (a) H_2, (b) CO_2, (c) CH_4, and (d) CO with $H_2O/C = 0.6$ (the scales are altered to provide adequate visualization of the surface plot)

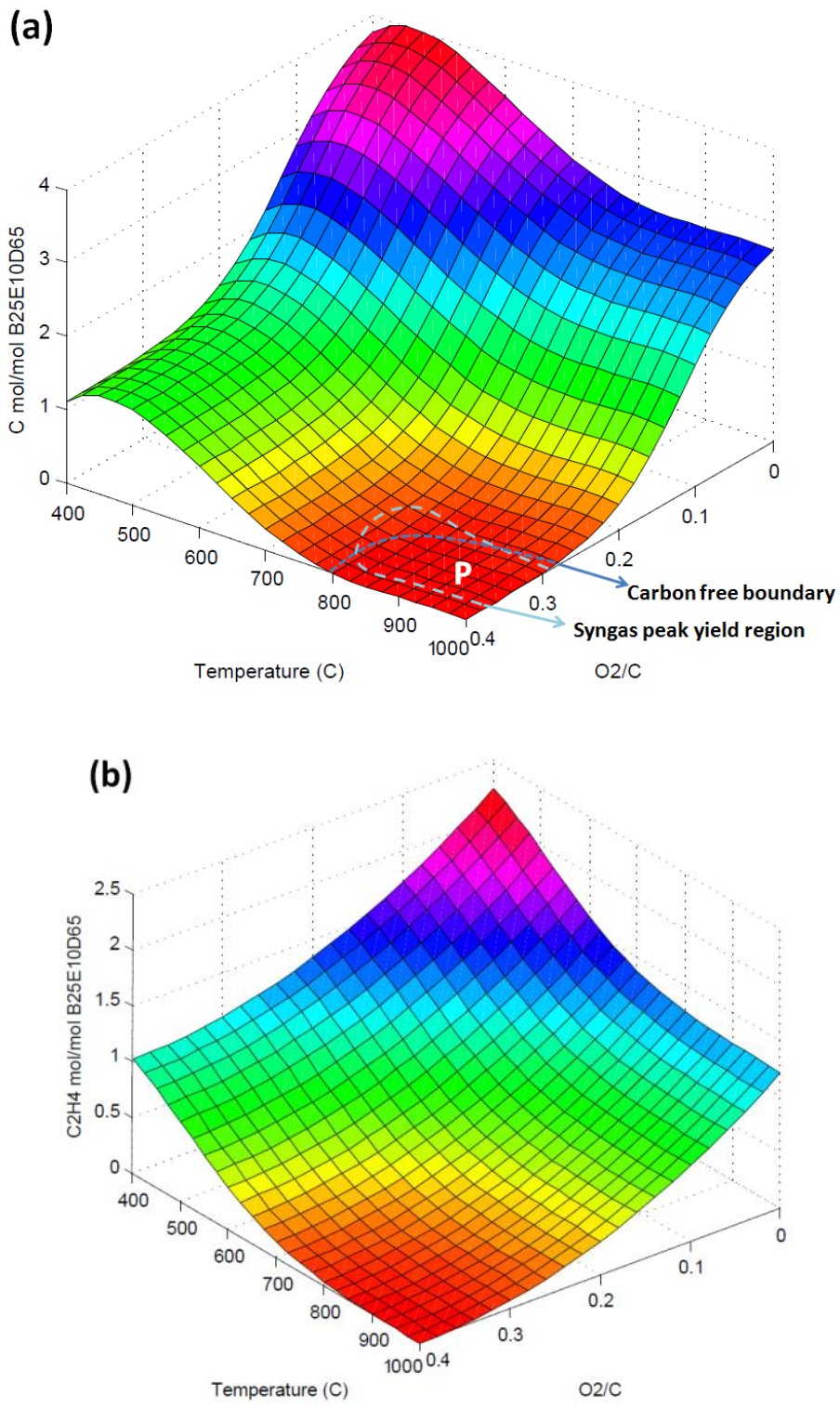

Figure 54: Equilibrium of ethylene and solid carbon content as the functions of O_2/C and reformer temperature in B25E10D65 ATR (H_2O/C = 0.6)

Experimental Tests

Figure 55(a) shows the samples of the studied fuels, including biodiesel, B25, B25E10D65, and diesel. As compared to diesel, biodiesel possesses high viscosity and high molecular weight, which makes it difficult to completely vaporize without fuel self-pyrolysis and solid carbon formation by applying the conventional approach which directly mixes biodiesel/steam/air [177]. Similar to the experimental setup in Section 4.1.2, the mixtures after biodiesel vaporization with steam/air were condensed to room temperature and collected prior to entering the reactor in order to simply evaluate the performance of the proposed customized reactant injection nozzle. Figure 55(b) compares

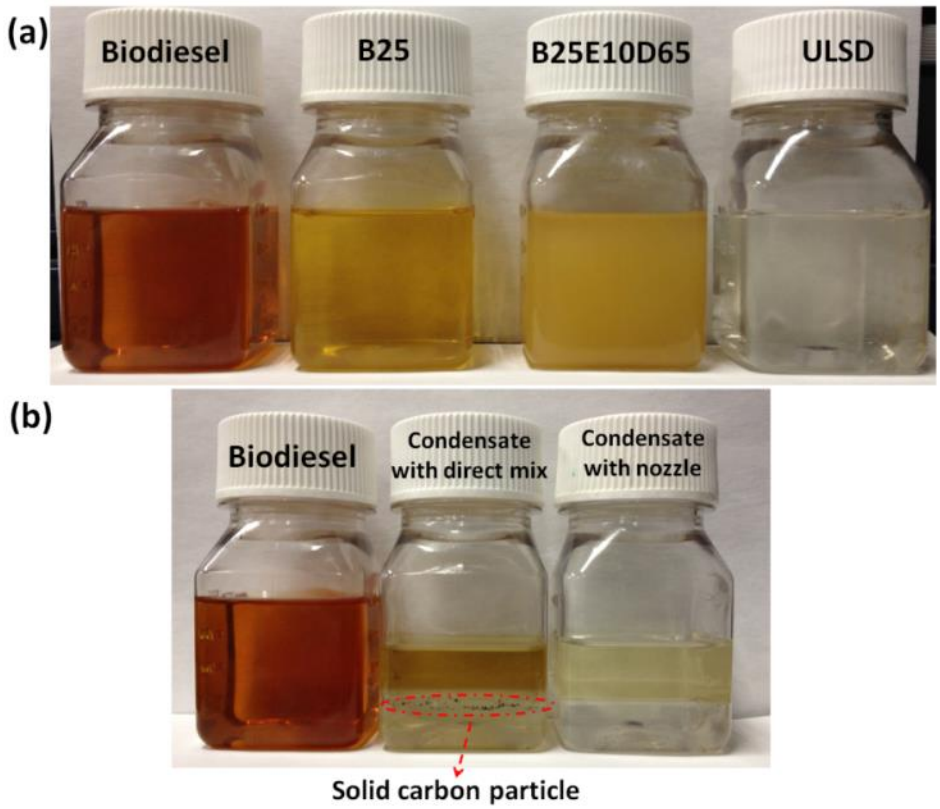

Figure 55: (a) Four studied samples of hydrocarbon fuels, (b) biodiesel sample and its condensed liquid after the vaporization step with and without the customized nozzle

the condensed liquid of biodiesel vaporized with conventional direct mix method (without the customized nozzle) and that with the customized nozzle, along with the original biodiesel fuel. The color of the condensed mixture vaporized with the proposed method is lighter than the one with direct mix approach, indicating the customized nozzle accelerates the biodiesel decomposition into lower hydrocarbon compounds. Significant amounts of carbon particles are found in the condensate of the mixtures with the direct mixing method (highlighted on Figure 55b) and these solid carbons would consequently flow along with the vaporized gases into the reformer and contaminate the catalyst bed.

Table 18. Gas yields of initial test points for the ATR of different fuels with total O/C=1.47, H_2O/C=0.6, and GHSV= 34,120hr^{-1} at 950^oC reformer temperature

Fuel	**Gas production rate(10^{-3}×mol/s)**						
	H_2	CO	CO_2	CH_4	C_2H_4	C_2H_6	Syngas yield
Diesel	1.705	1.102	0.207	0.012	undetectable	undetectable	2.807
Biodiesel	1.664	1.161	0.217	0.026	0.004	undetectable	2.825
B25	1.691	1.104	0.222	0.021	0.001	undetectable	2.795
B25E10D65	1.685	1.143	0.163	0.014	0.001	undetectable	2.828

Table 19 consolidates the gas yields of the experimental test points for the ATR of each studied fuel under the initial operating condition with reformer temperature = 950^oC, total O/C = 1.47, H_2O/C = 0.6, and GHSV = 34,120hr^{-1}. With the goal of achieving the same syngas yield, the amount of required input fuels can be determined and the differences between the actual production rates of syngas and the theoretical syngas yields are within 3%. The intensity of the microphone signal from the micro-soot meter shows the carbon concentration is below the instrument's resolution of 5 µg/m^3 during these test points, indicating there is no detectable solid carbon formed under the initial conditions for the ATR of different fuels. Relatively low or undetectable amounts

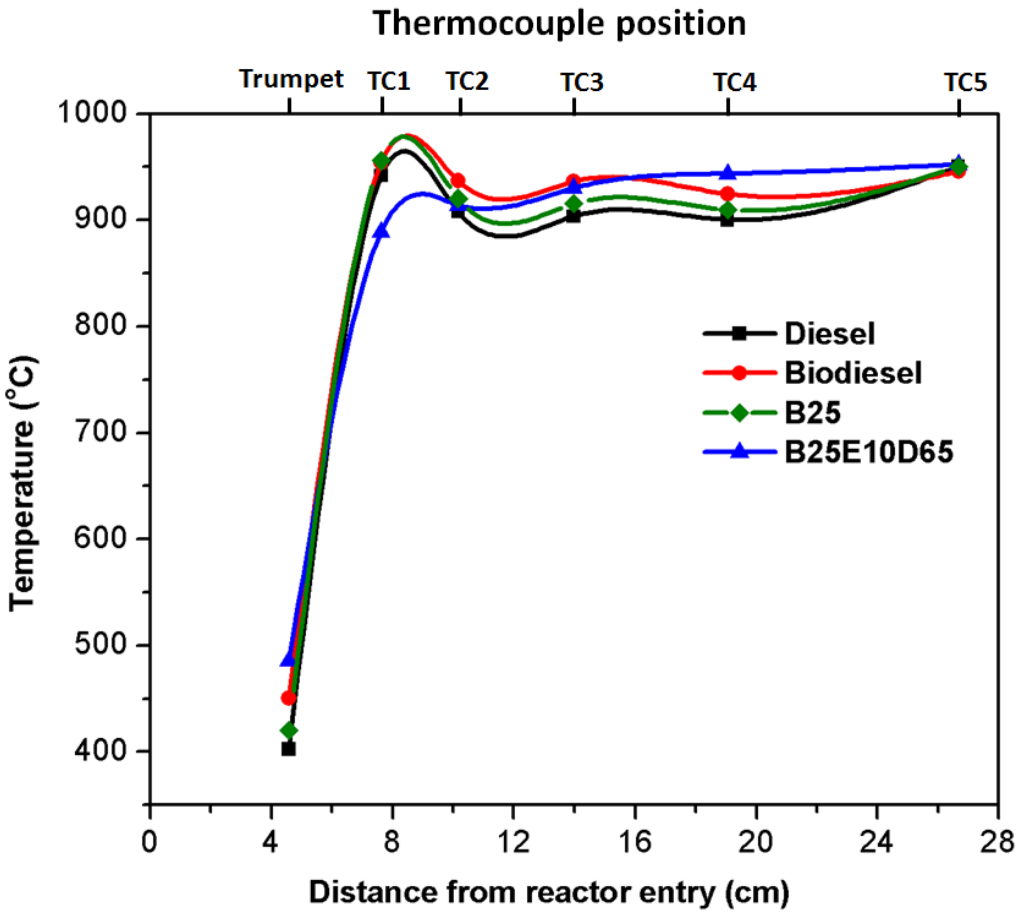

Figure 56: Reactor temperature profiles for ATR of four considered fuels under the initial operating conditions

of C_2H_4 and C_2H_6 for the ATR of these fuels also confirm the initial test points are within the carbon-free boundary. B25 and biodiesel, however, show high CH_4 production rate as compared to the other fuels. Figure 56 shows the temperature profiles of the reactor with the thermocouples located in six different places, including the reactor inlet trumpet tube temperature and the temperatures at five locations in the catalyst bed TC1 to TC5; see Figure 18. The reformation of diesel, biodiesel, and B25 has a similar trend of temperature profile throughout the reactor while the B25E10D65 ATR behaves in a

different manner. For instance, the ethanol fraction of B25E10D65 is mostly combusted with input air in the fuel mixing chamber due to its low flash point (at 13^{o}C) and releases significant amount of heat to promote the further vaporization of biodiesel/diesel fuel, which leads to the temperature near the reactor inlet (trumpet temperature) for B25E10D65 ATR is higher than the cases with diesel, biodiesel, and B25. For B25E10D65, the temperature near the front end of the catalyst bed (TC1) resulting from the oxidation of the fuel stays about 60^{o}C lower than the ATR of other fuels, which reduces the risk to create local hot spots in the catalyst and avoids degrading the catalyst performances at high temperature regions.

Air Reduction

Keeping other key parameters (H_2O/C, furnace controller temperature, and GHSV) constant, the total O/C was reduced from the initial test condition (total O/C = 1.47) by gradually reducing the input air flow. To avoid irreversible catalyst degradation from carbon deposition over a long period of time, air reduction was stopped when significant effluent carbon concentration was detected by the micro-soot meter. Figure 57 illustrates the effects of air reduction on the gas compositions for the ATR of diesel, biodiesel, B25, and B25E10D65. As the input air flow decreases, H_2, CO, and CO_2 are reduced while CH_4, C_2H_4, and C_2H_6 are rapidly increased, especially for the biodiesel ATR. When combined with the carbon concentration data detected by the in-situ micro-soot meter (shown on Figure 58), it is obvious that the syngas production (combination of H_2 and CO) declined significantly after the reformer enters the carbon formation regime for all the different fuels. For example, the reformate performance of biodiesel ATR is

maintained relatively stable prior to reaching the carbon formation boundary (total O/C = 1.26, Figure 57b). After entering the carbon formation region, syngas yield drops around 6.5% and 9.5% with first 12% of air reduction (total O/C from 1.26 to 1.19) and the second 12% of air reduction (total O/C from 1.19 to 1.12), respectively. It is pertinent to mention that as a major precursor to form solid carbon, ethylene is further accelerated with the growth of the carbon concentration in the reformer and its production rate is even higher than the grow rate of methane for all the fuels. The system resolution of the micro-soot meter (5 $\mu g/m^3$) is also included on Figure 58 and the carbon concentration value within this range is considered as zero. After air flow reaches the threshold points of carbon formation (with total O/C=1.12, 1.26, 1.24, and 1.16 for diesel, biodiesel, B25, and B25E10D65, respectively) and continuously reduces, the measured carbon concentration rapidly increases and becomes unstable. Biodiesel ATR requires more total O/C than diesel ATR to mitigate the carbon formation due to its higher molecular weight, while B25E10D65 ATR needs less total O/C than B25 to avoid solid carbon because of the low molecular weight of ethanol.

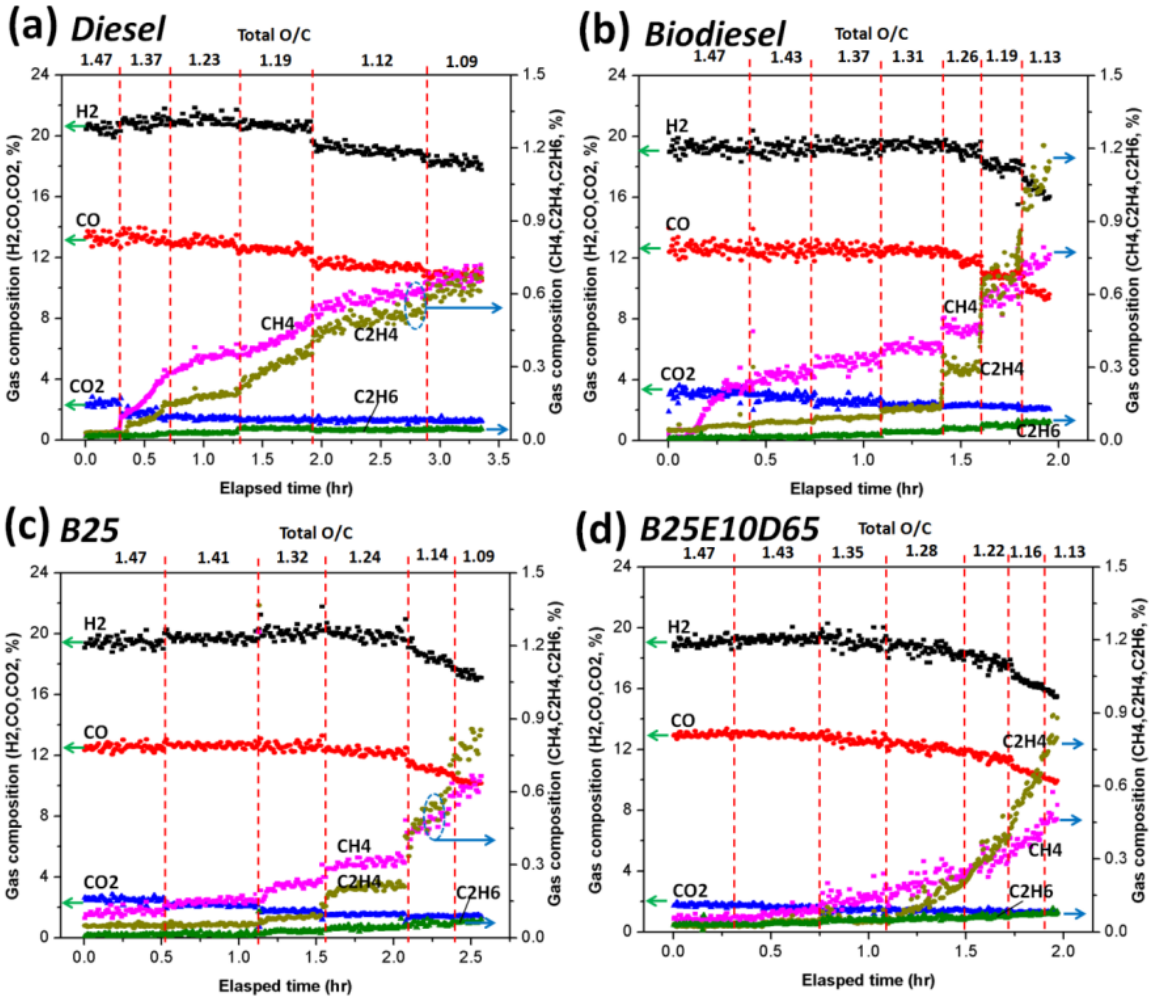

Figure 57: Effect of air reduction on gas compositions from ATR of (a) diesel, (b) biodiesel, (c) B25, and (d) 25E10D65

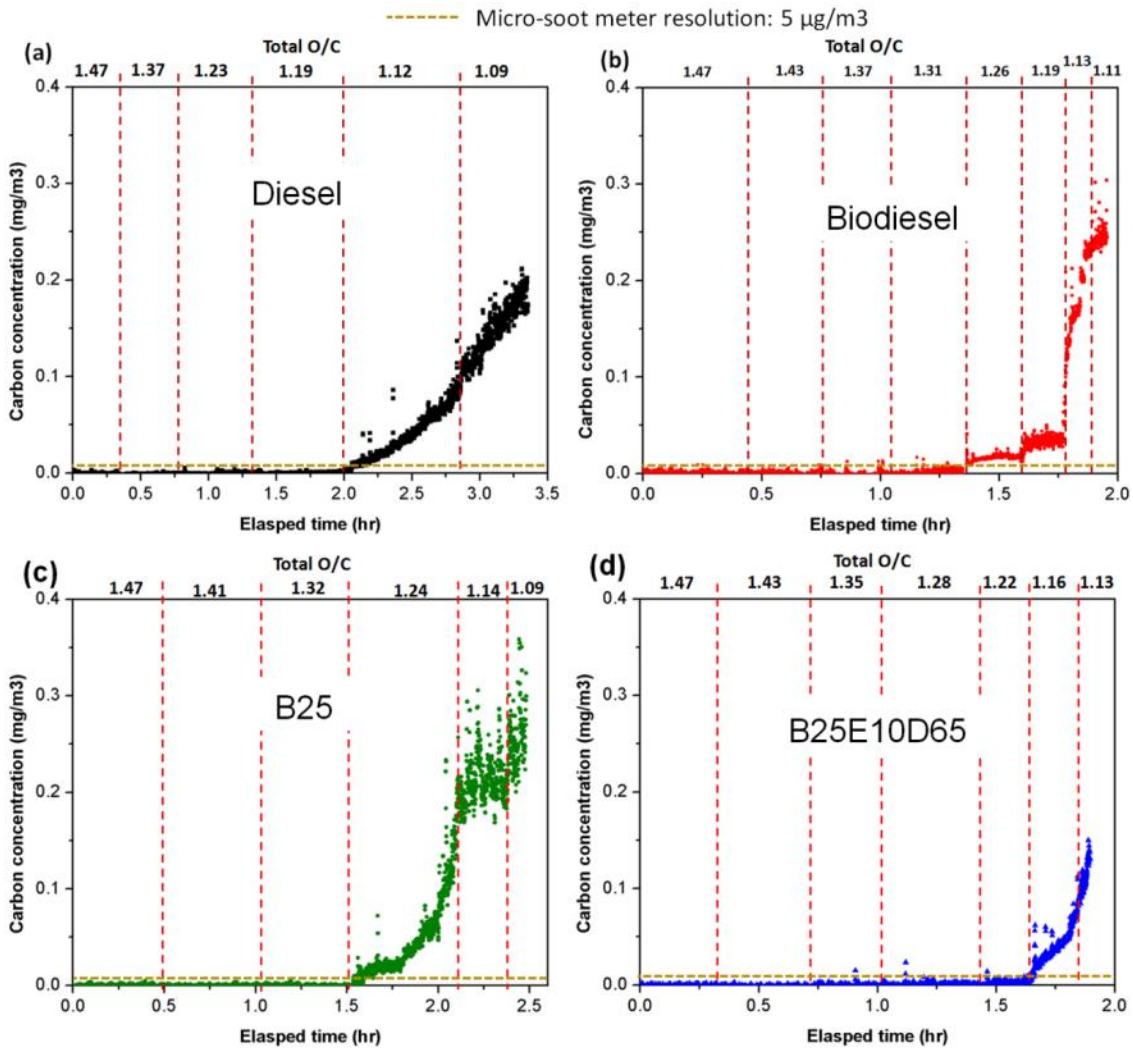

Figure 58: Impact of air reduction on solid carbon concentration from ATR of (a) diesel, (b) biodiesel, (c) B25, and (d) B25E10D65

Reformer Temperature Reduction

After initializing the experimental test points under the conditions of $H_2O/C=0.6$, total O/C=1.47, and GHSV=34,120 hr^{-1} at 950^oC reformer temperature (average of TC1~TC5), the furnace temperature controller was gradually reduced with a 0.1$^oC/s$ reduction rate. Figure 59 shows the effects of the reformer temperature on the gas composition for the reformation of different fuels and Figure 60 shows the carbon

evolution with the reduction of reformer temperature. As the reformer temperature reduces, the production of H_2 and CO stay fairly stable until the threshold temperatures to form solid carbon are reached (825, 900, 860, and 850^oC for the ATR of diesel, biodiesel, B25, and B25E10D65, respectively; see on Figure 60). After entering the carbon formation regime, syngas yield is significantly declined, especially for the case with B25E10D65 (Figure 59d). C_2H_6 concentration gradually increases with temperature reduction, while CO_2 concentration is largely independent of the reformer temperature. Figure 59 also shows that there is a sudden large increment in CH_4 concentration for either diesel ATR (940^oC) or B25 ATR (930^oC) or biodiesel ATR (960^oC) and after that, CH_4 gas concentration varies in inverse linear proportion with the reformer temperature. As the reformer temperature reduces below 850^oC, syngas production of B25E10D65 ATR declines significantly, because the temperature of the front end catalyst for B25E10D65 ATR is lower than for the reformation of other types of fuels and the reformer temperature directly affects overall temperature profiles across the reformer of B25E10D65 ATR. When combining Figure 59 with Figure 60, it is seen that C_2H_4 and solid carbon concentration for the reformation of each fuel not only have a similar pattern as a function of reformer temperature, but they also both have the instantaneous changes (i.e., C_2H_4 production rate rapidly increases when solid carbon starts to form) under the same threshold temperatures. These results confirm the consistency of the experimental data acquisition from mass spectrometer and the micro-soot meter, and emphasize the strong correlation between ethylene and solid carbon formation. The critical temperatures to form solid carbon are generally consistent with the results of the equilibrium models.

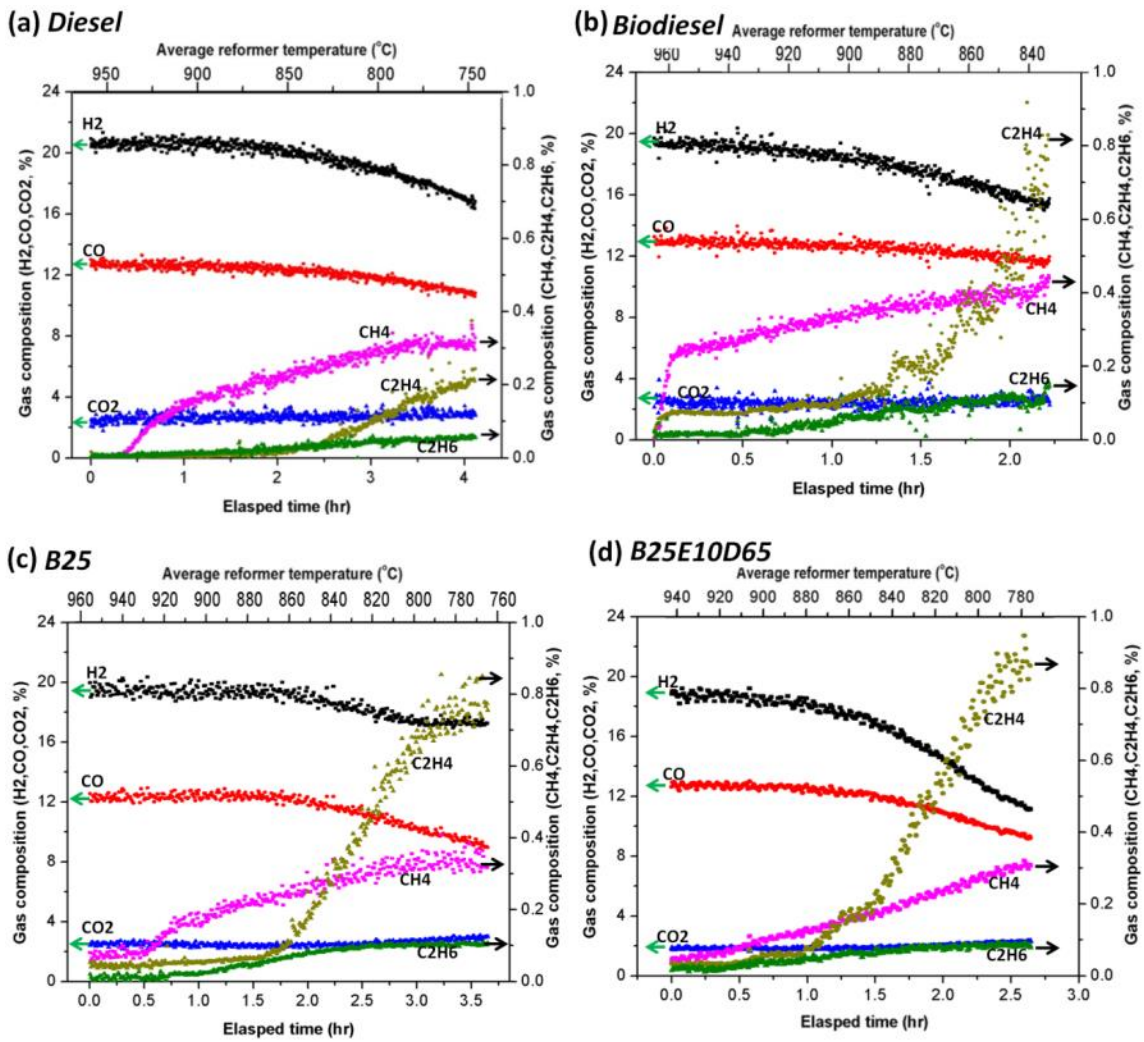

Figure 59: Effect of reformer temperature reduction on gas compositions from ATR of (a) diesel, (b) biodiesel, (c) B25, and (d) B25E10D65

Although the carbon evolution for diesel ATR and biodiesel ATR both behave in a stepwise increment pattern due to reformer temperature reduction, diesel ATR shows a gradual growth of carbon concentration with small magnitudes of sudden jumps prior to the carbon spike at 725^{o}C reformer temperature, while biodiesel ATR tends to frequently have large increments of carbon concentration. This indicates biodiesel with a high molecular weight has higher solid carbon formation rates than diesel, as the reformer temperature reduces and enters the carbon formation zones.

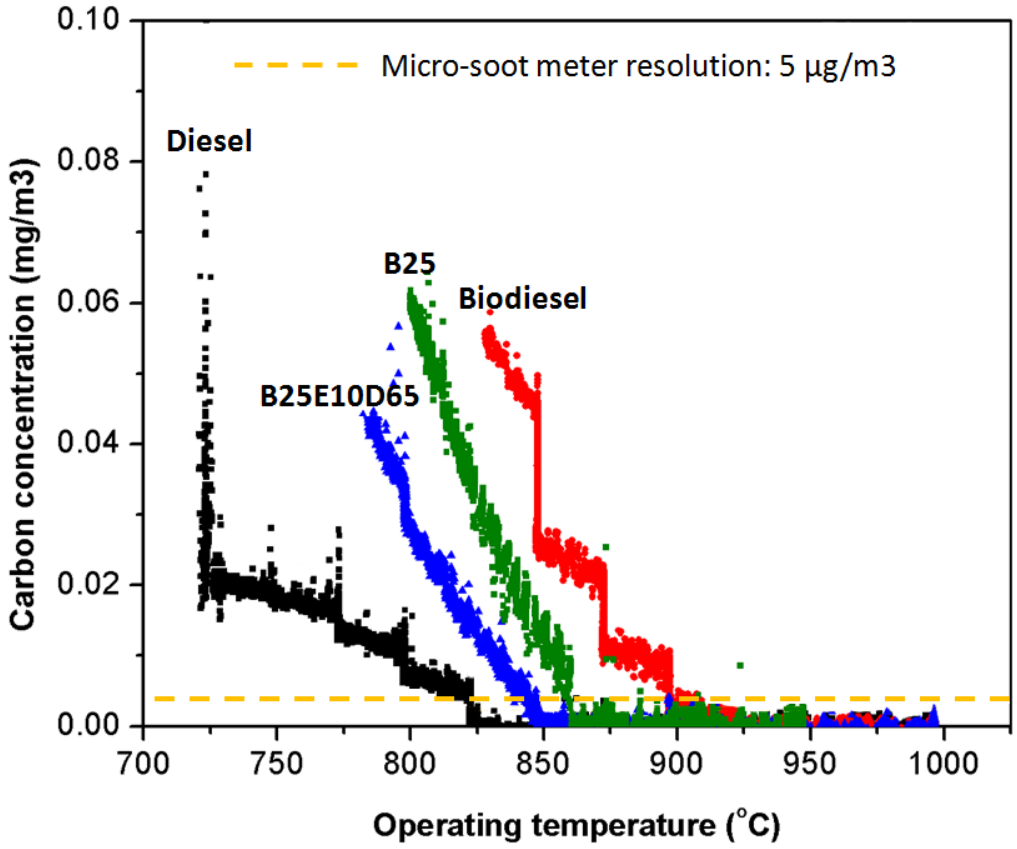

Figure 60: Impact of reformer temperature reduction on solid carbon concentrations from ATR of four studied fuels

Gas Hourly Space Velocity Change

By adjusting the nitrogen flow rate and keeping other parameters constant at the initial test condition, the single-tube reformer enables evaluation of the impacts of GHSV changes ranging from 30,000 to 52,000 hr^{-1}. Figure 61 and Figure 62 show the effects of GHSV changes on the gas composition and carbon concentration effluent from the reformer, respectively, for the ATR of the studied fuels. Although low GHSV increases the residence time of the reactant contact with the catalyst bed and enhances the complete

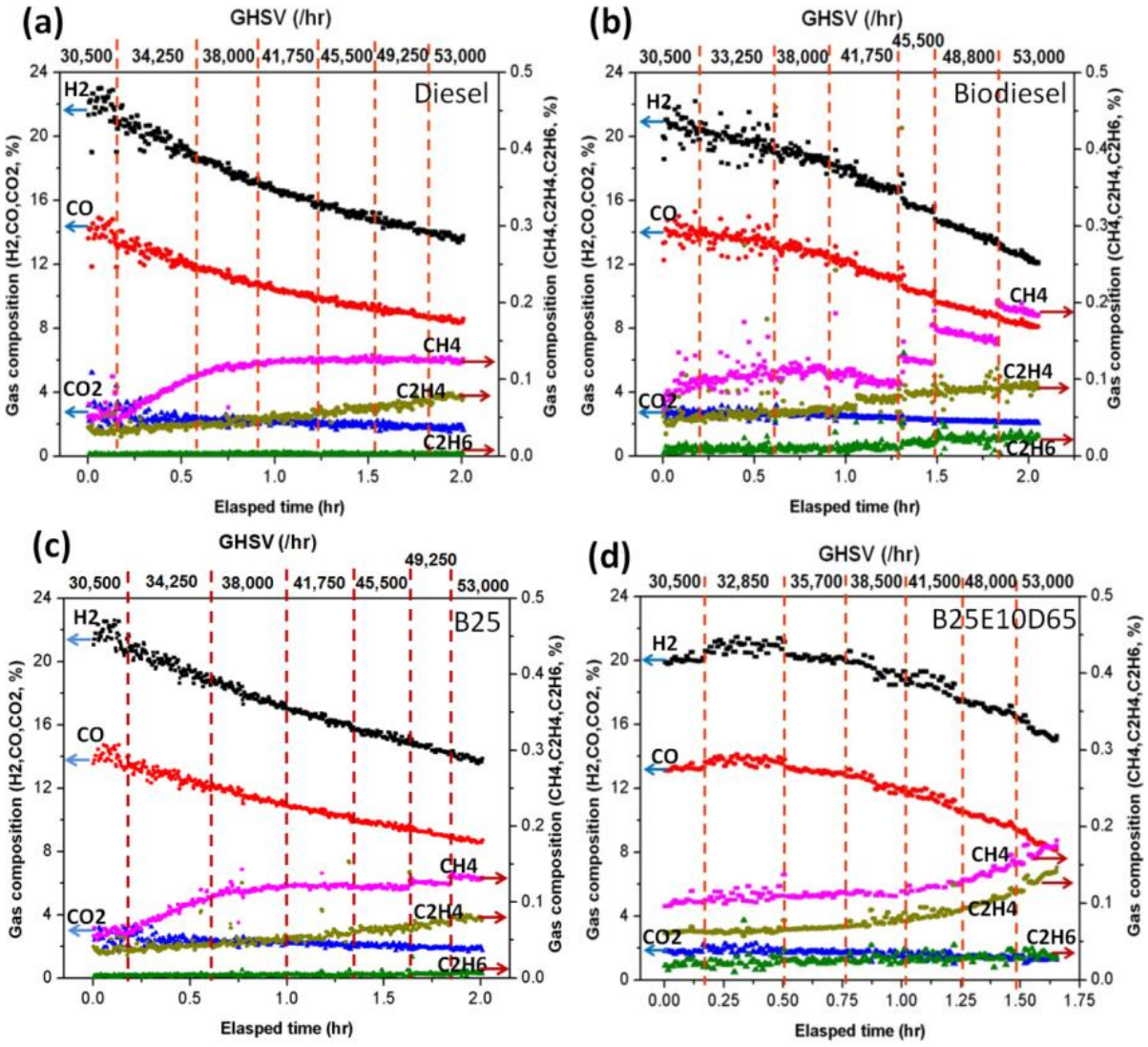

Figure 61: Effect of GHSV change on gas compositions from ATR of (a) diesel, (b) biodiesel, (c) B25, and (d) B25E10D65

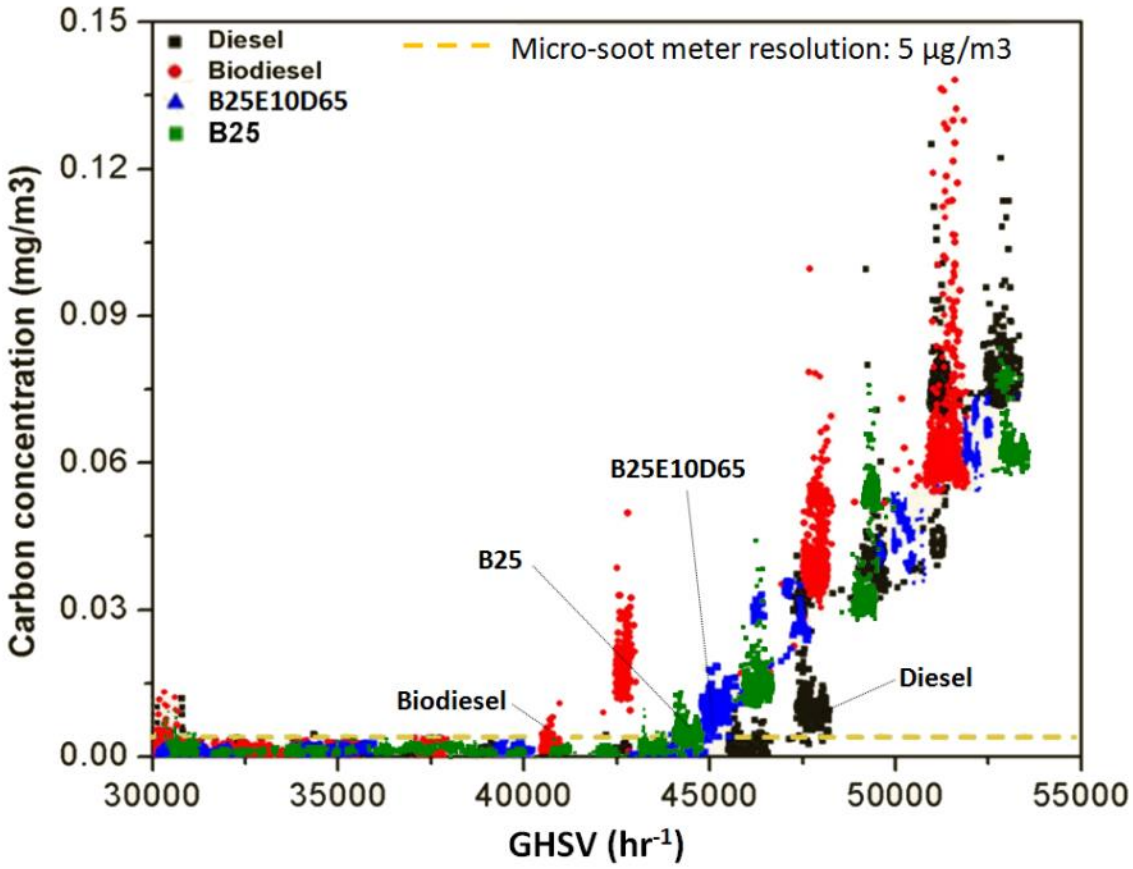

Figure 62: Impact of GHSV change on solid carbon concentration from ATR of four studied fuels

conversion of the fuels (especially for coke precursors such as olefins and aromatic compounds), it limits the production rates of syngas and leads to unstable gas production because of the low flow rate of nitrogen gas to continuously carry the input fuel (see Figure 61). For the ATR of each type of fuel, the concentrations of H_2 and CO are significantly diminished as the GHSV increases, whereas concentrations of light hydrocarbon gases (CH_4, C_2H_4, and C_2H_6) and solid carbon increase. These experimental results are in agreement with the outcomes derived from the kinetic model developed by Berry *et al.* to analyze the effects of the GHSV on the reformation of hydrocarbons [159].

High GHSV increases the production of a series of olefins (e.g., alkenes, dienes, and trienes) and accelerates carbon formation with volatile carbon activities, which may increase the possibility of hydrocarbon fuel breakthrough in the reactor [14,159]. Figure 62 shows that biodiesel ATR (with total O/C = 1.47 and H2O/C = 0.6) has a relatively narrow range of GHSV from 31,250 to 40,000 hr^{-1} to achieve stable reformate performance without forming solid carbon, while the feasible GHSV for diesel ATR ranges from 32,500 to 45,000 hr^{-1}. ATR of B25 and B25E10D65 have a similar GHSV operating range of 31,000 to 44,500 hr^{-1} to maintain stable reformate production.

Correlations between Solid Carbon and Ethylene

Olefinic and aromatic hydrocarbons have been known to be precursors for carbon formation during high hydrocarbon fuel reformation [159]. Ethylene produced by fuel pyrolysis at local fuel-rich areas is easier to convert to solid carbon than other hydrocarbons (e.g., benzene, hexane) and degrades the reformate performance of the reactor. Figure 63 plots the correlations between ethylene and carbon concentration for the ATR of the four fuels studied with respect to each set of parameters (air reduction, reformer temperature reduction, and GHSV changes). Although diesel ATR has low amounts of ethylene production as compared to the ATR of other type of fuels, it has higher carbon concentration, which suggests that there are significant amounts of other compounds besides ethylene in diesel ATR to form solid carbon (e.g., aromatics, naphthenes) [151,159]. For the case of biodiesel, it is shown that high carbon concentration is correlated to a large amount of ethylene, indicating that ethylene is a major contributor to solid carbon formation due to the low content of aromatic

hydrocarbons in biodiesel. B25E10D65 ATR shows relatively less carbon concentration, even with significant amounts of ethylene, which may be due to the lower hydrocarbon molecular weight (molar fractions of diesel, ethanol, and biodiesel are 51%, 34%, and 15%, respectively) than other studied fuels. In order to extrapolate the relationships between ethylene and carbon content associated with different hydrocarbon fuels in term of each set of variables, nonlinear regression was applied to fit the trends of the experimental data points. From the equilibrium analysis of carbon formation and ethylene production as functions of O_2/C and reformer temperature shown on Figure 54, exponential regression was selected to fit the data from the air reduction tests (Figure 63a) while polynomial regressions were applied to fit the cases with temperature reduction (Figure 63b) and GHSV changes (Figure 63c). The trend-lines fit well with the experimental data, as reflected in the high R^2 values.

(a)

Fuel	Fitting mode: Logistic Regression	R-Square
Diesel	y = 0.2988/(1+exp(-20.0718*(x-0.47727)))	0.975
B25	y = 0.23638/(1+exp(-9.59129*(x-0.60693)))	0.951
B25E10D65	y = 0.08278/(1+exp(-10.8967*(x-0.64621)))	0.963
Biodiesel	y = 0.23807/(1+exp(-10.4855*(x-0.85879)))	0.969

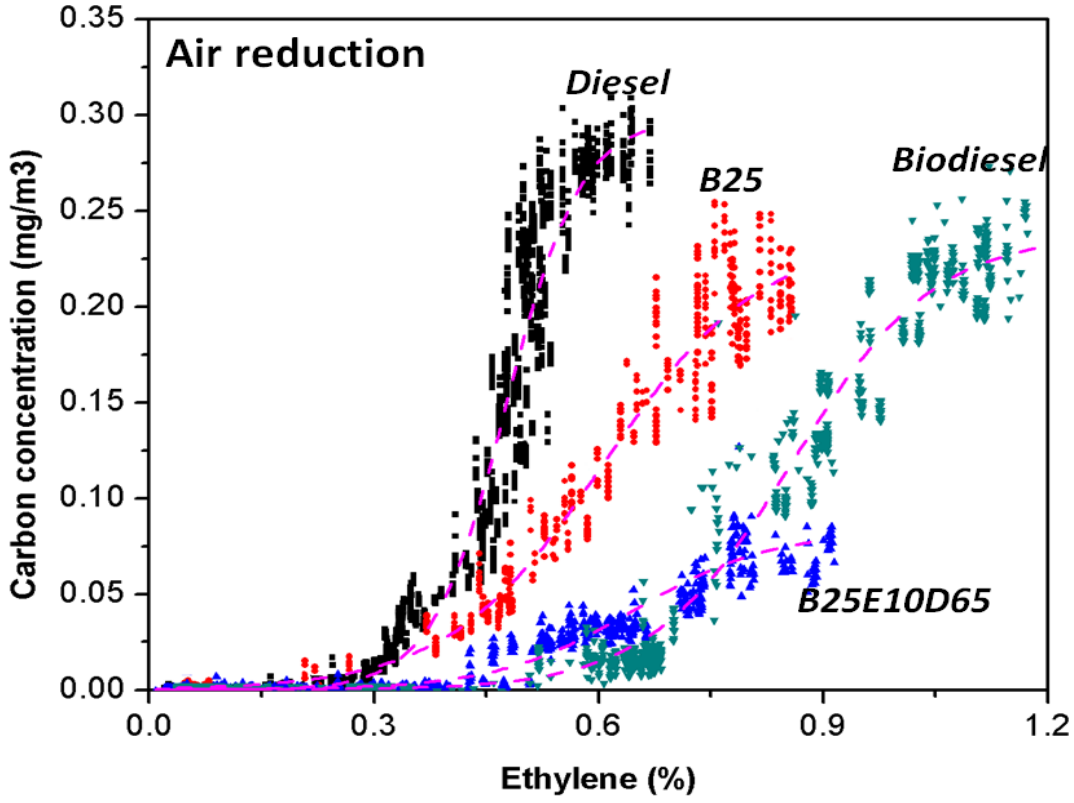

(b)

Fuel	Fitting mode: Polynomial Regression	R-Square
Diesel	y = 0.907*x^2+0.0771*x-0.002	0.955
B25	y = 0.0064*x^2+0.1406*x-0.0134	0.968
B25E10D65	y = 0.0229*x^2+0.0508*x-0.0054	0.972
Biodiesel	y = 0.0165*x^2+0.0463*x-0.0006	0.985

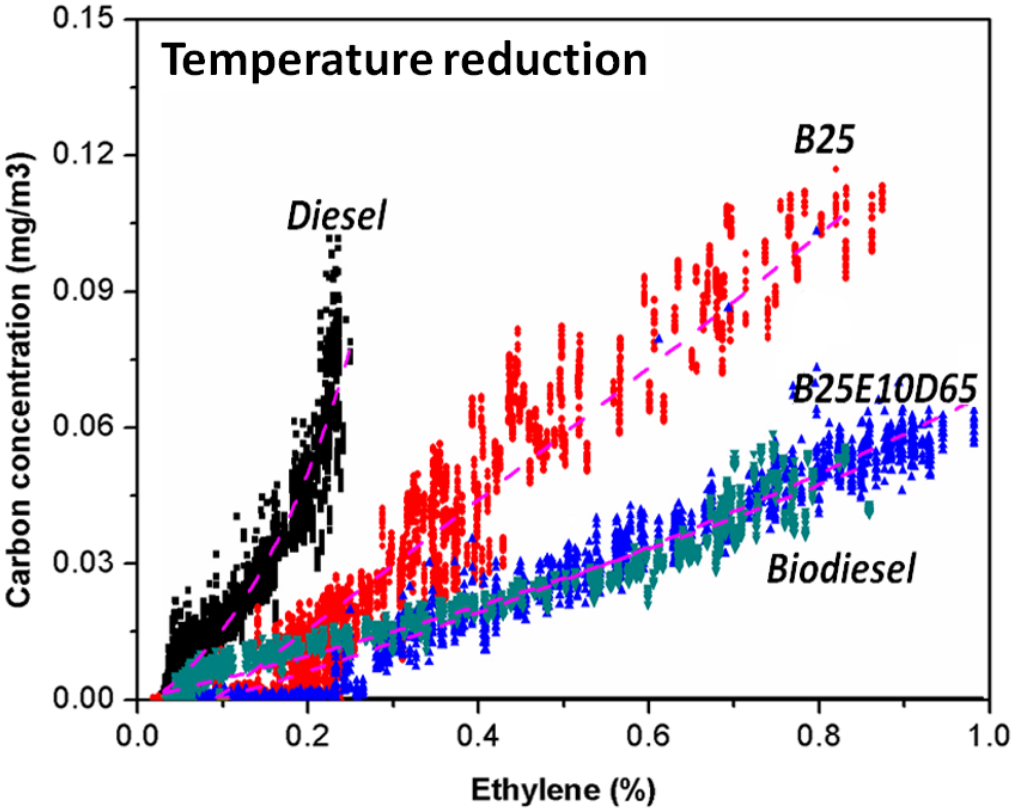

(c)

Fuel	Fitting mode: Polynomial Regression	R-Square
Diesel	y = -18.502*x^2+4.2104*x-0.1246	0.979
B25	y = 18.059*x^2-0.0956*x-0.0438	0.973
B25E10D65	y = -8.0538*x^2+2.6683*x-0.1367	0.965
Biodiesel	y = 2.6966*x^2+0.786*x-0.0477	0.984

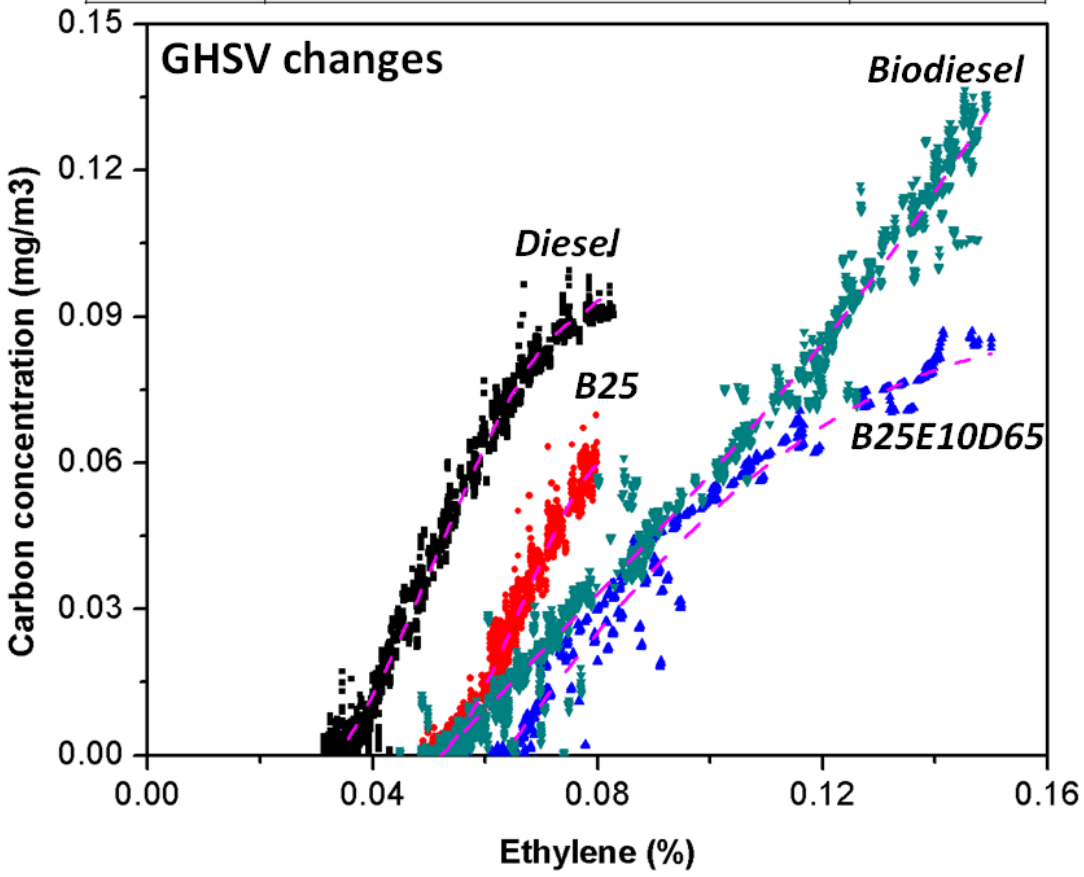

Figure 63: Correlations between ethylene and solid carbon concentration associated with (a) air reduction, (b) temperature reduction, and (c) GHSV changes

4.4.5. Summary

An experimental study of autothermal reforming for SOFC-APU applications was conducted with diesel blended with biodiesel fuels (B25 and B25E10D65). Diesel ATR and biodiesel ATR were considered as two baselines. The reformer conditions were

initialized with total O/C = 1.47, H_2O/C = 0.6, and GHSV = 34,120hr^{-1} at 950^oC reformer temperature and three sets of experimental tests were conducted to evaluate the effects of key reforming parameters (input air flow, reformer temperature, and GHSV). A customized nozzle integrated with a micro-size porous device was designed to finely atomize the input hydrocarbons and promote the homogenous mixing of fuel, water, and air to avoid hydrocarbon fuel self-pyrolysis prior to entering the reactor. The experimental investigations complimented with the thermodynamic modeling of fuel reformations helps effectively optimize the onboard reforming conditions of each type of fuel. Due to the high molecular weight of hydrocarbon compounds, biodiesel requires more oxidants (air/water) and higher operating temperature than diesel in order to mitigate the solid carbon formation during fuel reformations. Adding ethanol to biodiesel and diesel blends not only improves the fuel specifications (e.g., viscosity, poor fuel performance at low temperatures), but also alleviates the solid carbon formation during blended fuel reformations and reduces the occurrences of hot spot in the catalyst bed, which enhance the durability of the reformer. A photo-acoustic based AVL micro-soot meter was applied to determine the dynamic carbon particle concentration in the effluents from the reformer. Strong correlations between ethylene and carbon formation were observed in the reformation of studied fuels and they indicate the major contributor of solid carbon formation for biodiesel ATR is ethylene while there are likely significant amounts of other compounds (e.g., aromatics, naphthenes) besides ethylene that serve as carbon precursors in diesel ATR. This work has demonstrated that biodiesel, B25, and B25E10D65 could serve as promising alternative fuels for SOFC-APU applications in transportation sectors, if their operating conditions are well controlled within the carbon-

free regime. The results of these experiments are based only on the reformer and SOFC-APU system under steady-state conditions, and challenges encountered in actual applications (e.g., system start-up/shut-down, auto-ignition) are beyond the scope of this work. Furthermore, robustness of the reforming process needs to be further improved in order to comprehend real-world conditions (e.g., feedstock variations).

V. CONCLUSIONS AND RECOMMENDATIONS FOR FUTURE WORK

Bio-fuels such as ethanol and biodiesel are now being blended with conventional petroleum-based fuels and used in mobile applications, and bio-fuel use is projected to be continuously increasing in the near future. Fuel cells have been gradually deployed in the transportation and stationary power sectors because of their high energy conversion efficiency. Catalytic reformer technology enables the conversion of hydrocarbons to produce hydrogen rich-stream fuels, and thus facilitates bio-fuel applications in fuel cell-based systems. The combination of bio-fuels with fuel cells provides a potential pathway to low net GHG emissions power generation. When the bio-fuels derived from waste feedstocks, the economic, environmental, and social benefits are especially compelling.

Solid oxide fuel cell (SOFC) systems have been proposed for use as auxiliary power supply units during diesel truck idling period due to their high energy efficiency and low environmental impacts. However, a systematic analysis of bio-fuel options for SOFC applications has not previously been well explored in the open literature. Therefore, it was considered necessary to conduct a study to assess bio-fuel applications in SOFC systems from environmental, economic, and technological perspectives.

Chapter II demonstrated a methodology that integrated life cycle assessment (LCA) with thermodynamics to overcome the challenge of data acquisition during environmental assessment. This approach was applied to evaluate the environmental impacts of bio-fuel derived from waste biomass and bio-fuel consumption in SOFC-APUs. Results suggest that biodiesel from waste cooking oil and landfill gas from

municipal solid waste tend to have relatively low environmental impacts in term of greenhouse gas emission and total energy consumption. To generate 1 kWh auxiliary electricity, the total energy consumption of biodiesel-based and landfill gas-based SOFCs are 9.6 and 9.7 MJ, respectively, as compared to 13.8 MJ for conventional production with the full diesel engine. It is therefore evident that these two bio-fuels could be the promising options for SOFC-based systems. The results from this chapter also show biodiesel used in SOFC-APU system has significantly less environmental impact than conventional diesel, which helps promote the application of biodiesel blended with diesel. Therefore, Chapter III and IV investigated these blends from economic and technological aspects.

Chapter III developed a model to specify a bio-fuel blends by simultaneously capturing fuel market disturbances, bio-fuel tax credits, policy changes, and fuel properties when maximizing the production system profitability using the multi-objective optimization technique. The optimum composition of biodiesel-ethanol-diesel ternary blends was identified as 25% biodiesel blended with 10% ethanol and 65% of diesel. The model suggests the government policy of simultaneously implementing bio-fuel tax credits and mandates may not have a higher contribution to promoting bio-fuel production than the case with only tax credits with the goal of profit maximization. By utilizing waste-feedstock based bio-fuels in BED blends, the fuel producer can realize the benefits of reducing product cost and gaining high optimal profit. With the multi-objective optimization technique, the optimal composition of BED blend was determined as B25E10D65 and it was proposed to use this blend in applications of truck traveling

and idling with SOFC-APUs, which led to the analysis of B25E10D65 fuel reformation in the following chapter.

Chapter IV investigated the autothermal reforming performance of various bio-fuels/blends (e.g., diesel, biodiesel, biodiesel-diesel, and biodiesel-ethanol-diesel) under different operating condition, using both experimental tests and thermodynamic modeling. Several techniques were also described to overcome the technical barriers of heavy hydrocarbon catalytic reformation (such as coke formation, sintering, fuel-pyrolysis). A customized nozzle based on the micro-explosion method was designed and integrated with the single-tube reformer apparatus to improve fuel atomization and reforming efficiency. Carbon formation boundaries in the ATR of the various considered fuels were future identified and the correlations between solid carbon concentration and ethylene were explored. Biodiesel and bio-blends were found to process relatively low aromatics and naphthenes and they could be the viable fuel options for SOFC-APU system as long as the reforming conditions were achieved to avoid solid carbon formation, which have been elucidated in this study. One of the key findings in this chapter suggests that B25E10D65 can be a promising fuel used in SOFC-based APUs to supply auxiliary electricity service during truck idling and it has a higher syngas production than biodiesel under the same catalytic reforming condition (temperature, total O/C, H_2O/C, and GHSV). The customized nozzle used for fuel vaporization and oxidant mixing achieves homogenous atomization of input hydrocarbon fuels (e.g., diesel, biodiesel, B-diesel, and B25E10D65), and improves the performance of fuel catalytic reformation. Given the same operating condition (reforming temperature, total

O/C, H_2O/C, and GHSV), the hydrocarbon reforming performance follows the trend of diesel>B25E10D65>B-diesel>biodiesel (i.e., diesel reformation has highest syngas production, lowest risk of carbon formation, and least possibility of hot spot occurrence).

Future Work

The key findings from this dissertation have provided a foundation for further experimental and modeling studies, which could potentially facilitate bio-fuel applications in fuel cells and ultimately the commercialization of fuel cell-based systems. Some future directions are proposed as follows:

- **SOFC-based stationary applications**: Chapter II illustrated that besides biodiesel, landfill gas also has low environmental impacts. But because there are lacks of system compatibility, it is challenging to utilize gaseous fuels in transportation sectors. Thus, the present dissertation does not consider landfill gas as the fuel for SOFC-APUs. However, the SOFCs for stationary application have been widely proposed due to their high conversion efficiency with combining heat and power. Future efforts will be required to evaluate the landfill gas for stationary SOFCs applications from environmental, economic, and technological aspects.
- **Catalyst developments**: Chapter IV suggests the biodiesel based fuels have lower concentrations of aromatics and naphthenes, which require active noble metal catalyst to completely reform, than conventional diesel. A catalyst based on 2 wt.% of rhodium/ceria-zirconia catalyst wash-coated ceramic monoliths were used in this study for the reformation of all considered fuels. Therefore, it is intriguing to explore the catalyst compositions (either lowering the noble metal content or switching to

other types of catalyst such as perovskite or pyrochlore) for biodiesel reformation after sufficient vaporization using the customized nozzle.

- **Expanded assessment of bio-fuel production from waste-based feedstock**: The present dissertation describes several bio-fuel production path derived from waste biomass, which includes ethanol from corn stover, biodiesel from waste cooking oil, and landfill gas from municipal solid wastes. There are other attractive bio-fuel production paths, such as syngas from gasification/pyrolysis of wood biomass and biogas production from anaerobic digestion of food wastes. By conducting an expanded study on comparing various waste-based bio-fuel production approaches (from technological, environmental, and economic perspectives), practical bio-fuel production paths can be determined given a specific geographical region. The methodology of thermodynamic process simulation developed in this study can also be applied in these bio-fuel production paths.
- **Comprehensive economic & environmental analysis of SOFC-based stationary power systems**: Although solid oxide fuel cells have many advantages (e.g., high system efficiency, low environmental impact, and fuel flexibility), it is still difficult to compete with the conventional incumbent technologies due to the high system manufacturing cost. By utilizing waste-based bio-fuels (e.g., biogas) and developing high fuel conversion technologies, SOFC-based stationary system may enable reducing the total cost ownership. Therefore, a comprehensive study on analyzing the economic and environmental aspects of SOFC would help determine the potential benefits of fuel cell systems, especially in the use phase.

APPENDICES

A.1. Supporting Information for Life Cycle Assessment of Bio-fuel Options

Petroleum diesel from crude oil

New York State (NYS) is geographically located in Petroleum Administration for Defense Districts (PADD) I with 2.68% crude oil domestic extraction and 97.32% foreign import [190]. The GREET 1.8d model was applied to evaluate ultra-low sulfur diesel (ULSD) refinery from cruel oil and the delivery modes from well to pump [44]. In the crude oil refinery process, several main products (gasoline, jet fuel, diesel, and liquid petroleum gas) are refined. The energy use and greenhouse gas (GHG) emissions contributed from biodiesel fuel in the upstream (crude oil extraction, feedstock delivery, and refinery) were based on the mass allocation [190]. In order to supply a unit of auxiliary electricity to the truck, diesel fuel can be either direct engine combusted (Figure A1) or integrated with a solid oxide fuel cell auxiliary power unit (SOFC-APU, Figure A2). The SOFC stacks need to maintain 78% hydrogen fuel utilization in order to be consistent with the previous assumption of 30% net system efficiency for the SOFC-APU. The leftover effluent gases from stacks are combusted to supply heat for the reformer. Partial steam from exhaust stream is also recycled as an input for fuel autothermal reforming (see Figure A2).

Biodiesel from waste cooking oil (WCO)

Eighty-eight restaurants near the Rochester Institute of Technology (RIT) campus were selected and the WCO feedstock collected by a light duty truck following with a 12 mile path A-B-C-D (see Figure A3). Even though it is beyond the system boundary of

biodiesel production, it is noteworthy to mention that organic solid wastes (OSW) filtered from WCO can serve as a potential feedstock for biogas production with anaerobic digestion. Biopro^{TM} 380 Automated Biodiesel Processor (Springboard Biodiesel, LLC, Chico, CA) integrates several biomass processes (including dehydration, esterification reaction, transesterification reaction, water washing, and dehydration, see Figure A4). It takes 13 hours for WCO to convert into biodiesel for each run. Water consumption and waste water off-site treatment were also quantified in the flow diagram. The remaining methanol from the distillation step was reused for the next test run.

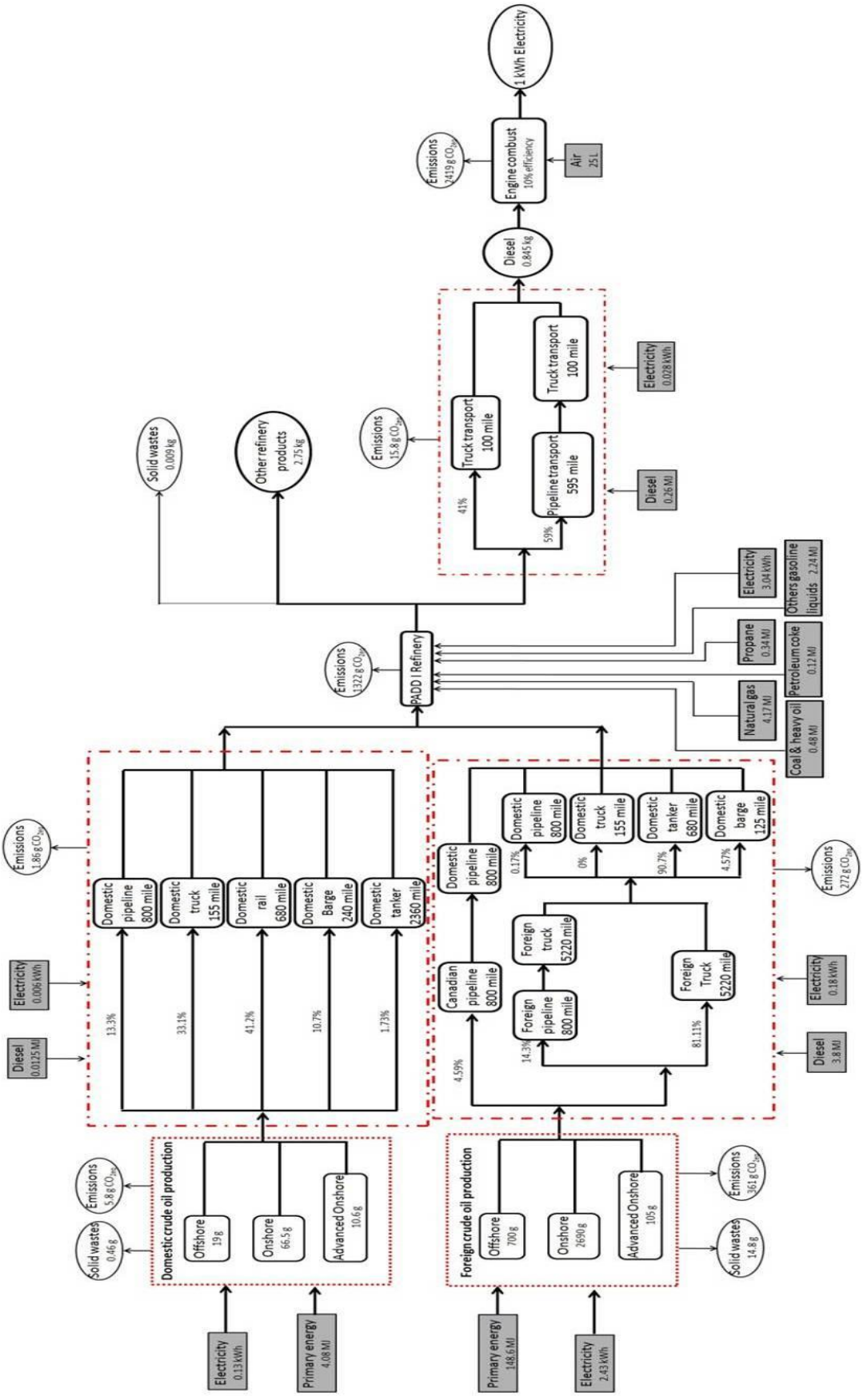

Figure A1: Flow diagram of diesel engine combustion to generate auxiliary electricity in NYS

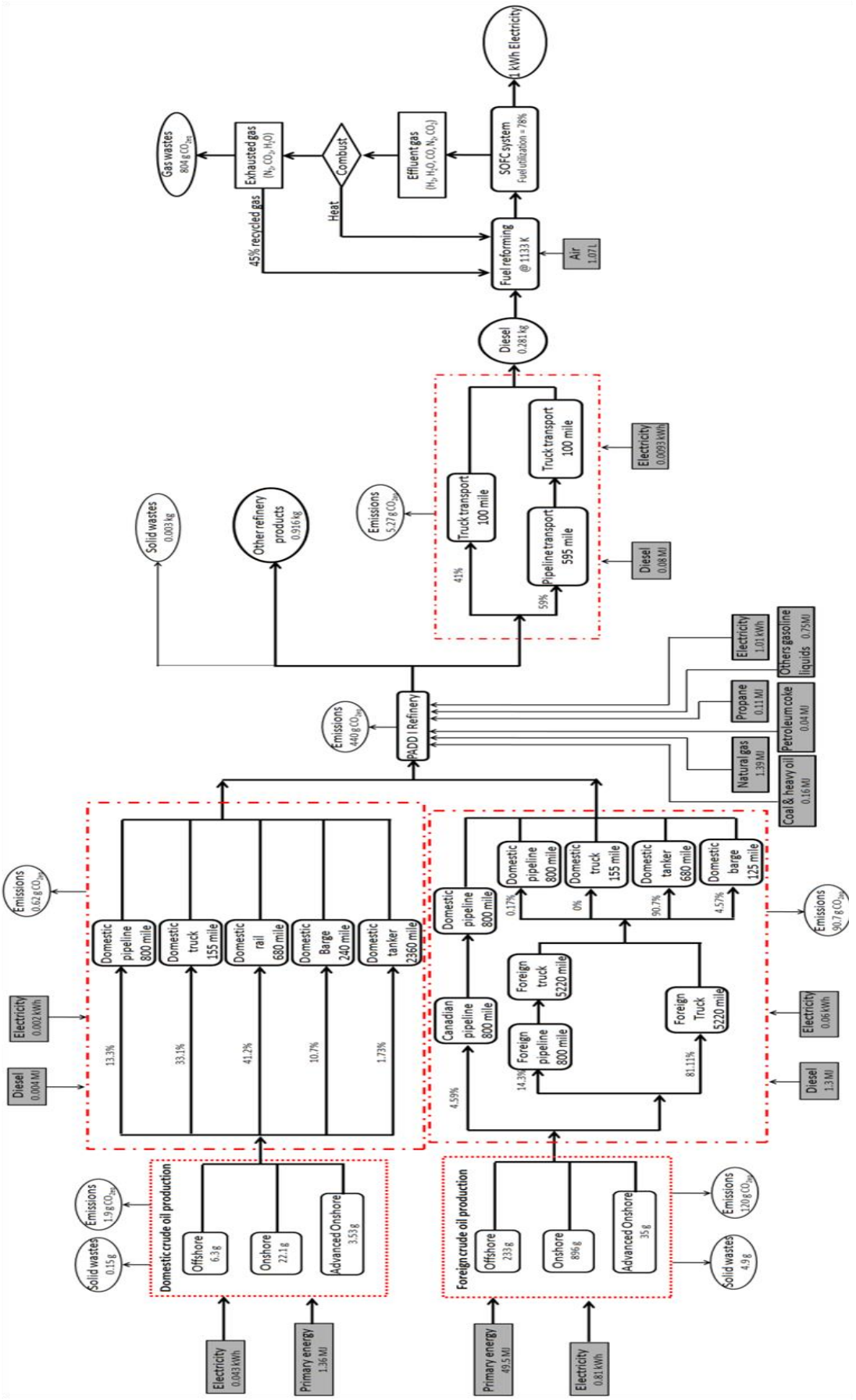

Figure A2: Flow diagram of diesel SOFC-APU to generate auxiliary electricity in NYS

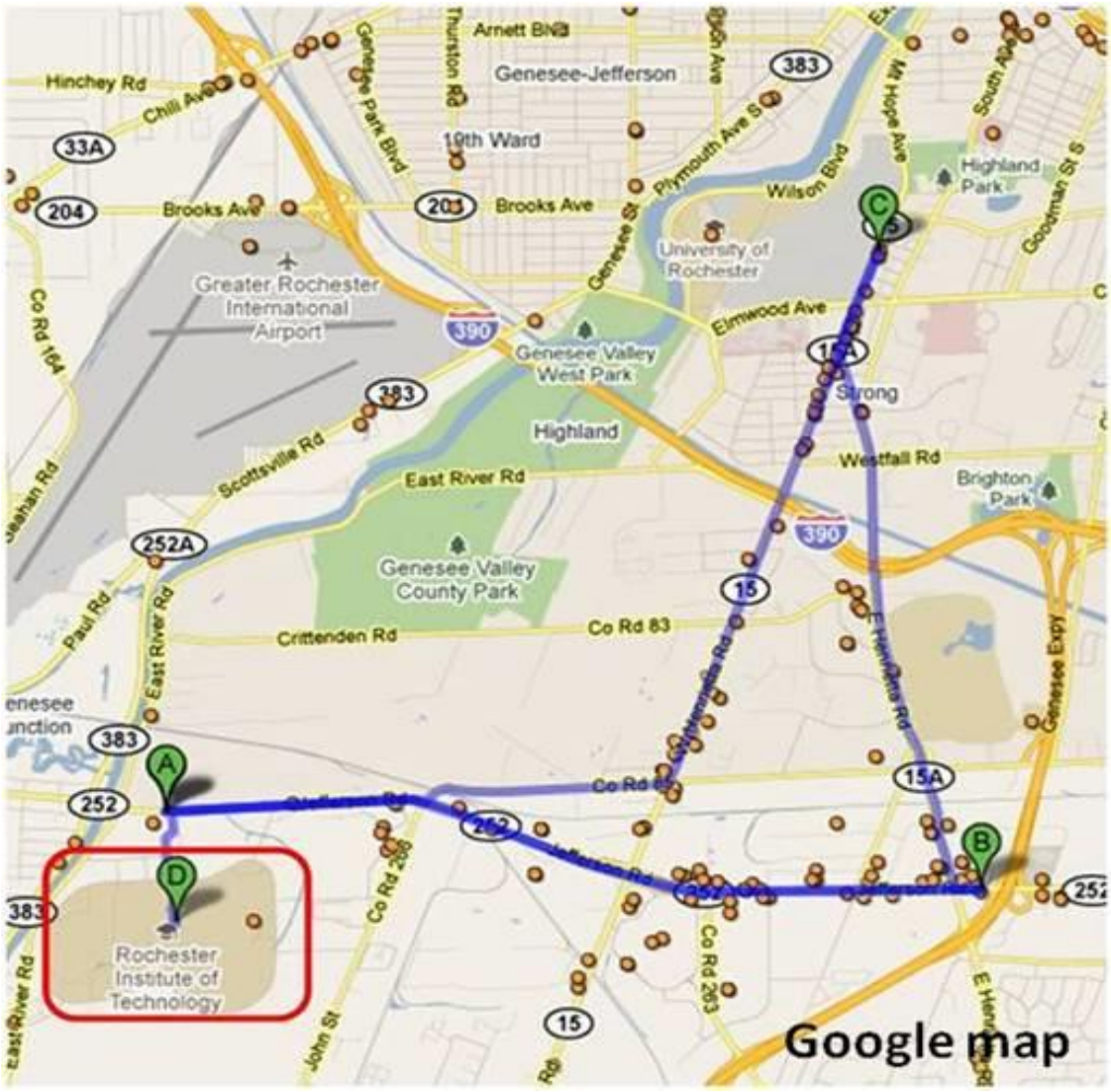

Figure A3: Waste cooking oil collecting pathway from restaurants near RIT campus

Ethanol from corn stover (CS)

The National Renewable Energy Laboratory (NREL) has developed a lignocellulosic biomass treatment process using co-current dilute acid prehydrolysis followed with enzymatic saccharification and co-fermentation [30]. By applying the same biomass processing techniques on this work, ethanol derived from CS was used as a fuel for truck auxiliary electricity applications with a SOFC-APU system (see on Figure A5).

Wojnar *et al.* have suggested that the average truck travel distance for CS feedstock delivery in NYS is 24 mile [191], however, the roundtrip travel pattern should be considered even if the truck returns empty [41]. An on-site waste water treatment was also considered in the system flowchart.

Compressed natural gas (CNG) from municipal solid waste (MSW)

Figure A6 illustrates the flow diagram of CNG derived from MSW with the SOFC-APU system. Landfill gas (LFG) is generally produced in an anaerobic digestion process from organic solid wastes (OSW) in MSW by controlling the operating conditions (e.g. wastes composition, moisture, oxygen content, and temperature). Even though LFG is monitored and shown with undetectable hydrogen sulfide content from the landfill site studied in this work, a pre-purification process is needed to mitigate hydrogen sulfide in that the compositions of LFG are also geographically varied and the SOFC-APU system is vulnerable to sulfur-containing gases. Because LFG is lighter than air, it diffuses and moves upward to the landfill surface [47]. After LFG is purified and carbon dioxide removal, it is compressed up to 27,571 kPa in the truck delivery tank and no additional energy consumption occurs during CNG the transfer process from the truck tank to gas stations because the tank pressure is high enough compared to the local distribution system (1480 kPa) [60].

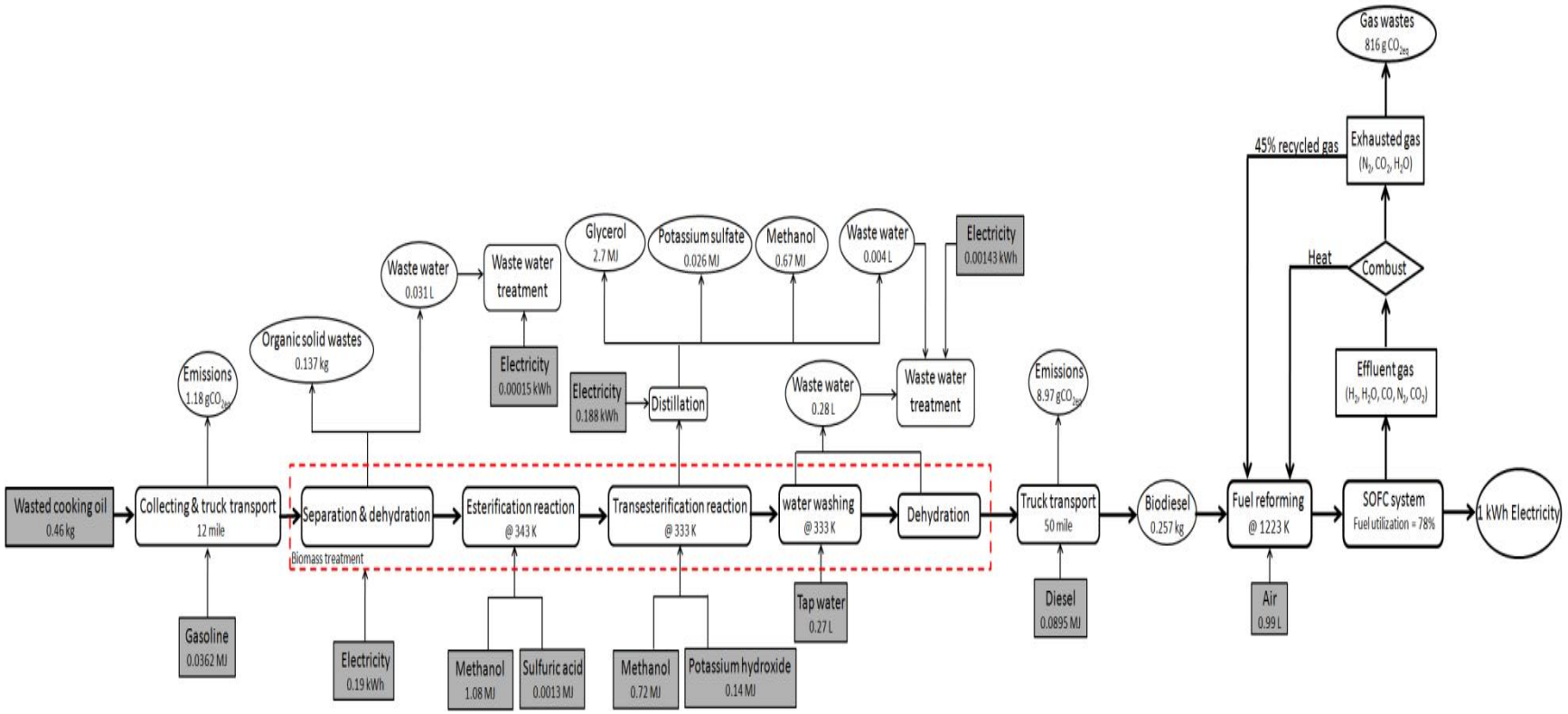

Figure A4: Flow diagram of biodiesel SOFC-APU pathway derived from WCO

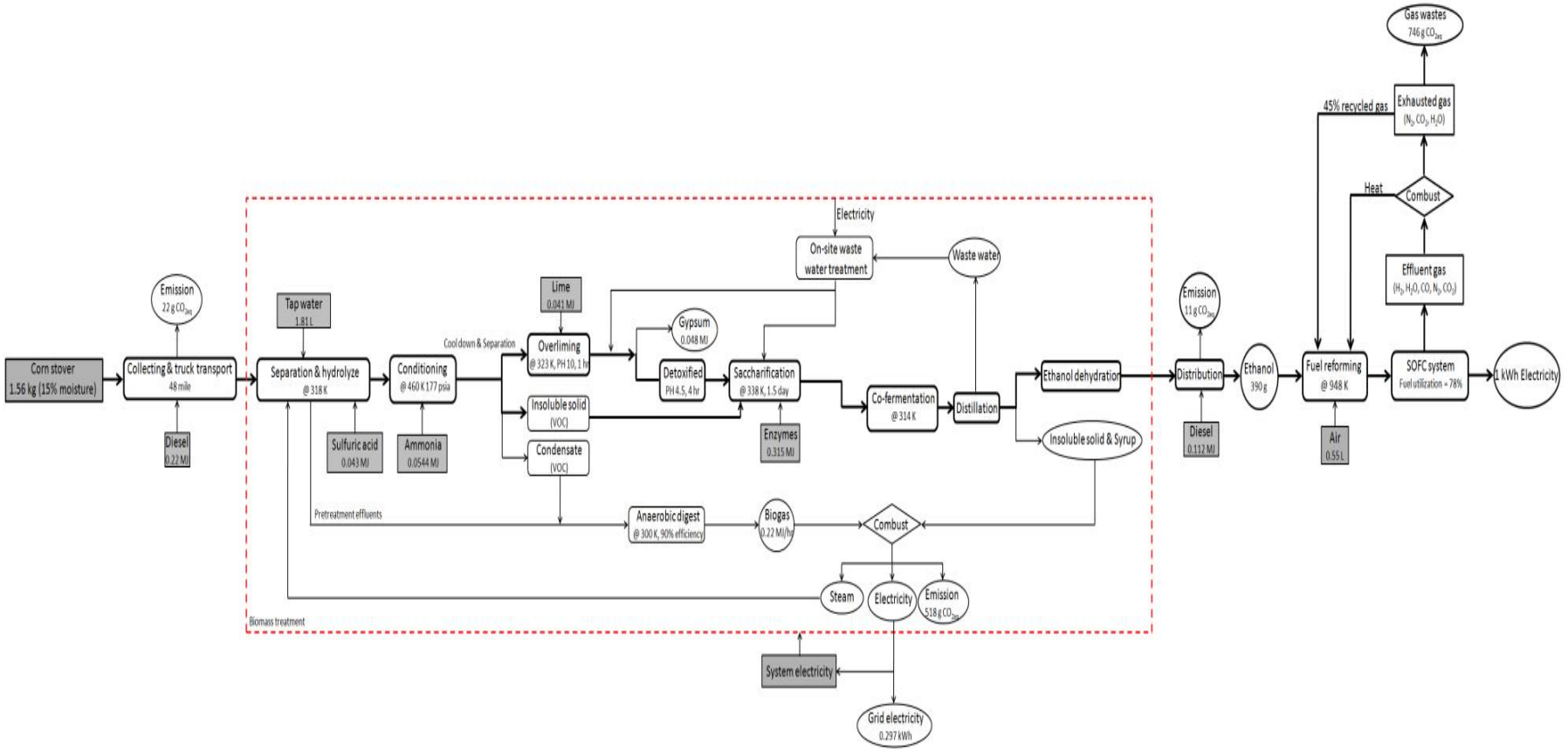

Figure A5: Flow diagram of ethanol SOFC-APU pathway derived from CS

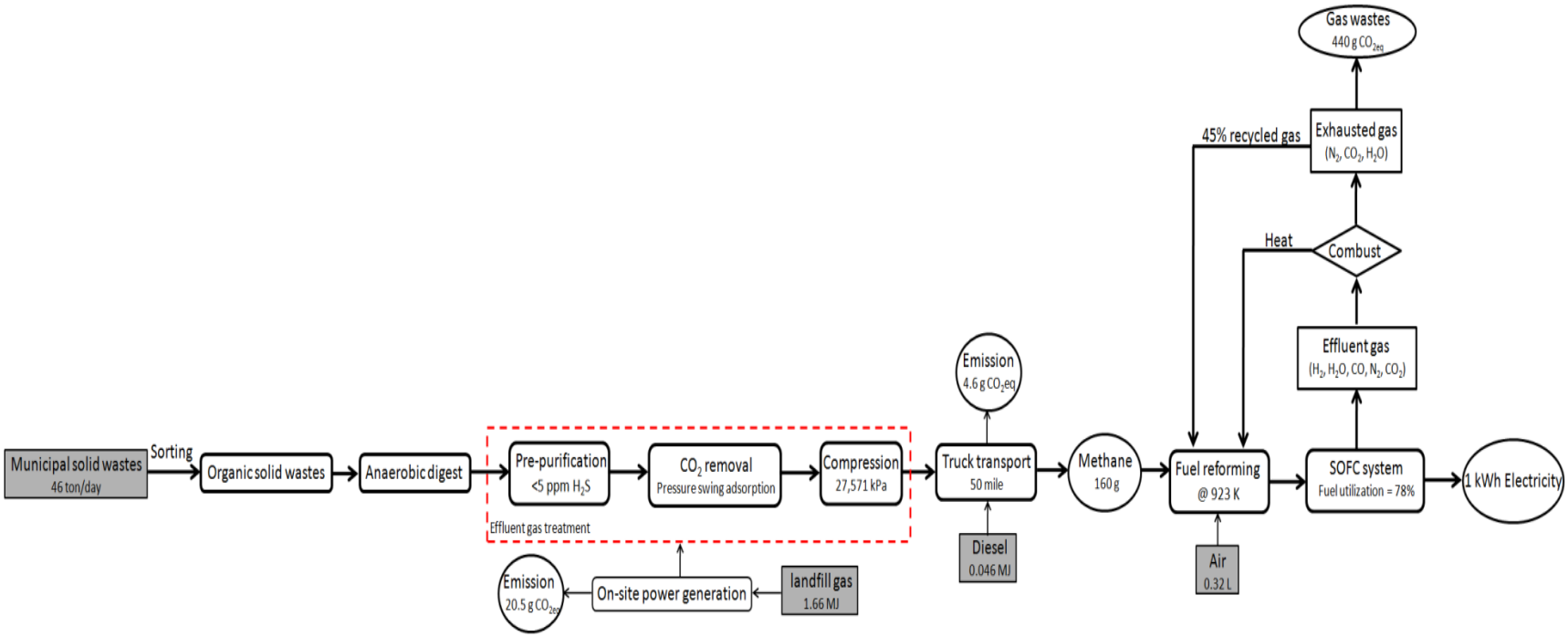

Figure A6: Flow diagram of CNG SOFC-APU pathway derived from MSW

A.2. Supporting Information for Optimization of Biodiesel-Ethanol-Diesel Blends

A.2.1. Mixing rule for hydrocarbon blends

Several mixing rules that are widely used in petroleum refining industries to predict the properties of blended fuels are listed below.

Kay's mixing rule [81,87,192]

$$\gamma_{mix} = \sum_{i}^{3} f_i * \gamma_i \tag{A1}$$

where γ_{mix} and γ_i are the properties of final mixed fuel and that of i^{th} raw input component, respectively, f_i is the volumetric fraction of i^{th} raw input component.

Semilogarithmic mixing rule [67,81,193]

$$\ln \gamma_{mix} = \sum_{i}^{3} f_i * \ln \gamma_i \tag{A2}$$

Grunberg-Nissan equation [87,88]

$$\ln \gamma_{mix} = \sum_{i}^{3} f_i * \ln \gamma_i + \sum_{i}^{3} \sum_{k}^{3} f_i * f_k * G_{ik} \tag{A3}$$

G_{ik} is the interaction term of i^{th} and k^{th} input fuel components, $G_{ik} = 0$ if $i = k$.

After reviewing previous work reported by other researchers on either binary blends or ternary blends of biodiesel, ethanol, and diesel, the experimental data of fuel properties were collected and compared with the predicted fuel specifications derived from different mixing rules. Absolute average deviation (AAD, Eq.(A5)) was used as a

measurement to determine the degree of difference between the predicted data and the experimental results:

$$D_i = \frac{R_P - R_E}{R_E} * 100\% \tag{A4}$$

$$AAD = \frac{\sum_{i}^{N} |D_i|}{N} \tag{A5}$$

where N is the number of data point, and R_p and R_E are the predicted and experimental value, respectively.

Kinematic viscosity (ASTM D445)

The most promising mixing rule originally proposed by Lederer *et al.* shown as Eq. (A6) enable achieving relatively low absolute error (<3%) between predicted results and experimental data to evaluate the kinematic viscosity of heavy oil and n-decane blends [89,194]. Eq.(A6) is further modified in order to be applied on ternary blends, as Eq.(A7)

$$\ln \nu_{mix} = \left(\frac{\alpha f_o}{\alpha f_o + f_s}\right) \ln \nu_o + \left(1 - \frac{\alpha f_o}{\alpha f_o + f_s}\right) \ln \nu_s \tag{A6}$$

$$\ln \nu_{mix} = \left(\frac{\alpha f_D}{\alpha f_D + \beta f_B + f_E}\right) \ln \nu_D + \left(\frac{\beta f_B}{\alpha f_D + \beta f_B + f_E}\right) \ln \nu_B + \left(\frac{f_E}{\alpha f_D + \beta f_B + f_E}\right) \ln \nu_E \tag{A7}$$

where ν_{mix}, ν_D, ν_B, and ν_E are the kinematic viscosities of the blends, diesel, biodiesel, and ethanol; f_D, f_B, and f_E are the volumetric fractions of diesel, biodiesel, and ethanol in the blends; α and β are both empirical constants.

Four different mixing rules including Kay's, Semilogarithmic, Grunberg-Nissan, and modified Lederer were applied to predicting the kinematic viscosity binary or ternary blends of diesel, biodiesel, and ethanol. Figure A7 shows the deviation of the predicted results and the empirical data presented in other reports. As compared to other mixing rules, modified Lederer equation shows the lowest AAD (4.73%), indicating a good fit of predicted results and empirical data. It is also worthwhile to mention that the modified Lederer equation shows a relatively low ADD (1.85%) for ternary blending. Thus, the modified Lederer mixing rule is chosen for kinematic viscosity prediction in this study.

Because kinematic viscosity is a temperature dependent factor and the practical BED blends are utilized under a wide temperature range environment, temperature conditions from 0 to 70 ^{o}C are integrated with the modified Lederer mixing rule to analyze the fuel viscosity at specific temperatures. After determining the temperature effect on the viscosity change of ethanol, biodiesel, and diesel from other report [85,194,195], the kinematic viscosity extrapolated from the modified Lederer Eq.(S7) was plotted as the function of temperature changes, as shown in Figure A8.

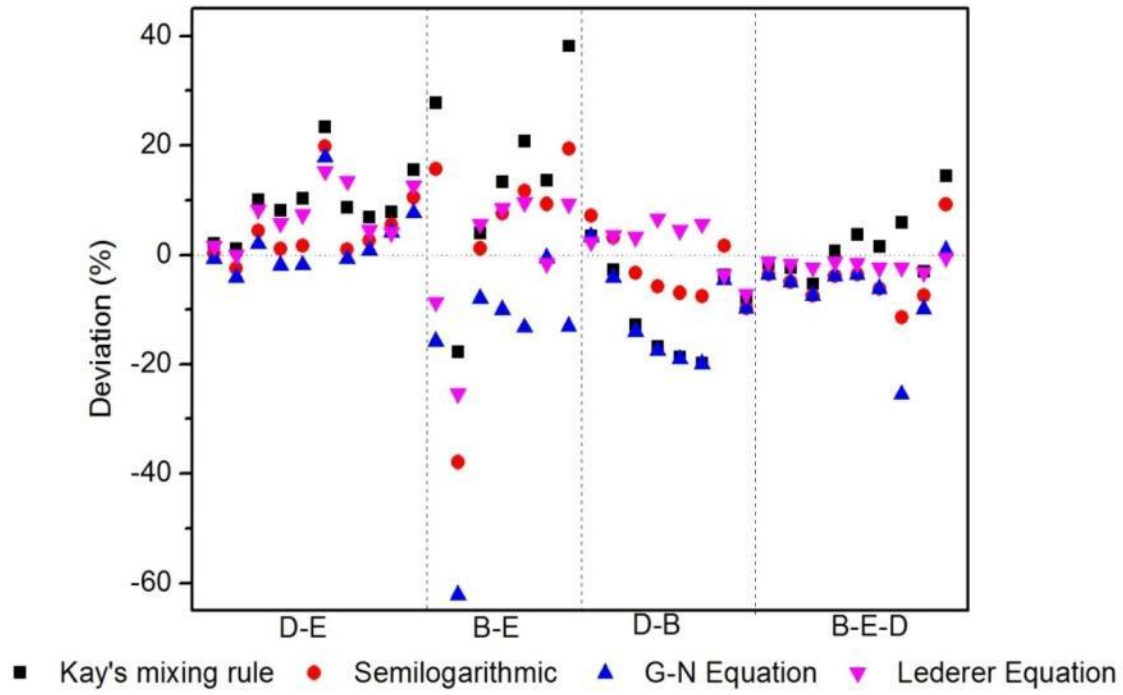

Figure A7. Deviations of kinematic viscosity between different mixing rules prediction and experimental data, Kay's (AAD: 10.42%), Semilogarithmic (AAD: 7.49%), Grunberg-Nissan (AAD: 9.48%), and Lederer (AAD: 4.73%)

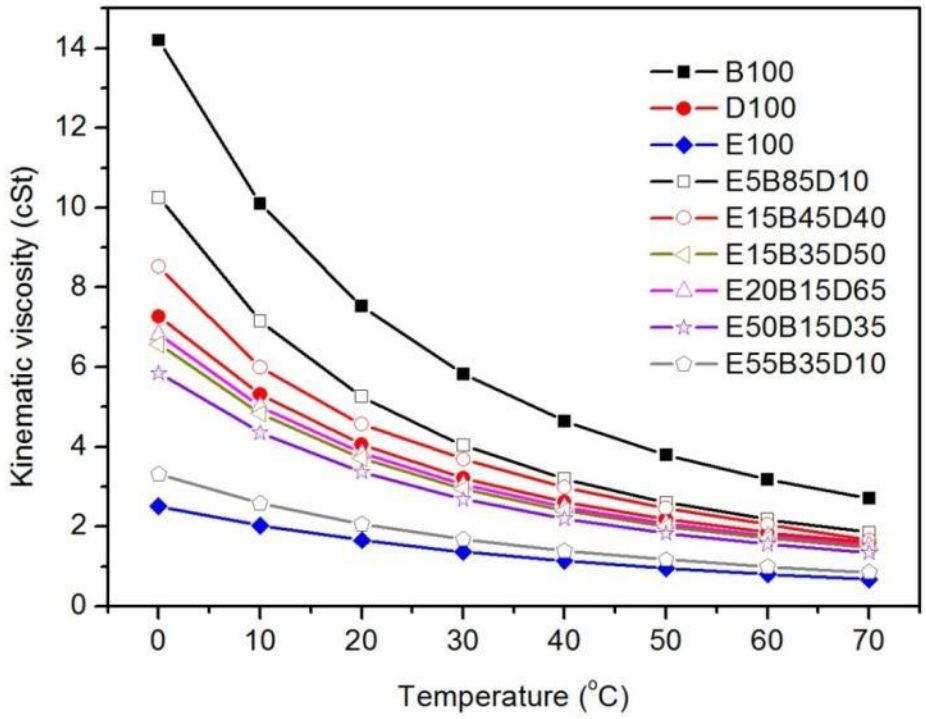

Figure A8. Predictions of kinematic viscosity of different BED blended compositions at temperature ranges from 0 to 70 ^{o}C

Cloud point (ASTM D2500)

Cloud point indicates the temperature at which the fuel starts to form wax crystals and cannot be pumped or injected into the engine. Three promising mixing rules to predict cloud point in fuel blending process (including Kay, Semilogarithmic, and Hu-Burns) were applied and compared to the empirical data, as illustrated in Figure A9. A mixing rule proposed by Hu and Burns is shown as Eq. (9) and it has the lowest AAD (5.11%) [93]. This mixing rule was explored to predict the cloud point of BED blends in this work.

$$T_{mix}^{1/a} = \sum_{i}^{3} f_i^{1/b} * T_i^{1/a} \tag{A8}$$

where T_{mix} and T_i are the cloud points of the blends and i^{th} component (in Kelvin unit); f_i is the volumetric fraction of i^{th} component in the blends, a and b are empirical constants.

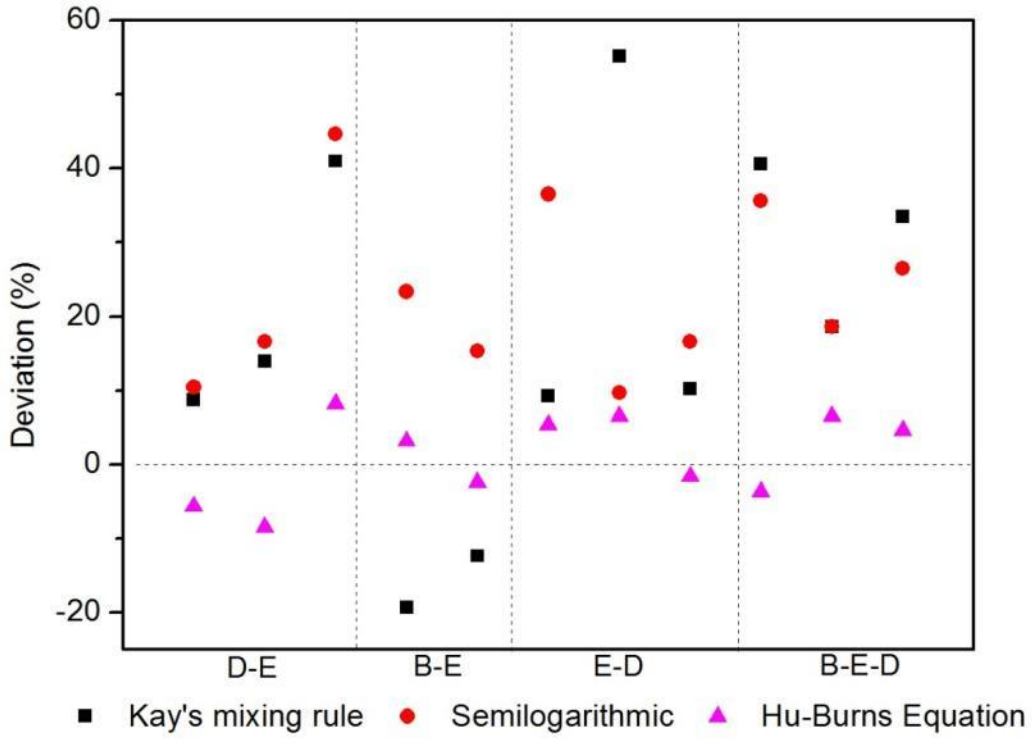

Figure A9. Deviations of cloud point between different mixing rules prediction and experimental data, Kay's (AAD: 23.91%), Semilogarithmic (AAD: 23.09%), and Semwal-Varshney (AAD: 5.11%)

Cetane number (ASTM D4737)

Cetane number is a measure of the ignition delay properties of the fuel and it is defined by the relative proportions of n-hexadecane and α-methylnapthalene. A high cetane number indicates a short ignition delay and provides more time for fuel to burn completely. Besides Semilogarithmic and Grunberg-Nissan equations, Kay's mixing rules based on volumetric and mass were both used for predicting cetane number of the blends. Figure A10 depicts the deviation of the predicted data from the corresponding mixing rules with the empirical results. Even though Kay's mixing rule by mass and Grunberg-Nissan both show relatively low AAD in predicting cetane number (4.64% and 3.07%, respectively), the later is applied in this work because it shows a close match for BED blends.

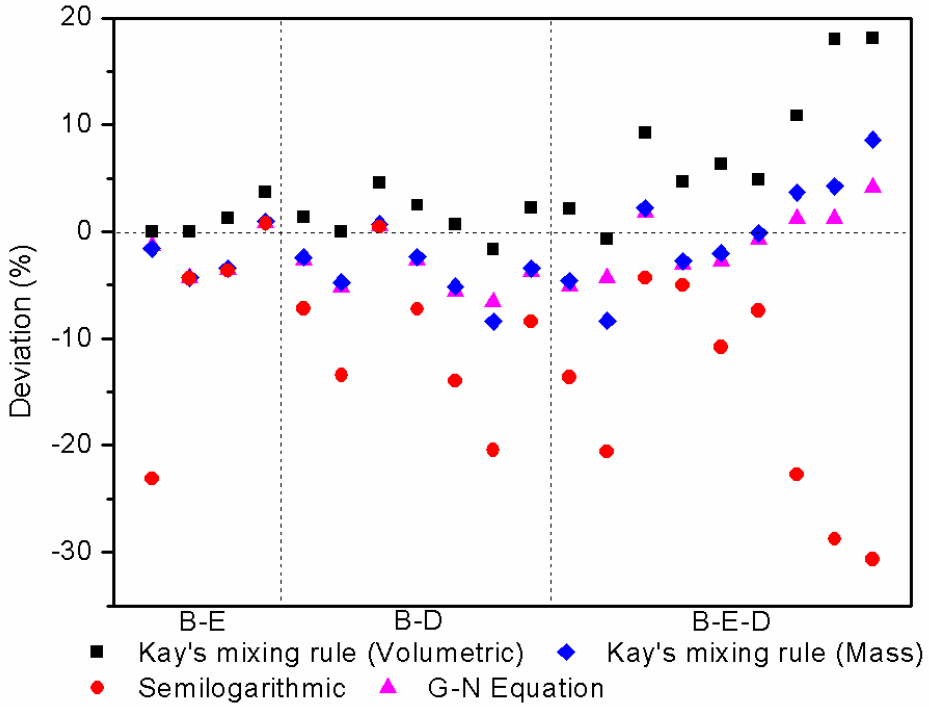

Figure A10. Deviations of cetane number between different mixing rules prediction and experimental data, Kay's volumetric (AAD: 4.64%), Kay's mass (AAD: 6.34%), Semilogarithmic (AAD: 12.34%), and Grunberg-Nissan (AAD: 3.07%)

Density (ASTM D941)

Even though four mixing rules (Kay volumetric, Kay mass, Semilogarithmic, and Grunberg –Nissan) were applied for predicting fuel density, there was no significant difference of deviation. Therefore, Kay's volumetric mixing rule with lowest AAD (0.46%) is chosen for density, LHV, and sulfur content prediction.

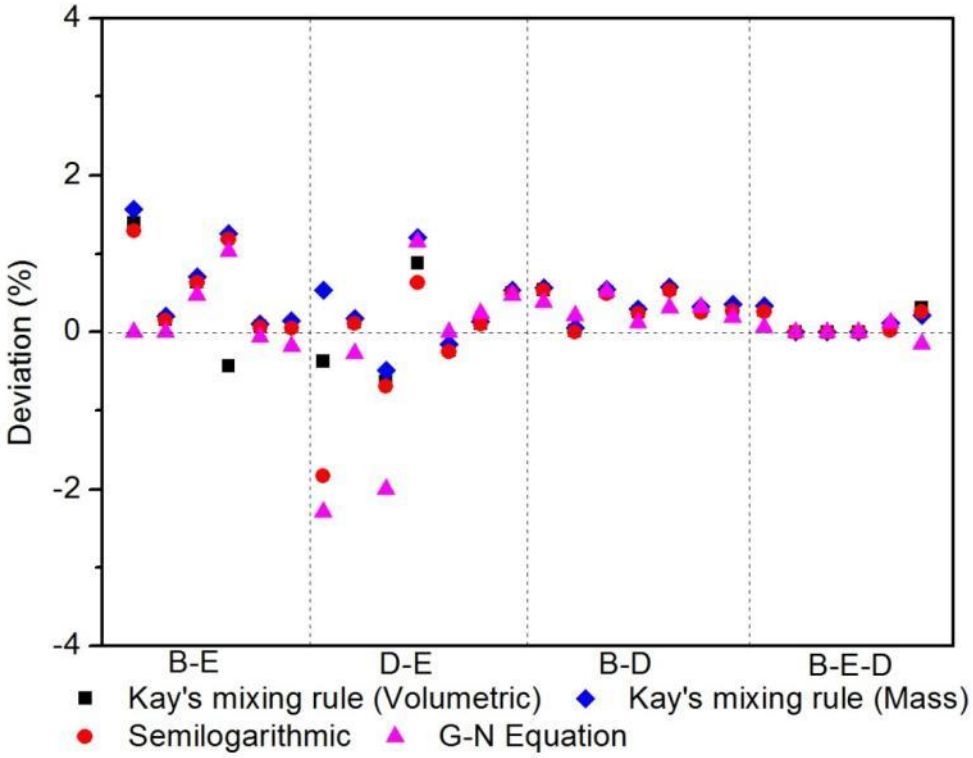

Figure A11. Deviations of density between different mixing rules prediction and experimental data, Kay's volumetric (AAD: 0.46%), Kay's mass (AAD: 0.71%), Semilogarithmic (AAD: 0.56%), and Grunberg-Nissan (AAD: 0.62%)

A.2.2. Bio-fuel derived from different representative feedstock

The specifications of bio-fuels are heavily dependent on their feedstock sources and there are various biomasses available in New York State for ethanol and biodiesel productions. This work selected ethanol derived from corn grain, switchgrass, and food

wastes, which represent 1st, 2nd, and 3rd generations of bio-fuel feedstocks. Similarly, biodiesel from soybean oil, algae, and waste cooking oil (WCO) were chosen. Fuel specifications of these bio-fuels are extrapolated from the open literature and listed in Table A1.

Table A1. Specifications of bio-fuels derived from various biomass feedstock

Bio-fuel	**Ethanol**			**Biodiesel**		
Biomass feedstock	Corn grain [196,197]	Switchgrass [46,196]	Food wastes [198]	Soybean oil [58,85]	Algae [29,199,200]	Waste cooking oil [201]
Production cost ($/L)	0.29	0.54	0.12	0.42	0.65	0.24
Fuel density (kg/L) @15 ^{o}C	0.792	0.789	0.795	0.885	0.864	0.953
Lower heating value (MJ/L)	19.94	19.52	17.85	33.5	35.4	31.8
Kinematic viscosity (cSt) @ 40 ^{o}C	1.13	1.2	1.25	5.15	5.2	5.5
Calculated cetane index	6.5	6.5	6.2	56.4	56.4	52
Cloud point (^{o}C)	-37	-37	-35	-1	-2	1
Sulfur content (ppm)	0	0	5	5	0	10
Molar weight (g/mol)	46	46	46	270	270	296

A.2.3. Data analysis from the report spreadsheet

Table A2. Slack analysis from the LINGO result report

Constraint	Available slack
Ethanol availability (million L/yr)	3.717356
Biodiesel availability (million L/yr)	3.502501
Cloud point upper limit for regular (^{o}C)	4.043627
Cloud point upper limit for premium (^{o}C)	3.991966
Maximum sulfur content for regular (ppm)	3.842811
Maximum sulfur content for premium (ppm)	2.698668
Minimum lower heating value for regular (MJ/L)	1.123564
Minimum lower heating value for premium (MJ/L)	0.7780964

Table A3. Dual price ranking

Constraint	Dual price (million dollar/unit incensement)
Viscosity upper limit (regular)	1.772843
Viscosity upper limit (premium)	1.101944
Availability of diesel	1.008027
Minimum cetane number require (regular)	0.5699373
Minimum cetane number require (premium)	0.3217986
Market energy demand reduction	0.1105458

A.2.4. Constraint relaxation of fuel specifications

Cetane number

Figure A12 provides the relaxation of the minimum cetane number limits for both regular and premium BED blends. As the cetane number requirement of regular BED blends reduce from 45 to 41.8 (7%), the petro-diesel fraction initially reduces and then keeps stable whereas bio-fuel portion proportionally increases to offset the diesel reduction. The contribution of this relaxation in term of optimal profit increment is 16.8% ($ 2.18 million) with diminishing return.

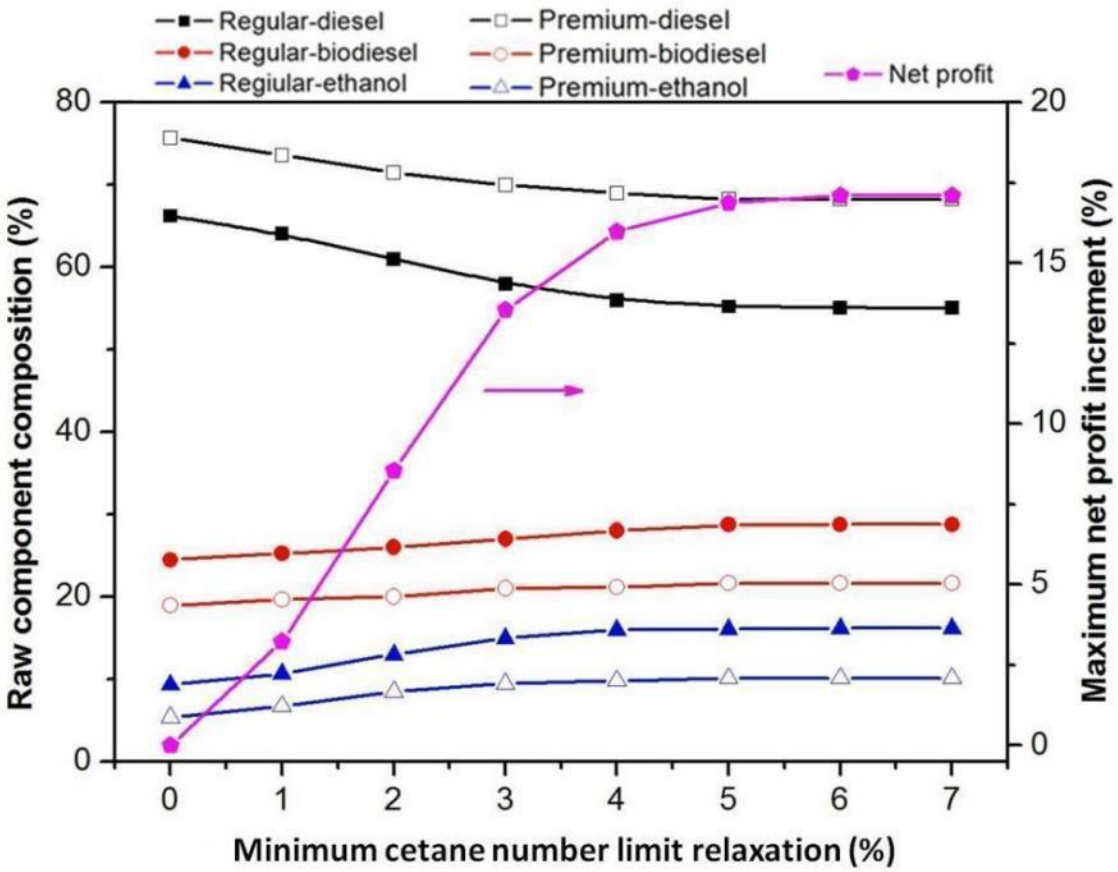

Figure A12. Changes of optimum raw component compositions and the maximum profit of BED blends with the relaxation of minimum cetane number limit constraint of blends

Lower heating value

Figure A13 shows biodiesel is gradually replaced with ethanol portion in the blends as the relaxation of LHV constraint increases because of the relatively high production cost of biodiesel, whereas diesel fraction maintains stable. The optimal profit increases linearly from $ 12.98 million to $ 16.61 million when minimum LHV constraints of regular BED blends and premium blends relax from 33 MJ/L to 31 MJ/L and from 34MJ/L to 32 MJ/L (6%), respectively.

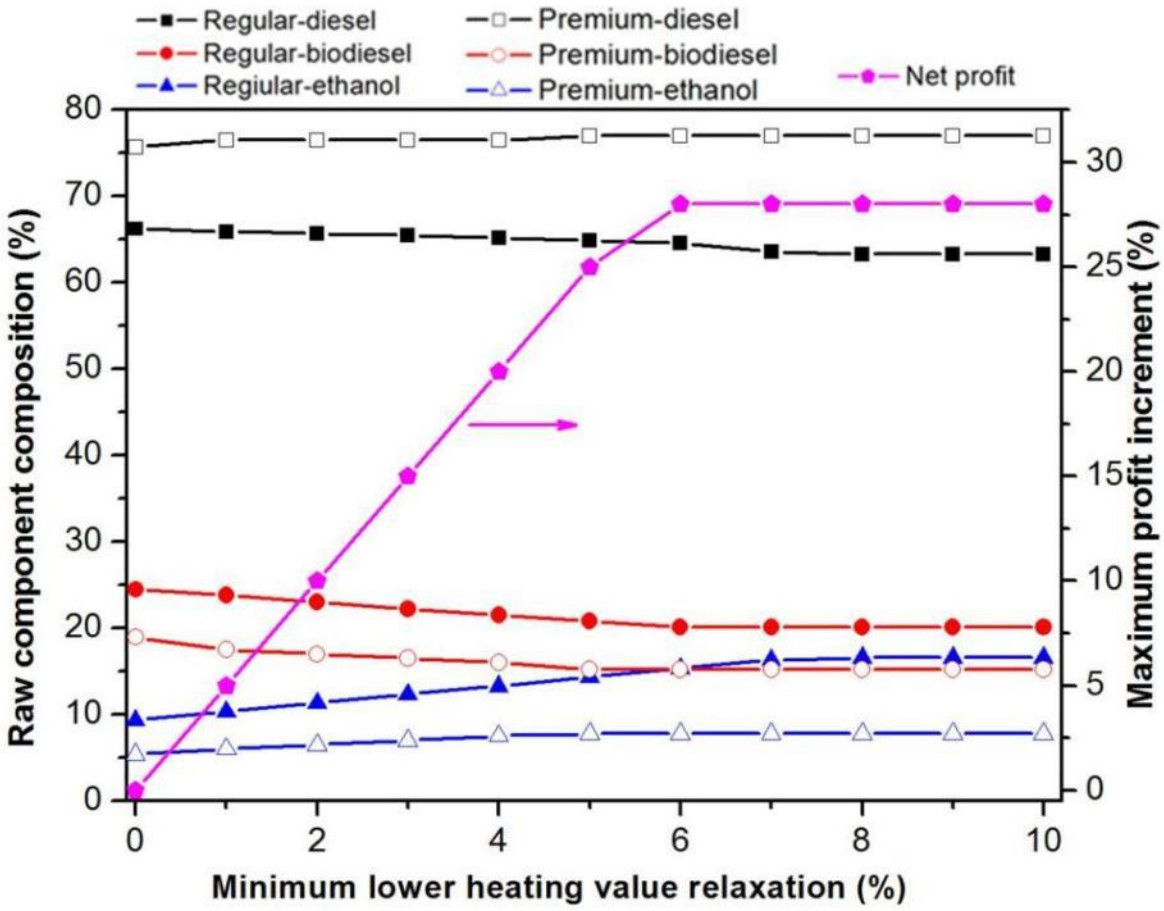

Figure A13. Changes of optimum raw component compositions and the maximum profit of BED blends with the relaxation of minimum LHV constraint of blends

REFERENCES

[1]. I.S. Nashawi, A. Malallah, M. Al-Bisharah, "Forecasting world crude oil production using multicyclic Hubbert model," *Energy & Fuels*, Vol. 24, pp. 1788-1800, 2010.

[2]. J.H. Wood, G.R. Long, D.F. Morehouse, "Long-term world oil supply scenarios: the future is neither as bleak nor rosy as some assert," U.S. Energy Information Administration (EIA), 2004, http://www.eia.gov/pub/oil_gas/petroleum/feature_articles/2004/worldoilsupply/oilsupply04.html.

[3]. U. Bardi, "Peak oil: the four stages of a new idea," *Energy*, Vol. 34, pp. 323-326, 2009.

[4]. U.S. Energy Information Administration, Annual Energy Review 2011, DOE/EIA-0384(2011), September 2012, http://www.eia.gov/totalenergy/data/annual/pdf/aer.pdf.

[5]. R.W. Jessup, "Development and status of dedicated energy crops in the United States," *In Vitro Cell. Dev. Biol. - Plant*, Vol. 45, pp. 282-290, 2009.

[6]. B.D. Yacobucci, R. Schnepf, "Selected issue related to an expansion of the renewable fuel standard (RFS)," CRS Report for Congress, December 2007, http://assets.opencrs.com/rpts/RL34265_20071203.pdf.

[7]. L.H. Goulder, M.R. Jacobsen, A.A. Benthem, "Unintended consequences from nested state and federal regulation: the case of the Pavley greenhouse-gas-per-mile limits," *J. Environmental Economics and Management*, Vol. 63, pp. 187-207, 2012.

[8]. A. Schell, H. Peng, D. Tran, E. Stamos, C. Lin, M.J. Kim, "Modeling and control strategy development for fuel cell electric vehicles," *Annual Reviews in Control*, Vol. 29, pp. 159-169, 2005.

[9]. EG&G Technical Services, Inc. Fuel Cell Handbook, 7th Edition, November 2004, U.S. National Energy Technology Laboratory, Under Contact No. DE-AM26-99FT40575.

[10]. L. Schlapbach, A. Züttel, "Hydrogen-storage materials for mobile applications," *Nature*, Vol.414, pp. 353-357, 2001.

[11]. A. Zuttel, "Material for hydrogen storage," *Materials Today*, Vol. 6, pp. 24-33, 2003.

[12]. C. Liu, Y.Y. Fan, M. Liu, H.T. Cong, H.M. Cheng, M.S. Dresselhaus, "Hydrogen storage in single-walled carbon nanotubes at room temperature," *Science*, Vol. 286, pp. 1127-1129, 1999.

[13]. B. Sakintuna, F. Lamari-Darkrim, M. Hirscher, "Metal hydride materials for solid hydrogen storage: A review," *Int. J. Hydrogen Energy*, Vol. 32, pp. 1121-1140, 2007.

[14]. T.A. Trabold, J.S. Lylak, M.R. Walluk, J.F. Lin, D.R. Troiani, "Measurement and analysis of carbon formation during diesel reforming for solid oxide fuel cells," *Int. J. Hydrogen Energy*, Vol. 37, pp. 5190-5201, 2012.

[15]. D. Shekhawat, J.J. Spivey, D.A. Berry, *Fuel cells: technologies for fuel processing*, 1st edition, Elsevier, 2011.

[16]. C. Wu, R. Liu, "Carbon deposition behavior in steam reforming of bio-oil model compound for hydrogen production," *Int. J. Hydrogen Energy*, Vol. 35, pp. 7386-7398, 2010.
[17]. A.E. Lutz, R.W. Bradshaw, L. Bromberg, A. Rabinovich, "Thermodynamic analysis of hydrogen production by partial oxidation reforming," *Int. J. Hydrogen Energy*, Vol. 29, pp. 809-816, 2004.
[18]. W. Wang, Y. Wang, "Dry reforming of ethanol for hydrogen production: thermodynamic investigation," *Int. J. Hydrogen Energy*, Vol. 34, pp. 5382-5389, 2009.
[19]. R.J. Braun, S.A. Klein, D.T. Reindl, "Evaluation of system configurations for solid oxide fuel cell-based micro-combined heat and power generators in residential applications*," J. Power Sources*, Vol. 158, pp. 1290-1305, 2006.
[20]. U.S. Environmental Protection Agency (EPA), Compilation of state, county, and local anti-idling regulations, Office of Transportation and Air Quality, 2006, http://www.epa.gov/region8/air/rmcdc/pdf/CompilationofStateIdlingRegulations.pdf.
[21]. D. Hennessy, "Solid oxide fuel cell diesel auxiliary power unit demonstration," DOE Peer Review 2012, DE-EE0000478:H2RA002, 2012, http://www.hydrogen.energy.gov/pdfs/review12/h2ra002_hennessy_2012_o.pdf.
[22]. X, Du, D.J. Hayes, "The impact of ethanol production on U.S. and regional gasoline markets," *Energy Policy*, Vol. 37, pp. 3227-3234, 2009.
[23]. R. Lai, "World crop residues production and implications of its use as a biofuel," *Environmental International*, Vol. 31, pp. 575-584, 2005.
[24]. M.E. Walsh, D.G. Ugarte, H. Shapouri, S.P. Slinsky, "Bioenergy crop production in the United States," *Environmental and Resource Economics*, Vol. 24, pp. 313-333, 2003.
[25]. P. Fairley, "Introduction: next generation biofuels," *Nature*, Vol. 474, pp. S2-S5, 2011.
[26]. U.S. EPA, What you should know about idling reduction, 2010, http://www.epa.gov/reg3artd/diesel/truck_idling_fs.pdf.
[27]. U.S. EPA, Emission facts: greenhouse gas emission from a typical passenger vehicle, 2005, http://www.epa.gov/otaq/climate/420f05004.htm.
[28]. M. Mintz, J.Han, M. Wang, C. Saricks, "Well-to-wheels analysis of landfill gas-based pathways and their addition to the GREET model," Argonne National Laboratory, ANL/ESD/10-3, 2010.
[29]. K. Soratana, A.E. Landis, "Evaluating industrial symbiosis and algae cultivation from a life cycle perspective," *Bioresource Technology*, Vol. 102, pp. 6892-6901, 2011.
[30]. S. Spatari, D.M. Bagley, H.L. Maclean, "Life cycle evaluation of emerging lignocellulosic ethanol conversion technologies," *Bioresource Technology*, Vol. 101, pp. 654-667, 2010.
[31]. L. Panichelli, A. Dauriat, E. Gnansounou, "Life cycle assessment of soybean-based biodiesel in Argentina for export," *Int. J. LCA*, Vol. 14, pp. 144-159, 2009.
[32]. J.F. Lin, D.F. Smith, D.F., C.W. Babbitt, T.A. Trabold, "Assessment of bio-fuel options for solid oxide fuel cell-based auxiliary power units," 2011 *IEEE*

International Symposium on Sustainable Systems and Technology (ISSST), May 2011.
[33]. A. Baral, B. Bakshi, "Thermodynamic metrics for aggregation of natural resources in life cycle analysis: Insight via application to some transportation fuels," *Environ. Sci. Technol.,* Vol.44, pp. 800-807, 2010.
[34]. W. Liao, R. Heijungs, G. Huppes, "Thermodynamic resource indicators in LCA: a case study on the titania produced in Panzhihua city, southwest China," *Int. J. LCA*, Vol. 17(8), pp. 951-961, 2012.
[35]. G. Wall, "Life cycle analysis of renewable energy systems," *Open Renew. Energy J.*, Vol. 4, pp. 72–77, 2011.
[36]. L., Gerber, M. Gassner, F. Marechal, "Systematic integration of LCA in process systems design: Application to combined fuel and electricity production from lignocellulosic biomass," *Computers and Chemical Engineering,* Vol. 35, pp. 1265-1280, 2011.
[37]. C. Jimenez-Gonzalez, S. Kim, M.R. Overcash, "Methodology for developing gate-to-gate life cycle inventory information," *Int. J. LCA,* Vol. 5, pp. 153-159, 2000.
[38]. S. Kim, M. Overcash, "Energy in chemical manufacturing processes: gate-to-gate information for life cycle assessment," *J. Chemical Technology and Biotechnology*, Vol. 78, pp. 995-1005, 2003.
[39]. C. Strazza, A.D. Borghi, P. Costamagna, A. Traverso, M. Santin, "Comparative LCA of methanol-fuelled SOFCs as auxiliary power systems on-board ships," *Appied Energy*, Vol. 87, pp. 1670-1678, 2010.
[40]. J. Lawrence, M. Boltze, "Auxiliary power unit based on a solid oxide fuel cell and fuelled with diesel," *J. Power Sources*, Vol. 154, pp. 479-488, 2006.
[41]. S.F. Tierney, A. Okie, R. Mukerji, M. Swider, R. Safuto, A. Jaggi, "Fuel diversity in New York electricity market," ISO New York Independent System Operator, 2008, http://www.nyiso.com/public/webdocs/documents/white_papers/fuel_diversity_11202008.pdf.
[42]. National Renewable Energy Laboratory, U.S. Department of Agriculture and U.S. Department of Energy, "Life cycle inventory of biodiesel and petroleum diesel for use in an urban bus," NREL/SR-580-24089, 1998, http://www.nrel.gov/docs/legosti/fy98/24089.pdf.
[43]. G. Wiltsee, "Urban waste grease resource assessment," NREL/SR-570-26141, 1998.
[44]. A. Aden, M. Ruth, K. Ibsen, J. Jechura, K. Neeves, J. Sheehan, B. Wallace, L. Montague, A. Slayton, J. Lukas, "Lignocellulosic biomass to ethanol process design and economics utilizing co-current dilute acid prehydrolysis and enzymatic hydrolysis for corn stover," NREL/TP-510-32438, 2002, http://www1.eere.energy.gov/biomass/pdfs/32438.pdf.
[45]. G. Steinfeld, R. Sanderson, "Landfill gas cleanup for carbonate fuel cell power generation," NREL/SR-570-26037, 1998.
[46]. S. Kim, B.E. Dale, "Allocation procedure in ethanol production system from corn grain: I. System expansion," *Int. J. LCA*, Vol. 7(4), pp. 237-243, 2002.

[47]. P.H. Nielsen, K.M. Oxenboll, H. Wenzel, "Cradle-to-gate environmental assessment of enzyme products produced industrially in Denmark by Novozymes A/S," *Int. J. LCA*, 2006, http://www.novozymes.com/en/sustainability/sustainable-solutions/life-cycle-assessments/Documents/Cradle%20to%20gate.pdf.
[48]. U.S. Energy Information Administration (EIA), PADD district imports by country of Origin, 2011, http://205.254.135.7/dnav/pet/pet_move_impcp_a1_Z00_ep00_ip0_mbbl_m.htm.
[49]. Argonne GREET Model 1.8d.1, 2011; http://greet.es.anl.gov/.
[50]. Y. Wang, S. Ou, P. Liu, Z. Zhang, "Preparation of biodiesel from waste cooking oil via two-step catalyzed process," *Energy. Convers. Manage*, Vol. 48, pp. 184-188, 2007.
[51]. J. Iqbal, W.A. Carney, S. LaCaze, C.S. Theegala, "Metals determination in biodiesel (B100) by ICP-OES with microwave assisted acid digestion," *The Open Analytical Chemistry J.*, Vol. 4, pp. 18-26, 2010.
[52]. W. Plains, Z. Wojnar, J. Jarnefeld, P.B. Woodbury, "Renewable fuels roadmap and sustainable biomass feedstock supply for New York. Appendix E: Analysis of sustainable feedstock production potential in New York State," NYSERDA Report 10-05, 2010.
[53]. Z. Wojnar, J.M.V. Nostrand, C. Rutzke, J. Jarnefeld, "Renewable fuels roadmap and sustainable biomass feedstock supply for New York," NYSERDA report 10-05, 2010.
[54]. Department of Environmental Conservation, NY. Municipal solid waste landfills in New York State, 2011, http://www.dec.ny.gov/chemical/23682.html.
[55]. NorthEast Southtowns Regional Solid Waste Management Plan 2000-2012, March 2003. http://www.regional-institute.buffalo.edu/Includes/UserDownloads/FinalPlan_full.pdf.
[56]. S.H. Chan, C.F. Low, O.L. Ding, "Energy and exergy analysis of simple solid-oxide fuel-cell power systems," *J. Power Source*, Vol. 103(2), pp. 188-200, 2002.
[57]. D. Tilman, J. Hill, C. Lehman, "Carbon-negative biofuels from low-input high-diversity grassland biomass," *Science*, Vol. 314, pp. 1598-1600, 2006.
[58]. H. Huo, M. Wang, C. Bloyd, V. Putshce, "Life-cycle assessment of energy and greenhouse gas effects of soybean-derived biodiesel and renewable fuels," Argonne National Laboratory, ANL/ESD/08-2, 2008.
[59]. SAIC, Scientific Applications International Corporation, Life cycle assessment: principles and practice, EPA/600/R-06/060, 2006, http://www.cs.ucsb.edu/~chong/290N-W10/EPAonLCA2006.pdf.
[60]. M. Wang, H. Lee, J. Molburg, "Allocation of energy use in petroleum refineries to petroleum products: implications for life-cycle energy use and emission inventory of petroleum transportation fuels," *Int. J. LCA*, Vol. 9, pp. 34-44, 2004.
[61]. L. Luo, E. Voet, G. Huppes, H. Haes, "Allocation issues in LCA methodology: a case study of corn stover-based fuel ethanol," *Int J. LCA*, Vol. 14, pp. 529-539, 2009.
[62]. How dependent are we on foreign oil? U.S. Energy Information Administration, 2012, http://www.eia.gov/energy_in_brief/foreign_oil_dependence.cfm.
[63]. J. Yan, T. Lin, "Biofuels in Asia," *Applied Energy*, Vol. 86, pp. S1-S10, 2009.

[64]. U.S. Department of Energy, Energy Independence and Security Act (EISA) of 2007, http://www.seco.noaa.gov/Energy/eisa_2007_femp.pdf.
[65]. H.M. Ismail, H.K. Ng, C.W. Queck, S. Gan, "Artificial neural networks modeling of engine-out responses for a light-duty diesel engine fuelled with biodiesel blends," *Applied Energy*, Vol. 92, pp. 769-777, 2012.
[66]. P. Kwanchareon, A. Luengnaruemitchai, S. Jai-In, "Solubility of a diesel-biodiesel-ethanol blend, its fuel properties, and its emission characteristics from diesel engine," *Fuel*, Vol. 84, pp. 1053-1061, 2007.
[67]. E. Alptekin, M. Canakci, "Determination of the density and the viscosities of biodiesel-diesel fuel blends," *Renewable Energy*, Vol. 33, pp. 2623-2630, 2008.
[68]. S. Fernando, M. Hannan, "Development of a novel biofuel blend using ethanol-biodiesel-diesel microemulsions: EB-diesel," *Energy & Fuels*, Vol. 18, pp. 1695-1703, 2004.
[69]. P. Weerachanchai, C. Tangsathitkulchai, M. Tangsathitkulchai, "Phase behaviors and fuel properties of bio-oil-diesel-alcohol blends," *World Academy of Science, Engineering and Technology*, Vol. 56, pp. 387-393, 2009.
[70]. D.H. Qi, H. Chen, L.M. Geng, Y.Z.H. Bian, X.C.H. Ren, "Performance and combustion characteristics of biodiesel-diesel-methanol blend fuelled engine," *Applied Energy*, Vol. 87, pp. 1679-1686, 2010.
[71]. Y. Kim, C. Yun, S.B. Park, S. Park, L.T. Fan, "An integrated model of supply network and production planning for multiple fuel products of multi-site refineries," *Computers and Chemical Engineering*, Vol. 32, pp. 2529-35, 2008.
[72]. S. Mouret, I.E. Grossmann, P. Pestiaux, "A novel priority-slot based continuous-time formulation for crude-oil scheduling problems," *Ind. Eng. Chem. Res.*, Vol. 48, pp. 8514-8528, 2009.
[73]. J.D. Kelly, J.L. Mann, "Crude-oil blend scheduling optimization: an application with multi-million dollar benefits," *Hydrocarbon Processing*, Vol. 43, pp. 47-53, 2003.
[74]. H. Zhou, J. Lu, Z. Cao, J. Shi, M. Pan, W. Li, Q. Jiang, "Modeling and optimization of an industrial hydrocracking unit to improve the yield of diesel or kerosene," *Fuel*, Vol. 90(12), pp. 3521-3530, 2011.
[75]. C.A. Mendez, I.E. Grossmann, I. Harjunkoski, P. Kabore, "A simultaneous optimization approach for off-line blending and scheduling of oil-refinery operations," *Computers and Chemical Engineering*, Vol. 30, pp. 614-634, 2006.
[76]. K. Glismann, G. Gruhn, "Short-term scheduling and recipe optimization of blending processes," *Computers and Chemical Engineering*, Vol. 25, pp. 627-634, 2001.
[77]. J. Li, Karimi, R. Srinivasan, "Recipe determination and scheduling of gasoline blending operations," *American Institute of Chemical Engineers*, Vol. 56(2), pp. 441-465, 2010.
[78]. M. Balat, H. Balat, "Progress in biodiesel processing," *Applied Energy*, Vol. 87, pp. 1815-1835, 2010.
[79]. A. Demirbas, "Political, economic and environmental impacts of biofuels: A review," *Applied Energy*, Vol. 86, pp. S108-117, 2009.
[80]. W.E. Tyner, "The US ethanol and biofuels boom: its origins, current status, and future prospects," *BioScience*, Vol. 58(7), pp. 646-653, 2008.

[81]. P. Benjumea, J. Agudelo, A. Agudelo, "Basic properties of palm oil biodiesel-diesel blends," *Fuel*, Vol. 87, pp. 2069-2075, 2008.
[82]. A. Srirangan, L. Akawi, M. Moo-Young, C.P. Chou, "Towards sustainable production of clean energy carriers from biomass resources," *Applied Energy*, Vol. 100, pp. 172-186, 2012.
[83]. L.R. Waterland, S. Venkatesh, S. Unnasch, R. McCormick, Safety and performance assessment of ethanol/diesel blends (E-diesel), NREL/SR-540-34817, 2003, http://www.nrel.gov/docs/fy03osti/34817.pdf
[84]. P.W. Gallagher, H. Brubaker, H. Shapouri, "Plant size: capital cost relationships in the dry mill ethanol industry," *Biomass and Bioenergy*, Vol. 28(6), pp. 565-571, 2005.
[85]. D. Pimentel, T.W. Patzek, "Ethanol production using corn, swtichgrass, and wood; biodiesel production using soybean and sunflower," *Natural Resources Research*, Vol. 14, pp. 65-76, 2005.
[86]. U.S. Energy Information Administration, 1994-2012 weekly U.S. regular and premium all formulations retail gasoline prices, 2012, http://205.254.135.7/dnav/pet/pet_pri_gnd_dcus_nus_w.htm
[87]. I. Barabas, I.A. Todorut, "Predicting the temperature dependent viscosity of biodiesel-diesel-bioethanol blends," *Energy & Fuels*, Vol. 25, pp. 5767-5774, 2011.
[88]. E.L. Lederer, "Viscosity of mixtures with and without diluents," *Proc. World Pet. Cong. Lond.*, Vol. 2, pp. 526-528, 1933.
[89]. M.A. Barrufet, A. Setiadarma, "Reliable heavy oil-solvent viscosity mixing rules for viscosities up to 450 K, oil-solvent viscosity ratios up to 4 105, and any solvent proportion," *Fluid Phase Equilibria*, Vol. 213, pp. 65-79, 2003.
[90]. X. Shi, X. Pang, Y. Mu, H. He, S. Shuai, J. Wang, H. Chen, R. Li, "Emission reduction potential of using ethanol-biodiesel-diesel fuel blend on a heavy-duty diesel engine," *Atmospheric Environment*, Vol. 40(14), pp. 2567-2574, 2006.
[91]. M. Lapuerta, O. Armas, R.G. Contreras, "Effect of ethanol on blending stability and diesel engine emissions," *Energy & Fuels*, Vol. 23(9), pp. 4343-4354, 2009.
[92]. G.K. Latinwo, D.S. Aribike, S.A. Kareem, "Comparative study of biodiesels produced from unrefined vegetable oils," *Nature and Science*, Vol. 8, pp. 102-106, 2010.
[93]. J. Hu, A.M. Burns, "New method predicts cloud, pour, flash points of distillate blends," *Hydrocarbon Processing*, Vol. 49(11), 213-216, 1970.
[94]. P.B. Semwal, R.G. Varshney, "Predictions of pour, cloud and cold filter plugging point for future diesel fuels with application to diesel blending models," *Fuel*, Vol. 74, pp. 437-444.
[95]. K.P.J. Williams, "Determination of gas oil cretane number and cetane index using near-infrared Fourier transform Raman spectroscopy," *Anal. Chem.*, Vol. 61, pp. 2553-2556, 1990.
[96]. S. Lebedevas, G. Lebedeva, V. Makareviciene, P. Janulis, E. Sendzikiene, "Usage of fuel mixtures containing ethanol and rapeseed oil methyl esters in a diesel engine," *Energy & Fuels*, Vol. 23(1), pp. 217-223, 2009.
[97]. Hydrogen Analysis Resource Center, Lower and higher heating value of fuels, U.S. Department of Energy,

http://hydrogen.pnl.gov/cocoon/morf/hydrogen/site_specific/fuel_heating_calculator.
[98]. M. Canakci, "Combustion characteristics of a turbocharged DI compression ignition engine fueled with petroleum diesel fuels and biodiesel," *Bioresource Technology*, Vol. 98, pp. 1167-1175, 2007.
[99]. X. Shi, Y. Yu, H, He, S. Shuai, J. Wang, R. Li, "Emission characteristics using methyl soyate-ethanol-diesel fuel blends on a diesel engine," *Fuel*, Vol. 84, pp. 1543-1549, 2005.
[100]. A.C. Hansen, Q. Zhang, P.W.L. Lyne, "Ethanol-diesel fuel blends – a review," *Bioresource Technology*, Vol. 96(3), pp. 277-285, 2005.
[101]. P.B. Woodbury, Z. Wojnar, J. Jarnefeld, "Renewable fuels roadmap and sustainable biomass feedstock supply for New York - Appendix E: Analysis of sustainable feedstock production potential in New York State," NYSERDA Report 10-5, 2010 March.
[102]. U.S. Department of Energy, Freedom CAR & Vehicle Technologies Program: Diesel engine. U.S. Department of Energy, 2003, http://www1.eere.energy.gov/vehiclesandfuels/pdfs/basics/jtb_diesel_engine.pdf.
[103]. U.S. Energy Information Administration, New York No.2 diesel sales/deliveries to on-highway consumers, 2012, http://www.eia.gov/dnav/pet/hist/LeafHandler.ashx?n=PET&s=K2DVHNSNY1&f=A.
[104]. U.S. Energy Information Administration, U.S. On-highway diesel fuel prices, http://www.eia.gov/petroleum/gasdiesel/.
[105]. U.S. Energy Information Administration, Short-term energy outlook, U.S. diesel fuel and crude oil price, http://205.254.135.7/forecasts/steo/report/prices.cfm.
[106]. B.D. Yacobucci "Biofuels incentives: a summary of federal programs," CRS Report for Congress, Congressional Research Service, 2012, http://www.fas.org/sgp/crs/misc/R40110.pdf
[107]. N.M. Ribeiro, A.C. Pinto, C.M. Quintella, G.O. Rocha, L.S.G. Teixeire, L.L.N. Guarieiro, M.C. Rangel, M.C.C. Veloso, M.J.C. Rezende, "The role of additives for diesel and diesel blended (ethanol or biodiesel) fuels: a review," *Energy & Fuel*, Vol. 21, pp. 2433-2445, 2007.
[108]. B.R. Moser, S.C. Cermak, T.A. Isbell, "Evaluation of castor and lesquerella oil derivatives as additives in biodiesel and ultralow sulfur diesel fuels," *Energy & Fuel*, Vol. 22, pp. 1349-1352, 2008.
[109]. A. Demirbas, "Competitive liquid biofuels from biomass," *Applied Energy*, Vol. 88, pp. 17-28, 2011.
[110]. H.D. Gorter, D.R. Just, "The economics of a blend mandate for biofuels," *Amer. J. Agr. Econ.*, Vol. 91(3), pp. 738-750, 2009.
[111]. M.J.S.D. Carvalho, P.R. Seidl, C.R.P. Belchior, J.R. Sodre, "Lubricant viscosity and viscosity improver additive effects on diesel fuel economy," *Tribology International*, Vol. 43, pp. 2298-22302, 2010.
[112]. US Environmental Protection Agency (EPA), The effect of cetane number increase due to additives on NOx emission from heavy-duty highway engines: final technical report, EPA420-R-03-02, 2003, http://www.epa.gov/oms/models/analysis/r03002.pdf.

[113]. M.M. Gui, K.T. Lee, S. Bhatia, "Feasibility of edible oil vs. non-edible oil vs. waste edible oil as biodiesel feedstock," *Energy*, Vol. 33(11), pp. 1646-1653, 2008.
[114]. The 2011 Fuel Cell Patent Review, *FuelCellToday*, http://www.fuelcelltoday.com/media/948977/the_2011_fuel_cell_patent_review.pdf.
[115]. S.C. Singhal, "Solid oxide fuel cells for stationary, mobile, and military applications," *Solid State Ionics*, Vol. 152, pp. 405-10, 2002.
[116]. M. Momirla, T.N. Veziroglu, "The properties of hydrogen as fuel tomorrow in sustainable energy system for a cleaner planet," *Int. J. Hydrogen Energy*, Vol. 30, pp. 795-802, 2005.
[117]. S.L. Garrison, B.J. Hardy, M.B. Gorbounov, D.A. Tamburello, C. Corgnale, B.A. vanHassel, D.A. Mosher, D.L. Anton, "Optimization of internal heat exchangers for hydrogen storage tanks utilizing metal hydrides," *Int. J. Hydrogen Energy*, Vol. 37, pp. 2850-2861, 2012.
[118]. I. Kang, J. Bae, G. Bae, "Performance comparison of autothermal reforming for liquid hydrocarbons, gasoline and diesel for fuel cell application," *J. Power Sources*, Vol. 163, pp. 538-546, 2006.
[119]. Kang I, Bae J, Yoon S, Yoo Y, Performance improvement of diesel autothermal reformer by applying ultrasonic injector for effective fuel delivery. *J. Power Sources*, 2007:172:845-52.
[120]. R.L. Borup, M.A. Inbody, J.I. Tafoya, D. Guidry, W.J. Parkinson, "Diesel reforming for SOFC auxiliary power units," Los Alamos National Laboratory, LA-UR-04-5370, 2004.
[121]. D.J. Liu, M. Krumpelt, "Activity and structure of perovskites as diesel-reforming catalysts for solid oxide fuel cell," *Int. J. Appl. Ceram. Technol*., Vol. 2, pp. 301-307, 2005.
[122]. B.D. Gould, X. Chen, J.W. Schwank, "n-Dodecane reforming over nickel-based monolith catalysts: Deactivation and carbon deposition." *Applied Catalysis A: General*, Vol. 334, pp. 277-290, 2008.
[123]. D.J. Haynes, A. Campos, D.A. Berry, D. Shekhawat, A. Roy, J.J. Spivey, "Catalytic partial oxidation of a diesel surrogate fuel using an Ru-substituted pyrochlore," *Catalysis Today*, Vol. 155, pp. 84-91, 2010.
[124]. Z. Porš, J. Pasel, A. Tschauder, R. Dahl, R. Peters, D. Stolten, "Optimised mixture formation for diesel fuel processing," *Fuel Cells*, Vol. 2, pp. 129-137, 2008.
[125]. S.D. Sovani, J.D. Crofts, P.E. Sojka, J.P. Gore, W.A. Eckerle, "Structure and steady-state spray performance of an effervescent diesel injector," *Fuel*, Vol. 84, pp. 1503-1514, 2005.
[126]. S.M. An, W.S. Kim, S.Y. Lee, "Spraying of liquid fuel for improvement of reforming performance for hydrogen generation," *Int. J. Hydrogen Energy*, Vol. 36, pp. 5342-5349, 2011.
[127]. S. Kim, H.H. Carstensen, A. Dean, J. Bae, "Investigation of gas-phase reactions in the mixing region for hydrocarbon autothermal reforming applications," *Int. J. Hydrogen Energy*, Vol. 37, pp. 7545-7553, 2012.

[128]. A. Sarioglan, H. Olgun, M. Baranak, A. Ersoz, H. Atakul, S. Ozdogan, "Diesel evaporation as the first step of hydrogen production," *Int. J. Hydrogen Energy*, Vol. 32, pp. 2895-2901, 2007.
[129]. J.R. Salge, B.J. Dreyer, P.J. Dauenhauer, L.D. Schmidt, "Renewable hydrogen from nonvolatile fuels by reactive flash volatilization," *Science*, Vol. 314, pp. 801-804, 2006.
[130]. C.E. Ejim, B.A. Fleck, A. Amirfazli A, Analytical study for atomization of biodiesels and their blends in a typical injector: Surface tension and viscosity effects. *Fuel*, 2007; 86:1534-44.
[131]. D. Tarlet, J. Bellettre, M. Tazerout, C. Rahmouni, "Prediction of micro-explosion delay of emulsified fuel droplets," *Int. J. Thermal Sciences,* Vol. 48, pp. 449-460, 2009.
[132]. A Lif, K Holmberg, "Water-in-diesel emulsions and related systems," *Advances in Colloid and Interface Sciences,* Vol. 231, pp. 123-126, 2006.
[133]. H. Nam, J.L. Alvarado, "Microexplosion detection in hexadecane and vegetable oil blends," Spring Technical Meeting of the Central States Section of The Combustion Institute," April 22-24, 2012, https://www.combustioninstitute.org/upload_resources/12S-131.pdf.
[134]. F.Y. Hagos, A. Rashid, A. Aziz, I.M. Tan, "Water-in-diesel emulsion and its micro-explosion phenomenon-Review," *Communication Software and Networks (ICCSN), 2011 IEEE 3rd International Conference,* May 27-29, 2011.
[135]. W Schindler, C Haisch, HA Beck, R Niessner, E Jacob, DA Rothe, "Photoacoustic sensor system for time resolved quantification of diesel soot emissions," SAE Paper 2004-01-0968, 2004.
[136]. J.F. Lin, T.A. Trabold, M.R. Walluk, D.F. Smith, "Biofuel reformation for solid oxide fuel cell applications, Part 1: fuel vaporization and reactant mixing," submitted to *Int. J. Hydrogen Energy*, Feb. 2013.
[137]. W. Yuan, A.C. Huansen, Q. Zhang, "Predicting the physical properties of biodiesel for combustion modeling," *American Society of Agricultural Engineers*, Vol. 46(6), pp. 1487-1493, 2003.
[138]. F. Ma, M.A. Hanna, "Biodiesel production: a review," *Bioresource Technology*, Vol. 70, pp. 1-15, 1999.
[139]. A.K. Agarwal, L.M. Das, "Biodiesel development and characterization for use as a fuel in compression ignition engines," *J. Eng. Gas Turbines Power*, Vol. 123, pp. 440-448, 2001.
[140]. A.W. Drews, "Standard test method for boiling range distribution of petroleum fractions by gas chromatography," *American Society for Testing and Materials International: D 2887-97, Manual on Hydrocarbon Analysis*, MNL3-EB/Jun. 1998.
[141]. M.R. Riazi, "Characterization and properties of petroleum fractions," *American Society for Testing and Materials Internationa*l, 1st ed., 2005.
[142]. M. Satou, D. Itoh, H. Hattori, T. Yoshida, "Evaluation of ring size distribution in a heavy oil based on boiling point and molecular weight distributions," *Fuel*, Vol. 79, pp. 339-348, 2000.

[143]. N. Laosiripojana, S. Assabumrungrat, "Catalytic dry reforming of methane over high surface area ceria," *Appl. Catal. B: Environmental*, Vol. 60, pp. 107-116, 2005.
[144]. C. Yu, D. Lee, S. Park, K. Lee, K. Lee, "Study on a catalytic membrane reactor for hydrogen production from ethanol steam reforming," *Int. J. Hydrogen Energy*, Vol. 34, pp. 2947-1954, 2009.
[145]. K. Faungnawakij, R. Kikuchi, K. Eguchi, "Thermodynamic analysis of carbon formation boundary and reforming performance for steam reforming of dimethyl ether", *J. Power Sources*, Vol. 164, pp. 73-79, 2007.
[146]. W Wang, Y Cao, "Hydrogen-rich gas production for solid oxide fuel cell (SOFC) via partial oxidation of butanol: thermodynamic analysis," *Int. J. Hydrogen Energy*, Vol. 35, pp. 13280-13289, 2010.
[147]. I .Kang, J. Bae, G. Bae, "Performance comparison of autothermal reforming for liquid hydrocarbons, gasoline and diesel for fuel cell application*," J. Power Sources*, Vol. 163, pp. 538-546, 2006.
[148]. R.D. Parmar, A. Kundu, K. Karan, "Thermodynamic analysis of diesel reforming process: Mapping of carbon formation boundary and representative independent reactions," *J. Power Sources*, Vol. 194, pp. 1007-1020, 2009.
[149]. S.R. Yenumala, S.K. Maity, "Reforming of vegetable oil for production of hydrogen: A thermodynamic analysis," *Int. J. Hydrogen Energy*, Vol. 36, pp. 11666-11675, 2011.
[150]. S. Yoon, I. Kang, J. Bae. "Effects of ethylene on carbon formation in diesel autothermal reforming," *Int J Hydrogen Energy*, Vol. 33, pp. 4780-4788, 2008.
[151]. K. Ahmed, K. Foger, "Fuel processing for high-temperature high-efficiency fuel cells," *Ind Eng Chem Res*, Vol. 49, pp. 7239-7256, 2010.
[152]. G. Rabenstein, V. Hacker, "Hydrogen for fuel cells from ethanol by steam-reforming, partial oxidation and combined auto-thermal reforming: A thermodynamic analysis," *J Power Sources*, Vol. 185, Vol. 1293, 1304, 2008.
[153]. K. Faungnawakij, N. Viriya-empikal, W. Tanthapanichakoon, "Evaluation of the thermodynamic equilibrium of the autothermal reforming of dimethyl ether," *Int J Hydrogen Energy*, Vol. 36, pp. 5865-5874, 2011.
[154]. X. Wang, M. Li, M. Wang, H. Wang, S. Li, S .Wang, X. Ma, "Thermodynamic analysis of glycerol dry reforming for hydrogen and synthesis gas production," *Fuel*, Vol. 88, pp. 2148-2153, 2009.
[155]. B.F. Hagh, "Optimization of autothermal reactor for maximum hydrogen production," *Int J Hydrogen Energy*, Vol. 28, pp. 1369-1377, 2003.
[156]. Y.S. Seo, A. Shirley, S.T. Kolaczkowski, "Evaluation of thermodynamically favourable operating conditions for production of hydrogen in three different reforming technologies*," J. Power Sources*, Vol. 108, pp. 213-225, 2002.
[157]. D. Shekhawat, D.A. Berry, T.H. Gardner, D.J. Haynes, J.J. Spivey, Effects of fuel cell anode recycle on catalytic fuel reforming, *J Power Sources*, Vol. 168, pp. 477-483, 2007.
[158]. G. Kolb, Fuel processing for fuel cells, Wiley-VCH Verlag GmbH & Co. KGaA, Weinheim, pp.30-38, 2008.
[159]. D.A. Berry, D. Shekhawat, T.H. Gardner, Development of reaction kinetics for diesel-based fuel cell reformers. Hydrogen, Fuel Cells, and Infrastructure

Technologies, FY 2003 Progress Report, http://www1.eere.energy.gov/hydrogenandfuelcells/pdfs/ivd15_berry.pdf
[160]. I. Aartun, H.J. Venvik, A. Holmen, P. Pfeifer, O. Görke, K. Schubert, "Temperature profiles and residence time effects during catalytic partial oxidation and oxidative steam reforming of propane in metallic microchannel reactors," *Catalysis Today*, Vol. 110, pp. 98-107, 2005.
[161]. M. Ni, Y.C. Leung, M.K.H. Leung, "A review on reforming bio-ethanol for hydrogen production," *Int J Hydrogen Energy*, Vol. 32, pp. 3238-3247, 2007.
[162]. C.J. Winter, "Hydrogen energy – Abundant, efficient, clean: A debate over the energy-system-of-change," *Int J Hydrogen Energy*, Vol. 34, pp. S1-S52, 2009.
[163]. G Collodi, F Wheeler, "Hydrogen production via steam reforming with CO2 capture," *Chemical Engineering Transactions*, Vol. 19, pp. 37-42, 2010.
[164]. J.F. Lin, T.A. Trabold, M.R. Walluk, D.F. Smith, "Autothermal reforming of biodiesel–ethanol–diesel blends for solid oxide fuel cell applications," *Energy & Fuels*, DOI: 10.1021/ef302013d.
[165]. P.V. Snytnikov, S.D. Badmaev, G.G. Volkova, D.I. Potemkin, M.M. Zyryanova, V.D. Belyaev, V.A. Sobyanin, "Catalysts for hydrogen production in a multifuel processor by methanol, dimethyl ether and bioethanol steam reforming for fuel cell applications," *Int J Hydrogen Energy*, Vol. 37, pp. 16388-16396, 2012.
[166]. U. Elghawi, K. Theinnoi, S. Sitshebo, A. Tsolakis, M.L. Wyszynski, H.M. Xu, R.F. Cracknell, R.H. Clark, A. Mayouf, "GC-MS determination of low hydrocarbon species (C1-C6) from a diesel partial oxidation reformer," *Int J Hydrogen Energy*, Vol. 33, pp. 7074-7083, 2008.
[167]. P. Leung, A. Tsolakis, J. Rodríguez-Fernández, S. Golunski, "Raising the fuel heating value and recovering exhaust heat by on-board oxidative reforming of bioethanol," *Energy Environ Sci.*, Vol. 3, pp. 780-788, 2010.
[168]. S. Sitshebo, A. Tsolakis, K. Theinnoi, "Promoting hydrocarbon-SCR of NOx in diesel engine exhaust by hydrocarbon and fuel reforming," *Int. J. Hydrogen Energy*, Vol. 34, pp. 7842-7850, 2009.
[169]. R. Subramanian, L.D. Schmidt, "Renewable olefins from biodiesel by autothermal reforming," *Angwe Chem Int Ed*, Vol. 44, pp. 302-305, 2005.
[170]. A.I. Tsyganok, T. Tsunoda, S. Hamakawa, K. Suzuki, K. Takehira, T. Hayakawa, "Dry reforming of methane over catalysts derived from nickel-containing Mg-Al layered double hydroxides," *J Catalysis*, Vol. 213, pp. 191-203, 2003.
[171]. A. Haryanto, S. Fernando, N. Murali, S. Adhikari, "Current status of hydrogen production techniques by steam reforming of ethanol: A review," *Energy & Fuels*, Vol. 19, pp. 2098-2106, 2005.
[172]. A. Shamsi, J.P. Baltrus, J.J. Spivey, "Characterization of coke deposited on Pt/alumina catalyst during reforming of liquid hydrocarbons," *Appl Catal A: Gen*, Vol. 293, pp. 145-152, 2005.
[173]. S.B. Wang, G.Q. Lu, "A comprehensive study on carbon dioxide reforming of methane over Ni/r-Al2O3 catalyst," *Ind. Eng. Chem. Res*, Vol. 38, pp. 2615-2625, 1999.
[174]. F. Alenazey, C.G. Cooper, C.B. Dave, S.S.E.H. Elnashaie, A.A. Susu, A.A. Adesina, "Coke removal from deactivated Co-Ni steam reforming catalyst using

different gasifying agents: an analysis of the gas-solid reaction kinetics," *Catal. Commun.*, Vol. 10, pp. 406-411, 2009.
[175]. G. Knothe, K.R. Steidley, "Lubricity of components of biodiesel and petrodiesel. The origin of biodiesel lubricity," *Energy & Fuels*, Vol. 19, pp. 1192-1200, 2005.
[176]. G.J. Kraaij, S. Specchia, G. Bollito, L. Mutri, D. Wails, "Biodiesel fuel processor for APU applications," *Int. J. Hydrogen Energy*, Vol. 34, pp. 4495-4499, 2009.
[177]. G.A. Nahar, "Hydrogen rich gas production by the autothermal reforming of biodiesel (FAME) for utilization in the solid-oxide fuel cells: A thermodynamic analysis," *Int. J. Hydrogen Energy*, Vol. 35, pp. 8891-8911, 2010.
[178]. G. Nahar, K. Kendall, "Biodiesel formulations as fuel for internally reforming solid oxide fuel cell," *Fuel Processing Technology*, Vol. 92, pp. 1345-1354, 2011.
[179]. S. Kim, H. Carstensen, A.M. Dean, J. Bae, "Investigation of gas-phase reactions in the mixing region for hydrocarbon autothermal reforming applications," *Int. J. Hydrogen Energy*, Vol. 37, pp. 7545-7553, 2012.
[180]. A.V. González, L.J. Pettersson, "Full-scale autothermal reforming for transport applications: The effect of diesel fuel quality," *Catal Today*, 2013, http://dx.doi.org/10.1016/j.cattod.2012.11.009.
[181]. D. Shekhawat, T.H.Gardner, D.A. Berry, M. Salazar D.J. Haynes, J.J. Spivey, "Catalytic partial oxidation of n-tetradecane in the presence of sulfur or polynuclear aromatics: Effects of support and metal," *Applied Catalysis A: General*, Vol. 311, pp. 8-16, 2006.
[182]. M. Simeone, L. Salemme, D. Scognamiglio, C. Allouis, G. Volpicelli, "Effect of water addition and stoichiometry variations on temperature profiles in an autothermal methane reforming reactor with Ni catalyst," *Int. J. Hydrogen Energy*, Vol. 33, pp. 1252-1261, 2008.
[183]. Z. Yang, Y. Zhang, X. Wang, Y. Zhang, X. Lu, W. Ding, "Steam reforming of coke oven gas for hydrogen production over a NiO/MgO solid solution catalyst," *Energy & Fuels*, Vol. 24, pp. 785-788, 2010.
[184]. D. Shekhawat, D. Berry, N. Siefert, D. Haynes, M. Smith, M. Gallagher, D. Floyd, M. Bergen, J. Spivey, Fuel processing R&D at NETL, 11th Annual SECA Workshop, Pittsburgh, PA, July 27-29, 2010, http://www.netl.doe.gov/publications/proceedings/10/seca/Abstracts/Shekhawat_Poster.pdf.
[185]. S. Pinzi, I.L. Garcia, F.J. Lopez-Gimenez, M.D. Luque de Castro, G. Dorado, M.P. Dorado, "The ideal vegetable oil-based biodiesel composition: A review of social, economical and technical implications," *Energy & Fuels*, Vol. 23, pp. 2325-2341, 2009.
[186]. S.Fernando, M. Hannan, "Development of a novel biofuel blend using ethanol-biodiesel-diesel microemulsions: EB-diesel," *Energy & Fuels*, Vol. 18, pp. 1695-1703, 2004.
[187]. D.Tarlet, J. Bellettre, M. Tazerout, C. Rahmouni, "Prediction of micro-explosion delay of emulsified fuel droplets," *Int. J. Thermal Sciences*, Vol. 48 pp. 449-460, 2009.
[188]. T. Kadota, H. Tanaka, D. Segawa, S. Nakaya, H. Yamasaki, "Microexplosion of an emulsion droplet during Leidenfrost burning," *Proceedings of the Combustion Institute*, Vol. 31, pp. 2125-2131, 2007.

[189]. S. Adhikari, S. Fernando, A. Haryanto, "A comparative thermodynamic and experimental analysis on hydrogen production by steam reforming of glycerin," *Energy & Fuels*, Vol. 21, pp. 2306-2310, 2007.
[190]. US Department of Agriculture and US Department of Energy, Life cycle inventory of biodiesel and petroleum diesel for use in an urban bus, NREL/SR-580-24089, 1998, http://www.biodiesel.org/resources/reportsdatabase/reports/gen/19980501_gen-339.pdf.
[191]. Landfill gas primer - An overview for environmental health professionals, Agency for Toxic Substances & Disease Registry; http://www.atsdr.cdc.gov/hac/landfill/html/ch2.html.
[192]. W. Yuan, A.C. Hansen, Q. Zhang, Z. Tan, "Temperature-dependent kinematic viscosity of selected biodiesel and blends with diesel fuel," *J. American Oil Chemists'* Society Vol. 82, pp. 195-199, 2005.
[193]. D. Fu, L. Chen, L. Qin, "Experiment and model for the viscosity of carbonated MSEA-MEA aqueous solution," *Fluid Phase Equilibria*, Vol. 319, pp. 42-47, 2012.
[194]. W. Yuan, A.C. Hansen, Q. Zhang, "Predicting the temeprature dependent viscosity of biodiesel fuels," *Fuel*, Vol. 88, pp. 1120-1126, 2009.
[195]. M.E. Tat, J.H.V. Gerpen, "The kinematic viscosity of biodiesel and its blends with diesel fuel," *JAOCS*, Vol. 76, pp. 1511-1513, 1999.
[196]. J.R. Kwiatkowski, A.J. McAloon, F. Taylor, D.B. Johnston, "Modeling the process and costs of fuel ethanol production by the corn dry-grind process," *Industrial Crops and Products*, Vol. 23, pp. 288-296, 2006.
[197]. A. McAloon, F. Taylor, W. Yee, K. Ibsen, R. Wooley, "Determining the cost of producing ethanol from corn starch and lignocellulosic feedstocks," NREL/TP-580-28893, 2000.
[198]. J.K. Kim, B.R. Oh, H.J. Shin, C.Y. Eom, S.W. Kim, "Statistical optimization of enzymatic saccharification and ethanol fermentation using food waste," *Process Biochemistry*, Vol. 43, pp. 1308-1312, 2008.
[199]. V. Kovacevic, J. Wesseler, "Cost-effectiveness analysis of algae energy production in the EU," *Energy Policy*, Vol. 38, pp. 5749-5757, 2010.
[200]. H. Xu, X. Miao, Q. Wu, "High quality biodiesel production from a microalga Chlorella protothecoides by heterotrophic growth in fermenters," *J. Biotechnology*, Vol. 126, pp. 499-507, 2006.
[201]. J.M.N. Kasteren, A.P. Nisworo, "A process model to estimate the cost of industrial scale biodiesel production from waste cooking oil by supercritical transesterification. Resources," *Conservation and Recycling*, Vol. 50, pp. 442-458, 2007.